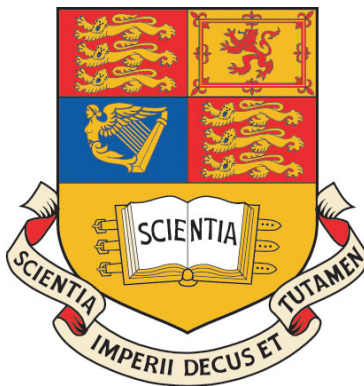


Design Synthesis and Optimisation of VTOL Personal Air Vehicles

by

Omar Katamish

Supervisor: Dr. V.C. Serghides



Department of Aeronautics
Imperial College of Science, Technology and Medicine
Prince Consort Road
London SW7 2BY

This thesis is submitted for the degree of Doctor of Philosophy of
Imperial College London

March 2012

Abstract

Personal Air Vehicles (PAVs) are envisaged to be the next logical step in mobility to alleviate modern transport problems. PAVs could combine the freedom of point-to-point personal mobility with the higher speeds of air travel. Hence the principal aim of this research programme was to develop a preliminary design and optimisation methodology for an innovative vertical take-off and landing (VTOL) PAV with a ducted fan propulsion system driven by a single turboshaft engine. A feasibility study conducted at the start of the programme concluded that a ducted fan powered VTOL PAV provides a flexible, quiet and safe point-to-point mobility platform free from runway constraints and any problems associated with jet efflux or exposed rotating components. To satisfy VTOL and forward flight requirements a design and optimisation methodology for ducted fans and contra-rotating lift fans was developed from a series CFD tests. With a single engine driving all the fans, a methodology was developed for the design of a system of interconnecting gears, gearboxes and shafts. To accommodate the propulsion system and all the other internal components of the aircraft, an innovative tri-surface configuration was generated by adopting a systems packaging approach. Weight minimisation through the use of composites and appropriate prediction methods was crucial to reducing the power requirements and fuel consumption. The aerodynamic surface interaction was explored and optimised using a vortex-lattice method. The same approach was also used to estimate the stability derivatives of the aircraft. The overall performance was analysed utilising the data produced from the above methodologies and that also included an analysis of the transition from hover to forward flight. All the above methodologies were integrated to form an automated PAV design synthesis which in combination with a MATLAB global optimiser is capable of producing variants of the baseline aircraft that are capable of meeting different mission and passenger capacity requirements while maximising a specified merit function.

Declaration

This is to certify that the research presented in this thesis has been carried out at Imperial College London, and has not been previously submitted to any other university for any degree or award. The thesis comprises only my original work. Due acknowledgments are made where appropriate.

Omar Katamish

Acknowledgements

First and foremost I offer my sincerest gratitude to my supervisor Dr. Varnavas Serghides who was abundantly helpful and offered invaluable assistance, support and guidance over the years of this Ph. D. journey.

Special thanks to Errikos Levis and Dhruve Patel for making the office a fun place to work. Their support and humour made the journey easier and a lot more enjoyable! I would also like to thank my other friends Ashley Taheri-Kadkhoda, Anthony Oxlade, Iván Roldan, Richard Hayden and Inji Darwish.

I am also greatly indebted to my family especially my sister Maha, my aunt Nihad and my uncle Fawzi. Most importantly, none of this would have ever been possible without the continued and unwavering support of my parents Ziad and Julieta. In these cases, words simply are not sufficient.

Contents

Abstract	i
Declaration	ii
Acknowledgements	iii
Table of Contents	iv
List of Figures	x
List of Tables	xv
Nomenclature	xvii
1 Introduction	1
1.1 Relevant Literature	3
1.1.1 Feasibility	3
1.1.2 Propulsion	3
1.1.3 Design Synthesis & Optimisation	4
2 Feasibility Study	5
2.1 Overview	5
2.2 The Current & Future State of Travel	6
2.3 The PAV Solution	8
2.4 Market Research	9
2.4.1 Determining a Market Model	9
2.4.2 Market Model and Results	11

2.4.3	Variation with Roadability	13
2.4.4	Variation with Cruise Velocity	14
2.4.5	Variation with Number of Passengers	15
2.4.6	Variation with Range	15
2.4.7	Variation with Easy-To-Fly Technology	16
2.4.8	Market Conclusions	17
2.5	PAV Categories	18
2.5.1	Single-mode	18
2.5.2	Dual-mode	19
2.5.3	<i>CTOL - Conventional Take-off and Landing</i>	20
2.5.4	<i>ESTOL - Extremely Short Take-off and Landing</i>	20
2.5.5	<i>VTOL - Vertical Take-off and Landing</i>	21
2.6	History of PAVs	21
2.6.1	Flying Car	21
2.7	Modern PAV Concepts	23
2.7.1	Terrafugia	23
2.7.2	AMV	24
2.7.3	Moller Skycar	25
2.7.4	Carter Aviation Technologies (CarterCopter)	26
2.7.5	NASA PAVs	27
2.8	Propulsion	28
2.8.1	Jet	28
2.8.2	Propeller	29
2.8.3	Fan	29
2.8.4	Rotor	30
2.9	Aerodynamics	31
2.10	Stability and Control	32
2.11	Structures and Weight	33
2.12	Environmental Effects	33
2.13	Operational Environment and Safety	34
2.14	Maintenance and Other Challenges	35

2.15	Outline of PAV Requirements	36
2.16	Other Applications	38
2.16.1	Military	38
2.16.2	Air Ambulance	38
2.16.3	Air Taxi - Business	38
3	Initial Sizing	39
3.1	Overview	39
3.2	Baseline Configuration	40
3.3	Carpet Plot	41
3.4	Mission Profile & Weight Fractions	42
3.5	Initial Sizing Methodology	43
4	Propulsion	47
4.1	Overview	47
4.2	Fan Design Theory	49
4.2.1	Cascade Theory	49
4.2.2	Blade Element Theory	52
4.3	Fan Design Methodology	54
4.3.1	Mixed Design Theory	54
4.3.2	Design Simplifications	56
4.3.3	Defining Models For CFD	57
4.4	CFD	61
4.5	Parametric Analysis	63
4.6	Fan Performance	65
4.7	CFD Fan Validation	68
4.8	Propulsion Methodology	70
4.9	Inlet & Guide Vane Design	75
4.9.1	Inlet Design - <i>Transition</i>	75
4.9.2	Guide Vane Design	78
4.9.3	Inlet & Guide Vane Methodology & Flowchart	79
4.10	Gear Design	81

4.11	Shaft Design	85
4.12	Engine Sizing	87
5	Systems Packaging	89
5.1	Overview	89
5.2	Fans, Gears & Shafts	90
5.3	Cabin	96
5.4	Undercarriage	98
5.5	2D Packaging	101
5.6	3D Packaging	110
6	Weight & Balance	114
6.1	Overview	114
6.2	Component Weights	115
6.3	Weight Validation	118
6.4	Aircraft Balance	121
7	Aerodynamics	124
7.1	Overview	124
7.2	Wing	125
7.3	Canard & Tail	127
7.4	Vortex Lattice Method - <i>Tornado</i>	129
7.5	Drag	129
7.6	Elliptical Lift Distribution	132
8	Stability	135
8.1	Overview	135
8.2	Static Stability	136
8.2.1	Longitudinal	136
8.2.2	Lateral	138
8.3	Dynamic Stability	139
8.3.1	Longitudinal	139
8.3.1.1	Phugoid	139

8.3.1.2	Short Period Pitching Oscillation	140
8.3.2	Lateral	141
8.3.2.1	Spiral	141
8.3.2.2	Dutch Roll	142
9	Performance	143
9.1	Overview	143
9.2	Cruise	143
9.3	Loiter	144
9.4	Climb Rate	145
9.5	Turn Rate	145
9.6	Specific Excess Power	146
9.7	Take-off Distance	147
9.8	Landing Distance	148
9.9	Transition Model	149
10	Optimisation	151
10.1	Overview	151
10.2	Global Optimiser	152
10.2.1	Interior-Point Algorithm	152
10.2.2	Global Search Algorithm	154
10.3	Input Parameters & Merit Function	154
11	Full Methodology Implementation	159
11.1	Operations of Design Methodology & Optimisation	159
11.2	Computer Program Architecture	162
11.2.1	MATLAB	162
11.2.2	VLM - <i>Tornado</i>	162
11.2.3	CFD - <i>ANSYS</i>	163
11.2.4	Programming Assessments	164
12	Case Study	167
12.1	Synthesis and Optimisation of a 4-Passenger PAV	167

12.1.1 Dimensions & Weights	174
12.1.2 Aerodynamics, Stability & Balance	176
12.1.3 Performance	178
12.2 Synthesis and Optimisation of a 6-Passenger PAV	182
12.2.1 Dimensions & Weights	188
12.2.2 Aerodynamics, Stability & Balance	190
12.2.3 Performance	192
13 Concluding Remarks	195
13.1 Discussion	195
13.2 Conclusion	201
13.3 Suggestions for Further Work	203
Bibliography	205
A Feasibility Study	209
A.1 Current PAV Performance Tables	209
B Propulsion	212
B.1 Fan Parametric Equations	212
B.2 Gear Volume Equations	213
B.3 Example of Thrust Calculation	214
C Initial Sizing	216
C.1 Carpet Plot Equations	216
D Systems Packaging	217
D.1 2D Packaging	217
E Weight & Balance	219
E.1 Component Weight Equations	219
E.1.1 Wing Group	219
E.1.2 Remaining Components	220
E.2 Weight Validation	222

F Aerodynamics	224
F.1 Wing Lift Coefficient Increment	224
F.2 Wing Moment Coefficient Increment	224
F.3 Canard Lift Coefficient Increment	225
F.4 Canard Moment Coefficient Increment	226
F.5 Horizontal Tail Lift Coefficient Increment	226
F.6 Horizontal Tail Moment Coefficient Increment	227
F.7 Drag	229
G Stability	230
G.1 Static Stability	230
G.2 Dynamic Stability	231
G.2.1 Phugoid	231
G.2.2 SPPO	231
G.2.3 Sprial	232
G.2.4 Dutch Roll	232

List of Figures

2.1	Door-to-Door travel speeds for automobile, commercial airliner and PAV	7
2.2	Circle of Transport Economics [1]	8
2.3	Market Maturation S-curves	10
2.4	traveller's motivational characteristics that influence which mode of transport they will use [6]	10
2.5	Research and development parameters which influence PAV design [6]	11
2.6	The variation of PAV market share with the variation of cost [6]	12
2.7	Distribution of vehicle choice for varied incomes and travel distances at baselines: \$100/hr and \$150/hr [6]	13
2.8	The variation of PAV market share with the variation of cost [6]	14
2.9	The variation of PAV market share for a dual-mode and single-mode PAVs [6] .	15
2.10	The variation of PAV choice distribution for a dual-mode and single-mode PAVs [6]	16
2.11	The variation of PAV market share with cruise velocity where: HS = 400 km/h, Baseline = 350 km/h, LS = 300 km/h [6]	17
2.12	The variation of PAV market share with number of passengers where: P6 = 6-passenger, Baseline = 4-passenger, P2 = 2-passenger [6]	17
2.13	The variation of PAV market share with range [6]	18
2.14	The variation of PAV market share with easy-to-fly technology where: S1 = without easy-to-fly technology [6]	18
2.15	PAV Categories	19
2.16	The VUIA 1 [19]	21
2.17	Flying car designs [20]	22

2.18	Unconventional PAV designs [21, 22]	23
2.19	The Terrafugia Transition PAV [23]	23
2.20	The AMV-211 PAV [24]	24
2.21	The Skycar PAV [22]	25
2.22	The Cartercopter PAVs [25]	27
2.23	The NASA Intra-Urban Gridlock Commuter (ESTOL PAV) [2]	27
2.24	Propfan designs [26]	30
3.1	Baseline Configuration	40
3.2	Baseline Configuration side profile	41
3.3	Carpet Plot	42
3.4	Mission Profile	43
3.5	Initial Sizing Methodology	46
4.1	Fan configuration	48
4.2	Fan layout configurations	48
4.3	Velocity triangles through a rotor stage.	49
4.4	Velocities and aerodynamic forces on a typical blade element.	52
4.5	Velocity triangles through a contra-rotor stage.	58
4.6	Lift fan rotor stage, <i>Bladegen</i>	62
4.7	Airbus A400M Scimitar propeller (swept blades) [19]	63
4.8	Fan CFD Outputs	63
4.9	Fan performance with varying pitch and Mach number	67
4.10	Comparing experimental and CFD fan performance data	69
4.11	Propulsion methodology overview	70
4.12	First stage of Propulsion methodology	72
4.13	Second stage of Propulsion methodology	73
4.14	Third stage of Propulsion methodology	74
4.15	Duct dimensions and variables for lift fan	76
4.16	Duct CFD Outputs	77
4.17	Guide Vane CFD Outputs	79
4.18	Duct and Guide Vane methodology for lift fan	80

4.19	Fan gear	81
4.20	Different gears configurations [45]	82
4.21	Gear tooth sizing	84
4.22	Engine data	87
5.1	Packaging of main lift fan, gears and guide vane	90
5.2	Fans, gears and shafts packaging x - y plane	91
5.3	Fans, gears and shafts packaging x - z plane	92
5.4	Fans, gears and shafts packaging y - z plane	92
5.5	Different gearbox designs	93
5.6	Fan tilt mechanism	93
5.7	F-35 Lift fan doors [19]	94
5.8	Fan positioning x - y plane	95
5.9	Rear section portioning x - y plane	95
5.10	Cabin seating configurations for a 6-PAX aircraft	96
5.11	Cabin conceptual design for a 4-PAX aircraft	97
5.12	Canopy conceptual design for a 4-PAX aircraft	97
5.13	Undercarriage placement	98
5.14	Undercarriage overturn angle	100
5.15	Internal component positioning x - y plane	102
5.16	Lifting surface positioning x - y plane	103
5.17	Engine intake and exhaust positioning x - y plane	104
5.18	Engine intake and exhaust positioning x - z plane	104
5.19	Structural beam positioning x - y plane	105
5.20	Fuselage control point locations x - y plane	106
5.21	Internal component positioning x - z plane	107
5.22	Fan, Gear and Shaft positioning x - z plane	109
5.23	Conic sections	110
5.24	3D packaged PAV - <i>Front view</i>	112
5.25	3D packaged PAV - <i>Rear view</i>	112
5.26	3D packaged PAV - <i>Lofted fuselage using conic sections</i>	113

6.1	Structural and Propulsion weight component proportions	117
6.2	Equipment and Total weight component proportions	117
6.3	Component CG positions the x-y plane	122
6.4	Structural component CG positions in the x-y plane	122
6.5	Component CG positions the x-z plane	123
7.1	Winglets design	127
7.2	Lift distribution iterations	133
7.3	Twist distribution	134
8.1	Coordinate system definitions for stability calculations	139
9.1	VTOL transition performance of a 4-passenger PAV	150
10.1	Evolution of optimisation process	158
11.1	PAV design synthesis flow chart	160
11.2	PAV Optimisation flow chart	161
12.1	Optimisation of a 4-passenger PAV	170
12.2	MATLAB generated 3D model of 4-passenger PAV - <i>Left front view, forward flight configuration</i>	171
12.3	MATLAB generated 3D model of 4-passenger PAV - <i>Left front view, hover configuration</i>	172
12.4	MATLAB generated 3D model of 4-passenger PAV - <i>Left rear view, forward flight configuration</i>	172
12.5	MATLAB generated 3D model of 4-passenger PAV - <i>Side view, forward flight configuration</i>	173
12.6	MATLAB generated 3D model of 4-passenger PAV - <i>Front view, forward flight configuration</i>	173
12.7	MATLAB generated 3D model of 4-passenger PAV - <i>Systems Packaging</i>	174
12.8	Specific Excess Power plot of the optimised 4-passenger PAV	180
12.9	VTOL transition performance of the optimised 4-passenger PAV	181
12.10	Optimisation of a 6-passenger PAV	184

12.11MATLAB generated 3D model of 6-passenger PAV - <i>Left front view, forward flight configuration</i>	185
12.12MATLAB generated 3D model of 6-passenger PAV - <i>Left front view, hover configuration</i>	186
12.13MATLAB generated 3D model of 6-passenger PAV - <i>Left rear view, forward flight configuration</i>	186
12.14MATLAB generated 3D model of 6-passenger PAV - <i>Side view, forward flight configuration</i>	187
12.15MATLAB generated 3D model of 6-passenger PAV - <i>Front view, forward flight configuration</i>	187
12.16MATLAB generated 3D model of 6-passenger PAV - <i>Systems Packaging</i>	188
12.17Specific Excess Power plot of the optimised 6-passenger PAV	193
12.18VTOL transition performance of the optimised 6-passenger air taxi	194
B.1 Propulsion fan thrust calculation	214
B.2 Lift fan thrust calculation	215
B.3 Pitch fan thrust calculation	215
D.1 Packaging of PAV in the $x - y$ plane	217
D.2 Packaging of PAV in the $x - z$ plane	218

List of Tables

2.1	Market model baseline PAV specifications [6]	12
2.2	Market model PAV specifications	19
3.1	Cessna 400 specifications [38]	45
3.2	Socata TBM 850 specifications [39]	45
4.1	Main fan variables	59
4.2	Lift fan input variable ranges	60
4.3	Propulsion fan input variable ranges	60
4.4	Propulsion fan design values	66
4.5	Fan validation geometrical data	68
4.6	Inlet and Duct input variable ranges	76
4.7	Guide Vane input variable ranges	78
4.8	Gear factors and values for face width calculation	83
4.9	Shaft factors and values for diameter calculation	86
5.1	Strut sizing variables	100
5.2	Fuselage skin (x, y) control points	106
5.3	Fuselage skin (x, z) control points	109
6.1	Composite weight factors [14]	116
6.2	Component Weights of a 4 passenger PAV	118
6.3	Component Weights of a Cessna 400	119
6.4	Component Weights of a Socata TBM 850	120
10.1	Design synthesis input variables	156

10.2 Optimiser input variables ranges	156
12.1 Input variables of a 4-passenger PAV optimisation	168
12.2 Output variables of a 4-passenger PAV optimisation	169
12.3 Dimensions of the optimised 4-passenger PAV	175
12.4 Component Weights of the optimised 4-passenger PAV	175
12.5 Aerodynamic values of the optimised 4-passenger PAV	176
12.6 Stability and Balance values of the optimised 4-passenger PAV	178
12.7 Performance values of the optimised 4-passenger PAV	179
12.8 Input variables of a 6-passenger PAV optimisation	182
12.9 Output variables of a 6-passenger PAV optimisation	183
12.10 Dimensions of the optimised 6-passenger PAV	189
12.11 Component Weights of the optimised 6-passenger PAV	189
12.12 Aerodynamic values of the optimised 6-passenger PAV	190
12.13 Stability and Balance values of the optimised 6-passenger PAV	191
12.14 Performance values of the optimised 6-passenger PAV	192
A.1 The Transition's performance data and dimensions [23]	209
A.2 The AMV-211's performance data and dimensions [24]	210
A.3 The Moller Skycar M400's performance data and dimensions [22]	210
A.4 The 2-seater CarterCopter's performance data and dimensions [25]	211
A.5 The NASA PAV concept's performance data and dimensions [2]	211
E.1 Wing component weight factors	220
E.2 Component Weights of a Pilatus PC-12	222
E.3 Component Weights of a Cessna 210	223
F.1 Wing lift and moment increment factors	225
F.2 Canard lift and moment increment factors	227
F.3 Horizontal tail lift and moment increment factors	228

Nomenclature

a	The speed of sound
\bar{a}	Average deceleration
ALT_{cruise}	Cruise altitude
AR	Wing aspect ratio
AR_{can}	Canard aspect ratio
AR_{eff}	Effective wing aspect ratio
AR_{htail}	Horizontal tail aspect ratio
AR_{vtail}	Vertical tail aspect ratio
b_w	Wing span
b_{can}	Canard span
B_{fus}	Fuselage maximum width
b_{htail}	Horizontal tail span
$B_{U/C}$	x -distance between nose and rear undercarriage
b_{vtail}	Vertical tail span
$b_{winglet}$	Winglet span
c	Local chord
\bar{c}	Mean aerodynamic chord
C_{can}	Canard volume coefficient
c_{crank}	Crank chord
c_f/c	Flap chord to wing chord ratio
$(c_f/c)_{can}$	Canardvator chord to canard chord ratio
$(c_f/c)_{htail}$	Elevator chord to horizontal tail chord ratio
$(c_f/c)_{vtail}$	Rudder chord to vertical tail chord ratio

C_{htail}	Horizontal tail volume coefficient
c_{rGV}	Guide vane root chord
C_{vtail}	Vertical tail volume coefficient
C_d	Aerofoil drag coefficient
C_{D_1}	Steady state drag coefficient for dynamic stability calculations
$C_{D_{cruise}}$	Cruise drag coefficient
C_{D_i}	Induced drag coefficient
$C_{D_{LP}}$	Leakage and protuberance drag coefficient
C_{D_U}	Drag derivative with respect to velocity
C_{D_0}	Profile drag coefficient
$C_{D_0 \text{ } U/C}$	Undercarriage profile drag coefficient
$C_{D_{flap}}$	Flap profile drag coefficient
$C_{D_{trim}}$	Trim drag coefficient
C_f	Skin friction coefficient
C_l	Aerofoil lift coefficient
C_{L_1}	Steady state lift coefficient for dynamic stability calculations
C_{l_α}	Aerofoil lift curve slope
$C_{L_{\alpha_{can}}}$	Canard lift curve slope
$C_{L_{\alpha_{htail}}}$	Horizontal tail lift curve slope
$C_{L_{\alpha_{PAV}}}$	PAV lift curve slope
$C_{L_{\alpha_w}}$	Wing lift curve slope
$C_{L_{\alpha_w \text{ } flap}}$	Wing lift curve slope flaps down
C_{l_β}	Roll moment derivative coefficient with respect to sideslip angle
$C_{L_{can}}$	Canard lift coefficient
$C_{L_{cruise}}$	Cruise lift coefficient
$C_{L_{htail}}$	Horizontal tail lift coefficient
$C_{L_{PAV}}$	PAV lift coefficient
C_{L_w}	Wing lift coefficient
C_{l_0}	Aerofoil zero angle of attack lift coefficient

$C_{L_{max \; clean}}$	Maximum lift coefficient clean
$C_{L_{max \; flaps}}$	Maximum lift coefficient flaps down
C_m	Moment coefficient
$C_{m_{can}}$	Canard moment coefficient
$C_{m_{fus}}$	Fuselage moment coefficient
$C_{m_{htail}}$	Horizontal tail moment coefficient
C_{m_w}	Wing moment coefficient
C_{m0}	Aerofoil zero lift moment coefficient
C_{n_β}	Yaw moment derivative coefficient with respect to sideslip angle
C_P	Power coefficient
C_T	Thrust coefficient
$C_{T_{x_1}}$	Steady state thrust coefficient for dynamic stability calculations
$C_{T_{x_U}}$	Lift derivative with respect to velocity
D	Drag
D_{duct}	Duct diameter
D_{fus}	Fuselage diameter
d_{tire}	Tire diameter
$\Delta C_{D_{0 \; flaps}}$	Flap profile drag coefficient
$\Delta C_{D_i \; flaps}$	Flap induced drag coefficient
$\Delta C_{L_{can}}$	Canard lift coefficient increment due to canardvator deflection
$\Delta C_{L_{htail}}$	Horizontal tail lift coefficient increment due to elevator deflection
ΔC_{L_w}	Wing lift coefficient increment due to flaps
$\Delta C_{m_{can}}$	Canard moment coefficient increment due to canardvator deflection
$\Delta C_{m_{htail}}$	Horizontal tail moment coefficient increment due to elevator deflection
ΔC_{m_w}	Wing moment coefficient increment due to flaps
Δn	Landing approach factor
$\partial\epsilon/\partial\alpha$	Downwash derivative
e	Oswald's efficiency factor
$Endurance$	Loiter endurance time

F	Lift curve slope fuselage factor
$F_{M_{max}}$	Main undercarriage maximum load
$F_{N_{dyn}}$	Nose undercarriage dynamic load
$F_{N_{max}}$	Nose undercarriage maximum load
$F_{N_{min}}$	Nose undercarriage minimum load
$f_{t/o}$	Take-off factor
$F_{U/C}$	Undercarriage load
FF	Drag form factor
g	Gravitational acceleration
h_{cabin}	Cabin height
h_{duct}	Duct height
h_{hub}	Hub height
$h_{hub_{LF}}$	Lift fan hub height
h_L	Landing obstacle height
H_{PAV}	PAV overall height
$h_{PF_{duct}}$	Propulsion fan duct height
$h_{t/o}$	Take-off obstacle height
h_{total}	Duct total height
h_0	Enthalpy
i_{can}	Canard incidence setting angle
i_{htail}	Horizontal tail incidence setting angle
i_w	Wing incidence setting angle
I_{xx}	Moment of inertia about x -axis
I_{yy}	Moment of inertia about y -axis
I_{zz}	Moment of inertia about z -axis
K_{can}	Canard induced drag factor
K_{htail}	Horizontal tail induced drag factor
K_{wing}	Wing induced drag factor

L_β	Roll moment derivative with respect to sideslip angle
L_{cabin}	Cabin length
L_{can}	Distance between canard and wing aerodynamic centres
L_{ENG}	Length of engine
L_{htail}	Distance between horizontal tail and wing aerodynamic centres
L_{PAV}	PAV overall length
L_r	Roll moment derivative with respect to yaw rate
$L_{U/C}$	Undercarriage strut length
L_{vtail}	Distance between vertical tail and wing aerodynamic centres
L/D	Lift-to-drag ratio
$(L/D)_{cruise_I}$	Optimisation input cruise lift-to-drag ratio
$(L/D)_{cruise_O}$	Optimisation output cruise lift-to-drag ratio
M_α	Pitch moment derivative with respect to angle of attack
$M_{\dot{\alpha}}$	Pitch moment derivative with respect to rate of angle of attack
M_q	Pitch moment derivative with respect to pitch rate
M_{cruise}	Cruise Mach number
M_{cruise_I}	Optimisation input cruise Mach number
\dot{m}	Mass flow rate
MF	Merit function
M_{tip}	Mach tip number
M_{tip}^U	Rotational velocity U Mach tip number
n	Load factor
N_β	Yaw moment derivative with respect to sideslip angle
N_{PAX}	Number of passengers
N_r	Yaw moment derivative with respect to yaw rate
N_b	Number of blades
$N_{b_{fan}}$	Fan number of blades
$N_{b_{PF}}$	Pitch fan number of blades
$N_{b_{GV}}$	Guide vane number of blades
$N_{b_{LF}}$	Lift fan number of blades
$N_{b_{PF}}$	Propulsion fan number of blades

P	Power
P_{0EQ}	Equivalent power
P_{10k}	Power at 10000ft altitude
P_{av}	Power available
P_{climb}	Power required for climb
P_{fPF}	Pitch fan power
P_{land}	Power required for landing
P_{LF}	Lift fan power
P_{total}	Total installed power
$P_{total_{hp}}$	Total installed power horsepower
P_{trans}	Power required for transition
P_i	Ideal power
$P_{i_{static}}$	Ideal power static
P_s	Specific excess power
Q	Interference factor
q	Dynamic pressure
R	Fan tip radius
R_D	Duct radius
r_{duct}	Duct inlet radius
R_{GfPF}	Pitch fan gear radius
R_{GLF}	Lift fan gear radius
R_{GPF}	Propulsion fan gear radius
$R_{GpinfPF}$	Pitch fan pinion gear radius
R_{GpinLF}	Lift fan pinion gear radius
R_{GpinPF}	Propulsion fan pinion gear radius
R_{GV}	Guide vane radius
r_h	Fan hub radius
R_{hub}	Fan hub radius

r_{hub_0}	Fan hub outer radius
r_{hub_i}	Fan hub inner radius
R_{fPF}	Pitch fan radius
R_{LF}	Lift fan radius
R_{PF}	Propulsion fan radius
R_{sg}	Gearbox gear radius
r_t	Fan tip radius
$Range$	Range
$Range_I$	Optimisation input range
$Range_O$	Optimisation output range
S_{can}	Canard reference area
S_{exp}	Wing exposed area
S_{htail}	Horizontal tail reference area
S_{ref}	Wing reference area
S_{vtail}	Vertical tail reference area
$SEAT_I$	Optimisation seat configuration input
SFC	Specific fuel consumption
S_{flap}	Flap reference area
SM	Static margin
T_{fPF}	Pitch fan thrust
T_{LF}	Lift fan thrust
T_{PF}	Propulsion fan thrust
$T_{PF_{static}}$	Propulsion fan static thrust
T_q	Torque
t/c	Thickness to chord ratio
$t_{1/2PH}$	Time to half amplitude Phugoid
$t_{1/2SP}$	Time to half amplitude Spiral
$Tr_{U/C}$	Undercarriage track
$(\bar{T}/W)_{t/o}$	Average thrust to weight ratio during take-off
U	Fan rotational velocity
U_1	Steady state cruise speed for dynamic stability calculations

U_t	Fan rotational tip velocity
V_{APP}	Approach speed
V_∞	Free stream velocity
V_{LOF}	Lift off speed
V_{ratio}	Blade relative velocity speed ratio
V_{stall}	Stall speed flaps down
$V_{stall\ clean}$	Stall speed clean
V_{STO}	Stall speed clean
V_{TD}	Touch down speed
V_v	Climb velocity
V_{cross}	Cross flow velocity
V_{cruise}	Cruise speed
V_{cruise_I}	Optimisation input cruise speed
Vol_{fan}	Fan volume
Vol_{GV}	Guide vane volume
Vol_{hub}	hub volume
V_r	Fan radial velocity
V^{rel}	Fan blade radial velocity
V_θ	Fan blade swirl velocity
V_x	Fan blade design axial velocity
V_{xa}	Fan blade actual axial velocity
W_{PAX}	Weight of passengers
w_{tire}	Tire width
W/P	Weight to power ratio
W/S	Wing loading
$(W/S)_{t/o}$	Take-off wing loading
W_0	Maximum take-off weight
W_e	Empty weight
W_f	Fuel weight

$\bar{x}_{ac_{can}}$	Canard aerodynamic centre location as a ratio of \bar{c}
$\bar{x}_{ac_{tail}}$	Horizontal tail aerodynamic centre location as a ratio of \bar{c}
$\bar{x}_{ac_{wing}}$	Wing aerodynamic centre location as a ratio of \bar{c}
\bar{x}_{CG}	Centre of gravity location as a ratio of \bar{c}
\bar{x}_{NP}	Neutral point location as a ratio of \bar{c}
\bar{x}_{ref}	Reference point location as a ratio of \bar{c}
x_{CG}	Centre of gravity x -axis location
Y_β	Lateral force derivative with respect to sideslip angle
y_{CG}	Centre of gravity y -axis location
Z_α	Vertical force derivative with respect to sideslip angle
z_{CG}	Centre of gravity z -axis location
α	Angle of attack
α_0	Aerofoil zero lift angle of attack
$\alpha_{0_{can}}$	Canard tail zero lift angle of attack
$\alpha_{0_{htail}}$	Horizontail tail zero lift angle of attack
α_{0_w}	Wing tail zero lift angle of attack
$\beta_{sideslip}$	Blade inlet angle
β_1	Blade setting angle
γ_{climb}	Climb angle
$\bar{\gamma}_L$	Average approach angle
Γ_{can}	Canard dihedral
Γ_{htail}	Horizontal tail dihedral
γ_{LOF}	Lift off angle
Γ_w	Wing dihedral
Γ_{vtail}	Vertical tail dihedral
δ	Blade pitch angle
δ_{can}	Canardvator deflection angle
δ_f	Flap deflection angle
$\delta_{flaperon}$	Flaperon deflection angle
δ_{htail}	Elevator deflection angle
Δ_{Range}	Range constraint factor

ζ	Conic section shape parameter
η	Efficiency
$\eta_{gear_{fPF}}$	Pitch fan gear efficiency
$\eta_{gear_{LF}}$	Lift fan gear efficiency
$\eta_{gear_{PF}}$	Propulsion fan gear efficiency
η_{inl}	Engine inlet efficiency
η_p	Propulsive efficiency
η_{static}	Fan static efficiency
λ_b	Fan blade taper ratio
$\Lambda_{c/4 \ can}$	Canard quarter chord sweep
$\Lambda_{c/4 \ htail}$	Horizontal tail quarter chord sweep
$\Lambda_{c/4}$	Wing quarter chord sweep
$\Lambda_{c/4 \ vtail}$	Vertical tail quarter chord sweep
λ_{GV}	Guide vane blade taper ratio
λ_i	Inflow ratio V_x/U
$\Lambda_{in \ LE}$	Inboard wing-fuselage section leading edge sweep
$\Lambda_{in \ TE}$	Inboard wing-fuselage section trailing edge sweep
$\Lambda_{out \ LE}$	Outboard wing section leading edge sweep
$\Lambda_{out \ TE}$	Outboard wing section trailing edge sweep
Λ_{max_t}	Maximum thickness sweep
λ_t	Blade tip inflow ratio V_x/U_t
λ_{can}	Canard taper ratio
λ_{htail}	Horizontal tail taper ratio
λ_w	Wing taper ratio
λ_{vtail}	Vertical tail taper ratio
μ'	Ground roll friction factor
μ_g	Ground roll friction coefficient
ξ_{DR}	Dutch roll damping ratio
ξ_{PH}	Phugoid damping ratio
ξ_{SPPO}	Short Period Pitching Oscillation damping ratio

ρ	Density of air
ρ_0	Density of air at S.L.
ρ_{alum}	Density of aluminium
ρ_{comp}	Density of composite
ρ_{steel}	Density of steel
σ	Fan solidity
σ_{fPF}	Pitch Fan solidity
σ_{LF}	Lift Fan solidity
σ_{GV}	Guide vane solidity
σ_{PF}	Propulsion solidity
σ_{max}	Centrifugal blade stress
σ_{10k}	Density ratio relative of the density at 10000ft
σ_{SL}	Density ratio relative of the density at S.L.
τ_w	Wall skin friction
ψ	Undercarriage overturn angle
$\dot{\psi}$	Turn rate
ω	Rotational velocity
Ω	Rotational speed
ω_{DR}	Dutch roll natural frequency
ω_{PH}	Phugoid natural frequency
ω_{SPP0}	Short Period Pitching Oscillation natural frequency

Chapter 1

Introduction

Throughout history humans have improved their quality of life through transport. It links the world together through large networks, increasing mobility, promoting economic growth and population expansion. Propelling and perhaps as a result of this growth, the daily utilisation of personal transport has increased, offering travel flexibility for business or leisure.

Although the growth of transport has been very beneficial to society, it is not without its problems. The rise in vehicle numbers due to increased travel demands is stretching the existing global system. Congestion is increasing and bringing with it problems for the economy and the environment [1]. Statistics show that road and air travel are going to double in the next 50 years, which implies that congestion will increase. Whilst technology has allowed for vehicle travel speeds to increase, the average speed for journeys remains constant at 48 km/h (30 mph) [2]. Transportation must constantly evolve to cope with these problems, so what is the next logical step?

Personal Air Vehicles (PAVs) are envisaged as the next logical step in mobility. PAVs are defined as self-operated aircraft that are affordable and easily operated by a large portion of the general population. The goal of these aircraft is to convey the freedom of personal mobility to the skies, effectively reducing journey times and improving overall quality of life.

The aim of this research was to produce an automated design synthesis and optimisation

program for vertical take-off and landing (VTOL) PAVs. A VTOL PAV provides a flexible, quiet and safe point-to-point mobility platform free from runway constraints and any problems associated with jet efflux or exposed rotating components. The research began with a feasibility study to identify the problems with the continued growth of transport and whether PAVs were a viable solution to these problems. An investigation was concluded into the possible market demand for PAVs. The various PAV categories were explored, highlighting the advantages and disadvantages of historical and modern PAV designs. The optimum PAV requirements were established and the design baseline configuration was chosen.

The baseline configuration was a ducted fan VTOL PAV driven by a single turboshaft engine and a system of gears and shafts. A propulsion methodology was developed through CFD analysis and regression techniques. The propulsion methodology encompassed the design of the ducted fans, duct inlets, guide vanes, gears and shafts.

An innovative tri-surface rear wing design was developed to accommodate all the fans, engine, cabin and other components. The aircraft was packaged in a packaging methodology using parametric distance equations to ensure it accommodated all the variations in component size. A component weight estimation methodology was developed to accurately predict the weight of the aircraft. Using the component weights the aircraft was balanced according to static stability criteria. A vortex-lattice method was incorporated into the synthesis to analyse the aerodynamic and stability characteristics of the aircraft. The performance of the aircraft including VTOL simulations was analysed to determine if the user inputted mission profile was met.

These methodologies were gathered into a complete PAV synthesis program written in MATLAB. A set of mission profile variables and aircraft geometry variables were chosen and then the synthesis was linked to a global optimiser.

1.1 Relevant Literature

1.1.1 Feasibility

Current studies into the state of traffic shows two things: An increase in the amount of travel miles to be expected, and the an increase in the amount of congestion. Studies have been conducted by the World Business Council For Sustainable Development [1], European Commission [3], NASA [2], Airbus and Boeing [4, 5].

The studies conducted by the World Business Council For Sustainable Development [1] and European Commission [3], both point to an increase in traffic congestion. The studies investigate the growth in the annual total distance travelled and the future trends of travel.

The studies conducted by Airbus and Boeing [4, 5] investigates the current transport market for regional flights, and show how the demand will increase rapidly in the future.

Several studies have been conducted to determine the feasibility of PAVs. NASA and various university researchers have conducted studies to determine the feasibility of PAVs. All off these studies can be generally broken down into three stages. The first stage being to determine whether a transport infrastructure can be setup to accommodate PAVs. The second concerns the marketability of such a vehicle and the third the availability of technologies to design a cheap, safe and practical PAV. The papers by Mark D. Moore [2] and J.-H. Lewe, D. DeLaurentis et al. [6, 7] have also been useful in this regard.

1.1.2 Propulsion

The core texts that address fan design are: H.I.H. Saravanamutto's *Gas Turbine Theory* [8], R.A. Wallis' *Axial Flow Fans & Ducts* [9] and J.G. Leishman's *Principles of Helicopter Aerodynamics* [10]. These texts cover fan design theory (cascade theory and blade element theory) for subsonic tip speeds. H.I.H. Saravanamutto qualitatively touches on supersonic tip speed design.

1.1.3 Design Synthesis & Optimisation

There are a few core texts that address preliminary design of aircraft: Daniel Raymer's *Aircraft Design: A Conceptual Approach* [11], Jan Roskam's *Airplane Design: Part I - VIII* [12], Egbert Torenbeek's *Synthesis of Subsonic Airplane Design* [13] and Leland Nicolai's *Fundamentals of Aircraft Design* [14]. These texts provide the foundation for aircraft conceptual and preliminary design, containing general design methodologies for various aircraft types and configurations. These methodologies were constructed from a combination of theoretical methods and statistical data on existing aircraft.

Although these texts contain design methodologies for various aircraft configurations, the methodologies are broad and do not cover all the material required for the design of non-conventional aircraft such as PAVs.

Design and optimisation methods developed by V.C. Serghides [15] to design and optimise a canard-delta combat aircraft have been widely adopted for several research programmes at Cranfield University and Imperial College London. Journals by R.H. Byrd et al. [16] and Ugray et al. [17] cover mathematical programming methods for global optimisation. These texts cover the design synthesis and multi-variate optimisation techniques required for this research programme.

Chapter 2

Feasibility Study

2.1 Overview

A feasibility study was conducted to identify the problems with modern travel and whether Personal Air Vehicles (PAVs) are a viable solution to alleviate these problems. The study explores the history of PAVs as well as modern designs and their varying categories. Subsequently an investigation into the available technologies that could be incorporated into a new novel PAV design was concluded.

The frequency and the number of people travelling has been increase steadily over the last century. With this increase, current transport infrastructures have become more stretched and congested. As a consequence, whilst technology has allowed for vehicle travel speeds to increase, the average speed for journeys has remained constant at 48 km/h (30 mph).

PAVs have been proposed as the next generation of personal travel since the inception of manned flight. Over the last century there have been many designs that have attempted to make personal flight accessible and affordable to the general public but with no real success.

Early PAV designs were mainly constrained by the limitations of the technology of the time. The challenge facing current concepts include various design, operational and environmental obstacles that must be overcome in order to preserve mobility, maintainability, marketability,

safety and affordability.

PAVs seek to provide a solution to current personal travel problems by alleviating congestion from roads and domestic flights, decreasing travel times and increasing the range that an individual can travel.

2.2 The Current & Future State of Travel

The growth of transport infrastructure will result in an expected doubling of the annual total distance travelled to 74 trillion (10^{12}) passenger-km over the next 40-50 years [1]. Out of the 32 trillion (10^{12}) passenger-km currently travelled annually, the top two most utilised modes of transport are the automobile and airliner (capturing 76% and 8% of those passenger-km respectively). [3].

This study will focus on the two regions that capture the largest portion of the annual total distance travelled, North America (31%) and Europe (19%). Travel statistics show that over the 9 years from 1995 to 2004, in Europe the total automobile distance travelled increased by 18%, meanwhile air travel increased by 49%. North America shows similar trends. The trends in travel growth all point to an increase of traffic and a growing congestion problem [3].

By 2026 it is estimated that 31.5% of the total world's air travel will be from domestic flights, of which the highest percentages are: North America (13.1%), Western Europe (8.6%) and the People's Republic of China (7.9%) [4].

A study in the United States by NASA (M. D. Moore) shows that the growth of travel volume is having an adverse effect on the door-to-door speeds of travel. The study showed that even though technology has allowed for automobile and airline speeds to increase, the average door-to-door speeds of these modes has remained constant or has even started to decrease over time. The current door-to-door speeds for these modes of transport compared to that of a PAV (average expected speed) can be seen in Figure 2.1 [2].

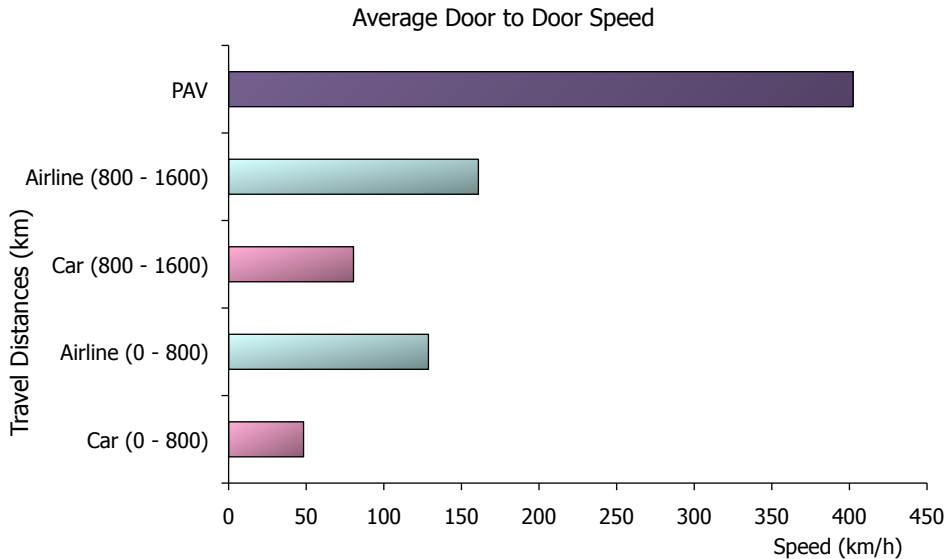


Figure 2.1: Door-to-Door travel speeds for automobile, commercial airliner and PAV

The low door-to-door speeds seen in Figure 2.1 suggest that many roads are operating at full capacity. Increasing road traffic will require more roads to be built to alleviate congestion, however urban congestion cannot be reduced simply by building new roads and therefore other solutions are required. Major airport hubs worldwide are also operating at full capacity constantly. Any further increase of air traffic will require an increase in airport capacity or new airports to be built, which can be very costly and is often very unpopular socially. There is evidence to suggest that building new roads and runways has a side effect of increasing global warming due to the tarmac's ability to absorb and retain heat [4].

The transport infrastructure supporting these two modes of travel is under constant strain, which is clearly manifested through congestion. There are three main problems with congestion: it has a detrimental impact on the environment due to excess vehicle emissions, there is a detrimental impact on the economy due to loss of working time and wasting of fuel, and it creates detrimental health effects due to stress.

Transport is essential to the growth and prosperity of any economy and must continue to develop. Figure 2.2 illustrates the benefits and flaws of transport. The key to reducing the negative effects of any transport system is through tackling the fundamental problems of congestion, emissions, noise and collisions. Eliminating these problems through new technolog-

ical developments and transport system renovations will enhance both mobility and economic progress [1].

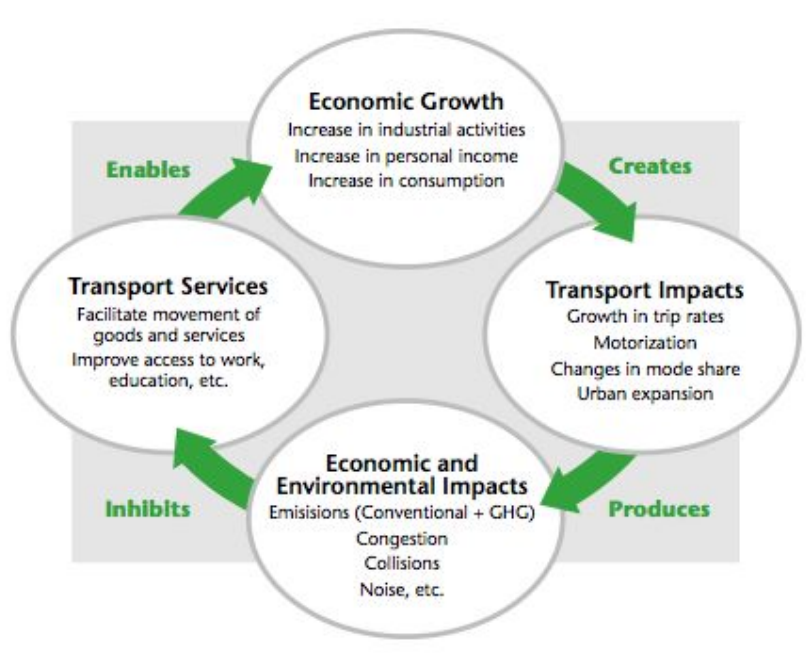


Figure 2.2: Circle of Transport Economics [1]

Stress from prolonged journeys has detrimental effects on health and well being. Stress is a contributing factor to many different diseases including: heart disease, backaches, insomnia, cancer and chronic fatigue syndrome; all of which can have serious negative impact on length and quality of life [18].

2.3 The PAV Solution

The first and foremost benefit of PAVs will be congestion relief and stimulating the economy.

Designing PAVs to be more fuel efficient than current automobiles and harnessing environmentally friendly fuel sources will decrease harmful emissions, thus reducing adverse affects on the environment [2].

To meet the increased demand for automobiles and commercial airline travel new roads and runways need to be built. PAVs could offer an alternative mode of transport which will reduce

the requirement for new roads [3, 4].

PAVs offer a quicker door-to-door form of transportation, saving time, and thus, money. From Figure 2.1 the average door-to-door speed of automobiles and commercial airliners is quite low. Depending on the PAV configuration, the estimated door-to-door speed of a PAV can be anywhere between 215-560 *km/h*. Journey times can be significantly reduced with a PAV.

PAVs demonstrate the ability to be a viable solution to the current problems of increasing travel demand.

2.4 Market Research

2.4.1 Determining a Market Model

The market capture capability of a PAV in relation to the current transport market (automobile and airline) was analysed first. Current automobile and general aviation sales show market saturation. Market saturation is observed by an S-curve shape in cumulative sales, implying that sales will remain at an annual constant output as can be seen in Figure 2.3. As a matter of economic theory saturation of the current market means that there is demand for a new form transport [6, 7].

Due to the multitude of variables that go into defining a new product, the conceptual designs that fulfil the criteria of a PAV are both numerous and diverse. However not all variations will satisfy the needs of a consumer. To capture a significant portion of the market, it is necessary to conduct a more detailed study of market behaviour using key variables that define the characteristics of a PAV. Determining the variables which are the most significant influence on PAV market share the first step in defining a marketable product [6]. Using engineering knowledge, an aircraft baseline configuration can be set.

There are three main systems that interact to impact the marketability of a product. The

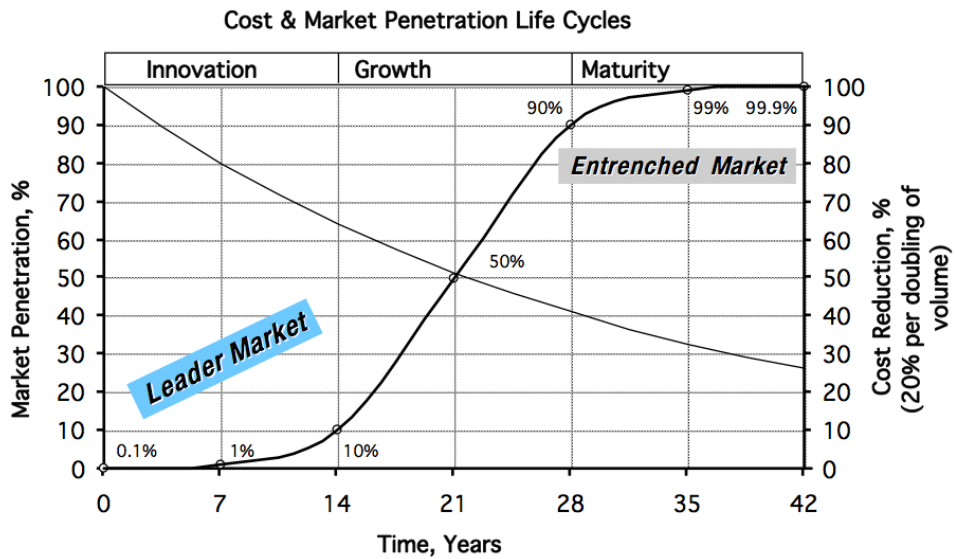


Figure 2.3: Market Maturation S-curves

first system is the consumer/traveller. The consumer's motivation to use a form of transport is governed by many variables such as income, accessibility and so on. A detailed overview can be seen in Figure 2.4 [6, 7].

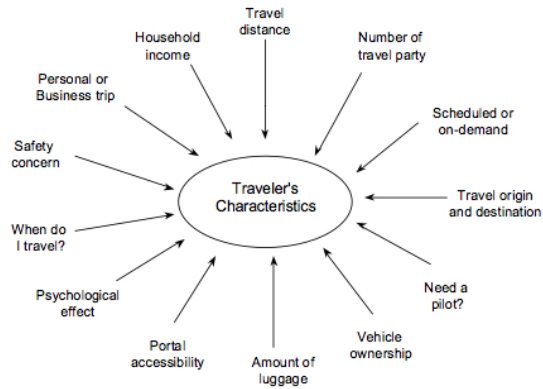


Figure 2.4: traveller's motivational characteristics that influence which mode of transport they will use [6]

The second system is that of the service providers, manufacturers and regulatory agencies. The regulatory agencies' primary objective is to maximise safety and security while reducing costs. Service providers and manufacturers' primary objectives are to maximise profit by meeting the consumer's needs [6].

The third system is that of the researchers and developers. With the input of all the data

and constraining factors from the other two systems, the researchers and developers make critical decisions to formulate a conceptual design and eventually a final product. The parameters which influence these decisions can be seen in Figure 2.5 [6].

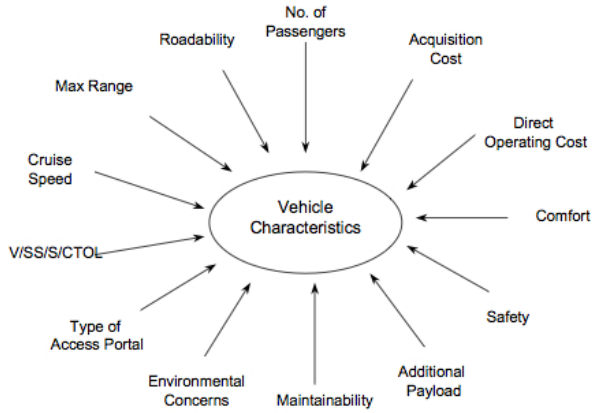


Figure 2.5: Research and development parameters which influence PAV design [6]

2.4.2 Market Model and Results

A study in the United States by Georgia Institute of Technology (J. -H. Lewe, et al.) designed a model of the emerging PAV market. The study used probability distribution functions of inputs from the three systems above, before employing the Monte Carlo simulation technique to produce them. The model was calibrated using current automobile market data, and then adjusted for a PAV. The study assumed that with technologies such as: a PAV air traffic system co-ordinated with differential GPS, highways in the sky ("Skyways"), all weather capability and synthetic vision would allow for cheaper, less intensive pilot training and licensing without affecting safety. A baseline configuration (control data) was decided upon and prescribed the following specification, seen in Table 2.1 [6, 7].

The value of the vehicle was broken down into an hourly operational cost and the simulation was run at varying costs of: \$150/hr, \$120/hr, \$100/hr, \$80/hr and \$60/hr. At each cost level the market share of the PAV was plotted against the market share of the competing forms of transport, namely the automobile and commercial airliners. Figure 2.6 shows the increase of PAV market share with decreasing cost. It was also seen that the automobile market remains

Mode	Single
V_{CRUISE} (75% power)	350 km/h
No. Passengers	4
Range	900 km
Take-off & Landing capability	Conventional (CTOL)
BFL	914 m
Easy-to-fly technology	Yes
All weather technology	Yes

Table 2.1: Market model baseline PAV specifications [6]

robust in the face of competition from the PAV [6].

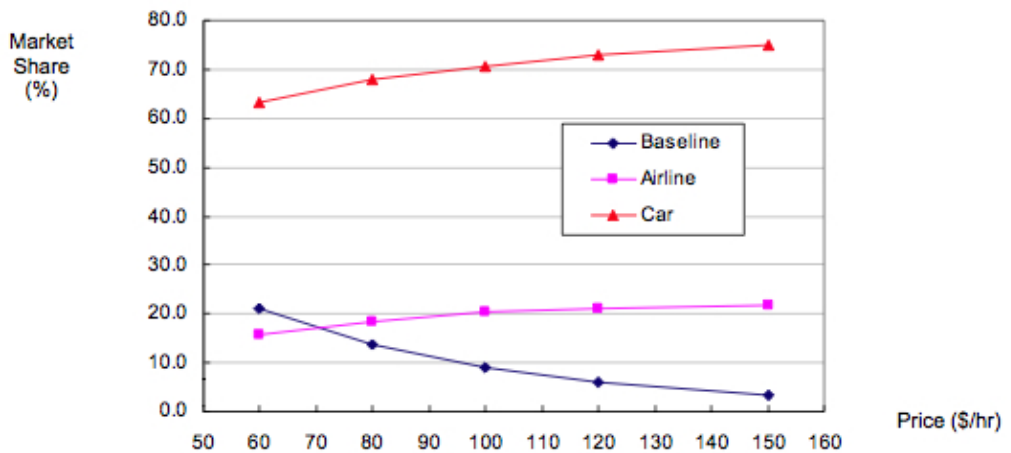


Figure 2.6: The variation of PAV market share with the variation of cost [6]

Using the PAV market model, a "market space" plot was produced for PAV costs of \$150/hr and \$100/hr, see Figure 2.7. Each point on the market space plot represents a consumer's vehicle choice given their annual income (y-axis) and travel distance of the journey that will be undertaken (x-axis).

Figures 2.6 & 2.7 show that for a cost of \$150/hr the PAV only captures 3% of the total market share, appealing mostly to earners in the top 5% income bracket (U.S.) [2, 6]. Reduction of the cost to \$100/hr shows a increase in market share capture of 10%, also pushing appeal

through into the top 20% income bracket (U.S.).

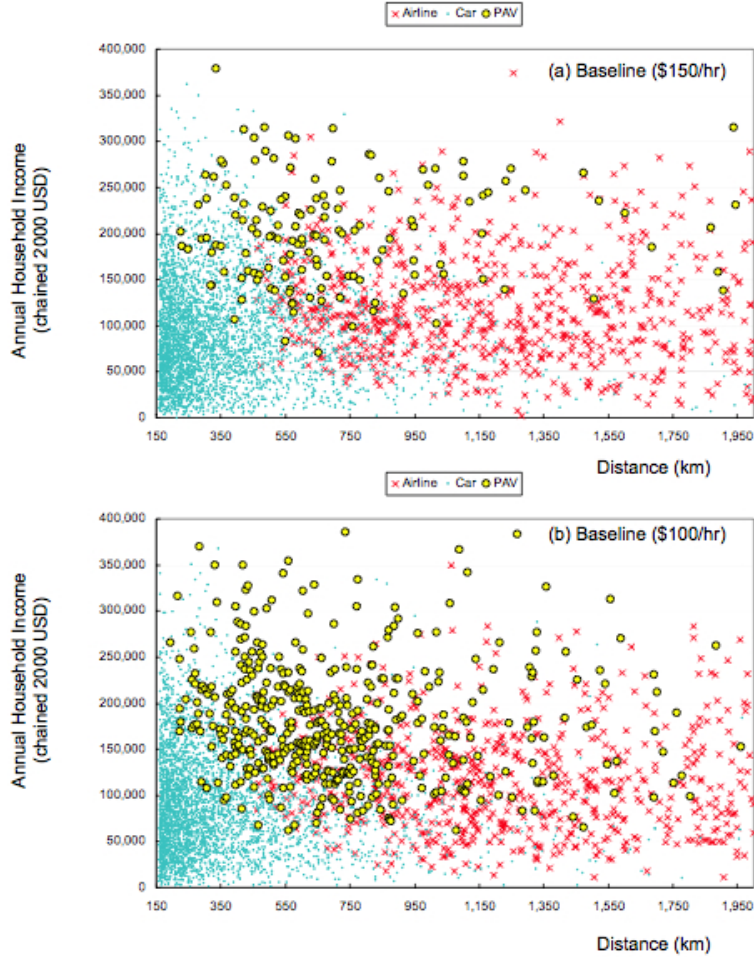


Figure 2.7: Distribution of vehicle choice for varied incomes and travel distances at baselines: \$100/hr and \$150/hr [6]

The market capture variation with cost can be seen more clearly in Figure 2.8, showing that PAV demand is skewed towards higher incomes whereas automobiles are preferred by lower income brackets over other modes of transport.

2.4.3 Variation with Roadability

To determine the most profitable configuration, more market simulations were run varying PAV characteristics such as: cruise velocity, number of passengers, single or dual-mode and range.

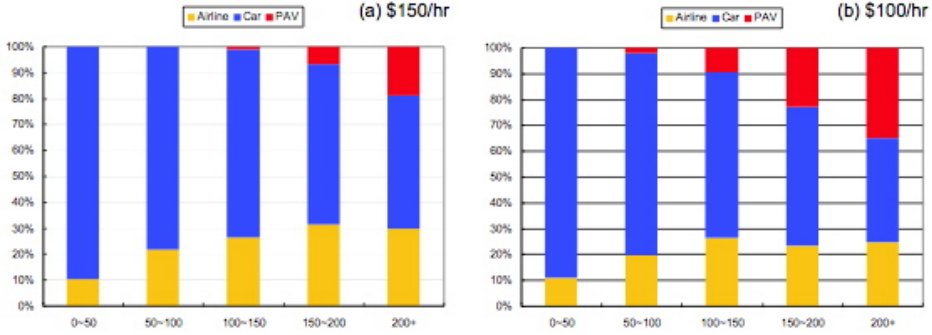


Figure 2.8: The variation of PAV market share with the variation of cost [6]

The market share variation for single and dual-mode can be seen in Figure 2.9. A dual-mode PAV is seen to capture a 5% higher market share at all cost values [6].

For the same market share of 5%, single-mode (\$129/hr) and dual-mode (\$150/hr) vehicles have very different "market space" plots, see Figure 2.10. The dual-mode has a larger spread, with more consumers electing to use it for lower distances. This suggests that a PAV would be in direct competition with the automobile [6].

Both configurations have advantages and disadvantages, Which the better choice depends on the cost effectiveness of the vehicle given the technological and safety limits of its conceptual design.

2.4.4 Variation with Cruise Velocity

The market share variation with cruise velocity can be seen in Figure 2.11 with a baseline cruise velocity of 350 km/h . The market share captured was quite sensitive to changes in cruise velocity. A 50 km/h increase or decrease in cruise velocity causes a 2 to 7% market share increase or decrease respectively. This implies that cruise velocity is an important variable in the vehicle's design [6].

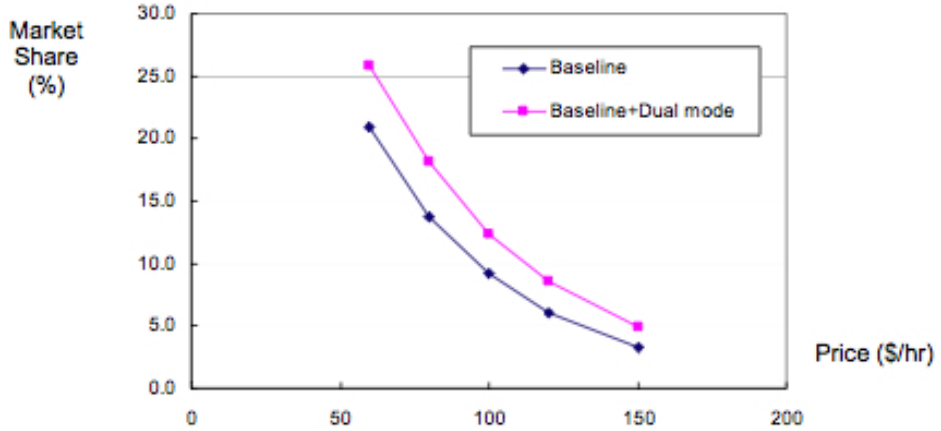


Figure 2.9: The variation of PAV market share for a dual-mode and single-mode PAVs [6]

2.4.5 Variation with Number of Passengers

The next scenario is market share variation with number of passengers, which can be seen in Figure 2.12. Although most car trips involve 1-2 passengers it was clear that consumers preferred vehicles with larger carrying capability. There is a 2-7% drop in market share between 4 and 2 passengers for varying costs. However there is only a 2% increase in market share for all costs between 4 and 6 passengers. This implies that 4-6 passenger vehicles are more likely to capture the largest market share [6].

2.4.6 Variation with Range

The market share variation with range in Figure 2.13 shows very little change in market share capture with variation of PAV range. A range increase from 600 km to 900 km shows only a 1-2% increase in market share, and from a range increase from 900 km to 1200 km shows only a 0-1% increase in market share. The market share decreases with increasing range because at 1200 km and higher, the PAV begins to compete directly with commercial airliners, Figure 2.7 [6].

Figures 2.7 & 2.13 show that the ideal market range for a PAV lies above 200 km . Any travel distances below 200 km are dominated by the automobile, and any travel distances above 950 km are dominated by commercial airliners [6]. However having the capability of increased

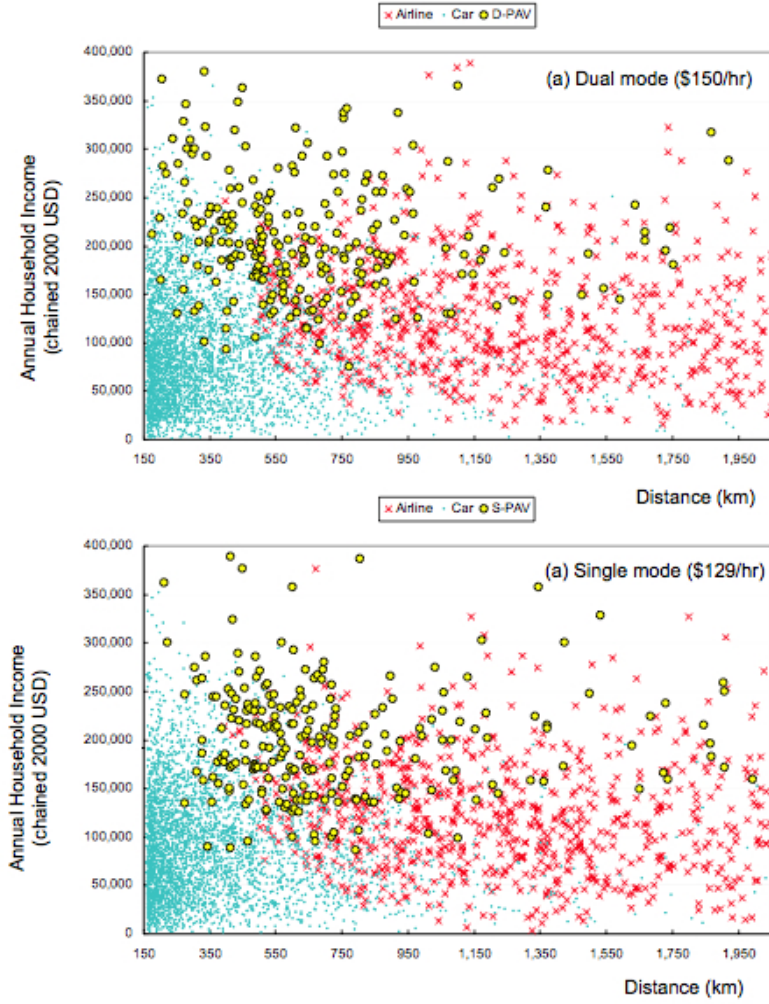


Figure 2.10: The variation of PAV choice distribution for a dual-mode and single-mode PAVs [6]

range above 950 km does not negatively effect the marketability of a PAV, but gives the aircraft the flexibility of travel distance choice.

2.4.7 Variation with Easy-To-Fly Technology

One of the main assumptions of this study is that technological advances will make flying easier, increase safety and reduce training costs. There is a significant drop in market share if this technology is not available or not implemented. Figure 2.14 shows this clearly. The success of PAVs being the next form of mass transport relies on the traffic system that will support it as well as easy-to-fly technology [6].

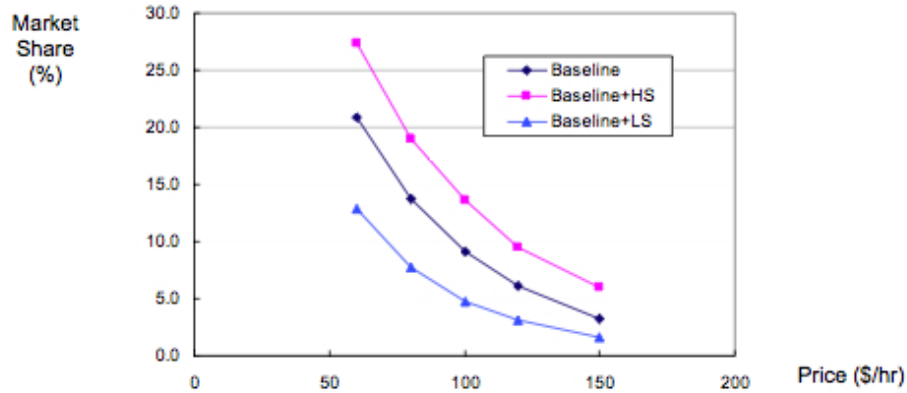


Figure 2.11: The variation of PAV market share with cruise velocity where: HS = 400 km/h, Baseline = 350 km/h, LS = 300 km/h [6]

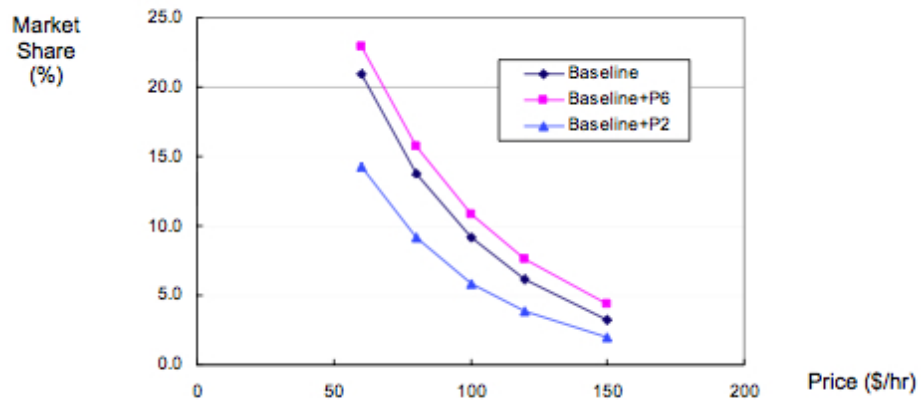


Figure 2.12: The variation of PAV market share with number of passengers where: P6 = 6-passenger, Baseline = 4-passenger, P2 = 2-passenger [6]

2.4.8 Market Conclusions

In order for PAVs to cater the consumer and perform well in the market in the future they need to have the minimum specifications seen in Table 2.2. The choice of single-mode or dual-mode as well as other vehicle variables will be determined with more research into the available technologies and will be discussed in later sections.

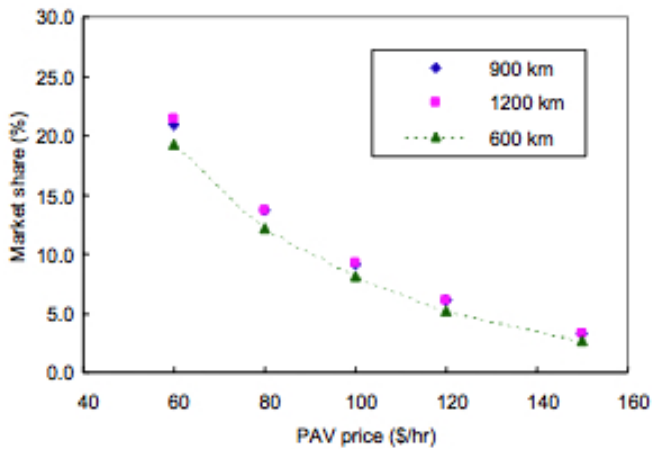


Figure 2.13: The variation of PAV market share with range [6]

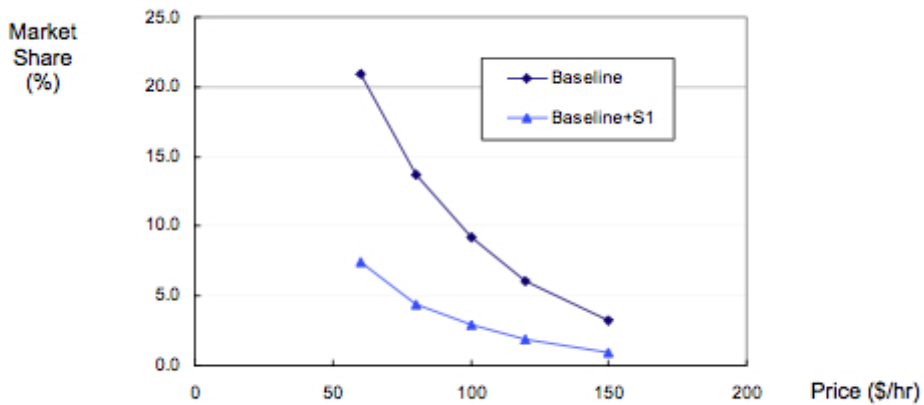


Figure 2.14: The variation of PAV market share with easy-to-fly technology where:
S1 = without easy-to-fly technology [6]

2.5 PAV Categories

PAV designs can be categorised into multiple categories depending on roadability, take-off and landing capability and type of propulsion. This can be seen in Figure 2.15.

2.5.1 Single-mode

Single-mode is the description of a PAV that operates only in the air and thus only needs to be optimised for air travel. This significantly reduces design complexity, reducing costs and maintenance problems.

Minimum V_{CRUISE}	400 km/h
No. Passengers	4-6
Range	$\leq 1000 \text{ km}$
Easy-to-fly technology	Yes
All weather technology	Yes

Table 2.2: Market model PAV specifications

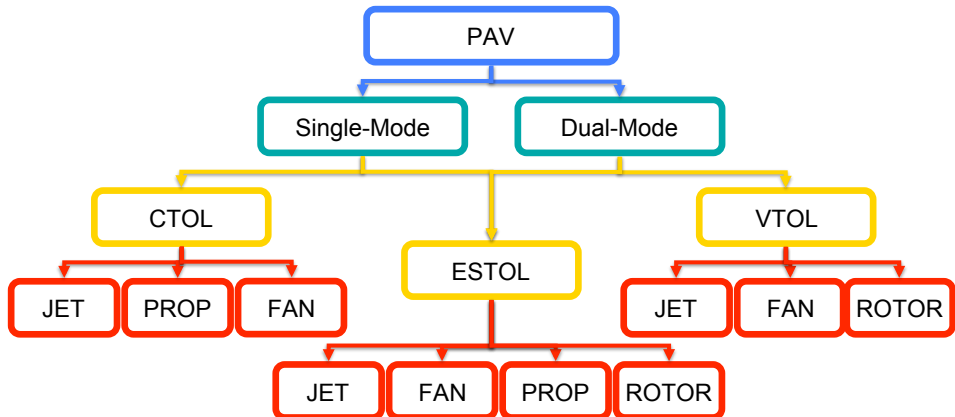


Figure 2.15: PAV Categories

A single-mode vehicle is not without its disadvantages. Depending on its take-off capability, such a vehicle might require a hub and spoke system, meaning that a substitute transport to and from an airport/runway will be required.

2.5.2 Dual-mode

Dual-mode, is the description of a PAV which can operate both on land and in the air. The advantage of a dual-mode configuration over a single-mode is that it is a wholly self-sufficient form of personal transport. The vehicle does not need to be substituted for another at any point in a journey (mission profile).

However dual-mode vehicles are more complicated to design, due to the demands of combining the design criteria of both a road worthy vehicle and an airworthy aircraft. Increased complexity, increases costs and maintenance problems arise as a result of these challenges.

A further disadvantage of dual-mode PAVs is maintaining their airworthiness. Any damage to the vehicle during road use could nullify its airworthiness, thus making it dangerous to fly. This will also add to insurance and maintenance costs.

2.5.3 CTOL - *Conventional Take-off and Landing*

PAVs are further subdivided by their take-off and landing capability. CTOL vehicles are defined by a BFL (balanced field length) in the order of $\sim 300\text{-}915\text{ m}$ [2]. The advantages of a CTOL vehicle include lower engine power required for take-off versus that of a similar vehicle with a non-conventional take-off and landing capability. This means that only a small engine is required, thus reducing weight and fuel consumption.

A CTOL design requires the use of runways, thus constraining users to a hub and spoke system similar to that of light aircraft. The abundance of small airports in the United States makes a CTOL PAV a viable option. However other countries may not have such an existing infrastructure. A dual-mode CTOL is a more practical vehicle for the user but also a more complex and therefore costly design.

2.5.4 ESTOL - *Extremely Short Take-off and Landing*

ESTOL (or Super-STOL) are defined by a BFL in the order of $\sim \leq 150\text{ m}$ [2]. The advantages of ESTOL vehicles are the same as for CTOL ones. The only exception is that shorter take-off and landing would allow the vehicle to operate on considerably shorter runways. This is especially advantageous for use near urban areas where large spaces are scarce.

The disadvantages of ESTOL are similar to the disadvantages of CTOL with one further addition. ESTOL capability is not easily achieved without incorporating technologies such as thrust vectoring (power-lift technology), circulation control and extreme high lift devices. Such technologies improve the performance of the vehicle but in turn increase design complexity and thus operational costs over those of CTOL vehicles.

2.5.5 VTOL - *Vertical Take-off and Landing*

VTOL vehicles are defined by a BFL in the order of $\sim \leq 30\text{ m}$ [2]. Use of VTOL vehicles negates the need for a runway and all travel is direct (point-to-point), which implies that a VTOL vehicle does not need to be dual-mode. The disadvantage of vertical take-off is the weight penalty incurred due the requirement of a larger engine, greater power and the high fuel consumption during take-off and landing.

2.6 History of PAVs

2.6.1 Flying Car

The idea of a PAV was born shortly after powered flight was achieved by the Wright brothers in 1903. The first PAV designs came about through the merging two concepts, the aeroplane and automobile. One of the first designs was VUIA 1, designed by Tajan Vuia seen in Figure 2.16 which was completed in December 1905 and flew for 12 m in March 1906 [19].

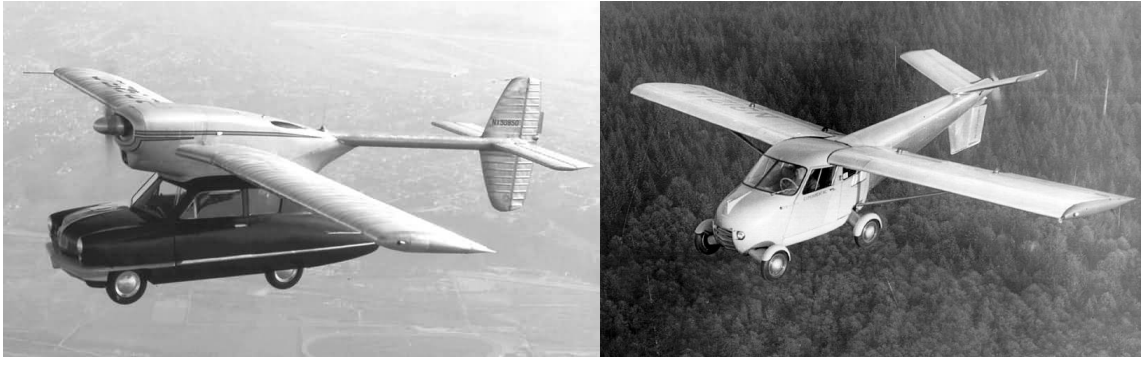


Figure 2.16: The VUIA 1 [19]

Many flying car (i.e. dual-mode) designs followed, with no real success. The 1940s and 50s brought about designs such as the Aerocar and Convaircar, see Figure 2.17. The Convaircar was designed by the aerospace company Convair and first flew in 1947. It was a 2-passenger CTOL vehicle completely composed of fibre-glass with detachable engine housing, wings and

tail section. The high cost of manufacture and limited market potential eventually halted its production [20].

The Aerocar was conceived by Moulton Taylor and certified in 1956. The Aerocar was a 2-passenger, CTOL vehicle with a maximum road speed of 97 km/h and maximum airspeed of 177 km/h . Again limited market potential halted its production [20].



(a) Convaircar

(b) Aerocar

Figure 2.17: Flying car designs [20]

There have also been many less conventional PAV designs, such as the Avrocar and Moller XM-4, see Figure 2.18. Though the Avrocar was a military project it had potential to be a PAV, as a 2-passenger VTOL vehicle, it was powered by a lift fan in the center of a saucer shaped body. It was designed by John Frost and first flew in 1959. The project was cancelled due to the vehicle's poor performance, instability and high cost of production [21].

The Avrocar inspired more recent PAV designs such as the Moller XM-4, first flown in 1974. Although the Moller XM-4 was more stable than the Avrocar, the vehicle exhibited poor forward velocity and as such lost its potential to be a practical PAV [22].



(a) Avrocar

(b) Moller XM-4

Figure 2.18: Unconventional PAV designs [21, 22]

2.7 Modern PAV Concepts

2.7.1 Terrafugia

Terrafugia was founded by a group of Aeronautics graduates from Massachusetts Institute of Technology. The Terrafugia design, the *Transition*, is a 2-passenger dual-mode CTOL PAV as can be seen in Figure 2.19 [23].



Figure 2.19: The Terrafugia Transition PAV [23]

The Transition performance data and dimensions can be seen in Table A.1. The Transition uses standard automobile petrol increasing its user friendliness. The folding wings also reduce the vehicle's width making it more roadworthy and easier to store. A CTOL configuration allows for a small, fuel efficient engine, which in combination with the vehicle's low weight means that its fuel consumption is low [23].

The Transition's range is similar to that of a car. This will be a problem for longer journeys, especially since the vehicle has to take-off and land from a runway (i.e. local airport). Further,

with only 2-passengers the Transition is more likely to be on the lower end of the marketability scale. Another disadvantage of the Transition common to dual-mode PAVs is maintaining its airworthiness, as any damage during road use could invalidate the airworthiness of the vehicle, making it dangerous to fly. As discussed earlier this will also add to insurance and maintenance costs.

Assuming that the door-to-door speed of the vehicle is its cruise speed, using Figure 2.1 it can be seen that the Transition is 43 km/h faster than a commercial airline for travel distances below 800 km , and only 11 km/h faster for travel distances between 800-1600 km . Therefore this vehicle on average has the ability to reduce journey times by 25% and 6% respectively.

2.7.2 AMV

AMV Aircraft was founded in 1996 by Attila J. Melkuti. The main AMV design, the *AMV-211* is a 2-passenger single-mode VTOL PAV, which can be seen in Figure 2.20 below. The single ducted fan is both a source of lift and thrust [24].

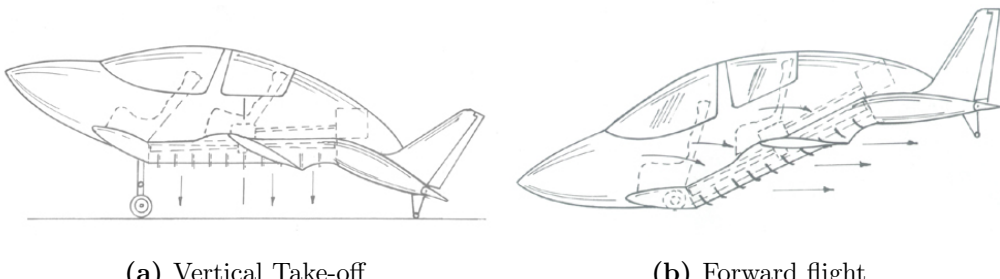


Figure 2.20: The AMV-211 PAV [24]

Avoiding the gyroscopic and mechanical complications of tilt-rotor technology, whilst still using a large fan for propulsion, the AMV-211 is a simple design. The vehicle has VTOL capability and only needs to tilt forward for the fan to produce a thrust component in the forward direction. With sufficient forward speed the aerodynamic surfaces (wings, tail and fin) then become the main source of lift and stability.

The AMV-211's performance data and dimensions can be seen in Table A.2. The predicted range is very high, approximately one and a half times that of a car ($1111\ km$). Assuming that the door-to-door speed of the vehicle is its cruise speed, then using Figure 2.1 it can be seen that the AMV-211 is $273\ km/h$ faster than a commercial airline for travel distances below $800\ km$, and $241\ km/h$ faster for travel distances between 800 - $1600\ km$. Hence this vehicle on average has the ability to reduce journey times by 68% and 60% respectively. The medium range coupled with the VTOL capability means that travel is direct and point-to-point over large distances [24].

However being a VTOL vehicle there is a weight penalty and the aircraft has a maximum baggage capacity of only $27\ kg$. In forward flight the fan is not lined up with the flow direction, so a large percentage of the thrust is wasted. Like the Transition, the AMV-211's number of passengers puts the vehicle in a weaker market position.

2.7.3 Moller Skycar

Moller International was founded by Dr. Paul Moller in the late 1980s. Moller International has designed many unconventional vehicles over the years, see Figure 2.18b, but they are currently working on the Moller Skycar M400, see Figure 2.21. This particular vehicle is a 4-passenger single-mode VTOL PAV [22].



Figure 2.21: The Skycar PAV [22]

The Skycar M400's performance data and dimensions can be seen in Table A.3. Like the Transition, the Skycar also uses folding wings to reduce the vehicle's width for easy storage. The predicted range is high and approximately one and a half times that of a car ($1200\ km$).

Assuming that the door-to-door speed of the vehicle is its cruise speed, using Figure 2.1 it can be seen that the Skycar is 362 km/h faster than a commercial airline for travel distances below 800 km , and 330 km/h faster for travel distances between $800\text{-}1600 \text{ km}$. Consequently on average this vehicle has the ability to reduce journey times by 74% and 67% respectively. Another positive aspect of the Skycar is its VTOL capability, making travel direct and point-to-point.

With its 4-passenger carrying capability and high cruise speed the Skycar is more marketable than the previous two designs. However controlling the vehicle during transition and hover will be difficult, considering that each fan is coupled to its own engine, rather one engine driving all the fans.

2.7.4 Carter Aviation Technologies (CarterCopter)

Carter Aviation Technologies was founded by Mr. Jay Carter, Jr. in 1994 with the aspirations to combine the best of rotorcraft technology with that of fixed wing. CarterCopter's more recent projects involve single-mode PAVs ranging from 2-6 seater with VTOL capability as seen in Figure 2.22. The CarterCopter design incorporates autogyros with high aspect ratio wings optimised for cruise (i.e. gyroplane). The vehicles in Figure 2.22 have fixed wings which are optimised for cruise and are thus small. Low speed lift is provided by the rotor and high speed lift is provided by the wings [25].

The 2-seater CarterCopter's performance data and dimensions can be seen in Table A.4. The predicted range is approximately one and a half times that of a car (1207 km). Assuming that the door-to-door speed of the vehicle is its cruise speed, the CarterCopter is 80 km/h faster than a commercial airline for travel distances below 800 km , and 48 km/h faster for travel distances between $800\text{-}1600 \text{ km}$. This implies that this vehicle has the ability to reduce journey times by 38% and 23% respectively. The CarterCopter is very fuel efficient due to its small engine. Its VTOL capability gives it the advantage of direct point-to-point travel.

The problem with an open rotor is safety. The high rotational speeds of both the propeller and main rotor are a hazard and may cause severe injury or death. The rotors are very large

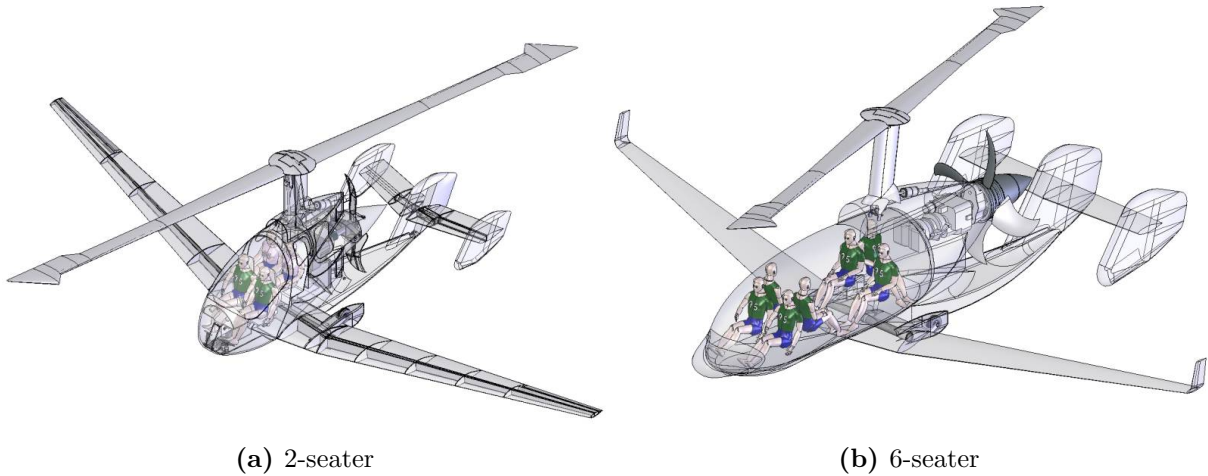


Figure 2.22: The Cartercopter PAVs [25]

and vulnerable to collision and damage especially when the vehicle is manoeuvring close to the ground.

2.7.5 NASA PAVs

The final PAV concept is the NASA Intra-Urban Gridlock Commuter, a dual-mode 1-2 passenger ESTOL PAV seen in Figure 2.23 [2].



Figure 2.23: The NASA Intra-Urban Gridlock Commuter (ESTOL PAV) [2]

The ESTOL capability of the NASA PAV comes from its unique shape, based on the Lipisch Aerodyne and Custer Channel Wing. The propeller in the duct creates a large amount of lift at low velocities allowing the vehicle to take-off over very short distances [2]. This technology is discussed in more detail in section 2.9.

The NASA PAV is capable of $32\text{-}48 \text{ km/h}$ on the road, allowing functionality in an urban environment. [2] The NASA PAV's performance data and dimensions can be seen in Table A.5; like the previous concepts above, the NASA PAV has folding wings, which reduce the vehicle's width making it more road worthy and easy to store. A small fuel efficient engine in combination with the vehicle's low weight means that the fuel consumption is also low. The ESTOL capability gives the vehicle the advantage of being able to use smaller runways closer to urban areas.

Like the Transition and AMV-211, the NASA PAV is only a 2-passenger vehicle, and will have reduced marketability compared to higher capacity PAVs. The range is low and similar to that of a car. This will be a problem for longer journeys, especially since the vehicle has to take-off and land from a runway (i.e. local airport). Assuming that the door-to-door speed of the vehicle is its cruise speed, using Figure 2.1 it can be seen that the NASA PAV is 112 km/h faster than a commercial airline for travel distances below 800 km , and 80 km/h faster for travel distances between $800\text{-}1600 \text{ km}$. Therefore on average this vehicle has the ability to reduce journey times by 47% and 33% respectively.

2.8 Propulsion

2.8.1 Jet

Jet propulsion is the most efficient form of propulsion for high speed travel (transonic and supersonic). However jet propulsion is more expensive than the other propulsion systems described in this section. The use of jet propulsion would significantly reduce the affordability of the PAV.

Jet propulsion is very loud and therefore constrained from operating near residential and urban areas. It is also a safety hazard due to the high temperature and velocity efflux from the propulsion system.

Pulsed ejector thrust augmenters (PETAs) are essentially pulse jet engines that are sur-

rounded by an ejector which augments the thrust. For any significant thrust contribution, a large numbers of PETAs are required. This increases redundancy and efficiency of the propulsion system, but generates considerable levels of noise and as such would not be suitable to operate within urban areas [2].

2.8.2 Propeller

Propeller propulsion is more efficient than jet propulsion at subsonic speeds. A vehicle driven by a cheap, light and compact piston or turboprop engine would help keep its weight down. Propeller propulsion is significantly less noisy than jet propulsion, meaning that vehicle can operate near residential and urban areas. The key problem with propellers is safety. Exposed rotating blades can be easily damaged through collision and can also cause severe injury or death.

Propellers limit the vehicles capability to CTOL. However coupled with a vertical thrusting component such as a main rotor, a vehicle can become VTOL. The propeller can also increase a vehicle's cruise speed as shown by the Cartercopter design in Figure 2.22.

2.8.3 Fan

Fan propulsion is efficient for subsonic travel and VTOL. Fans are similar to propellers but are usually ducted and can have a much higher solidity. Although they are similar to propellers, when ducted they can generate the same amount of thrust as a propeller using the same power, but with a diameter reduction. This size reduction conserves space, but there is a small added weight penalty from the duct or nacelle, which can be reduced through material selection and efficient fan design.

Driven by a cheap, light and compact piston or turboprop engine means that the weight of the engine will not unduly affect the weight of the vehicle. A well designed fan is less noisy than a propeller, thus a vehicle can operate near residential and urban areas. Though fans have dangerous rotating components, the ducts provide protection from damage or injury.

A propfan as seen in Figure 2.24 provides an alternative to a turboprop and it can operate at transonic speeds. Propfans are extremely efficient at high speed with all the advantages of a normal propeller. However propfans also have their own disadvantages. Operating at close to sonic speeds, the noise generated is significant and exposed rotating blades can be easily damaged or cause severe injury. Any blade failure has potentially serious consequences for the PAV or its surroundings [11].

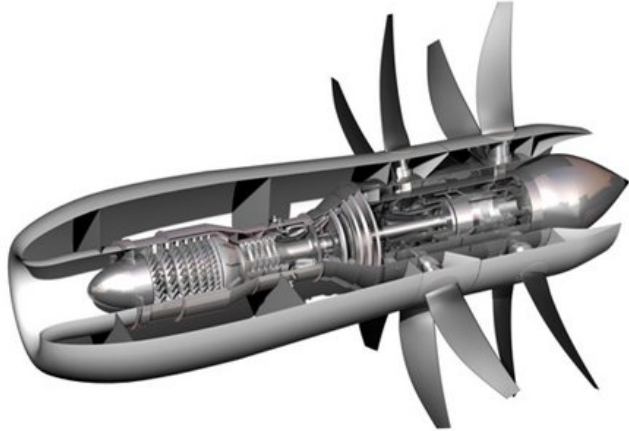


Figure 2.24: Propfan designs [26]

2.8.4 Rotor

Rotor propulsion is the most effective form of propulsion for VTOL, however of a rotor limits the ability to cruise at high forward speed, because they are limited to operating below supersonic tips speeds.

Some designs incorporate a fan or a propeller for forward propulsion and use rotor blades for VTOL only. However when rotating during high speed forward flight, the rotors tend to produce considerable drag. One solution can be seen on the Cartercopter design in Figure 2.22. Reference [25] demonstrates that reducing the RPM of a rotor during forward flight reduces the drag, however it also causes aerodynamic instability. At a critical advance ratio the aerodynamic centre on the retreating blade shifts from the quarter-chord point to the three quarter-chord point. This causes a flutter/divergence in the retreating blade. Carter-

copter have resolved this problem (on a teetering rotor) by stiffening the blades and adding weights to the blade tips.

Like propellers, the high rotational speed of the rotor is highly dangerous and may cause injury or death. Rotors are vulnerable to collision and damage especially when the vehicle is manoeuvring on or close to the ground. This compromises the airworthiness of the vehicle and raises questions as to the safety and insurance of such a vehicle.

Tilt-rotor technology is an alternative solution to producing a VTOL vehicle which can also cruise at high speeds. One example of the adoption of this technology is the Boeing V-22 Osprey. Though tilt-rotor technology is available, there are associated with it high mechanical complexities and triple redundant systems requirements that will increase the weight and cost of any vehicle employing it.

2.9 Aerodynamics

From the market study it was shown that the higher the cruise speed, the higher the market share. Therefore the optimum design should be designed to cruise at high subsonic speeds. To achieve the most fuel efficient design, the vehicle is required to have high lift and low drag (i.e. a high lift-to-drag ratio). As the vehicle will spend most of its time in cruise the high lift-to-drag ratio required means that the wing should have a medium to high aspect ratio (AR). The higher lift and lower drag characteristics of a Blended Wing Body (BWB) design, offers another option for maximising the lift-to-drag ratio.

Compactness is also a requirement of any PAV for space conservation, easy storage and roadability. This can be achieved using either folding or telescoping/retractable wings. However there are weight penalties and increased design complexities involved with all of these.

Although telescoping wings are neater in design than folding wings, the storage of the outboard section in the inboard section takes up valuable space, leaving less room for fuel and posing a systems packaging challenge. Folding wings provide less of a systems packaging chal-

lenge but require structural strengthening at the joints. Careful consideration is also required when linking fuel lines and electrical wiring to the outboard section.

Two promising technologies that evolved from VTOL/ESTOL research were the Custer Channel Wings and Circulation Control (CC) [27]. The Custer Channel Wing uses the propeller slipstream to increase the flow velocity on the suction surface of the wing. This produces an increase in lift similar to that of high lift devices and an efficient downward thrust deflection without the requirement for mechanical moving parts. The total lift increase is thus a sum of the increased flow velocity (circulation) and downward deflection. This technology was shown to increase the maximum C_L of an aircraft to approximately 8.5 [27].

However at low speeds it was observed that the control surfaces response became very poor especially at high angles of attack. It was also observed that high angles of attack caused non-uniform flow to form around the propeller, stalling the propeller. At high angles of attack the pilot would also experience reduced visibility [27].

2.10 Stability and Control

Fly-by-wire technology is available for VTOL control during hover. The development of fly-by-wire into easy-to-fly technology and automated control will reduce the skill requirement to fly.

Propeller, fan and rotor based vehicles can control thrust by changing RPM or the pitch of the rotating blades. Varying pitch is more responsive than varying RPM, however varying pitch involves more mechanical complexity and cost.

Gyroscopic effects from large rotating components (e.g. lift fan or main rotor) are a problem for stability especially at low speeds or hover, when the vehicle requires finer control. There are two solutions to eliminate these gyroscopic effects: the vehicle could be fitted with an anti-torque device such as a tail rotor, or two contra-rotating components could also be used.

Another stability problem when a vehicle is hovering comes from cross wind conditions. Rotor aircraft deal with gusts by blade flapping. However cross flows over the inlet of other propulsion systems (e.g. lift fan or jet) can distort flow sufficiently causing blade stall (surge). This can be controlled by curved inlet ducts, circulation control and/or guide vanes. Guide vanes at the outlet can also be used for thrust vectoring and thus more control during hover.

A simple conventional design for forward flight enables the use of conventional control surfaces. This reduces the mechanical complexity of the vehicle and also reduces instability. If an unconventional design is required to fulfill the design criteria, then mixed control surfaces could be used.

2.11 Structures and Weight

The structural design of the vehicle will depend on its shape, expected aerodynamic loads, materials and airworthiness regulations. Careful material selection and use of composites will drastically reduce the weight of the vehicle, making it more fuel efficient.

2.12 Environmental Effects

Noise is one of the main environmental concerns when designing a transport vehicle. Noise regulations for automobiles and aircraft are becoming stricter. Currently automobiles have to meet the European noise regulations of 74 dBA (decibels A-weighted measurements) [28]. Aircraft have varying noise regulations according to their size, but commercial aircraft normally lie in the region of 90-100 dBA at a distance of 450 m from the ground just after lift-off [29].

The main source of noise from an aircraft is engine noise, followed by airframe noise during approach. Engine noise can be reduced by designing components with acoustic absorbent materials and through careful aerodynamic analysis [29].

Engine emissions are also an important environmental factor. Although engine technology is constantly improving and emissions are decreasing, the possibility of using greener fuels

(biofuels or hydrogen) is a choice that should be considered.

2.13 Operational Environment and Safety

Proper transport infrastructure is required before PAVs can become a reality, with automated air traffic control, skyways and automated vehicle control.

The assumptions that air traffic control in the near future will be automated, and that easy-to-fly technology [30] will be available are very reasonable. Air traffic control procedures and equipment are becoming obsolete and require updating. A great deal of research and development is being completed to create a more decentralised air traffic management system that allows aircraft free flight. This is intended to lessen the burden on air traffic control, and gives more freedom to the pilot [31, 32, 33].

Free flight enables flight using direct routes, optimal altitudes, ease of weather hazard avoidance and use of favourable winds to save fuel, time and operational costs. Technologies such as GPS tracking, collision alert systems and four dimensional (i.e. space and time) navigation will allow safer and more optimal use of the skies [31].

Synthetic vision is another technology which is being developed for flight in the future. Synthetic vision involves creating a virtual image of the terrain in case of adverse weather or night flying. Synthetic vision also shows the pilot all the required information on screen such as flight path and landmarks [34, 35].

UAV technology has broadened the field of automated control, especially with multiple vehicles operating in the close proximity of each other. This technology is transferable to PAVs operating in large numbers in the sky. Automated control offers a computerised system that will increase collision avoidance as well as optimise the flight paths of all vehicles in the system [36, 37].

There are two cases of engine failure to be considered. First is engine failure during conven-

tional flight. If the vehicle is designed with a moderate to high lift-to-drag ratio then it can be glided down safely. However if the vehicle has a low lift-to-drag ratio or is in an urban area and cannot find space to land, then a parachute can be deployed to bring the vehicle to a safe rest. Second is engine failure during hover, can be addressed by installing an undercarriage that can deal with high velocity impacts such as the CarterCopter design and/ or some sort of inflatable arrest device.

Ideally the vehicle should be stored in a garage but design precautions should be taken to prevent wildlife damaging the vehicle or entering the propulsion system. Covers could be used to close any inlets or outlets when the vehicle is not being operated. The vehicle should also be designed to structurally withstand bird strike.

Another important factor that the market share study did not take into account was the size of the vehicle. It can be assumed that if the vehicle is too large and cannot be stored in a garage, the less market share it will capture. So the PAV should be designed to be as compact as possible.

A single-mode VTOL PAV will require a designated take-off platform in crowded urban areas, especially for larger 6-passenger designs. This will limit the chances of collisions with obstacles such as trees, power lines and tall buildings.

2.14 Maintenance and Other Challenges

Like automobile and aircraft regulations, PAVs should be checked and maintained at regular intervals. Checks should be completed after a certain number of flight hours, a certain block of time or after a certain number of take-offs and landings.

With the freedom to fly anywhere, control of airspace and borders will require a system to monitor and manage international travel. Specific PAV hubs similar to border checkpoints can be used to manage travellers entering the country. That will enable immigration and customs control. The vehicle's GPS transponder can carry relevant information such that any unautho-

rised breach of airspace can be detected.

The creation of a PAV training and license authority coupled with a new transport system are key requirements for ensuring safety and traffic regulation. The incorporation of easy-to-fly technology into the design will reduce pilot training times and costs, and as such enable PAV technology to be used by a large portion of the population.

Automobile insurance is compulsory in the United States and Europe. similarly insurance for light aircraft can also be easily obtained. It may therefore be assumed that PAVs will be easy to insure in a similar fashion to automobiles and light aircraft. Companies like Terrafugia have already organised an insurance package for their vehicle.

Governments receive a large amount of income from road tax (e.g. U.K.) to maintain the quality and safety of road transportation system. A tax on PAVs could also be implemented to do the same for a PAV transportation system.

2.15 Outline of PAV Requirements

The purpose of this feasibility study was to determine the technologies and over all requirements to design a functional and practical PAV. From this study it maybe concluded that the required technologies are either being developed or maturing, so the assumption that they will be available in the near future is reasonable.

At this stage of the feasibility study a configuration outline of the PAV design methodology can be determined. Due to the nature of engineering, a lot of compromises between different technologies were made in order to produce a practical design.

According to Figure 2.15 the first option to be decided would be whether the PAV will be dual or single-mode. Though the study showed a higher market share for a dual mode configuration, the mechanical complexity of trying to design such a vehicle would be very challenging. The cost increase might also lead to a reduction in the market share capture equivalent to that

of a single-mode vehicle.

A single-mode VTOL design still provides the required mobility of point-to-point travel and without the mechanical and safety complexities of a dual-mode design; with this in mind a single-mode VTOL configuration was chosen.

The next option from the flow chart seen in Figure 2.15 was the choice of propulsion system. The three choices were a jet, a fan or a rotor. Jet engines provide significant amounts of thrust but they are noisy and potentially dangerous in residential areas. Rotors also provide a lot of thrust, but the top speed of the aircraft is limited, even with compound rotor designs. The large high speed rotating components are also hazardous and vulnerable to damage. A combination of lift fan and propulsive/control fans driven by a small turboshaft engine were chosen, maximising safety and compactness whilst minimising noise and emissions.

The market study showed that the market share captured was very sensitive to cruise speed changes. With ducted fans high subsonic speeds can be achieved. The PAV may be designed aiming for speeds in the order of 463-593 *km/h*. To maximise cruise capability, high lift-to-drag ratios are required. This means that the PAV will be a BWB with high wing loading and moderate to high aspect ratio wings.

The market share captured was shown to increase with the number of passengers. The design methodology will be scalable accommodating, from 1-7 passengers, maximising marketability. Any passenger capacity higher than 7 would take the PAV into other market regions.

The greater the range of the aircraft, the bigger market share was captured. Even though a market gap was found between automobile and commercial airline for journeys between 200 *km* and 950 *km* in Figure 2.7, a design range greater than 950 *km* will still increase marketability.

2.16 Other Applications

2.16.1 Military

A military version of the established baseline configuration could be designed as a mobile personnel carrier. Since this research's aim is to develop design methodology for such a vehicle, the technology can be scaled to match military requirements. Manoeuvrability, VTOL capability and compact storage whilst being able to carry cargo or men are all appealing qualities to the military.

2.16.2 Air Ambulance

Most of current air ambulance services are helicopters. Helicopters provide the ability to land at any accident scene, access remote areas and take those injured to the nearest hospital quicker speeds than conventional ambulances. However helicopters are very expensive to purchase and maintain. Their top speed is limited by rotor technology. A modified PAV would be cheaper and quicker, yet still exploiting all the advantages of VTOL capability.

2.16.3 Air Taxi - Business

A lot of people travel for business; in 2003 the United Kingdom for example it was found that 15% of all travelled miles were for business. One fifth (i.e. 20%) of all journeys 350 miles (563 km) or more were for business. With PAV technology trip times can be reduced giving businesses the ability to travel further and reach more people in a certain time frame.

Chapter 3

Initial Sizing

3.1 Overview

The initial sizing process outlines a methodology for estimating the size and weight for a given aircraft. To estimate the size of the aircraft, a qualitative estimate of the location of all the aircraft's components was outlined in a sketch (baseline configuration). Using an initial weight estimate, the thrust required for hover and cruise could be calculated in order to establish the size of the fans required. This would in return determine the size of the rear part of the fuselage. An initial weight estimate was used to determine the wing size, coupled with a carpet plot to find the optimum wing loading (W/S).

To estimate the weight of the aircraft, a mission profile was outlined. The mission profile segmented the typical stages of flight for a PAV from which the total fuel consumed can be estimated. Using empirical formulae, initial aerodynamic estimates, propulsion data (methodology: thrust, power & SFC), statistical weight data and the total fuel consumed, the maximum take-off weight of the aircraft was estimated.

Initial sizing provided a good initial estimate of the aircraft's size and weight before more detailed calculations were performed.

3.2 Baseline Configuration

The baseline configuration and propulsion concepts of this PAV were originally conceived by Dr. V.C. Serghides at the beginning of the research programme. A plan and a side view of the baseline aircraft are illustrated in Figures 3.1 & 3.2. The propulsion system is described in detail in Chapter 4. A fan crucifix formation was chosen to maximise control during hover, Figure 4.2. The overall layout of the aircraft is integrated with the propulsion system in such a way so that the centre of gravity of the aircraft is in close proximity to the resultant thrust vector in VTOL mode. This led to a long coupled canard configuration with an aft-located main wing and twin boom mounted V-tail.

The engine is located between the cabin and lift fan, driving the fan system through a series of bevel gear sub-system. A turboshaft engine was selected to drive all the fans as it was compact enough to fit in the PAV while being powerful enough to drive all the fans during VTOL.

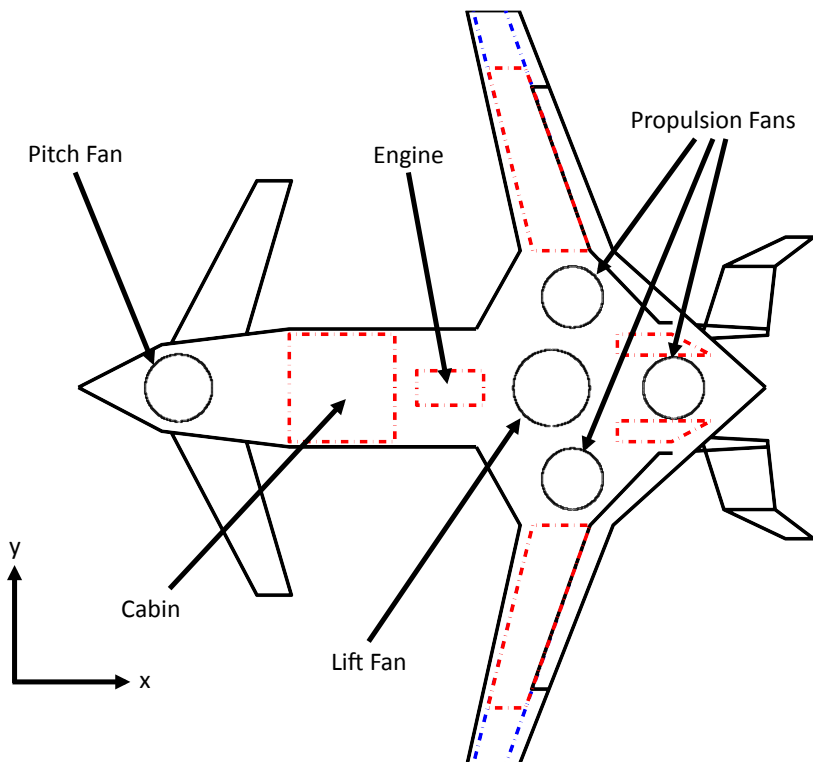


Figure 3.1: Baseline Configuration

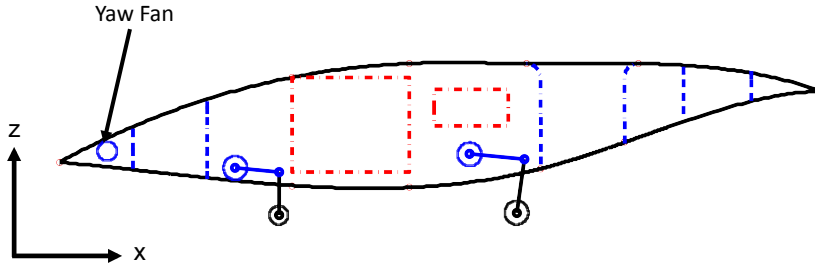


Figure 3.2: Baseline Configuration side profile

3.3 Carpet Plot

A carpet plot is used to obtain an initial estimate of the optimum wing loading (W/S) and weight to power ratio (W/P) and thus determine the aircraft's size and power requirements. The optimum point is located where the highest wing loading meets the highest weight to power ratio within the area of applicability. The equations in Appendix C.1 [11, 12] were used to determine the area of applicability.

Compiling data on single engine turboprop aircraft, it was found that the maximum lift coefficient was $2.0 \leq C_{L_{max\ flap}} \leq 2.54$. To maximise the wing loading the maximum lift coefficient flaps down was assumed to be $C_{L_{max\ flap}} = 2.5$. An average profile drag value for an aircraft with similar operational requirements was found to be $C_{D0} = 0.022$. Thus this zero-lift-drag value was chosen for initial sizing purposes.

The two main limiting factors illustrated in Figure 3.3 were: the stall speed of the aircraft limited by the FAR23 requirements as $31.4\text{ }ms^{-1}$ ($61\text{ }kts$) and the weight to power ratio requirement for VTOL. Compiling data for VTOL aircraft with ducted fans showed that the average weight to power requirement is $W/P = 2.1\text{ }kg/kW$. However, compiling data for single engine turboprop showed that the power requirement normally lies in the region $W/P = 5 - 6\text{ }kg/kW$. It can clearly be seen that there is a penalty to be paid of excessive power in order to have VTOL capability. The optimum wing loading is governed by the stall speed and the optimum weight to power ratio by the fan power requirements for VTOL capability.

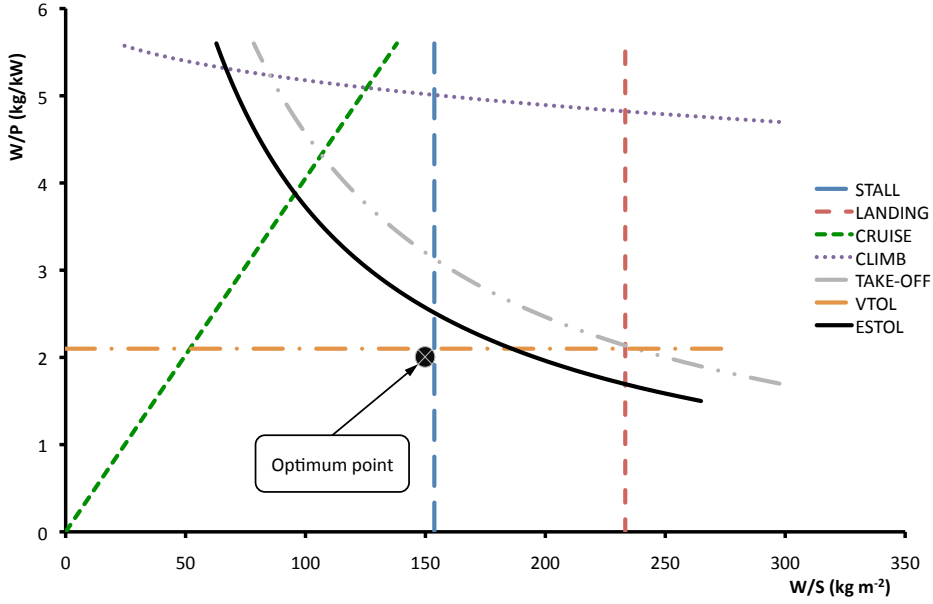


Figure 3.3: Carpet Plot

3.4 Mission Profile & Weight Fractions

A mission profile Figure 3.4 was outlined in order to determine an initial estimate of the MTOW (W_0) and fuel weight (W_f) of the aircraft. The MTOW and fuel weight were both estimated through an iterative methodology Figure 3.5 incorporating the propulsion methodology Figure 4.11 and weight fraction equations.

Other than the cruise and loiter segments, each weight fraction (W_i/W_{i-1}) was determined by calculating the fuel used to complete each segment. This was done by determining the time required, average power required and specific fuel consumption (SFC) for each segment Eqn 3.1. An equation for SFC Eqn 4.57 was determined using engine data and empirical formulae.

$$W_{f_{i,i+1}} = \left[\frac{(P_i \cdot SFC_i) + (P_{i+1} \cdot SFC_{i+1})}{2} \right] \cdot (t_{i+1} - t_i) \quad (3.1)$$

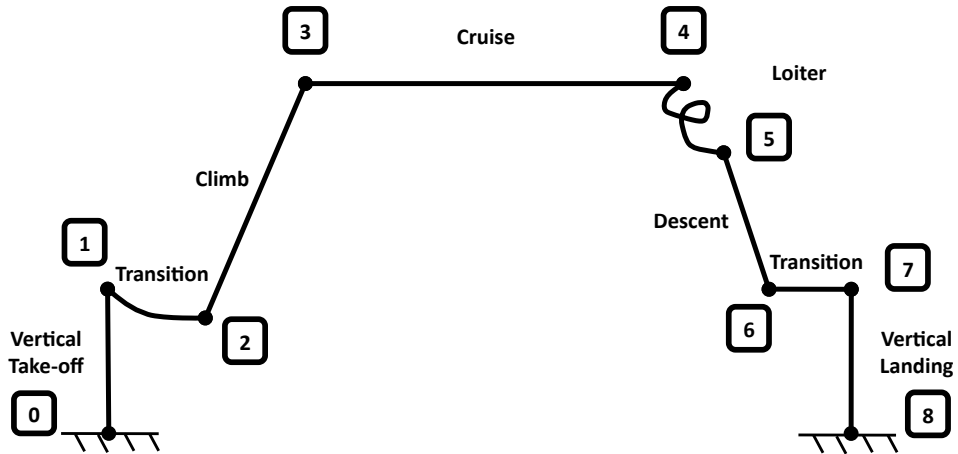


Figure 3.4: Mission Profile

3.5 Initial Sizing Methodology

The initial sizing methodology of the aircraft was the product of the mission profile, weight fraction calculations and empty weight equation. The empty weight equation Eqn 3.2 was developed from a combination of weight trends for twin piston-prop and single turboprop aircraft.

$$\log_{10}(W_e) = \frac{\log_{10}(W_0) + 0.1669}{1.1182} \quad (3.2)$$

FAR23 requirements state that a single passenger's weight can be between 77 kg and 85 kg . For this design it was decided that the weight of a single passenger would be 80 kg and the maximum luggage weight per passenger was 10 kg . The most important segment of the mission profile was the cruise segment, having the highest fuel consumed. From Eqn 3.3 it can be seen the all the variables are independent except for SFC, which is determined by the engine power and forward speed. Thus the cruise lift-to-drag ratio, range and cruise speed were set as user-defined variables.

These values used in the methodology to determine the weight fractions were variables and could be modified to vary the mission profile and thus design. The values stated in this section are examples to illustrate how the methodology works.

For the VTOL segment (0-1) it was decided that the PAV would ascend vertically at a slow enough pace to control and so the vertical take-off speed was set at 91 m/min (300 ft/min). It was decided that the aircraft should transition at a satisfactory altitude to avoid obstacles and give the aircraft enough height to transition safely. This transition altitude was set to 91 m (300 ft). The transition segment (1-2) was assumed to be 40 secs long. The power consumption for the initial segments was assumed to be maximum total power (P_{total}). Using Eqn 4.57 the SFCs for both segments were calculated with $M_\infty = 0$. For the climb segment (2-3) it was assumed that the aircraft would ascend at a 10° angle of attack to a user defined cruise altitude, climbing at an average of 610 m/min (2000 ft/min). The power required for the climb (P_{climb}) was estimated to be the average of the power used in cruise and the power used by the propulsion fans during hover. The cruise segment (3-4) was defined by Eqn 3.3 [11].

$$\frac{W_4}{W_3} = \exp\left(\frac{-Range \cdot SFC}{(L/D) \cdot \eta_p}\right) \quad (3.3)$$

The loiter segment (4-5) was determined by Eqn 3.4 [11] with the endurance set as 30 mins . The loiter speed was assumed to be at half that of cruise speed and at a user defined altitude below that of the cruise altitude.

$$\frac{W_5}{W_4} = \exp\left(\frac{-Endurance \cdot SFC \cdot V}{0.866(L/D) \cdot \eta_p}\right) \quad (3.4)$$

The values for the descent segment (5-6) were similar to that of the climb segment except the power was estimated to be at idle (15% of the power used in climb). The second transition segment (6-7) was estimated to be 60 secs long, with a power usage equivalent to the weight ratio, $P_{trans} = (W_6/W_0) \cdot P_{total}$. The landing segment (7-8) used similar values as the take-off segment except the power used was assumed to be linked to the weight ratio, $P_{land} = (W_7/W_0) \cdot P_{total}$. Using reference [11] a suggested 6% fuel reserve was also incorporated into the methodology.

After determining the weight fractions for each segment, a new maximum take-off weight

was estimated. The fuel weight was calculated from the weight fractions and the empty weight was calculated from Eqn 3.2. A new maximum take-off weight was then estimated from Eqn 3.5 [11].

$$W_{0_{i+1}} = \frac{W_{PAX} + W_{PAY}}{1 - (W_f/W_{0_i}) - (W_f/W_{0_i})} \quad (3.5)$$

As can be seen from Figure 3.5 the whole initial sizing process was repeated iteratively until the maximum take-off converged to a reasonable value. The variables that could be user defined provided flexibility in the overall optimisation methodology, allowing for variation of the PAV according to the market competition, for example, smaller personal aircraft (Cessna 400, Table 3.1) or larger air taxies (Socata TBM 850, Table 3.2).

Number of passengers	4 (inc. pilot)
Range	2000 km
V_{cruise}	435 km/h
Cruise Altitude	~ 3000 m

Table 3.1: Cessna 400 specifications [38]

Number of passengers	6 (inc. pilot)
Range	2800 km
V_{cruise}	555 km/h
Cruise Altitude	~ 9500 m

Table 3.2: Socata TBM 850 specifications [39]

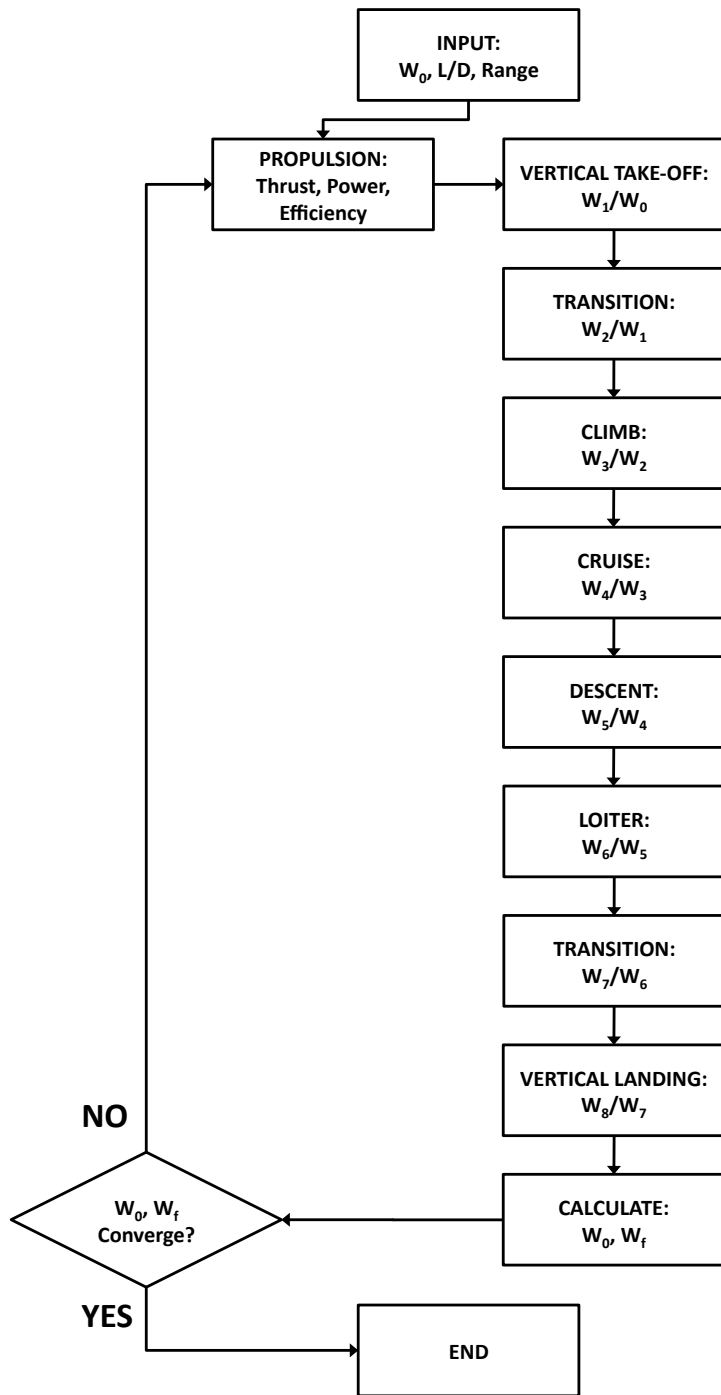


Figure 3.5: Initial Sizing Methodology

Chapter 4

Propulsion

4.1 Overview

Having chosen ducted fans as the main source of propulsion for the VTOL PAV, the layout and positioning of the fans and power plant needs to be determined. The idea of using the same propulsion system for both hover and forward flight as used on VTOL aircraft (e.g Bell Boeing V-22 and BAe Harrier) demonstrated stability and controllability issues during transition to forward flight. Having separate or a combination of power plants for hover and forward flight (e.g. Dassault Mirage III-V and Yakovlev Yak-38) showed stability during transition, but the aircraft were burdened by the added weight penalty of an extra propulsion system [40]. This prompted the choice of a blend of both designs or augmented power plant for hover (e.g. Lockheed Martin F-35). The propulsion system of a single power plant (turboshaft engine) driving a large lift fan as well as 4 smaller fans for control during hover, of which 3 tilt forward during transition to forward flight Figures 4.1 & 4.2 was chosen. For VTOL capability the lift fan was positioned as close as possible to the CoG (Centre of Gravity) to reduce extreme pitching moments. To minimise gyroscopic forces on the PAV, the lift fan design was chosen to have dual rotor contra-rotating fans. The more smaller control/propulsion fans are placed around the lift fan for control during hover. They also rotate to propel the aircraft forward.

With the baseline configuration and basic layout determined, the first step in sizing the aircraft was to size the fans. This meant that a simple fan design methodology needed to

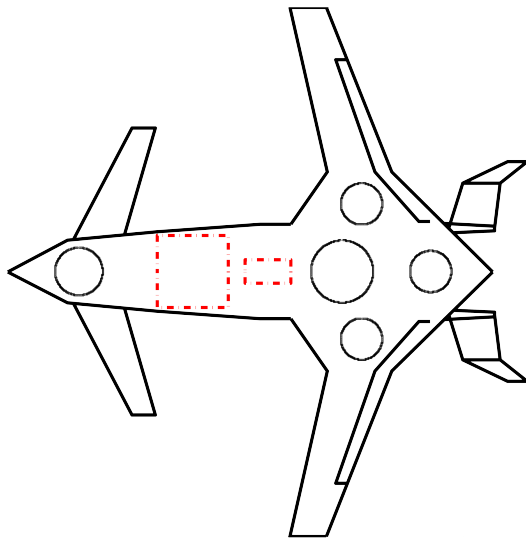


Figure 4.1: Fan configuration

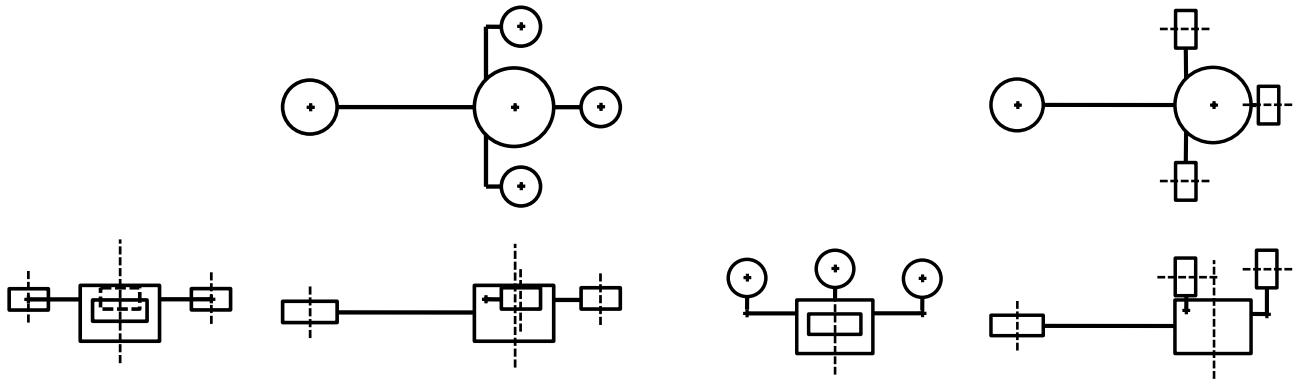


Figure 4.2: Fan layout configurations

be developed. To maximise controllability it was decided that the control/propulsion fans were variable pitch. Then using cascade and blade element theory the fundamental variables (geometric and fluid) of blade design were identified and used to produce various ift fan and control/propulsion fan models. These models were meshed and run in a CFD package (*ANSYS: Bladegen, Turbogrid and CFX* respectively) at varying pitch attitudes. The resulting data was gathered and a parametric analysis was done to produce a methodology that could be used to design a fan from a given set of geometric and fluid inputs.

The same process of producing a design methodology for fans was repeated for the other propulsion components such as duct guide vanes and duct inlets geometry. Using the compo-

nents the optimum propulsive unit for a given role could be generated.

These methodologies were then incorporated into a propulsion optimisation code to minimise the power required to produce a given thrust from user defined geometric inputs.

4.2 Fan Design Theory

4.2.1 Cascade Theory

Cascade theory is used to design axial fans and axial compressors, both industrial and aeronautical. Cascade theory breaks down the 3D blade system into a system of 2D models using rotational, axial and whirl velocities (U , V_x , V_θ) at a station r between 0 and blade tip (r_t), Figure 4.3. The diagram assumes the inlet whirl velocity ($V_{\theta 1}$) is zero [8, 9].

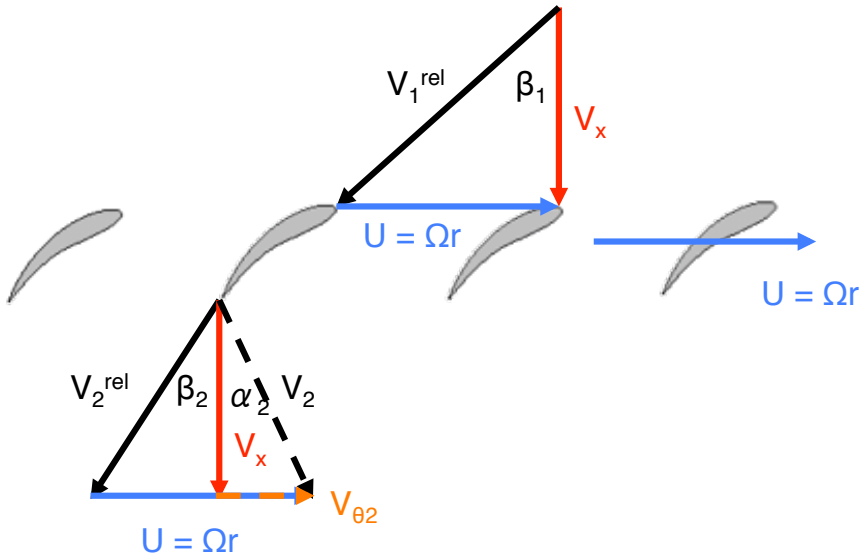


Figure 4.3: Velocity triangles through a rotor stage.

Using the design assumption that the axial velocity V_x is kept constant, from the geometry of the velocity triangles two Eqns 4.1 & 4.2 are obtained.

$$\frac{U}{V_x} = \tan \alpha_1 + \tan \beta_1 \quad (4.1)$$

$$\frac{U}{V_x} = \tan \alpha_2 + \tan \beta_2 \quad (4.2)$$

An expression for the power input required can be found using the change of angular momentum passing through the rotors, giving Eqn 4.3. Using the relations in Eqns 4.1 & 4.2 the power equation can be expressed in terms of the inlet and outlet blade angles as can be seen in Eqn 4.4 [8].

$$P = \dot{m}U(V_{\theta 2} - V_{\theta 1}) \quad (4.3)$$

$$P = \dot{m}UV_x(\tan \beta_1 - \tan \beta_2) \quad (4.4)$$

The power input is translated into a pressure and stagnation temperature rise. The higher the temperature rise, the higher the pressure difference across a rotor stage and consequently the higher the axial velocity. The efficiency of the compression process is also dependent on the efficiency of the stagnation temperature rise across the rotor.

To achieve a high pressure rise across a rotor stage whilst maximising efficiency it was noted that a high blade tip speed U_t , high axial velocity V_x and high fluid deflection ($\beta_1 - \beta_2$) was required in the fan design.

The sum of vector components of the axial and rotational velocities produces the relative velocity entering the rotor i.e. $V_1^{rel} = \sqrt{V_x^2 + U^2}$. The maximum relative velocity will occur at the tip and thus tip Mach number $M_{tip} = V_{1t}^{rel}/a$ (where a is the speed of sound), governs magnitude of both rotational and axial velocities. Industrial gas turbines are normally designed with axial velocities of 150 ms^{-1} , whilst advanced aero-engines can be up to $200\text{-}250 \text{ ms}^{-1}$. This means for that a given U_t , the M_{tip} can reach the order of 1.5 [8].

For high hub-tip ratios ($\frac{r_h}{r_t} \sim 0.8$) the variation in blade rotational speed U across the blade is very small. Thus the blade design can be approximated using a 2D model, from the velocity

triangle at the mean radius of the blade. However for low hub-tip ratios ($\frac{r_h}{r_t} \leq 0.4$) the variation of U from root to tip is large. The variation of U means that the relative velocity vector V_1^{rel} varies in magnitude and direction from root to tip. Consequently the only way to maximise efficiency is to vary the blade geometry (i.e. β_1) from blade to tip, matching the air angles (velocity triangles) at all radii [8].

Three dimensional flow conditions also imply that a flow must have a radial velocity component, although it is often small compared to the axial and whirl velocities. The inertia forces in the radial direction occur due to: the centripetal force associated with circumferential flow, the radial component of force related to the flow along a curved streamline and finally the radial component of the force needed to produce a linear acceleration along a streamline.

Balancing the pressure and inertia forces acting on the fluid and neglecting the radial velocity ($V_r \ll V_\theta, V_x$) produces the radial equilibrium equation, Eqn 4.5 [8].

$$\frac{1}{\rho} \frac{dp}{dr} = \frac{V_\theta^2}{r} \quad (4.5)$$

From Eqn 4.5 an energy equation varying with radius can be developed, thus producing the vortex energy equation, Eqn 4.6.

$$\frac{dh_0}{dr} = V_x \frac{dV_x}{dr} + V_\theta \frac{dV_\theta}{dr} + \frac{V_\theta^2}{r} \quad (4.6)$$

Assuming the frequently used design condition of constant specific work at all radii, then although the stagnation enthalpy h_0 will increase in the axial direction through the rotor stage, the radial variation will remain constant. As a consequence $\frac{dh_0}{dr} = 0$ in any plain between blade rows. Also assuming another design condition, that V_x remains constant at all radii, then the vortex equation is reduced to the free vortex condition, Eqn 4.7. Thus implying that the whirl varies inversely with radius.

$$\frac{dV_\theta}{dr} = -\frac{V_\theta}{r} \implies V_\theta r = constant \quad (4.7)$$

It can be seen that constant specific work, constant axial velocity and the free vortex variation of whirl velocity all satisfy the radial equilibrium equation, Eqn 4.5. These conditions thus define the elementary steps to blade design, known as free vortex blading. Although free vortex blading has some disadvantages, it is widely utilised and provides sufficient material for preliminary design [8].

4.2.2 Blade Element Theory

Blade element theory (BET) is used for the design of propellers, industrial fans and rotor blades. Like cascade theory, BET breaks down the 3D blade system into system of 2D models. The 2D models use the rotational velocity U , axial velocity V_x and blade angular geometry at a station r between 0 and blade tip (R or r_t) to determine aerodynamic forces on each blade section, Figure 4.4 [10].

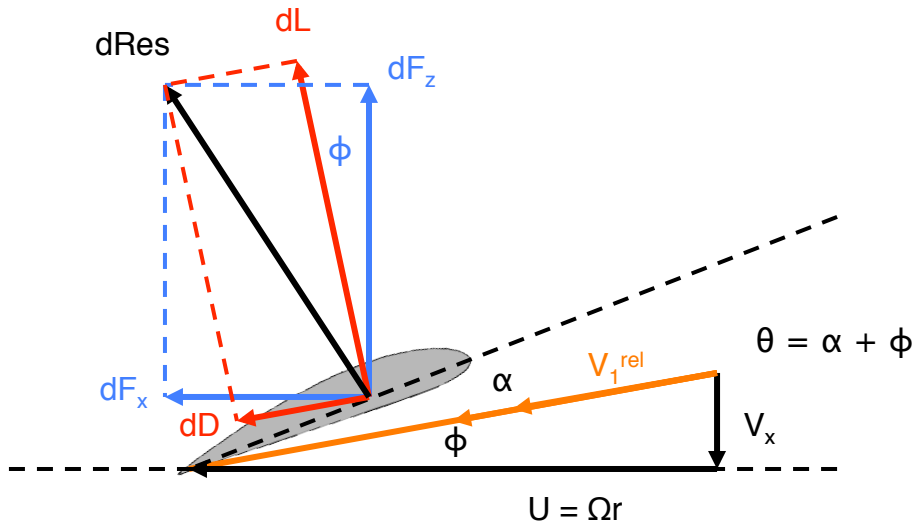


Figure 4.4: Velocities and aerodynamic forces on a typical blade element.

The incremental lift dL and drag dD per unit span on the blade element can be expressed in terms of aerofoil characteristics, Eqns 4.8, where C_l and C_d are the lift and drag coefficients respectively.

$$\begin{aligned} dL &= \frac{1}{2}\rho V_1^{rel2} c C_l dr \\ dD &= \frac{1}{2}\rho V_1^{rel2} c C_d dr \end{aligned} \quad (4.8)$$

The aerodynamic forces can be broken down into components in the axial z and rotational x direction, Eqns 4.9 [10].

$$\begin{aligned} dF_z &= dL \cos \phi + dD \sin \phi \\ dF_x &= dL \sin \phi - dD \cos \phi \end{aligned} \quad (4.9)$$

The incremental equations for thrust, torque and power are defined in Eqns 4.10, where N_b is the number of blades [10].

$$\begin{aligned} dT &= N_b \ dF_z \\ dQ &= N_b \ dF_x \ r \\ dP &= N_b \ dF_x \ \Omega r \end{aligned} \quad (4.10)$$

Combining Eqns 4.10 & 4.9, assuming small angle theory and that ϕdD is negligible results in Eqns 4.11.

$$\begin{aligned} dT &= N_b \ dL \\ dP &= N_b (\phi \ dL + dD) \ \Omega r \end{aligned} \quad (4.11)$$

The definition of incremental thrust and power coefficients can be seen below in Eqns 4.12 & 4.13.

$$dC_T = \frac{dT}{\rho A(\Omega R)^2} \quad (4.12)$$

$$dC_P \equiv dC_Q = \frac{dQ}{\rho A(\Omega R)^2 R} \quad (4.13)$$

Using the assumption that $\phi = \lambda_i = \frac{V_x}{U}$ and that $x = \frac{U}{U_t} = \frac{r}{R}$, combining Eqn 4.11 with Eqns 4.12 & 4.13 results in Eqns 4.14 & 4.15 [8, 9]. Where: α_0 is the aerofoil zero-lift angle of attack, the inflow ratio at the tip is $\lambda_t = \frac{V_x}{U_t}$, the lift-curve slope is $C_{l\alpha}$ and the solidity is $\sigma = \frac{N_b c}{\pi R}$ [10].

$$C_T = \frac{1}{2}\sigma \int_0^1 [x^2 + \lambda_t^2] C_{l\alpha} (\alpha - \alpha_0) dx \quad (4.14)$$

$$C_P = \frac{1}{2}\sigma \int_0^1 [x^3 + x\lambda_t^2][\lambda_i C_{l\alpha} (\alpha - \alpha_0) + C_d] dx \quad (4.15)$$

4.3 Fan Design Methodology

4.3.1 Mixed Design Theory

The main goal of the fan design methodology is to produce a method of determining the performance (T, P, η_p) of a ducted fan for a given set of input variables (fluid and geometrical). Although cascade theory and blade element theory can give the performance of a designed fan, both have constraints.

Cascade theory is used to design aero-engines that have high solidities and high tip Mach numbers of up to $M_{tip} = 1.5$. Tip Mach numbers of up to 1.5 are normally encountered in turbofan engines where the aircraft is travelling at transonic speeds, or lift fan designs where a compact high thrust design is required (e.g. Lockheed Martin F-35). However blade design at such high tip Mach numbers becomes very complex and requires a lot of power. Shock control becomes essential to limit noise signature, decrease viscous losses from shock-boundary layer interaction and increase compression efficiency. Thus the fans are of high solidity to control shocks between the blades, and the blades require sweep and complex aerofoil shaping, in order to produce an efficient design [8].

Blade element theory is used to design propellers, industrial fans and rotor blades. These are generally of lower solidity than aero-engine components and operate at subsonic to transonic Mach numbers. Blade element theory is the simple integration of local lift and drag coefficients across a blade to provide the performance of a fan, consequently the aerofoil sections chosen are essential in producing the optimum design. However, to produce enough thrust at a high

subsonic speed ($M \sim 0.5$), the design will definitely encounter compressibility effects and drag divergence. Although the equations can be modified to take into account compressibility effects, as in cascade theory the blades would require sweeping and detailed (supercritical) aerofoil design to produce an efficient design.

Both design theories provide a method for easily designing and optimising a single fan case. However cascade theory focuses on the temperature and pressure rises across a fan through the imparted flow deflection ($\beta_1 - \beta_2$). The power required is also calculated using the deflection of the flow as seen in Eqn 4.4. This however assumes that the blade axial velocity imparted through the fan is as designed, which is not always the case. While blade element theory is more applicable to the design requirements, much more detailed design of the blade geometry is needed. With the focus on the individual aerofoil aerodynamic characteristics at various stations the variables become too numerous. Further, neither theory can predict the performance of the fan accurately when operating close to or at stall.

It was decided that a simple methodology with a limited number of variables that would output the thrust, power and efficiency was required for fan design. A methodology that could use the input data to define a fan's performance as well as easily provide sufficient information to produce the fan's geometry.

Both theories involve blade twisting to place each aerofoil at the correct angle of attack. However, choosing cascade theory methodology to shape the fans meant that the aerofoil section design could be simplified to thickness (t/c) and camber via inlet and outlet angles (β_1, β_2). The inlet and outlet angles were controlled by the radius of the fan (R), the rotational speed (Ω) and fluid variables: axial velocity (V_x), free stream velocity (V_∞) and relative velocity ratio (V_{ratio}). To minimise complexity further it was decided that the design method was to be based on free vortex blading, which meant assuming constant specific work, constant axial velocity and the free vortex variation of whirl. To complete the geometrical data of the fan, from blade element theory, the solidity (σ) and number of blades (N_b). It was decided that the pitch of the fans would be able to be varied (δ), to improve performance and increase controllability during hover. With certain constraints and simplifications, using these fundamental eight input

variables ($R, \Omega, V_x, V_\infty, V_{ratio}, \sigma, N_b, \delta$), any fan geometry could be defined.

With these variables and now the ability to design output the fan geometry, the performance characteristics of the fan was the next goal. Accurate performance data of various fans was required in order to perform a parametric analysis and thus put together a new methodology for fan design. It was therefore decided that CFD models with varying geometries composed from input variables ($R, \Omega, V_x, V_\infty, V_{ratio}, \sigma, N_b, \delta$) would provide sufficient data. Before this could be executed however, further geometric constraints needed to be defined for the models.

4.3.2 Design Simplifications

With the incorporation of variable pitch into the design of the fans, the rotational speed was kept constant ($\Omega = constant$). Geometrical constraints were required in order to simplify the design process. Most propeller designs have roughly constant chord distribution and so each blade (projection) was assumed to have a linear taper with a taper ratio of $\lambda_b = 0.75$.

Although area is a function of radius, for rotor design there are two components that govern the inlet/outlet area; the tip radius r_t and the hub radius r_h . The hub-tip ratio $\frac{r_h}{r_t}$ also governs the effective blade length. To reduce the amount of input variables, the hub-tip ratio was kept constant ($\frac{r_h}{r_t} = 0.2$). To further reduce the number of input variables, the aerofoil maximum thickness to chord ratio was also kept constant. The root section was kept at $t/c = 0.22$, mid-section $t/c = 0.15$ and the tip $t/c = 0.10$. Thickness at the root is mainly for structural rather than aerodynamic purposes, so a value of 22% was chosen. For modern propellers, thickness at the tip is normally between 6% and 10%, so a value of 10% was chosen.

With all of the above taken into consideration the blade of each fan test case was divided up into 10 stations from root to tip. The camber of the aerofoil at each section was determined by a given velocity ratio V_{ratio} . The lower the velocity ratio, the higher the compression ratio and the higher the aerofoil camber. However velocity ratio is limited by de Haller's criteria ($V_{ratio} \geq 0.72$), which states that excessive efficiency losses occur if the velocity ratio is less than 0.72 [8]. For a given velocity ratio, the relative velocity at the outlet V_2^{rel} could be calculated.

This was used to determine the outlet angle β_2 and therefore the aerofoil camber, Eqn 4.16.

$$\cos \beta_2 = \frac{V_x}{V_2^{rel}} \quad (4.16)$$

It can be seen, that if $V_x > V_2^{rel}$ the expression in Eqn 4.16 ceases to be correct. The root of the blade is where the relative velocity is at its minimum value. As a consequence the velocity ratio is constrained by a minimum outlet angle β_2 requirement at the root of the blade (i.e. $V_{ratio} \cdot V_1^{rel} > V_x$).

Since the camber was determined by the $(\beta_1 - \beta_2)$ deflection of the flow, to minimise complexity further the aerofoil profiles were chosen as NACA 00xx series with thicknesses as outlined earlier.

To prevent any instabilities or control problems from gyroscopic forces during transition, the lift fans were designed to be dual and contra-rotating. The velocity triangles were modified as seen in Figure 4.5. The contra-rotor was then designed using the same method previously stated for single rotors except with the added swirl $V_{\theta 2}$ seen in Figure 4.5 exiting the rotor and entering the contra-rotor (i.e. $V_{\theta 2} = V_{\theta 3} \neq 0$ and $V_2 = V_3$).

Since PAVs will be designed to operate at subsonic speeds ($M_\infty \sim 0.25$ to 0.5) and in residential areas, the priority was to limit the aircraft's noise signature and reduce the complexity of its blade design in the process. This was done by limiting the tip Mach number to $M_{tip} < 0.95$.

4.3.3 Defining Models For CFD

After the simplifications the variables that could be used to define the any fan geometry, and performance outputs can be seen below in Table 4.1. The main outputs required for any fan design methodology are thrust, power and efficiency (static and propulsive). The thrust could be calculated from Eqn 4.17. However, from the equation it can be seen that the magnitude

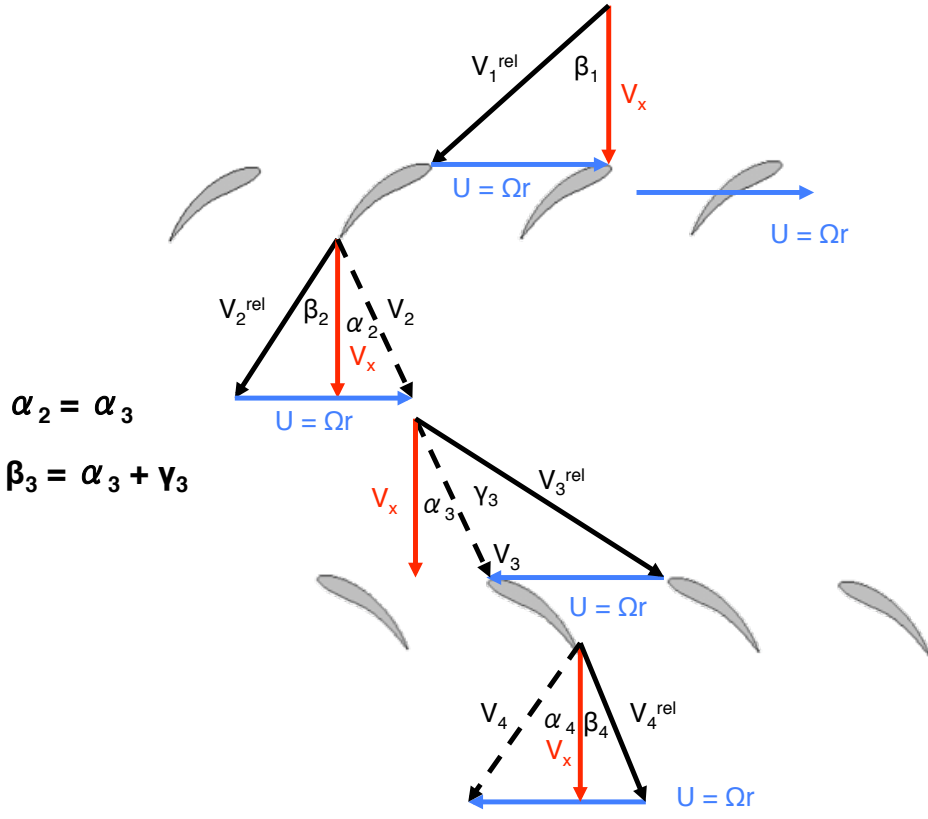


Figure 4.5: Velocity triangles through a contra-rotor stage.

of thrust produced is dependent on the actual axial velocity through the fan (V_{xa}), the outlet area (A), the density of air (ρ) and the free stream velocity (V_∞). Depending on the geometry of the fan and the pitch of the blades, the axial velocity experienced through the fan will not always be the design axial velocity. Therefore the actual axial velocity (V_{xa}) is also one of the output values required from the CFD tests.

$$T = \rho V_{xa} (V_{xa} - V_\infty) A \quad (4.17)$$

The static fan efficiencies were calculated using the ratio of the ideal power to actual power outputted from the CFD in Eqns 4.18 and 4.19 .

$$P_{i_{static}} = \frac{1}{2} T V_{xa} \quad (4.18)$$

$$\eta_{static} = \frac{P_{i_{static}}}{P} \quad (4.19)$$

INPUT VARIABLES	
R or r_t	Radius (tip radius) (m)
Ω	Rotational speed (RPM)
V_x	Design axial velocity (ms^{-1})
V_{ratio}	Relative velocity ratio across fan = $\frac{V_2^{rel}}{V_1^{rel}}$
V_∞	Free steam velocity (ms^{-1})
N_b	Number of blades
σ	Solidity = $\frac{N_b c_r}{\pi R}$
δ	Pitch ($^\circ$) or ($rads$)
OUTPUT VARIABLES	
V_{xa}	Actual axial velocity (ms^{-1})
T	Thrust (N)
P	Power (kW)
η_p	Efficiency

Table 4.1: Main fan variables

The propulsive fan efficiencies were calculated using the ratio of the ideal power to actual power outputted from the CFD in Eqns 4.20 and 4.21 .

$$P_i = T V_\infty \quad (4.20)$$

$$\eta_p = \frac{P_i}{P} \quad (4.21)$$

To minimise the weight of the aircraft and reduce the complexity of the design, it was decided the lift fans would not include pitch control. The remaining variables were gathered and given range constraints in order to produce varying fan models for CFD testing. The input variable ranges for the lift fan can be seen in Table 4.2.

The variable range constraints which could cover the biggest variation of designs within the predicted operational envelope were set for the propulsion/control fans as seen in Table 4.3. The pitch setting of $\delta = 0^\circ$ is the blade orientation for the design conditions of the propulsion

R	$0.500 - 1.500 \text{ m}$
V_x	$40 - 130 \text{ ms}^{-1}$
V_{ratio}	$0.72 - 1.00$
M_{tip}	< 0.95
σ	$0.35 - 1.85$
N_b	$5 - 24$

Table 4.2: Lift fan input variable ranges

fan (V_x and $V_\infty = V_{cruise}$).

R	$0.275 - 0.600 \text{ m}$
V_x	$50 - 250 \text{ ms}^{-1}$
V_{ratio}	$0.72 - 1.00$
V_∞	$0 - V_x$
M_{tip}	< 0.95
σ	$0.30 - 1.00$
N_b	$3 - 16$
δ	$-15^\circ - 20^\circ$

Table 4.3: Propulsion fan input variable ranges

A selection algorithm was compiled to produce 30 different lift fan designs and 30 propulsion/control fan models (excluding pitch and free stream velocity). The algorithm randomly selected values for each variable range making sure that tip Mach number or velocity ratio constraints were not violated. Using these values, geometrical models (blade angles and chord distribution) were generated ready for CFD input. The randomness of the values ensured the distribution of data sufficiently so that most of the geometrical variations were covered, consequently making it easier to find a correlation between the inputs and outputs.

The lack of pitch variation or free stream velocity (i.e. static cases only) resulted in only 30 different lift fan cases that were studied in CFD. Factoring in varying pitch angles ($-15^\circ, -10^\circ, -5^\circ, 0^\circ, 10^\circ, 15^\circ, 20^\circ$) and free stream velocities ($V_\infty = V_x - 30 \text{ ms}^{-1}, V_\infty = V_x/2, V_\infty = V_x$) resulted in 123 propulsion/control fan static and 308 non-static cases.

The propulsion fan (forward flight) CFD cases were run at 3048 m (10000 ft), while the static cases were run at sea level. Some initial test runs were done to see the effect of altitude variation on the results. These tests showed that the actual axial velocities did not vary. However the power varied closely with density. From blade element theory and Eqns 4.17 & 4.20 it can be seen that with a constant axial velocity, thrust and power are directly proportional to the air density. This implies that the forward flight power regression models could be adjusted by multiplying the power by the density ratio in Eqn 4.22, where ρ_{10k} is the air density at 3048 m (10000 ft). The static models could also be adjusted by multiplying the power by the density ratio in Eqn 4.23, where ρ_0 is the air density at sea level.

$$\sigma_{10k} = \frac{\rho}{\rho_{10k}} \quad (4.22)$$

$$\sigma_{SL} = \frac{\rho}{\rho_0} \quad (4.23)$$

4.4 CFD

To be able to produce accurate parametric equations and determine an accurate correlation between the input and output variables, accurate CFD modelling, meshing and results were required. It was decided that the most accurate way of producing results for the parametric analysis was to use specialised turbomachinery CFD software (*ANSYS: Bladegen, Turbogrid and CFX*).

The fan models (cases) were generated in *ANSYS: Bladegen* and then the models were meshed using *ANSYS: Turbogrid*, as can be seen in Figure 4.6.

The inlet and outlet boundary conditions were chosen as pressure boundaries, with the free stream total pressure being applied at the inlet and the free stream static pressure at the outlet. Reference [41] suggested that for turbomachinery a shear stress transport (SST) $k - \omega$ turbulence model should be used, with a turbulence level of 1% to 5%. It also suggested that

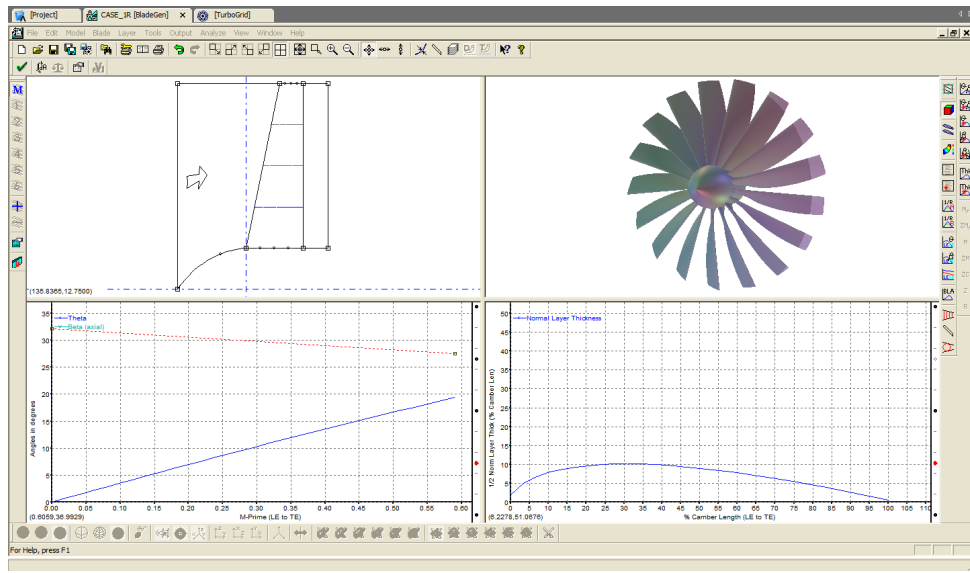


Figure 4.6: Lift fan rotor stage, *Bladegen*

a minimum of 400,000 cells should be used for 3D models.

Having done some initial CFD tests using compressible conditions, it was clear that more complicated aerofoil/blade shaping and detailed design was required to produce a fan that did not produce shocks that caused large losses in efficiency. The process of detailed blade design is time consuming and requires experimental testing and data. The most current propeller designs can reach sonic tip speeds and still have high performance values. This implies that compressibility effects have been delayed or controlled through careful blade sweep, chord distribution and aerofoil selection (supercritical and slender) as can be seen in Figure 4.7. Thus it could be assumed that performance values from an incompressible CFD test could emulate that of a carefully designed fan within the bounds of reason. These performance characteristics could be extracted through further detailed blade design.

The 461 different meshes were loaded with the correct boundary conditions and were then they were entered into the solver *ANSYS: CFX*. Some of the visual outputs from the CFD can be seen in Figure 4.8.



Figure 4.7: Airbus A400M Scimitar propeller (swept blades) [19]

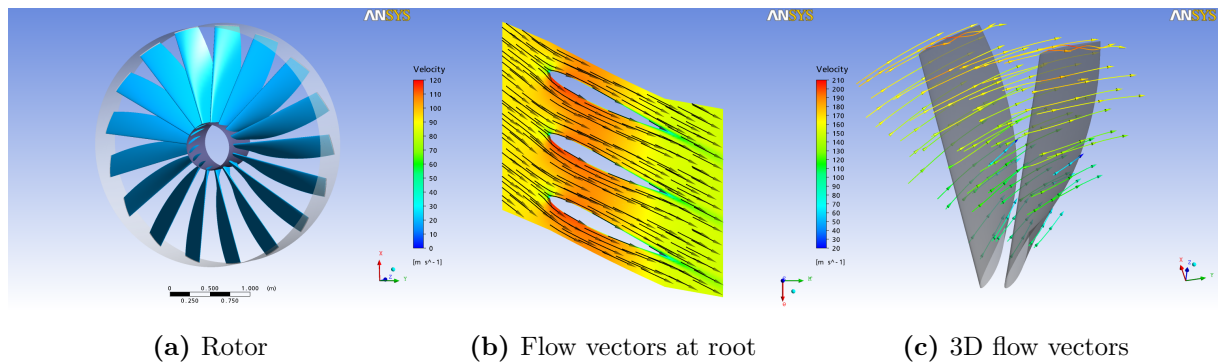


Figure 4.8: Fan CFD Outputs

4.5 Parametric Analysis

The parametric analysis was done using multivariable linear regression techniques. One chosen variable can be expressed in terms of several input variables in the forms seen in Eqns 4.24 (Linear) & 4.25 (Logarithmic) [42]. A coefficient of determination (R^2) can be calculated to determine the degree of correlation of the data, and thus the accuracy of the regression model.

$$y = a_0 + a_1x_1 + a_2x_2 + a_3x_3 + \dots + a_nx_n \quad (4.24)$$

$$\log_{10}(y) = a_0 + a_1\log_{10}(x_1) + a_2\log_{10}(x_2) + a_3\log_{10}(x_3) + \dots + a_n\log_{10}(x_n) \quad (4.25)$$

The input variables from the fan models and the results from the CFD were compiled together. These data were processed using the MATLAB linear regression function and the resulting regression models can be seen in Appendix B.1. The coefficient of determination (\mathbf{R}^2) for most of the regression models were between 0.91-0.95, with mean errors of $\bar{\varepsilon} = 4\%$ for V_{xa} and $\bar{\varepsilon} = 7 - 10\%$ for P .

The regression models for control/propulsion fans were separated into static (hover) and forward flight models as well as by design axial velocity. For forward flight and hover, propulsion fans with axial design speeds of $125 \leq V_x \leq 200 \text{ ms}^{-1}$ were chosen and can be seen in Eqns 4.26 - 4.29 (where $M_{tip}^U = U_t/a$). For hover lift fans with axial design speeds of $125 \leq V_x \leq 200 \text{ ms}^{-1}$ and front pitch fan with axial design speeds of $V_x \leq 125 \text{ ms}^{-1}$ were chosen. The equations for actual axial velocity and power for forward flight can be seen in Eqns 4.26 & 4.27.

$$V_{xa}/V_x = 1.5818 + 0.0689 \cdot R + 0.2297 \cdot M_{tip}^U + 0.0009 \cdot N_b + 0.1599 \cdot \sigma - 0.0036 \cdot V_x - 0.9664 \cdot V_{ratio} + 0.0043 \cdot V_\infty + 0.4859 \cdot \delta - 1.6898 \cdot \delta^2 \quad (4.26)$$

$$P = -441.3 + 0.1235 \cdot T + 517.6 \cdot M_{tip} - 24.658 \cdot R - 0.0165 \cdot \Omega - 0.0966 \cdot N_b + 200.3 \cdot \sigma - 4.2417 \cdot V_{xa} + 2.6076 \cdot V_\infty + 2.1308 \cdot V_x + 362.8 \cdot \delta + 1124 \cdot \delta^2 \quad (4.27)$$

The equations for actual axial velocity and power for hover (static) can be seen in Eqns 4.28 & 4.29.

$$V_{xa}/V_x = 3.0491 + 0.1711 \cdot R + 0.4854 \cdot M_{tip}^U - 0.0058 \cdot N_b + 0.3873 \cdot \sigma - 0.0022 \cdot V_x - 2.8346 \cdot V_{ratio} - 0.0714 \cdot \delta + 0.2517 \cdot \delta^2 \quad (4.28)$$

$$P = -206.8 + 0.0600 \cdot T + 1150 \cdot M_{tip} - 719.8 \cdot R - 0.0740 \cdot \Omega - 3.809 \cdot N_b + 187.3 \cdot \sigma - 2.984 \cdot V_{xa} + 2.170 \cdot V_x + 718.5 \cdot \delta \quad (4.29)$$

The equations for actual axial velocity and power for the lift fan static cases can be seen in Eqns 4.30 & 4.31.

$$\begin{aligned} V_{xa}/V_x = & 1.0696 + 0.1040 \cdot R + 0.4119 \cdot M_{tip}^U - 0.0026 \cdot N_b + 0.1160 \cdot \sigma \\ & - 0.0031 \cdot V_x - 0.3967 \cdot V_{ratio} \end{aligned} \quad (4.30)$$

$$P = 10^{-14.1184} \cdot T^{1.9322} \cdot M_{tip}^{-3.2121} \cdot R^{0.9589} \cdot \Omega^{2.9807} \cdot N_b^{0.1499} \cdot \sigma^{-0.0557} \cdot V_{xa}^{-0.9702} \quad (4.31)$$

The models for the pitch fans were chosen with the axial design speed range of $V_x \leq 125 \text{ ms}^{-1}$ for hover. The equations for actual axial velocity and power for the front pitch fan can be seen in Eqns 4.32 & 4.33.

$$\begin{aligned} V_{xa}/V_x = & 1.0204 - 0.3205 \cdot R + 1.1226 \cdot M_{tip}^U - 0.0030 \cdot N_b - 0.0104 \cdot \sigma \\ & - 0.1709 \cdot V_x - 0.7237 \cdot V_{ratio} \end{aligned} \quad (4.32)$$

$$\begin{aligned} P = & -174.6 + 0.0485 \cdot T + 182.6 \cdot M_{tip} - 61.159 \cdot R - 0.0177 \cdot \Omega + 0.8749 \cdot N_b \\ & + 34.346 \cdot \sigma + 0.8788 \cdot V_{xa} + 1.1086 \cdot V_x + 663.8 \cdot \delta + 739.5 \cdot \delta^2 \end{aligned} \quad (4.33)$$

4.6 Fan Performance

With the parametric equations for propulsion developed, the performance of a given design could be analysed. Consequently the most optimum design could be determined for the cruise speed by thrust matching. This was the foundation of the propulsion methodology. Designing the fans for an aircraft drag of $D = 1911 \text{ N}$ (637 N per fan). an optimum set of values for the given fan radius of 0.314 m can be seen in Table 4.4.

Using Eqns 4.26 & 4.27, the performance of the fan was plotted for varying pitches and Mach numbers, Figure 4.9. The fan was optimised to deliver the highest efficiencies close to the cruise Mach number ($M = 0.31$). The efficiency of the fan is very sensitive to any variation of blade pitch angles outside the optimum deflection as can be seen in Figure 4.9. The highest thrust is seen to be generated by a deflection of $\delta = 10^\circ$, but higher deflections lead to a thrust drop and the power increase, indicating that the blade is starting to stall.

T_{req}	637 N
R	0.314 m
Ω	7400 rpm
V_x	129.5 ms^{-1}
V_{ratio}	0.936
V_∞ (cruise)	102.9 ms^{-1}
σ	0.55
N_b	12
δ (at cruise)	0°
Altitude (cruise)	3048 m (10000 ft)

Table 4.4: Propulsion fan design values

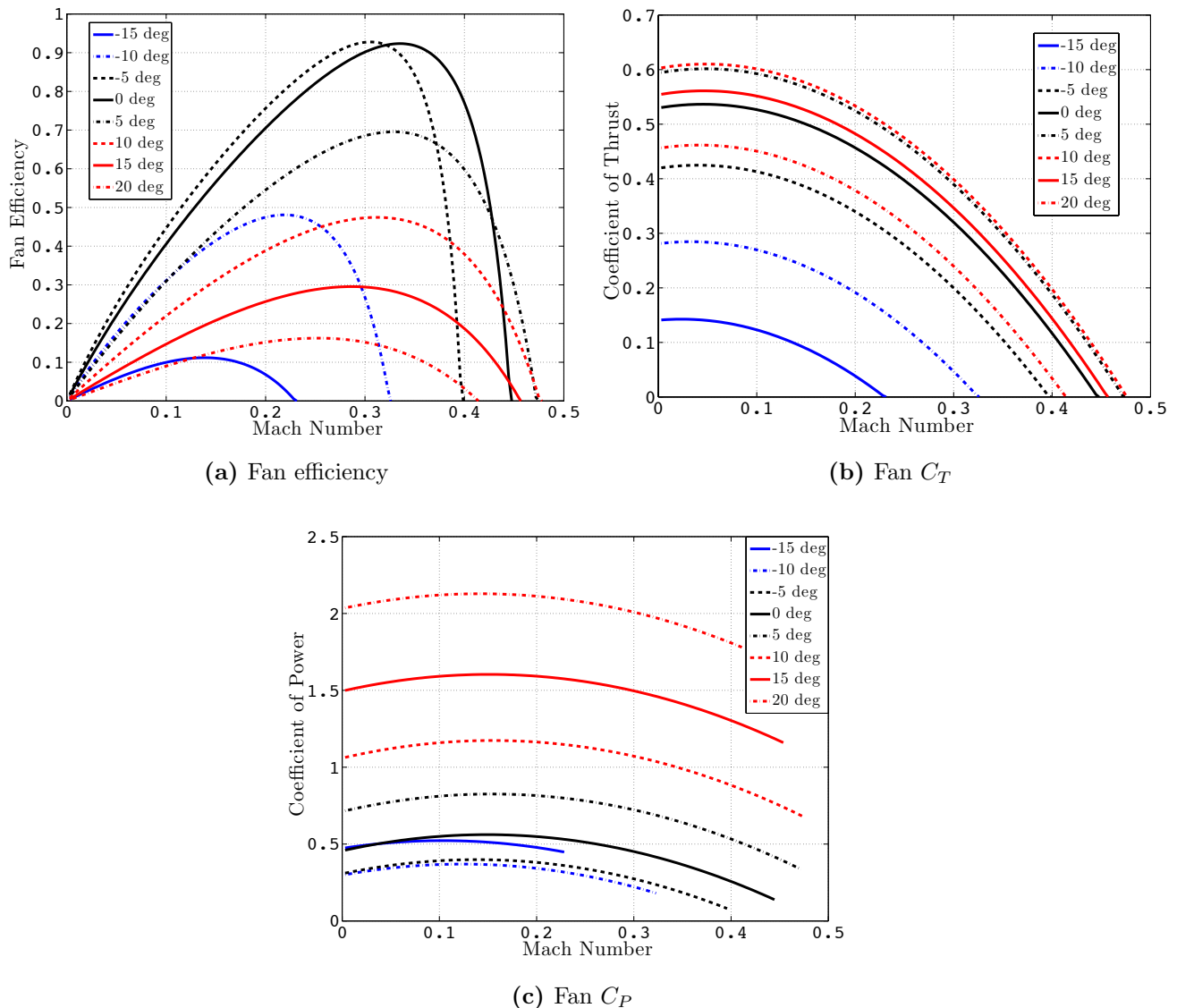


Figure 4.9: Fan performance with varying pitch and Mach number

4.7 CFD Fan Validation

The CFD was validated against experimental data from reference [43]. Reference [43] provided the geometrical data of a 1.22 m diameter fan as can be seen in Table 4.5. The fan was run at $RPMs$ between 4000 and 6000 ($M_{tip} \simeq 0.97$) with a 5° pitch increase. The CFD case was run at 5000 RPM at the same pitch. The comparison of the experimental and CFD results can be seen in Figure 4.10.

r/R	chord (m)	β_1 ($^\circ$)	t/c
0.333	0.0953	43	0.19
0.500	0.0914	31	0.12
0.600	0.0889	25	0.10
0.700	0.0813	20	0.08
0.800	0.0711	17	0.07
0.900	0.0635	13	0.06
1.000	0.0584	10	0.05

Table 4.5: Fan validation geometrical data

Figure 4.10 shows that the experimental data correlates with the CFD tests. It can also be seen that even though the CFD tests were conducted assuming incompressible flow, the assumption holds for well designed blades. The mean square errors are: $\bar{\varepsilon} = 6\%$ for thrust, $\bar{\varepsilon} = 2\%$ for power and $\bar{\varepsilon} = 3\%$ for efficiency. These errors are partly due to variation in RPM , because reference [43] does not state a specific RPM run for each data point.

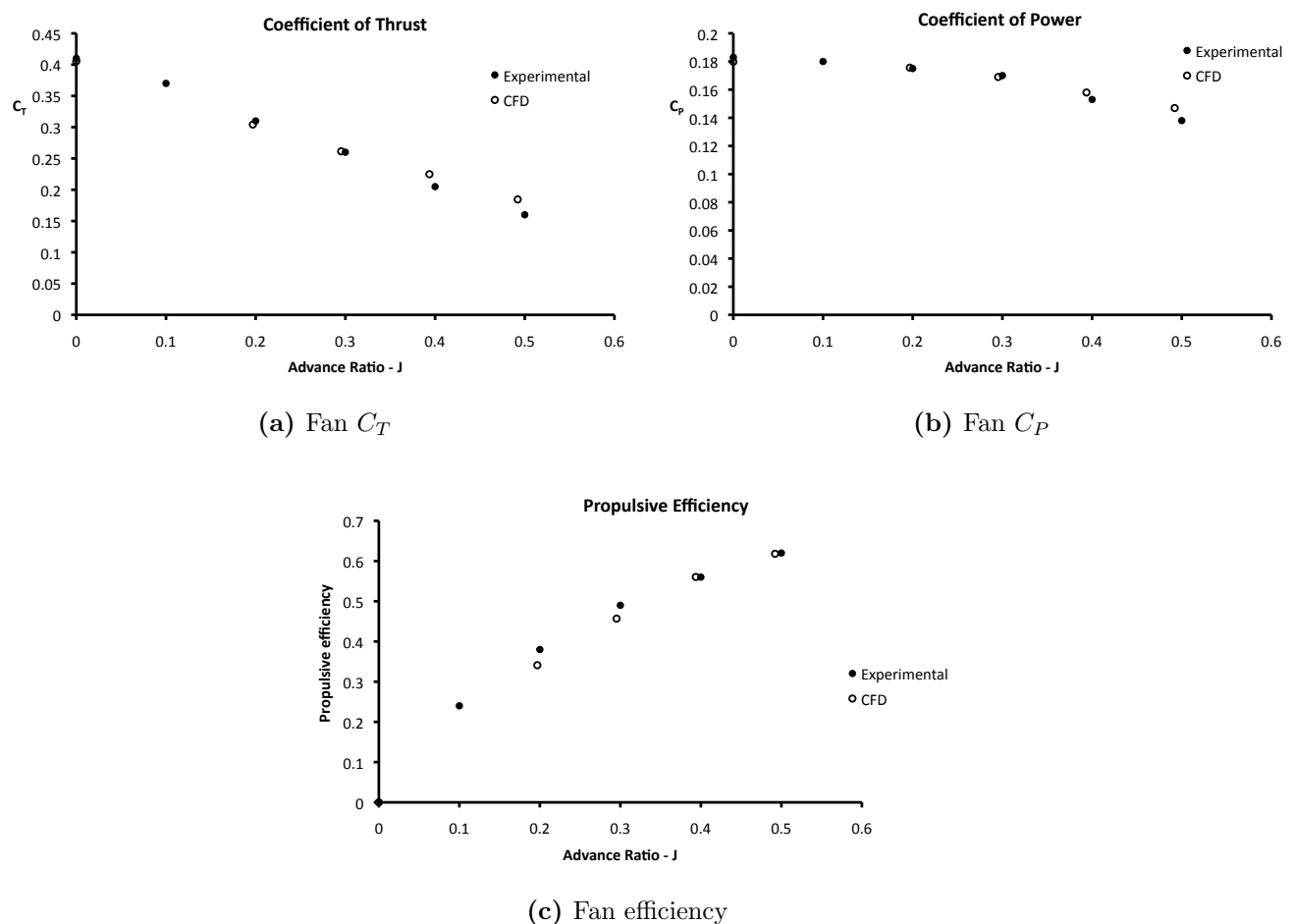


Figure 4.10: Comparing experimental and CFD fan performance data

4.8 Propulsion Methodology

Having established accurate parametric models for fan design, these models were used to setup a propulsion optimisation methodology, an overview of which can be seen in Figure 4.11. The stages are detailed in Figures 4.12, 4.13 & 4.14 respectively.

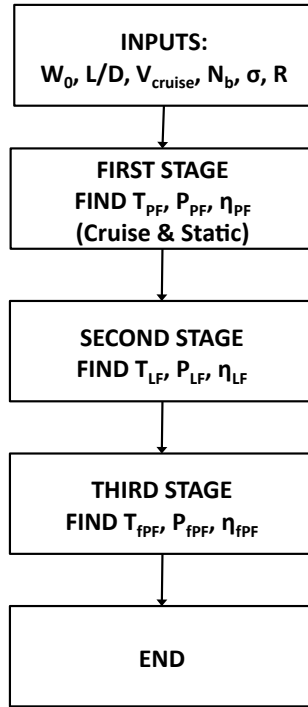


Figure 4.11: Propulsion methodology overview

The initial inputs: maximum take-off weight (W_0), weight-to-thrust ratio (W/T), cruise speed (V_{cruise}) and geometrical inputs of the fan; radii, solidities and number of blades were entered into the methodology. These initial inputs outline the performance goals required for the fans. The maximum take-off weight outlines the total thrust required for hover and VTOL. Reference [40] suggests that for VTOL capability with a non-jet propulsion aircraft, the fans are required to produce thrust of the order 1.1 times the maximum take-off weight. The lift-to-drag ratio and cruise speed provide a drag estimate and thus the thrust required at cruise.

The first stage Figure 4.12 matches the forward flight thrust required (T_{PF}) to the drag at cruise. Then various blade pitches are examined using the parametric models. Any configura-

tions that meet all the constraints set (e.g $M_{tip} < 0.95$) are then saved. The data is reduced to the fan with the highest efficiency and lowest power consumption for the user inputted radius. This optimum fan design is then selected for integration into the PAV. The static thrust ($T_{PF_{static}}$) these fans can produce is also calculated and used in the next stages to determine the VTOL capability of the PAV.

The second and third stages Figures 4.13 & 4.14 follow similar patterns to that of the propulsion fans in Figure 4.12. The remaining thrusts (T_{LF} , T_{fPF}) needed to balance the moments of the aircraft in hover as well as maintain VTOL capability are calculated. The lift fan is optimised for hover with no pitch control. The pitch fan is examined under similar criteria as the propulsion fan but optimised for hover instead. The data is reduced to the single fans with the highest efficiency and lowest power consumption at each radius. The desired fan radius for each lift and pitch are then selected for integration into the PAV.

An sample of the results from fan methodology can be seen in Appendix B.3. The show the results from hundreds of variable variations and the selection of the most optimum point.

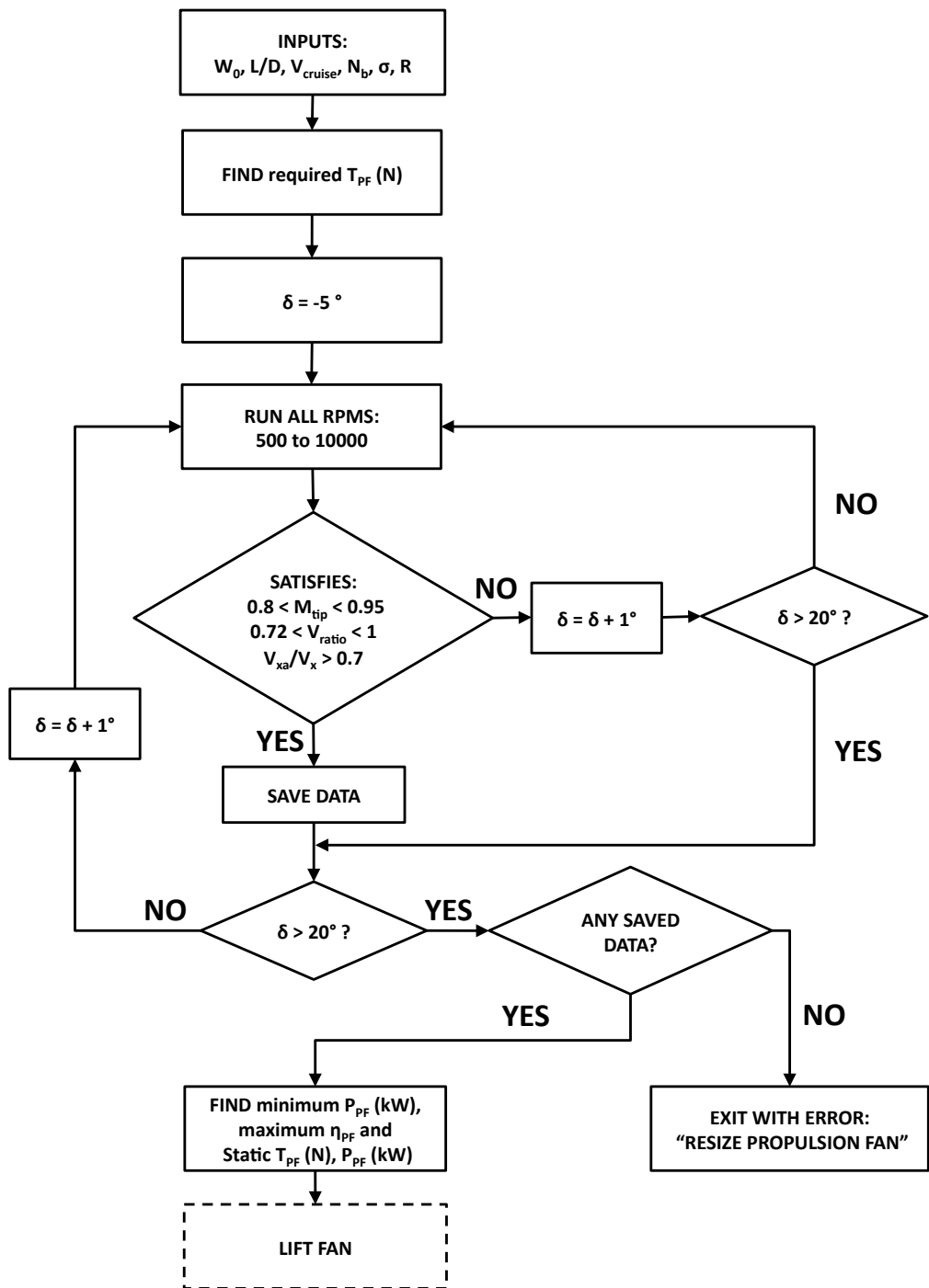


Figure 4.12: First stage of Propulsion methodology

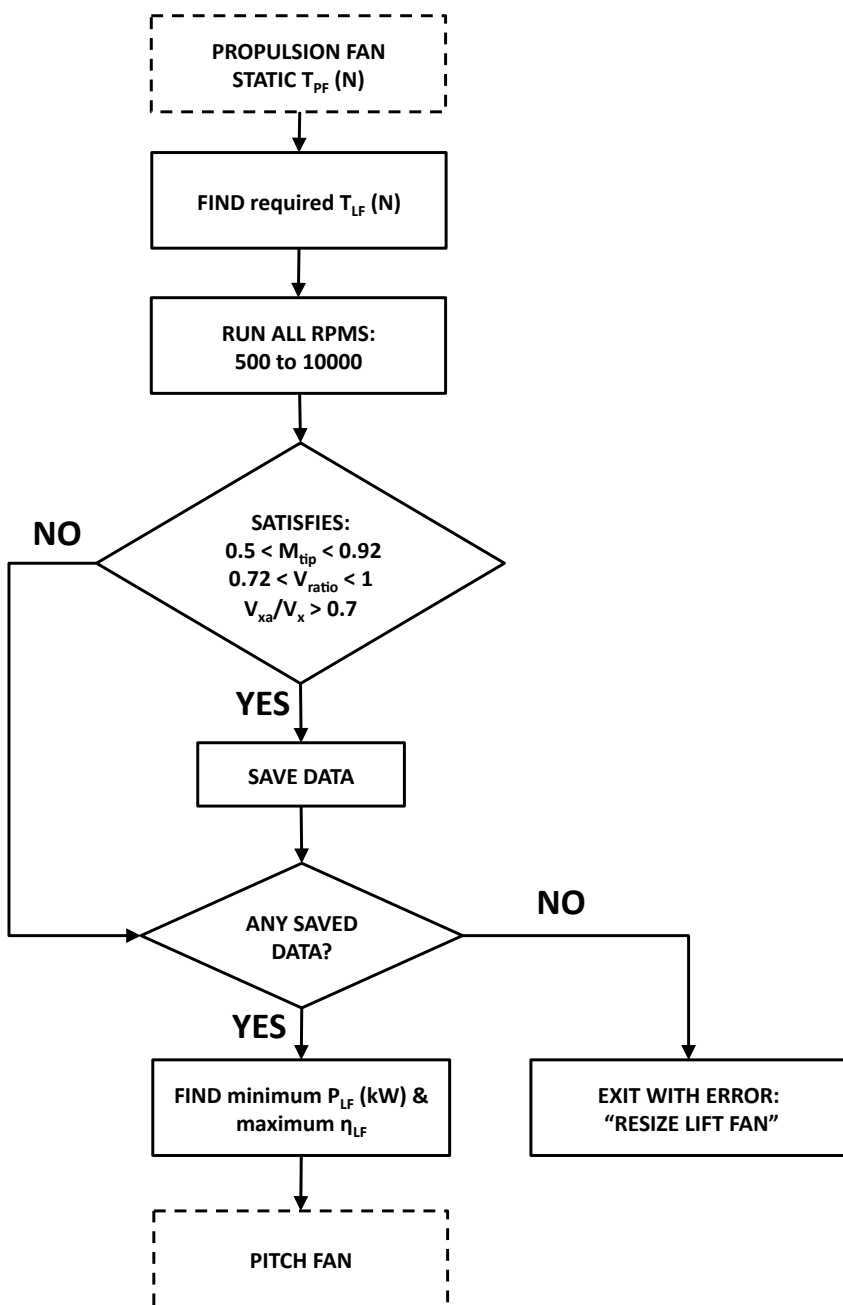


Figure 4.13: Second stage of Propulsion methodology

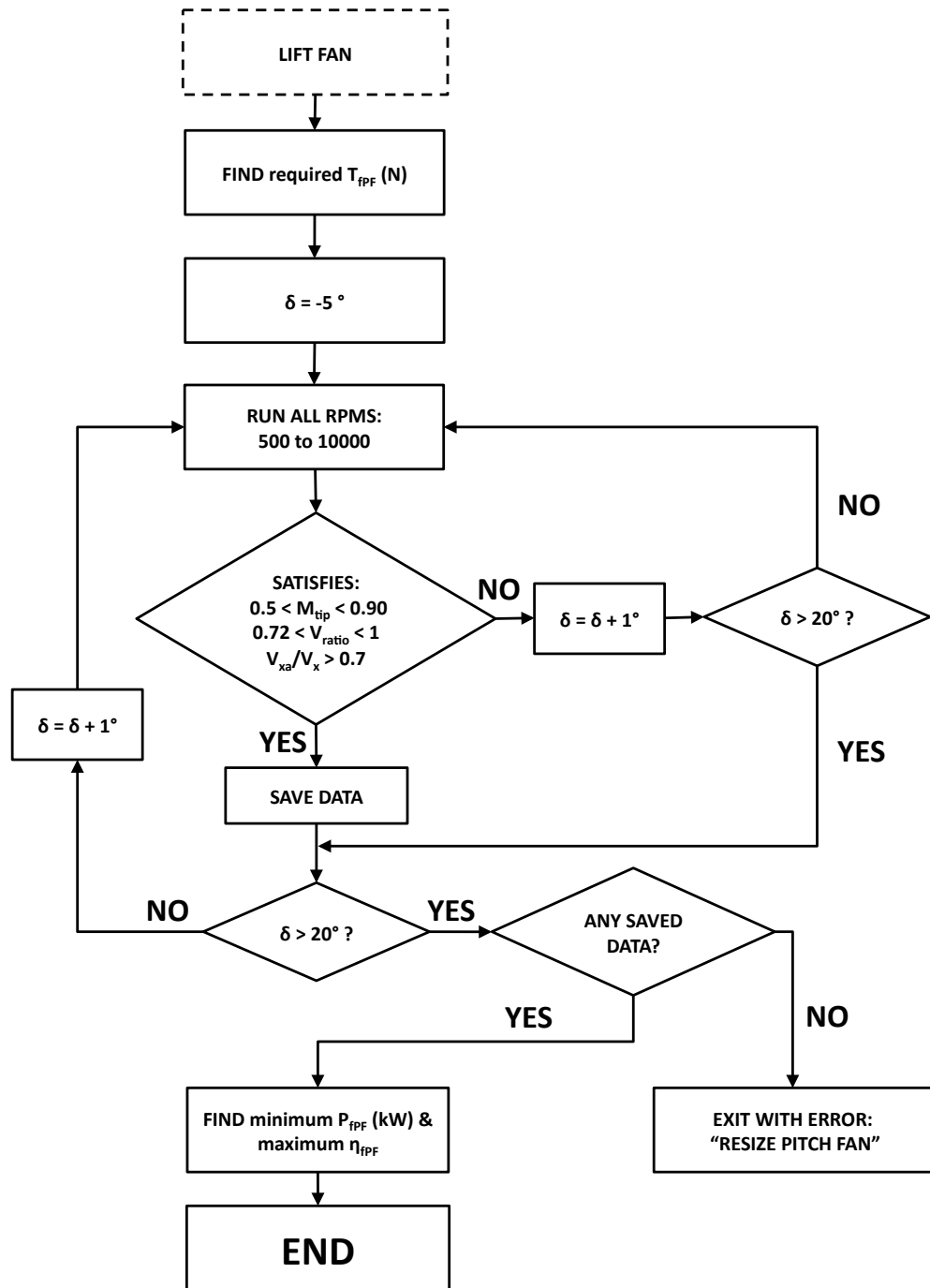


Figure 4.14: Third stage of Propulsion methodology

4.9 Inlet & Guide Vane Design

A sizing methodology was also required for the inlet and inlet guide vanes. The aim of the inlet was to prevent separated flow from entering the fan during transition from hover to forward flight. Guide vanes were designed to straighten/correct the flow's angle entering the rotor, for any flight regime. Both devices reduce the possibility of fan surge (blade stall). A similar process to that of the fan design was followed. The key variables that affect flow angle and control separation were identified and then varying CFD models were tested. The resulting data was used to form parametric equations.

4.9.1 Inlet Design - *Transition*

The primary function of the inlet is to prevent separation. Its secondary function is to straighten the flow into the guide vanes. This is done by giving the flow enough curvature to the inlet to turn into the duct.

The main variable outputs that describe the flow behaviour at a specific point entering the duct were found to be the inlet angle of the flow (α_1) and the wall skin friction (τ_w). The skin friction direction determined if the flow was separated or not. A negative value implied the flow at the wall was in the opposite direction to the mean flow, and thus in a separated recirculation region. By increasing the curvature at the duct entrance, the separation could be eliminated [9]. Increasing the duct length also decreased the possibility of surge (blade stall) due to reattachment of the flow before entering the fan. However increasing the duct length without eliminating separation would increase the fan power requirements and could also create packaging problems.

The variables that dictate the variation in inlet angle and separation were identified as: radius of the duct ($R_D = R_{LF}$), cross flow velocity (V_{cross}), axial velocity through the duct/fan (V_{xa}), radius of the duct inlet (r_{duct}) and total height of the duct (h_{total}). These dimensions and variables can be seen illustrated in Figure 4.15. The radius of the duct is considered equal to the radius of the fan.

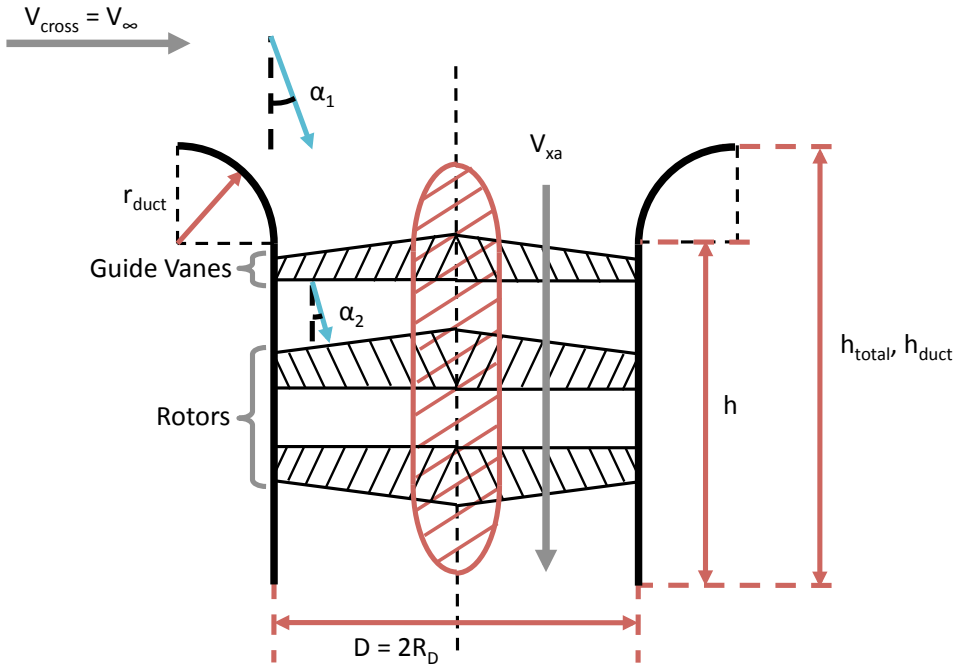


Figure 4.15: Duct dimensions and variables for lift fan

The same selection algorithm that was used to decide fan geometry was used to produce 30 different duct designs within the variable ranges listed in Table 4.6. These varying duct designs were generated ready for CFD input. The randomness of the values ensured sufficient distribution of data so that most of the geometrical variations were covered; consequently making it easier to find a correlation between the inputs and outputs.

R_D	$0.500 - 1.500 \text{ m}$
V_{cross}	$10 - 80 \text{ ms}^{-1}$
V_{xa}	$40 - 130 \text{ ms}^{-1}$
r_{duct}/D_{duct}	$0 - 0.315$
r_{total}/D_{duct}	$0.1 - 1$

Table 4.6: Inlet and Duct input variable ranges

The 30 varying duct models were CFD tested and some of the visual outputs can be seen in Figure 4.16. The data were gathered and the resulting regression models were produced,

Eqns 4.34 - 4.37.

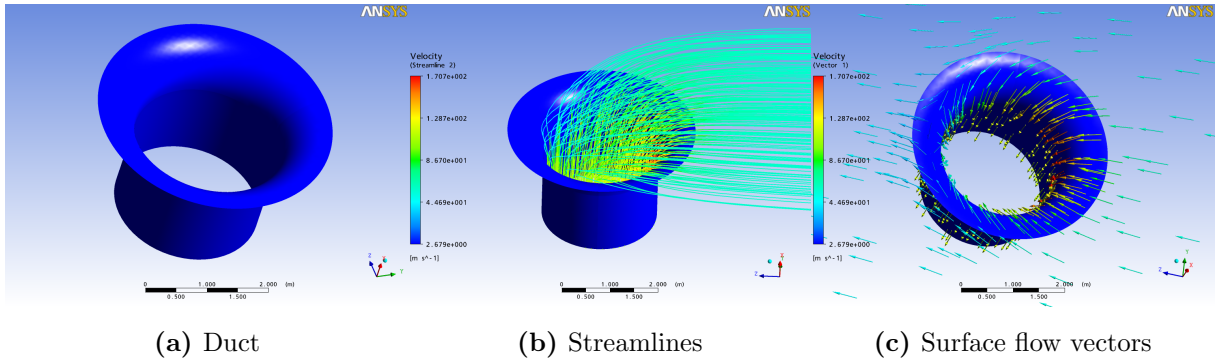


Figure 4.16: Duct CFD Outputs

The duct results were split into two readings; one quarter of the total duct height from the inlet ($h_{total}/4$), Eqns 4.34 & 4.35 and half way down the duct ($h_{total}/2$), Eqns 4.36 & 4.37.

$$\alpha_1|_{h/4} = 10^{-0.8383} \cdot R_D^{0.0617} \cdot V_{cross}^{0.9855} \cdot V_{xa}^{-0.8668} \cdot (r_{duct}/D_{duct})^{-0.0142} \cdot (h_{total}/D_{duct})^{-0.4071} \quad (4.34)$$

$$\begin{aligned} \tau_w|_{h/4} = & -4.9798 - 1.7779 \cdot R_D - 0.0860 \cdot V_{cross} + 0.1572 \cdot V_{xa} \\ & + 8.5267 \cdot r_{duct}/D_{duct} + 3.0783 \cdot h_{total}/D_{duct} \end{aligned} \quad (4.35)$$

$$\alpha_1|_{h/2} = 10^{-1.3544} \cdot R_D^{0.1141} \cdot V_{cross}^{0.9777} \cdot V_{xa}^{-0.8247} \cdot (r_{duct}/D_{duct})^{-0.0100} \cdot (h_{total}/D_{duct})^{-0.7352} \quad (4.36)$$

$$\begin{aligned} \tau_w|_{h/2} = & -9.4268 + 1.2434 \cdot R_D - 0.0865 \cdot V_{cross} + 0.1462 \cdot V_{xa} \\ & + 33.802 \cdot r_{duct}/D_{duct} - 1.1799 \cdot h_{total}/D_{duct} \end{aligned} \quad (4.37)$$

4.9.2 Guide Vane Design

The primary function of guide vanes is to ensure that the flow entering the fan is straight to prevent surge. The main variable output was identified as the guide vane exit angle (α_2).

To simplify the guide vane design the same geometrical constraints used for the fan design were implemented. The taper ratio was selected as $\lambda_{GV} = 0.75$. The hub-tip ratio $\frac{r_h}{r_t}$ was also kept constant at 0.2. The aerofoils used were all symmetrical (NACA 00xx series) and their thicknesses were as follows: root section $t/c = 0.22$, mid-section $t/c = 0.18$ and the tip $t/c = 0.12$.

The variables that determined the output were identified as: radius of the guide vane ($R_{GV} = R$), Number of blades ($N_{b_{GV}}$), root chord ($c_{r_{GV}}$), guide vane inlet angle (α_1), axial velocity through the duct/fan/guide vane (V_{xa}) and solidity (σ_{GV}). The guide vane radius was considered equal to the fan radius when analysed.

The same selection algorithm that was used to select fan and duct geometry was used to produce 30 different guide vane designs within the variable ranges listed in Table 4.7. These were generated ready for CFD input.

R_{GV}	$0.300 - 1.500 \text{ m}$
$N_{b_{GV}}$	$8 - 26 \text{ ms}^{-1}$
$c_{r_{GV}}$	$0.050 - 0.365 \text{ m}$
α_1	$0 - 0.314 \text{ rads}$
V_{xa}	$40 - 130 \text{ ms}^{-1}$

Table 4.7: Guide Vane input variable ranges

The guide vane models were CFD tested and some of the visual outputs can be seen in Figure 4.17. The relevant numerical data were gathered and the results were used to form a regression model Eqn 4.38.

$$\alpha_2 = 10^{-0.3059} \cdot R_{GV}^{0.8553} \cdot N_{b_{GV}}^{-1.2707} \cdot c_{r_{GV}}^{-1.5873} \cdot \alpha_1^{1.2377} \cdot V_{xa}^{0.1274} \quad (4.38)$$

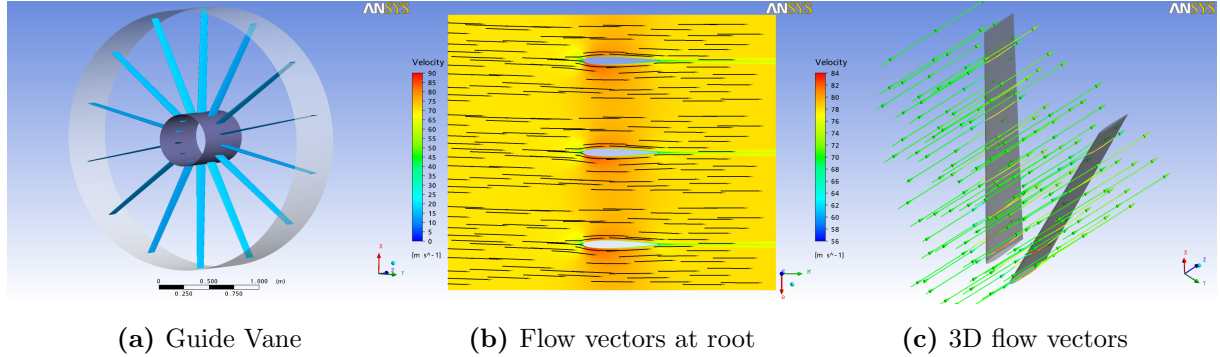


Figure 4.17: Guide Vane CFD Outputs

4.9.3 Inlet & Guide Vane Methodology & Flowchart

Using the parametric models for the duct and guide vanes an optimisation methodology was put together Figure 4.18. The radius and axial velocity are entered into the methodology from the static fan equations. The cross flow velocity was assumed to be 1.2 times the stall velocity of the aircraft. This was to ensure that fan surge is delayed until the aircraft's weight is fully supported by the lifting surfaces. The number of guide vane blades is kept constant ($N_{b_{GV}} = 22$) to minimise the complexity of the methodology.

The duct is initially sized and packaged to house all the relevant components (fans and guide vanes). The methodology proceeds to check for separation along the duct using Eqns 4.35 & 4.37. If separation is detected the duct inlet radius (r_{duct}) is increased. The process is repeated until no separation is detected. The inlet angle (α_1) is then calculated using Eqn 4.34. This angle is used to calculate the guide vane exit angle (α_2). If this angle exceeds 1.5° , then the root chord of the guide vane is increased and the duct is resized to fit the larger guide vane. The process is repeated until the guide vane exit angle is below 1.5° .

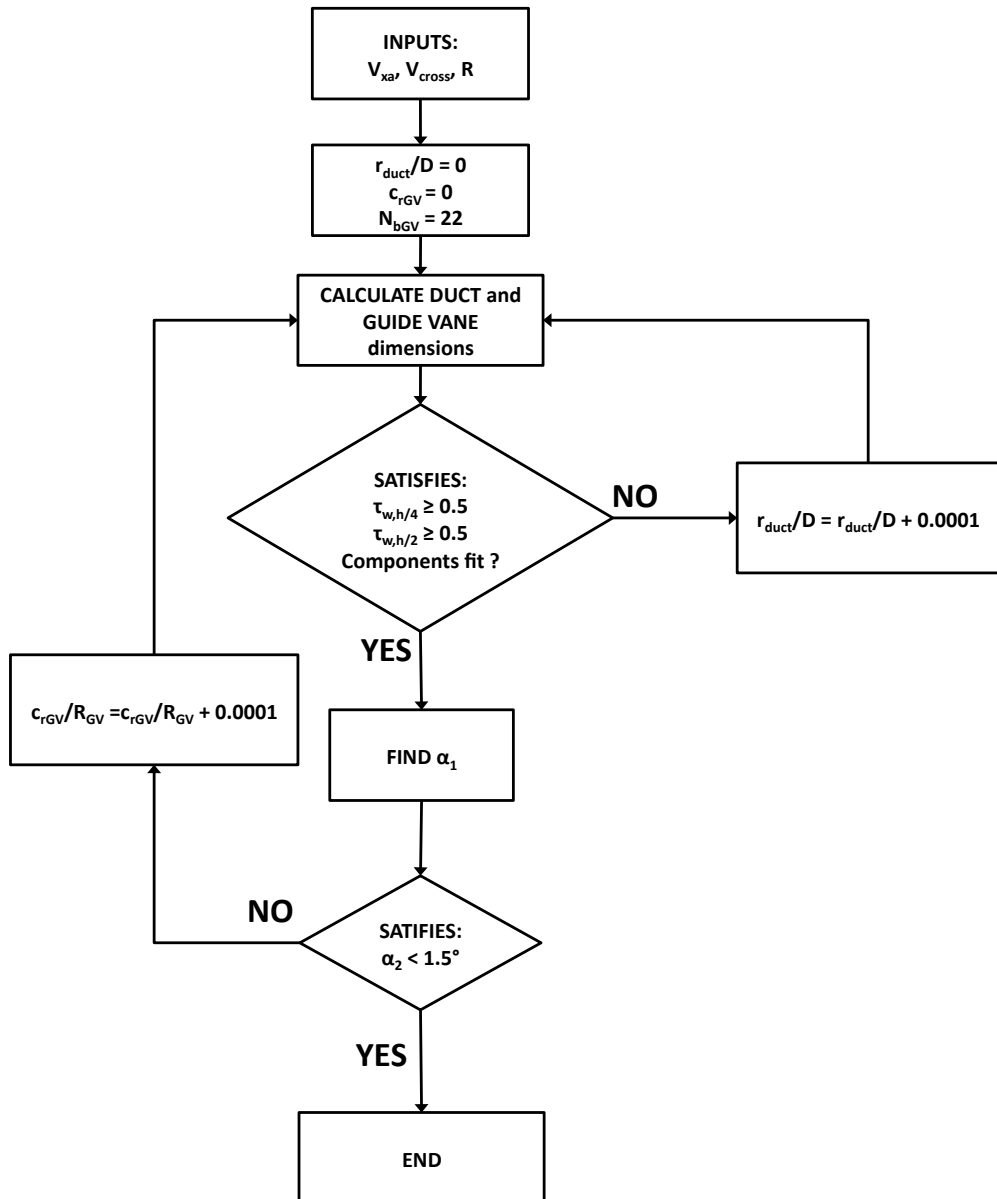


Figure 4.18: Duct and Guide Vane methodology for lift fan

4.10 Gear Design

It was decided that a single engine would be used to drive all the fans through a series of gears, shafts and gearboxes to minimise control problems and reduce weight. To further reduce the number of gearboxes required, it was also decided that the fans would be integrated with the gear systems. The fans would consequently be considered as large gears (wheel) and thus driven by a much smaller gear (pinion) through their circumferences as illustrated in Figure 4.19.

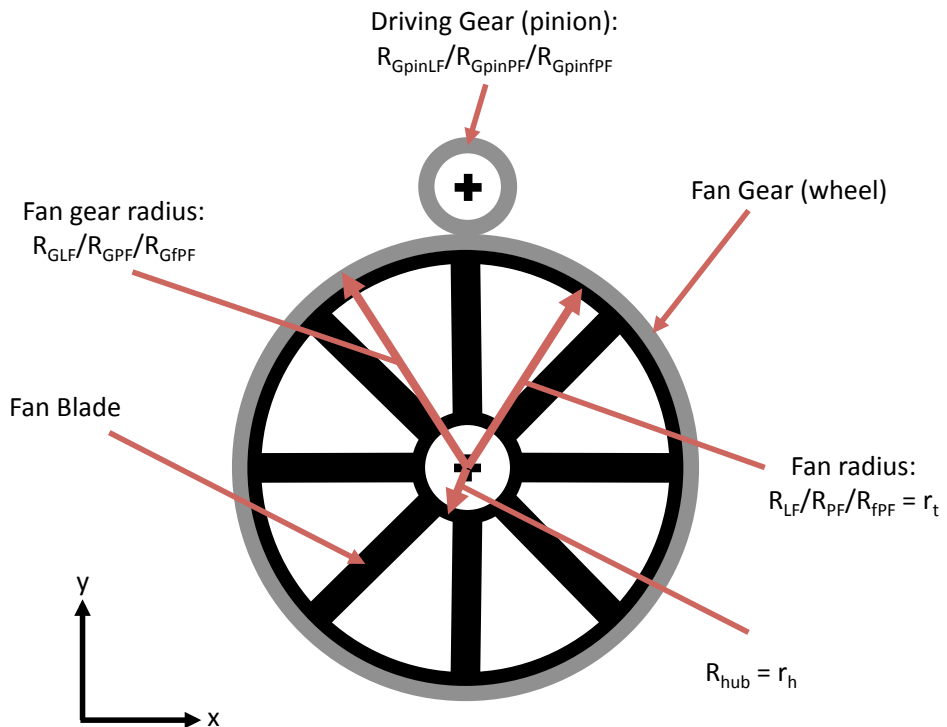


Figure 4.19: Fan gear

For illustrative purposes Figure 4.19 shows the driving gear in the same plane as the fan (spur gear configuration), however to reduce complexity, bevel gear as opposed to spur gear configurations were chosen because of their ability to transmit motion through to a different plane or different angle and with high efficiency ($\sim 95\text{-}99\%$) [44] as can be seen in Figure 4.20.



(a) Spur gear

(b) Bevel gear

(c) Angled bevel

Figure 4.20: Different gears configurations [45]

Using the Eqns 4.39 - 4.44, Table 4.8 and Figure 4.21 the gears were sized to meet the power requirements for each fan. Using reference [44], calculations showed that for high speed, high stress and long life machinery the optimum gear material was nitrided or carburised steel. Having identified the optimum gear material, the gear factors could be distinguished. Reference [44] also suggested the gear factors for high stress and long life machinery shown in Table 4.8.

Eqns 4.39 & 4.40 are the face width sizing equations; where I is the geometry factor, u the gear ratio, z_p the number of teeth on the pinion, m_n the diametral pitch and d_{pitch} ($2R_p$) the pitch (gear) diameter of the pinion. The face width is the width of a single tooth as seen in Figure 4.21. The size of the face width determines the contact stress of the gear. Both equations need to be satisfied to for the optimum tooth size. Eqn 4.39 determines the face width required to resist the maximum foreseeable loads, while Eqn 4.40 determines the face width required to resist fatigue failure.

$$F_{wd} = P_i \left[\frac{RPM}{4.11} \frac{I \cdot C_v}{C_m C_a} \left(\frac{S_{AC} \cdot d_{pitch}}{C_p} \cdot \frac{C_{lf} C_h}{C_t C_r} \right)^2 \right]^{-1} \quad (4.39)$$

$$F_{wd} = \frac{P_i}{m_n} \left[\frac{RPM \cdot d_{pitch}}{719.48 \cdot C_a} \left(\frac{J}{C_b C_m C_s} \right) \left(\frac{S_{AB} \cdot C_{lf}}{C_t C_r} \right) \right]^{-1} \quad (4.40)$$

$$I = \frac{\cos\phi}{2} \cdot \frac{u \cdot \sin\phi}{1 + u} \quad (4.41)$$

$$u = \frac{RPM_w}{RPM_p} = \frac{R_w}{R_p} = \frac{z_w}{z_p} \quad (4.42)$$

$$z_p = -1.7364 \cdot u + 54.7 \quad (4.43)$$

$$m_n = d_{pitch}/z_p \quad (4.44)$$

Gear Factors for high stress, long life, steel (alloy) gear	
C_m	1.125
C_t	1
C_v	0.95
C_a	1.25
C_r	1.5
C_{lf}	1
C_h	1
C_p	2800
C_b	1
C_s	0.65
S_{AC} (allowable contact stress)	1310 MPa
S_{AT} (allowable bending fatigue stress)	158.6 MPa
ϕ	20°
J	0.33
RPM	20000

Table 4.8: Gear factors and values for face width calculation

The engine RPM and thus pinion driving the fan RPM was assumed to be that of a typical turboshaft free turbine, i.e. 20000 rpm. The height of a single gear tooth WD was assumed to be the value of diametral pitch m_n . Consequently the pinion gear face width could be sized by determining the maximum value that satisfied both Eqns 4.39 & 4.40, after which the rest of the dimensions for the wheel and pinion could be determined. This process was repeated iteratively, increasing the wheel diameter until none of the dimensions conflicted with that of the fan.

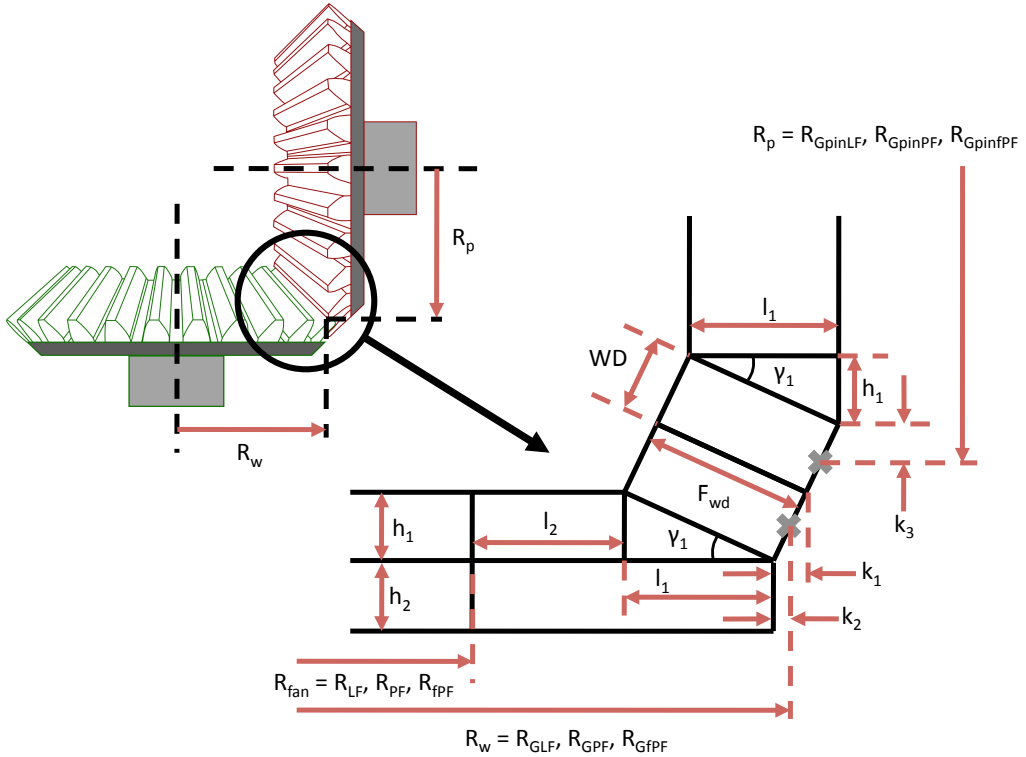


Figure 4.21: Gear tooth sizing

Since the fans are driven from their circumference, the blades had to be secured to both the hub and the tip. This proved to be both aerodynamically and structurally beneficial. The lack of tip clearance minimises blade tip losses and thus increases the propulsive efficiency of the fan. The blade being secured from both ends means that the structural bending moments are reduced significantly. Thus the only structural constraint was the centrifugal stress experienced during rotation at high rotational velocity. The structural stress was then calculated from Eqn 4.45, where ρ_b is the material density of the blades.

$$\sigma_{max} = \frac{\rho_b}{2} U_t^2 \left[1 - \left(\frac{r_h}{r_t} \right)^2 \right] \quad (4.45)$$

The lift fan and pitch fan were only required during VTOL and thus it was decided that they would be decoupled from their gears during forward flight. This would be done by installing a clutch mechanism between the wheel (fan) gears and the fan circumference, which would allow the engine to continue to provide power to the propulsion fans without rotating the lift or pitch

fan. The gear system layout and packaging can be seen in further detail in Chapter 5.

All the gears were assumed to be designed to high tolerances and to be held in position by bearings to avoid any gear slipping. The materials used for the gear system were to reduce the risk of failure and minimise the weight of the system. These design assumptions are cautious and thus through detailed design the system could be optimised and the weight of the aircraft could be reduced further.

4.11 Shaft Design

The shafts connecting all the gears were designed using the Eqns 4.46 - 4.51 and Table 4.9 [46]. The shafts were designed to be hollow to reduce weight, with a inner to outer diameter ratio of $d_i/d_0 = 0.65$. The bending moment of the beam was assumed to be the minimum value generated by the weight of the shaft, see Eqn 4.48. The torque of each shaft was calculated using Eqn 4.46.

$$T_q = \frac{P_{shaft}}{\omega} \quad (4.46)$$

$$B = \frac{1}{1 - \left(\frac{d_i}{d_0}\right)^4} \quad (4.47)$$

$$M = \frac{W_{shaft} \cdot g \cdot L_{shaft}}{8} \quad (4.48)$$

The fatigue limit of the shafts were calculated using Eqn 4.49, while the corrected fatigue limit was calculated using Eqn 4.50 and the factors in Table 4.9. The correction factors were suggested by reference [46] in order to achieve long life and high reliability design.

$$\sigma_{f,m}^* = \sigma_f^* \left\{ \left[1 - 77.8 \left(\frac{T_q}{d_0^3 \cdot \sigma_y} \right)^2 \right]^{\frac{1}{2}} - 10.2 \left(\frac{M}{d_0^3 \cdot \sigma_u} \right) \right\} \quad (4.49)$$

$$\sigma_f = \sigma_{f,m}^* \cdot k_a \cdot k_b \cdot k_c \cdot k_d \cdot k_e \cdot k_f \cdot k_g \quad (4.50)$$

The diameter of the shaft required to fulfil all the torsion, bending and fatigue criteria was calculated using Eqn 4.51 and a safety factor of $SF = 2$. The process was repeated iteratively until the diameter of the shaft converged.

Shaft Factors for high stress, long life, steel shaft	
Material	Carburised Steel (SAE 1045)
k_a	0.8
k_b	$\left(\frac{d_0}{0.76}\right)^{-0.068}$
k_c	0.95
k_d	1.25
k_e	1.5
k_f	1
k_g	1
σ_u	724 MPa
σ_y	634 MPa
σ_f^*	323 MPa

Table 4.9: Shaft factors and values for diameter calculation

$$d_0^3 = \frac{32 \cdot SF}{\pi} B \left[\left(\frac{M}{\sigma_u} + \frac{0.25 \cdot M}{\sigma_f} \right)^2 + \frac{3}{4} \left(\frac{T_q}{\sigma_y} + \frac{0.25 \cdot T_q}{\sigma_f} \right)^2 \right]^{\frac{1}{2}} \quad (4.51)$$

4.12 Engine Sizing

A database of various turboprop and turboshaft engines was compiled in order to determine a correlation between the power rating and the size of the engine. No correlation was found between the diameter or the length of the engine and power or the length and power as shown in Figure 4.22a. Using the data the average engine dimensions were selected as diameter $w_{eng} = 0.55 \text{ m}$ and length $L_{eng} = 1.10 \text{ m}$. A linear correlation between engine weight and power was determined from the data in Figure 4.22b, which was represented by Eqn 4.52 (where power is in kW). The methodology for engine weight estimation was validated with a Pratt & Whitney PT6 turboshaft engine and was found to lie on the trend line. The dimensions of the Pratt & Whitney PT6 turboshaft engine were a diameter of 0.58 m and length of 1.50 m . The width of the PT6 is similar to the average diameter of 0.55 m but the length of 1.50 m is above the average value of 1.10 m . However this just illustrates further the lack of correlation of engine dimensions seen in Figure 4.22a and so the average length of 1.10 m is an acceptable value.

$$W_{ENG} = 0.0653 \cdot P_{total} + 131.71 \quad (4.52)$$

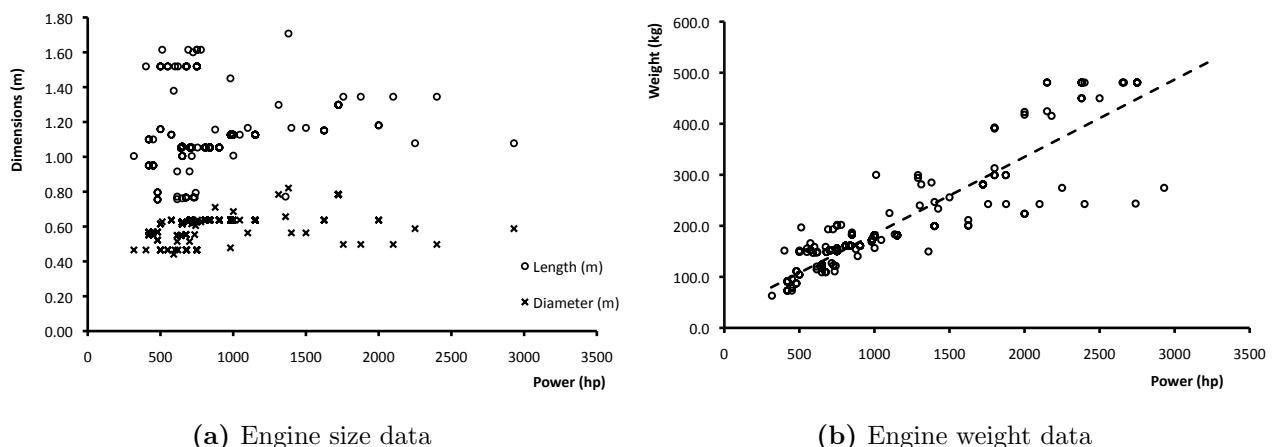


Figure 4.22: Engine data

Turboprop and turboshaft engines normally drive propellers or rotors that rotate at a much lower RPM than what the engines provide. Consequently the engines come with a reduction

gearbox. The fans being incorporated into the gear system, the gear ratios were expected to be high due to the difference in gear diameters as seen in Figure 4.19. The high gear ratio allowed for a high *RPM* input from the engine to the lift fan and so the reduction gearbox was not required. This reduced the weight of the engine by 10-15%.

The installed power of the engine was determined by the gear efficiency of all the gear boxes and the engine inlet efficiency. Reference [12] suggests that a well designed inlet has an efficiency of $\eta_{inl} = 0.98$, and also suggests that extra power is consumed from mechanical and electrical components, $P_{mech} = 2.5 \text{ kW}$ and $P_{elec} = 1.5 \text{ kW}$ respectively.

The gearboxes were assumed to have an efficiency of $\eta_{gear} = 0.98$. Subsequently the gear efficiency of the propulsion fans were calculated as 90.4%, and the gear efficiencies of the lift fan and pitch fan were calculated as 96.0%. Therefore the installed power was calculated using Eqn 4.53.

$$P_{total} = \left[\frac{3 \cdot P_{PF}}{\eta_{gear_{PF}}} + \frac{P_{LF}}{\eta_{gear_{LF}}} + \frac{P_{fPF}}{\eta_{gear_{fPF}}} \right] / \eta_{inl} + P_{mech} + P_{elec} \quad (4.53)$$

The power and SFC variation with Mach number and altitude were calculated using Eqns 4.54, 4.55, 4.56 & 4.57 [14].

$$P_{10k} = \frac{P_{total}}{1.17} \quad (4.54)$$

$$P_{0EQ} = 2.67P_{10k} - 1.33P_{total} \quad (4.55)$$

$$P_{av} = P_{0EQ} \left[\frac{\rho}{\rho_0} + 0.75 \left(\frac{\rho}{\rho_0} \right)^{0.85} M_\infty \right] \quad (4.56)$$

$$SFC = 10^{0.247} P_{total_{hp}}^{-0.161} (1 - M_\infty) \quad (4.57)$$

Chapter 5

Systems Packaging

5.1 Overview

Systems Packaging is the first step to determining an aircraft's shape, size and weight. Coupled with component weight estimation, the aircraft can be balanced to meet stability requirements by shifting components to move the CG (Centre of Gravity) or wing aerodynamic centre to an appropriate position.

The goal was to produce an methodology where all the individual system components could be accommodated easily within the aircraft as well as shifted freely to account for variations in component sizes. The baseline configuration provided an idea of the positioning of the main components, such as the fans, wing, canard, tail, cabin and engine. These components were then positioned accurately along with all the other required systems.

The PAV was initially packaged in 2D planes, firstly the x - y plane and then the x - z plane. The first step was to determine the size of the individual components and then proceed to position them. The rear of the aircraft being the defining section containing propulsion fans, lift fan and wing was packaged first. Subsequently the front of the PAV was packaged to accommodate all the remaining components. With the 2D packaging completed the aircraft was then packaged in 3D to check that none of the components were protruding out of bounds.

5.2 Fans, Gears & Shafts

The aircraft was built around the lift fan, as most of the gears, shafts and main structural points were positioned as consequence of the lift fan position. Hence the lift fan was packaged as seen in Figure 5.1. The lift fan duct was initially packaged using the duct and guide vane methodology Figure 4.18, by sizing the duct and lip to prevent separation. However if the total height of all the components ($h_{comp_total} = hub_{GV} + 2hub_{LF} + 2R_{GpinLF}$) in Figure 5.1 did not fit the duct, the duct height (h_{duct}) was lengthened accordingly. The duct was sized to meet both the aerodynamic criteria and fit all the components ($h_{comp_total} \geq 0.85h$ where $h = h_{duct} - r_{duct}$ from Figure 4.15).

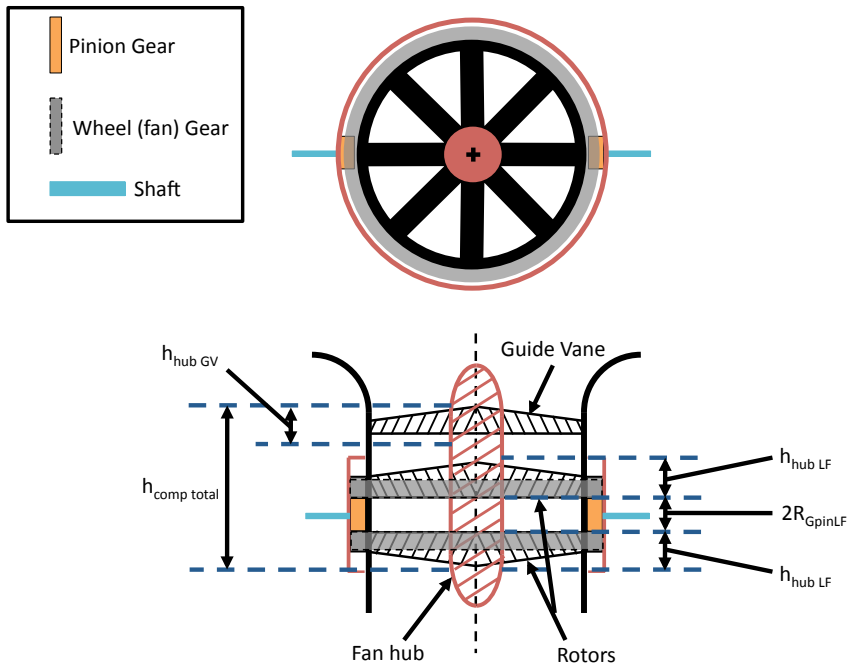


Figure 5.1: Packaging of main lift fan, gears and guide vane

The components in the duct consisted of the hub height, lift fan pinion gear radius and the guide vane hub height. The hub height was developed through parametric analysis of the root chord dimensions of the fans, Eqn 5.1. This ensured that the root chord leading or trailing edge of the fan blade did not protrude from the hub and interfere with other components. The lift fan pinion gear was sized according to the gear ratio required from the engine to the fan. This was done in the gear sizing methodology in Chapter 4. The guide vane hub was sized according

to the guide vane root chord determined in the duct and guide vane methodology Figure 4.18.

$$h_{hub} = 10^{0.8202} \cdot R_{fan}^{0.8949} \cdot N_{b_{fan}}^{-0.9060} \cdot \sigma_{fan}^{0.9712} \cdot \Omega_{fan}^{-0.1085} \quad (5.1)$$

After the packaging of the lift fan, the rear of the aircraft could be packaged. All the connecting shafts, gearboxes and rotation mechanisms were laid out. A total of 8 gearboxes and 13 shafts were used to drive all the fans. The basic layout of the gears, shafts and gearboxes connected to the lift fan can be seen in Figures 5.2, 5.3 & 5.4. The position of these components was dependent on the fan sizes, as shown in detail in the latter stages of this Chapter.

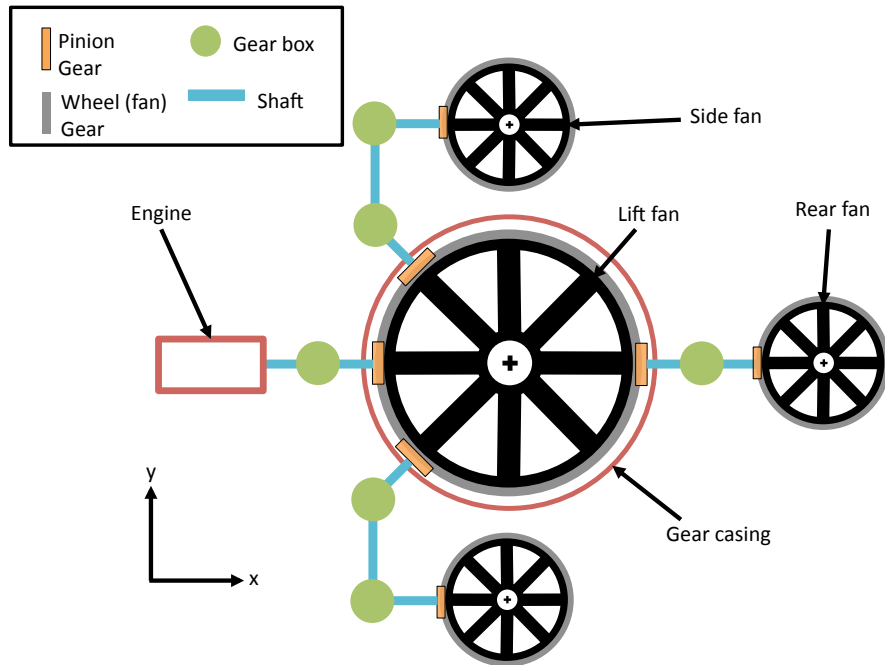


Figure 5.2: Fans, gears and shafts packaging x - y plane

A gearbox was required at any point that required a change of shaft direction or fan rotation. This meant each fan required a minimum of two gearboxes to account for the changes in direction and/or fan rotation requirement.

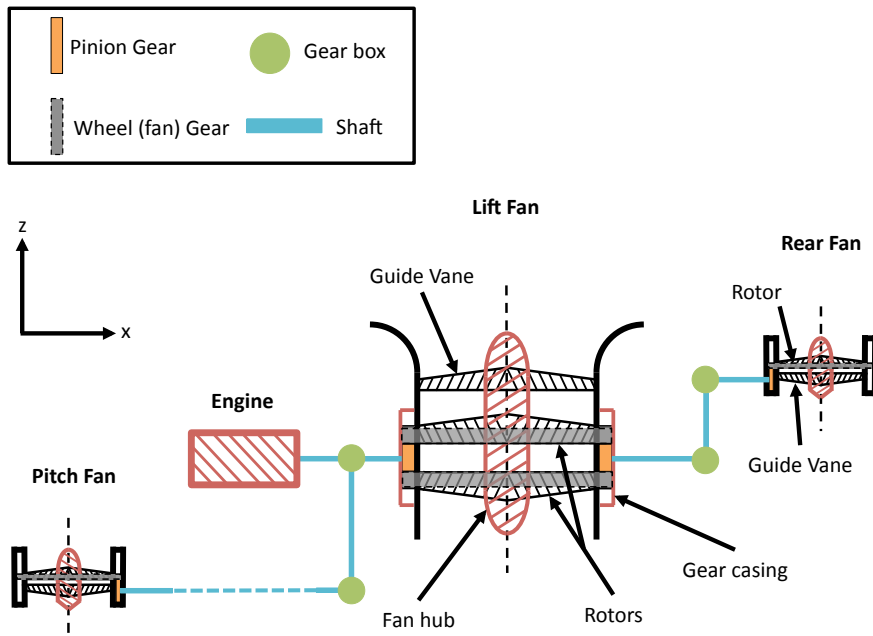


Figure 5.3: Fans, gears and shafts packaging x - z plane

The gearboxes were comprised of 3 different designs as seen in Figure 5.5. The rotating gearbox design was used to tilt the propulsion fans as illustrated in Figure 5.6. Small electric motors drive the rotation as well as the doors that open to allow access to the fans. An example of the fan doors can been seen on the F-35 in Figure 5.7.

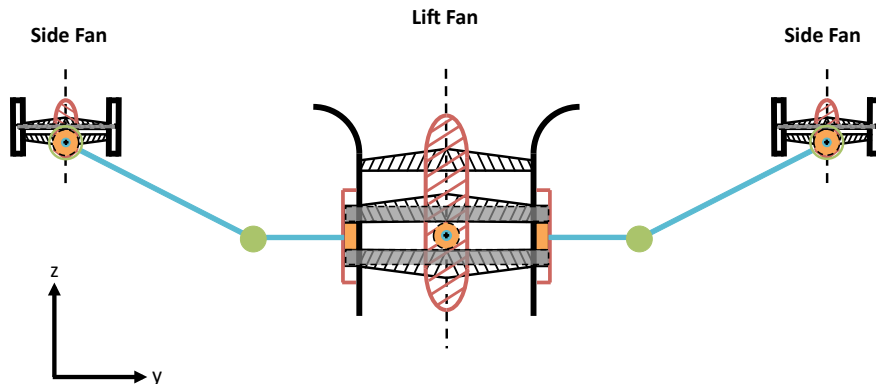


Figure 5.4: Fans, gears and shafts packaging y - z plane

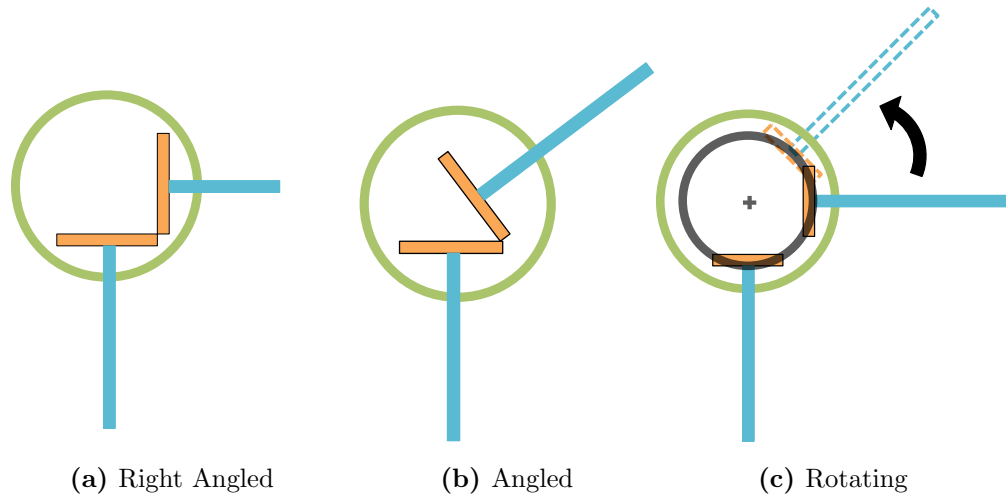


Figure 5.5: Different gearbox designs

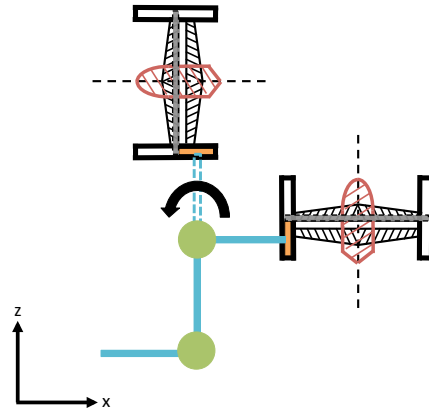


Figure 5.6: Fan tilt mechanism

The fan doors seen in Figure 5.7, open only during VTOL operation (i.e. hover). During forward flight the doors are closed maintaining the aircraft's aerodynamic shape and preventing cavity drag.

With the basic layout of the fans, gears and shafts determined as seen in Figures 5.2, 5.3 & 5.4, the rest of the aircraft could be packaged. Consequently the exact distances and component position boundaries could be established.

The foundation of the aircraft's packaging was lift fan and the propulsion fans at rear of the aircraft. Having established a basic layout of the fans, gearboxes and shafts; more detailed

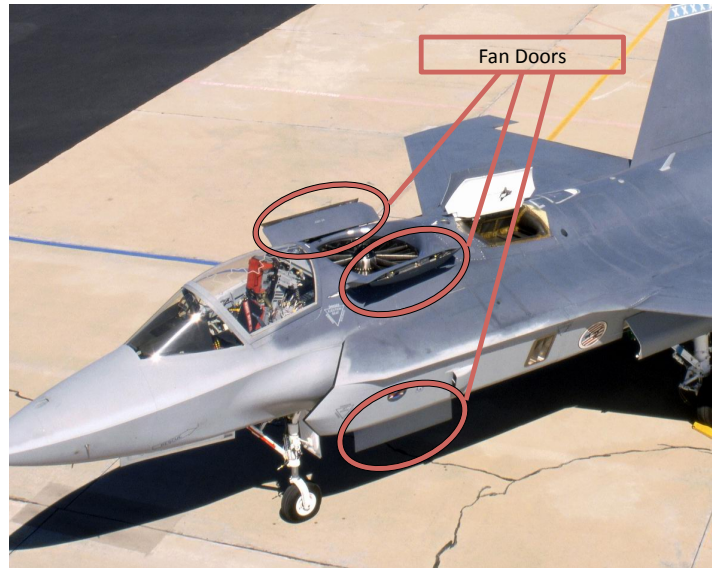


Figure 5.7: F-35 Lift fan doors [19]

positioning of all the components could begin. Parametric equation for the positions of all the components were developed, allowing for variation in size and translation.

Since the lift fan was the initial packaging point, the aircraft was assembled from the rear first Figure 5.8, with the lift fan serving as the reference point. All the fans were positioned spanwise (y -axis) on the $y = 0$ line except for the side propulsion fans. The side fans were parametrically positioned as a function of the lift fan, side fan and gearbox gear (R_{sg}) radii. Thus preventing components from overlapping and providing space for main structural spars/beams, gearboxes and shafts. The lateral crank position y_{crank} is the point where the wing begins, and was positioned as a function of the side fan radius.

The centre of the rear section was expected to be deep due to the lift fan and so rear section would have to be tubular to accommodate all the components. To maximise the lifting capability of the aircraft, the section housing the side propulsion fan would be blended from the wing into an aerofoil shape (inboard wing-fuselage section). The boundaries were established by the structural beam as seen in Figure 5.9.

The initial chordwise (x -axis) positioning of the propulsion fans, sizing rear fuselage width and inboard wing-fuselage section were referenced to the lift fan. The shape of the rear of

the aircraft was determined by parametric equations as seen in Figure 5.8. The sweep angles ($\Lambda_{in\ LE}$, $\Lambda_{in\ TE}$), defining the inboard section of the wing/fuselage taken from the centre of the aircraft ($y = 0$) to the crank ($y = y_{crank}$), would be used to define and alter the wing's chordwise position to balance the aircraft in Chapter 6. These sweep angles also determine the chordwise position of the side propulsion fan, with the variable (Δx_Λ) also seen in Figure 5.8.

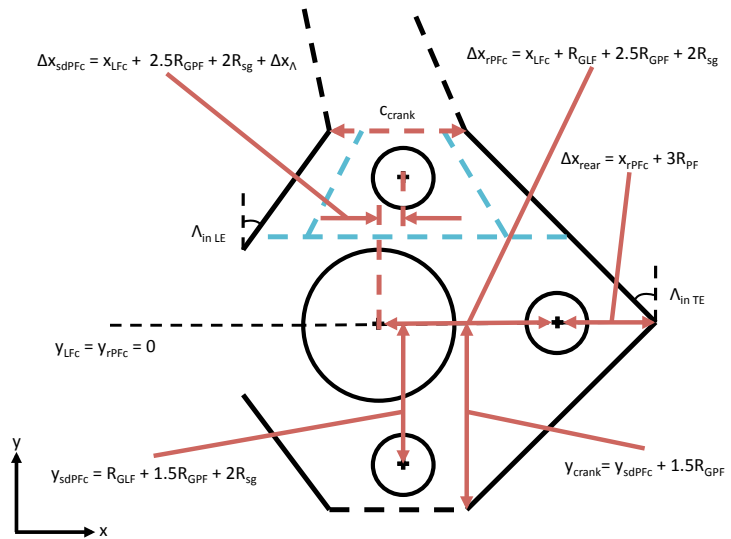


Figure 5.8: Fan positioning x - y plane

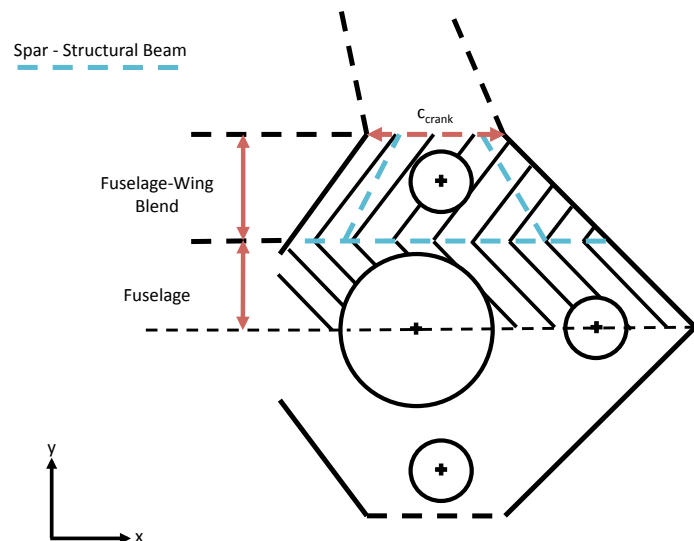


Figure 5.9: Rear section portioning x - y plane

5.3 Cabin

The goal of packaging the cabin was to develop a methodology that incorporates the various seating positions for a 1-7 passenger (PAX) configuration. The aim was to keep the CG of the cabin either in the middle or as rearward as possible and thus aid in balancing the aircraft. This implied that a shorter wider cabin would be a more optimal solution. However, a wider cabin would incur weight and drag penalties. The optimum cabin would therefore be decided later during aircraft optimisation. An example of the possible seating configurations for a 6-passenger aircraft can be seen in Figure 5.10.

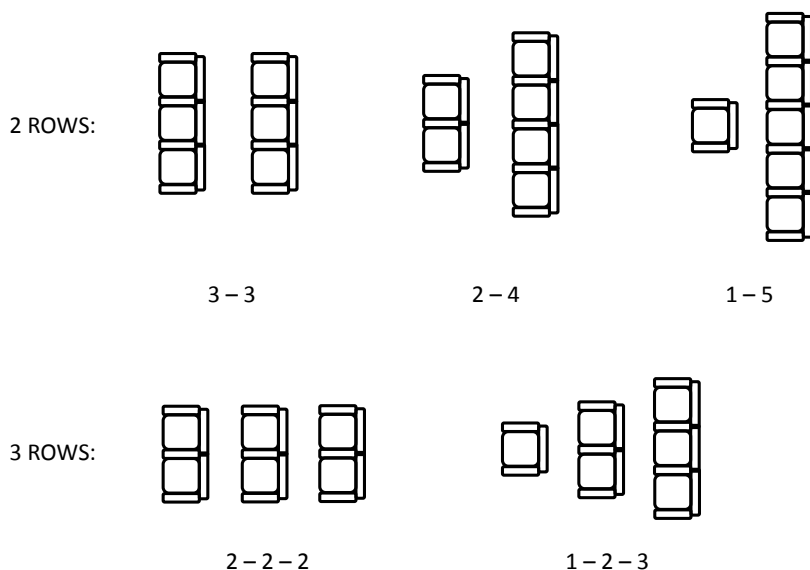


Figure 5.10: Cabin seating configurations for a 6-PAX aircraft

The size of the seats was determined by standard seat regulations. The seat pitch was chosen to be 0.86 m , the total seat height 1.08 m , seat width 0.50 m and the arm rest width 0.063 m [12]. The cabin height was chosen to be 1.25 m to give enough headroom for passengers. The cabin width is dependent on the seating configuration.

A conceptual design of the canopy, flight deck and cabin can be seen in Figures 5.11 & 5.12. FAR23 requirements state that pilot requires a clear view 20° below the horizontal which was incorporated into the canopy design. The canopy was designed using acrylic glass material to allow for maximum visibility and minimum weight.

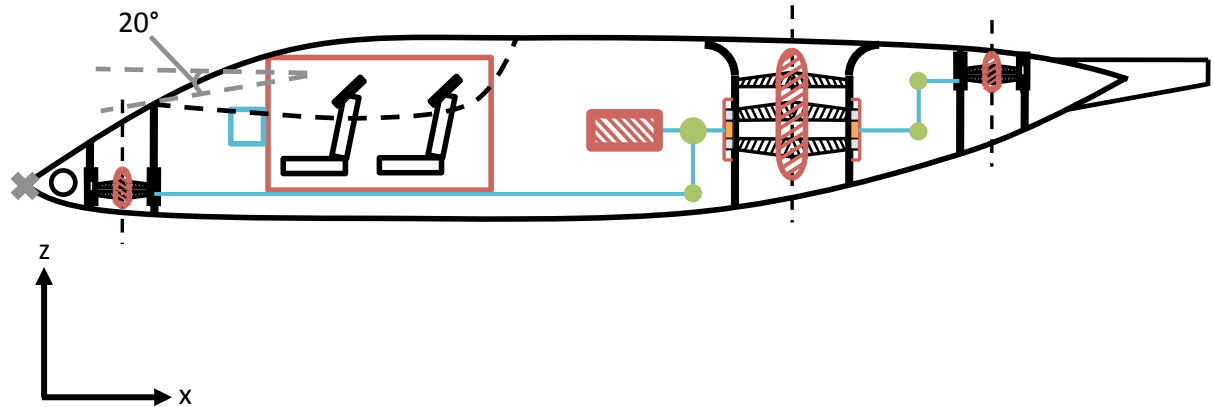


Figure 5.11: Cabin conceptual design for a 4-PAX aircraft

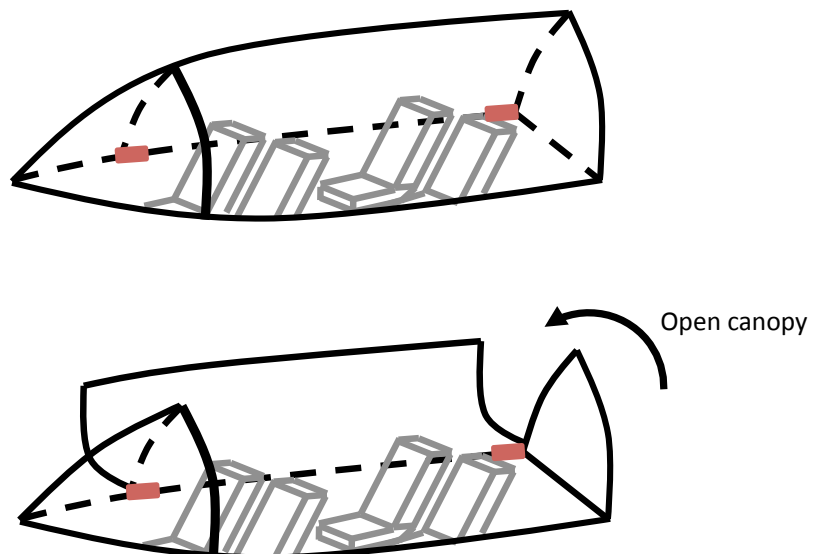


Figure 5.12: Canopy conceptual design for a 4-PAX aircraft

5.4 Undercarriage

It was decided the PAV would incorporate a tricycle undercarriage configuration with single tires on each strut. An undercarriage sizing and placement methodology was put together using the Figure 5.13 and Eqns 5.2 - 5.5 [12].

The nose undercarriage attachment position was set a constant distance of 0.2 m forward of the cabin, due to the spacial constraints of the pitch, Figure 5.15. Consequently the rear undercarriage was placed ($x_{U/C_{main}}$) where the requirements $M_f/B_{U/C} < 0.20$ and $M_a/B_{U/C} > 0.05$ were fulfilled.

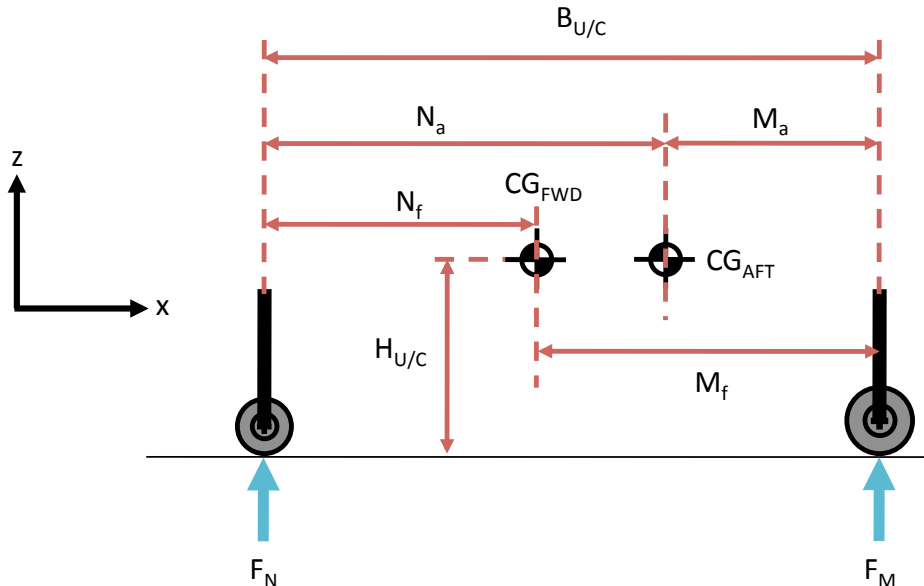


Figure 5.13: Undercarriage placement

$$F_{M_{max}} = \frac{W_0 \cdot N_a}{2B_{U/C}} \quad (5.2)$$

$$F_{N_{max}} = \frac{W_0 \cdot M_f}{B_{U/C}} \quad (5.3)$$

$$F_{N_{min}} = \frac{W_0 \cdot M_a}{B_{U/C}} \quad (5.4)$$

$$F_{N_{dyn}} = F_{N_{max}} + \frac{3.048 \cdot W_0 \cdot H_{U/C}}{g \cdot B_{U/C}} \quad (5.5)$$

A method for determining tire diameter sizing was developed using data of various tire sizes Eqn 5.6. The tire widths for the weight range expected for a PAV were shown to be constant around $w_{tire} = 0.1067 \text{ m}$.

$$d_{tire} = 1.164 \times 10^{-4} \cdot F_{U/C} + 0.2123 \quad (5.6)$$

The lateral rear tire contact points with the ground were governed by the overturn angle (ψ) as illustrated in Figure 5.14. The track of the rear undercarriage was then calculated using requirement $\psi < 63^\circ$ and Eqns 5.7 & 5.8 [12].

$$\xi = \arctan \left(\frac{Tr_{U/C}}{N_{CG}} \right) \quad (5.7)$$

$$\psi = \arctan \left(\frac{H_{U/C}}{N_{CG} \cdot \sin(\xi)} \right) \quad (5.8)$$

The struts diameters were sized using Eqn 5.9 and the maximum strut forces obtained from Eqns 5.3 & 5.5. The rear undercarriage are assumed to absorb all the kinetic energy of landing. The stroke of shock absorbers was sized using Eqn 5.10. The values in Table 5.1 represent FAR23 requirements and the maximum efficiencies for tires and shock absorbers. The maximum vertical touch down velocity (V_{vTD}) was chosen to a higher velocity than for a normal aircraft due to its VTOL capability. The length of the strut the was then decided to be 15% larger than the shock absorber stroke.

$$d_{strut} = 0.0125 + 0.00527 \cdot (F_{max})^{\frac{1}{2}} \quad (5.9)$$

$$s_{strut} = \left[\left\{ 0.5 \left(\frac{F_{M_{max}}}{g} \right) \cdot V_{vTD}^2 \middle/ (N_{strut} \cdot F_{M_{max}} \cdot N_g) \right\} - \eta_{tire} s_{tire} \right] \middle/ \eta_{strut} \quad (5.10)$$

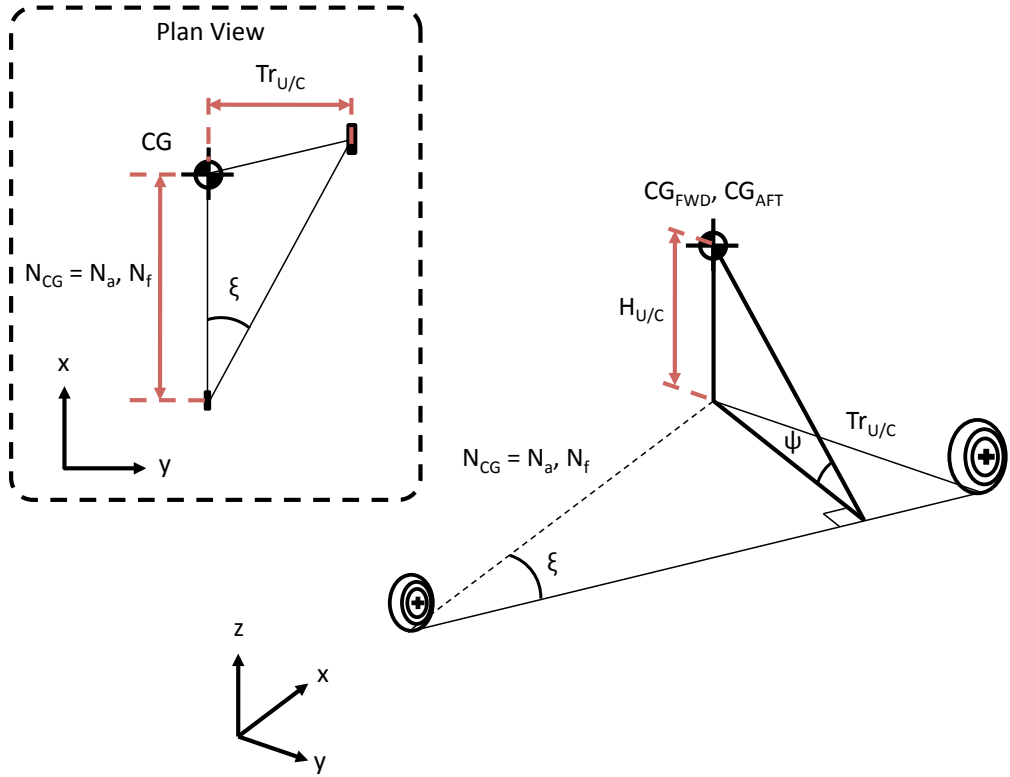


Figure 5.14: Undercarriage overturn angle

Shock absorber sizing variables and values		
Variable	Symbol	Value
Tire energy absorption efficiency	η_{tire}	0.47
Shock absorber energy absorption efficiency	η_{strut}	0.8
Gear load factor	N_g	3
Number of struts	N_{strut}	2
Tire deflection	s_{tire}	$d_{tire}/2$
Shock absorber deflection	s_{strut}	-
Maximum touch down velocity	V_{vTD}	$3.3 - 4.9 \text{ ms}^{-1}$

Table 5.1: Strut sizing variables

5.5 2D Packaging

The task of packaging the aircraft was initially conducted in 2D. This was done by positioning all the components of the aircraft in two different planes $x-y$ and $x-z$. This provided the exact co-ordinates (x, y, z) and the boundaries of each component. The fully 2D packaging of the PAV in the $x-y$ and $x-z$ planes can be seen in Figures D.1 & D.2 respectively. To determine the length and width of the aircraft and link it to the rear section developed in Figure 5.8, the chordwise and spanwise positions of the rest of the components were determined.

The first component to be positioned forward of the lift fan, was the engine. The engine was sized following the method stated in Chapter 4 (Propulsion). With the gears, shafts and gearboxes sized from the engine power requirements, the engine was positioned a parametric distance forward of the lift fan as a function of those components as illustrated in Figure 5.15. The next component positioned forward of the engine was the cabin. The cabin was sized according to a give seating configuration, as seen for a 6 passenger aircraft Figure 5.10. The rear of the cabin was located half a fan radius from the front of the engine. The avionics are then extended 0.5 m forward of the cabin. The nose undercarriage was sized using the methodology above and the attachment point was placed $x = 0.2$ m forward of the the cabin and $y = 1.5w_{n_{tire}}$ from the centreline. The nose undercarriage was laterally shifted (y -axis) 1.5 tire widths to accommodate the shaft going to the pitch fan shown in Figure 5.22. The pitch fan was positioned a sufficient chordwise distance from the nose undercarriage so as not to overlap. The nose of the aircraft was then located 3 pitch fan radii from the centre of the fan. The rear undercarriage like the nose undercarriage was sized and placed using the undercarriage methodology seen in the previous section. The attachment point was initially positioned (x -axis) half way between the engine and lift fan, and the moved forward if required. The attachment point could not be moved further rearward due to the lift fan. However the strut was set at a reward rake angle if required.

To have effective control over the position of the CG (centre of gravity) to balance the aircraft if necessary, two sets of fuel tanks were integrated into the aircraft. Fuel tanks in the wing Figure 5.15 and feeder tanks in the rear section of the fuselage Figure 5.19. The fuel tanks

in the wings lay between the front spar ($0.13 x/c$) and the rear spar ($0.75 x/c$), as well as in between y_{crank} and 85% semi span ($0.85 \cdot b_w/2$). The feeder tanks were positioned to fit in the gap between the main structural beams and the rear propulsion fan.

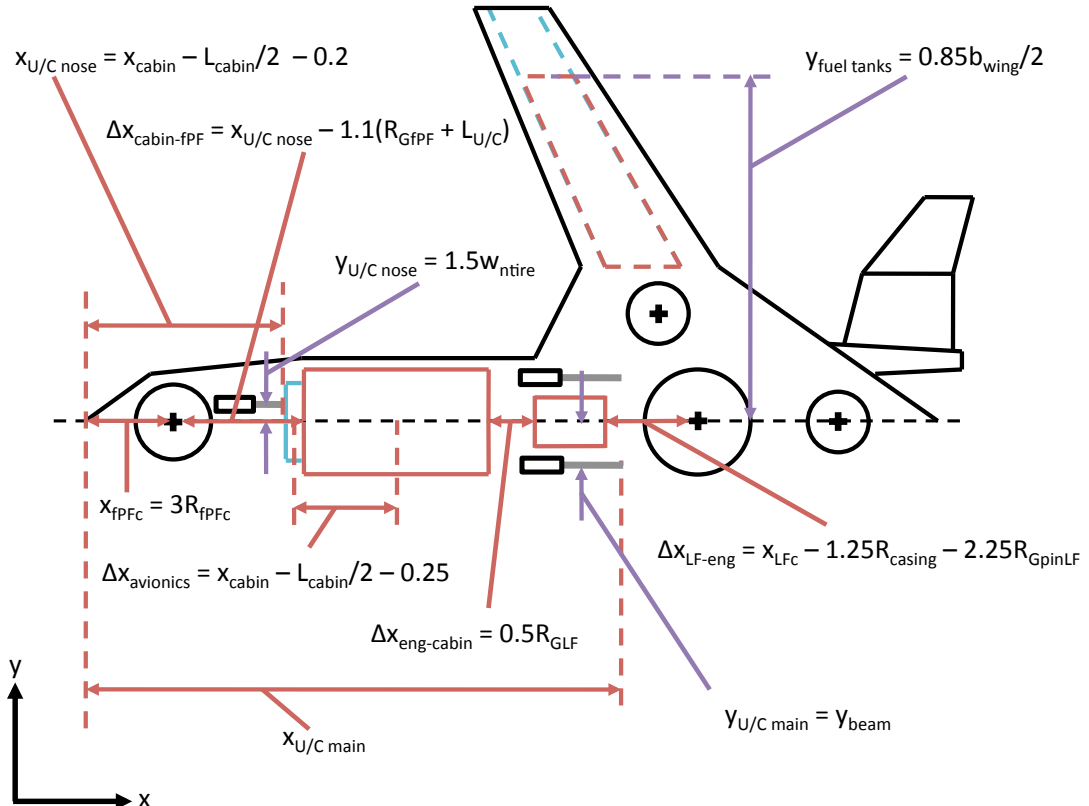


Figure 5.15: Internal component positioning x - y plane

The aerodynamic surfaces were positioned as illustrated in Figure 5.16. As stated previously, the wing chordwise position was dictated by the sweep angles ($\Lambda_{in\ LE}$, $\Lambda_{in\ TE}$) of the inboard wing/fuselage section. The geometry of the wing itself was governed by aerodynamic values and the aerodynamic methodology in Chapter 7, including the sweep of the wing itself ($\Lambda_{out\ LE}$, $\Lambda_{out\ TE}$). The canard was positioned as far forward as possible to increase its moment arm and thus decrease its size and weight. Both the canard's spanwise and chordwise position were made dependent on the position of the fuselage skin control points (x_{2-skin} , y_{2-skin}) seen in Figure 5.20. The root chord of the horizontal tail was located at the boom ($y = y_{boom}$) and spanned to the edge of the side propulsion fans in order to move the vertical tail out of the wake of the fans. The size of the vertical tail size and shape was dependent on the aerodynamic

requirements for lateral stability in Chapter 8. A strake was incorporated in the design to improve the aerodynamic characteristics of the aircraft. Its dimensions were chosen to maximise its size and functionality.

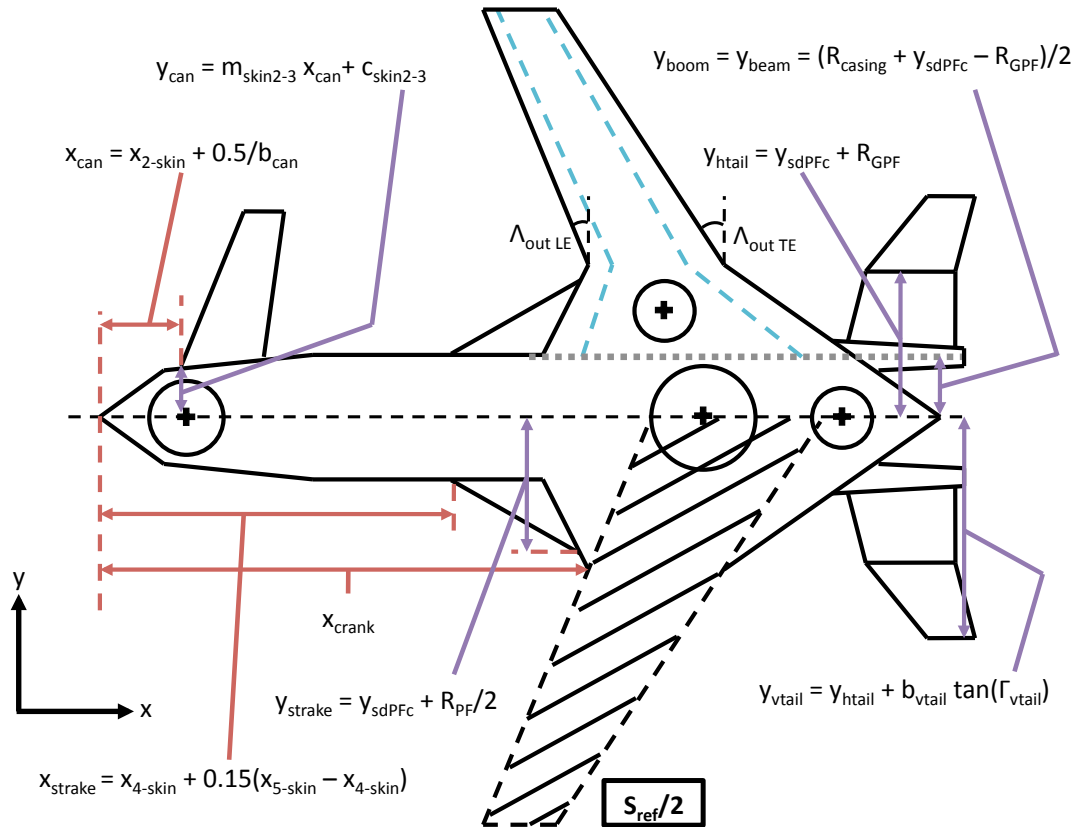


Figure 5.16: Lifting surface positioning x - y plane

The engine intakes and exhausts were positioned as in Figures 5.17 & 5.18. The aircraft was designed with side-pods intakes on either side of the aircraft. Their position was optimum as to avoid ingestion of debris or cause aerodynamic interference with the wing or fans. The exhaust was designed to exit the bottom of the aircraft in between the side and lift-fan.

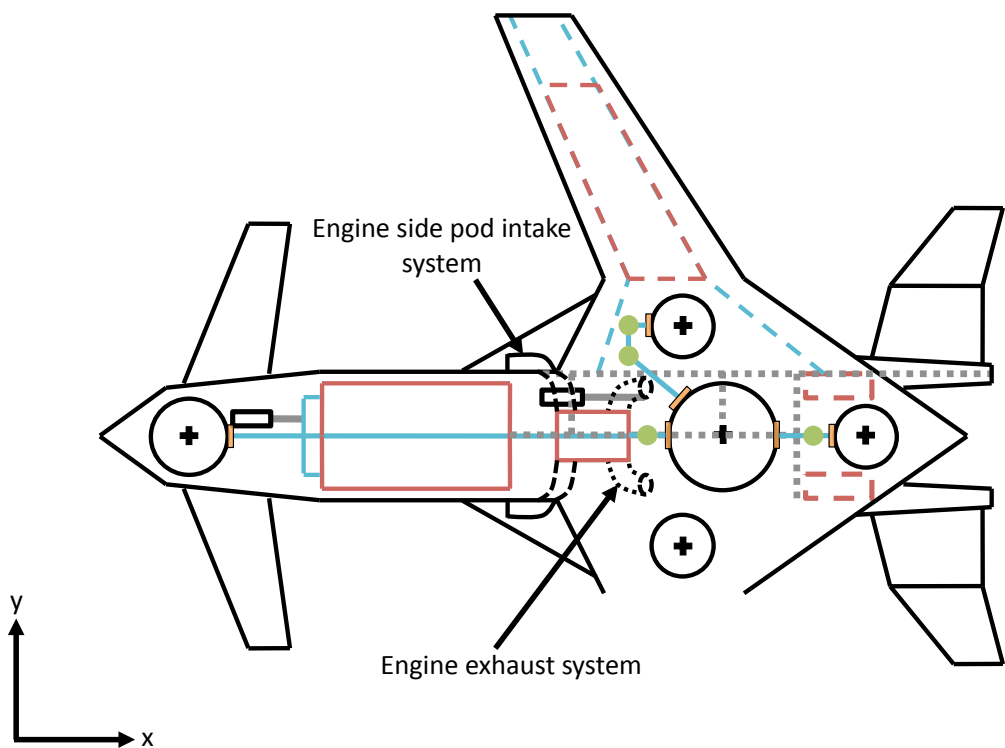


Figure 5.17: Engine intake and exhaust positioning x - y plane

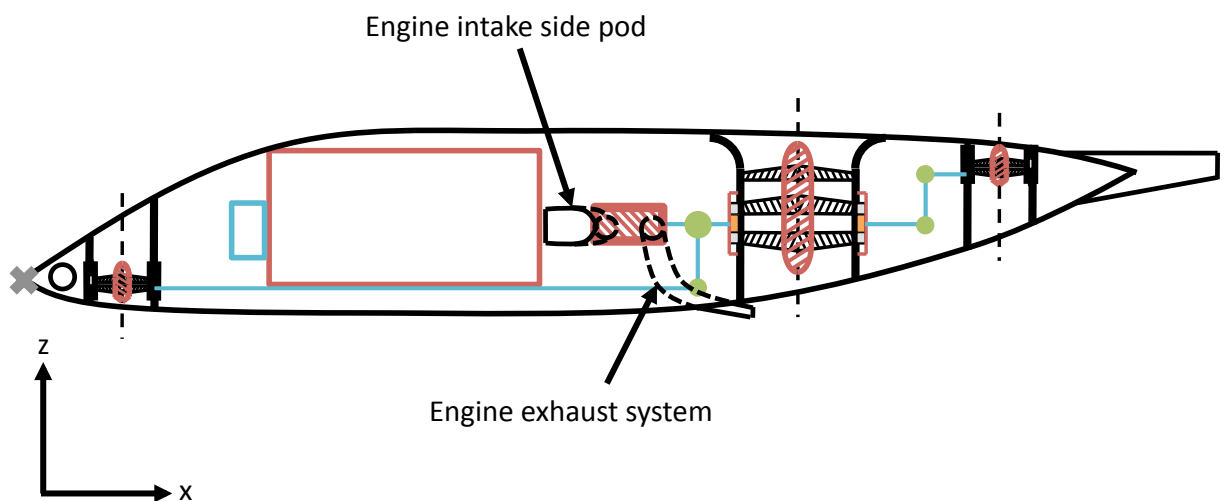


Figure 5.18: Engine intake and exhaust positioning x - z plane

The main structural beams and cross braces were positioned as illustrated in Figures 5.16 & 5.19. The beams and cross braces serve as: structural strengthening to withstand the large fuselage bending moments from VTOL, mounting points for the lift fan and wing, and reinforcement of the tail booms. The beams were placed directly inbetween the lift fan gear casing and the side propulsion fan gear casing, which resulted in the tail booms being positioned in the same spanwise location. The middle cross brace and the keel were positioned to go through the lift fan guide vanes and thus provide mounting points for the hub and rotors. The rear cross brace was positioned behind the gear casing of the lift fan and behind the tilt gearbox of the rear propulsion fan. The front cross brace was place directly over the engine.

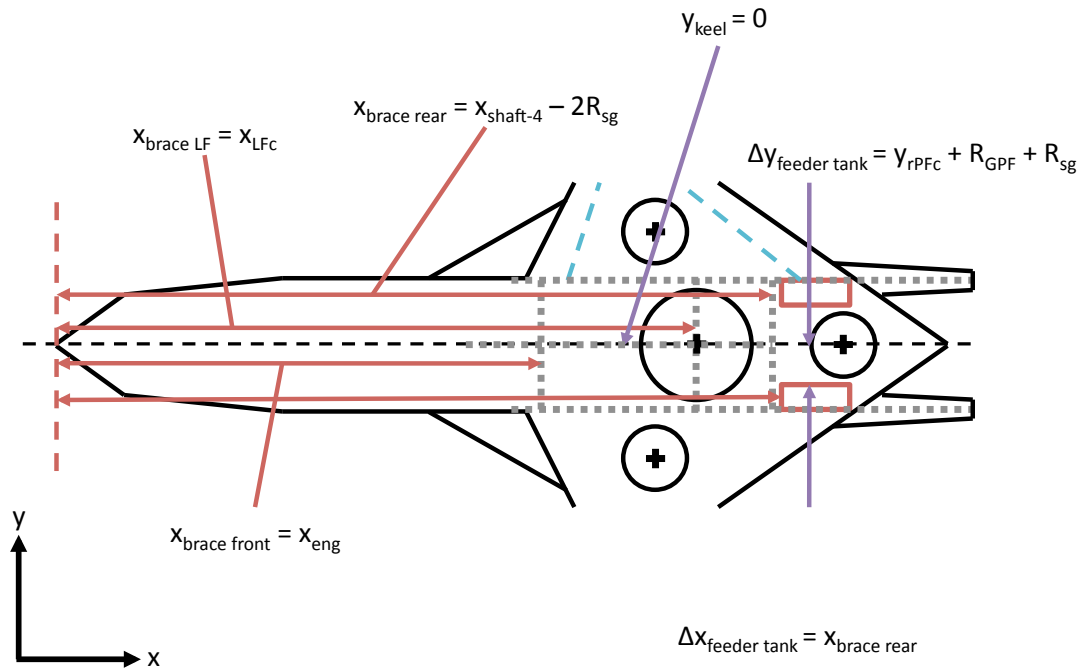


Figure 5.19: Structural beam positioning x - y plane

Figure 5.20 shows the fuselage skin (x, y) control points. The values for these positions can be seen in Table 5.2. The control points were used to control the shape of the fuselage to ensure that all the internal components were packaged neatly within the aircraft. These points were then later used as guide in the 3D packaging section.

Packaging the aircraft in the x - y plane provided the x and y position of all the individual component. The next step was to determine the z positions by packaging the aircraft in the

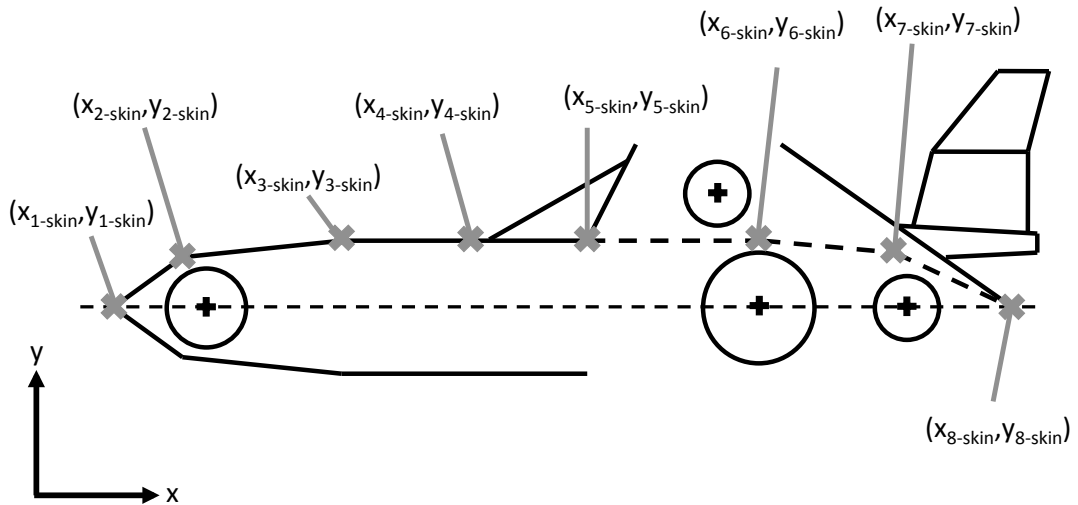


Figure 5.20: Fuselage control point locations x - y plane

Fuselage skin (x, y) control points		
i	x_{i-skin}	y_{i-skin}
1	0	0
2	$x_{fPFc} - 0.5R_{fPF}$	$1.3R_{fPF}$
3	$x_{cabin} - L_{cabin}/2$	$1.3R_{fPF}$
4	$x_{cabin} + L_{cabin}/2$	$1.1 \cdot w_{cabin}/2$
5	$x_{4-skin} + (x_{6-skin} - x_{4-skin})/2$	$1.1 \cdot w_{cabin}/2$
6	x_{LFC}	$x_{sdPFc} - R_{PF}$
7	$x_{7-skin} + (x_{9-skin} - x_{7-skin})/2$	$0.65(y_{7-skin} - y_{9-skin})$
8	L_{fus}	0

Table 5.2: Fuselage skin (x, y) control points

x - z plane as illustrated in Figure 5.21. Many of the positions of the rear components were dependent on the positioning of the structural beams. Components such as the lift fan and wing were to be mounted on these structural beams. Furthermore the beams defined the position of the booms as they formed the main part of the boom structure. A high wing and low canard configuration was chosen to eliminate the wake interaction of the canard with the wing and propulsion fans. Hence the wing was to dictate the position of the beams and other components dependent on the beams. The wing was positioned at a point where all the components could be easily packaged.

As a consequence of positioning the wing, the beam and boom height were also defined, which in turn moved the lift fan mounting point (through the guide vane) to a lower position, also moving the rotors and gears lower. The lift fan duct length was increased accordingly to accommodate the change. The engine was then aligned with the lift fan pinion gear as show in Figure 5.21.

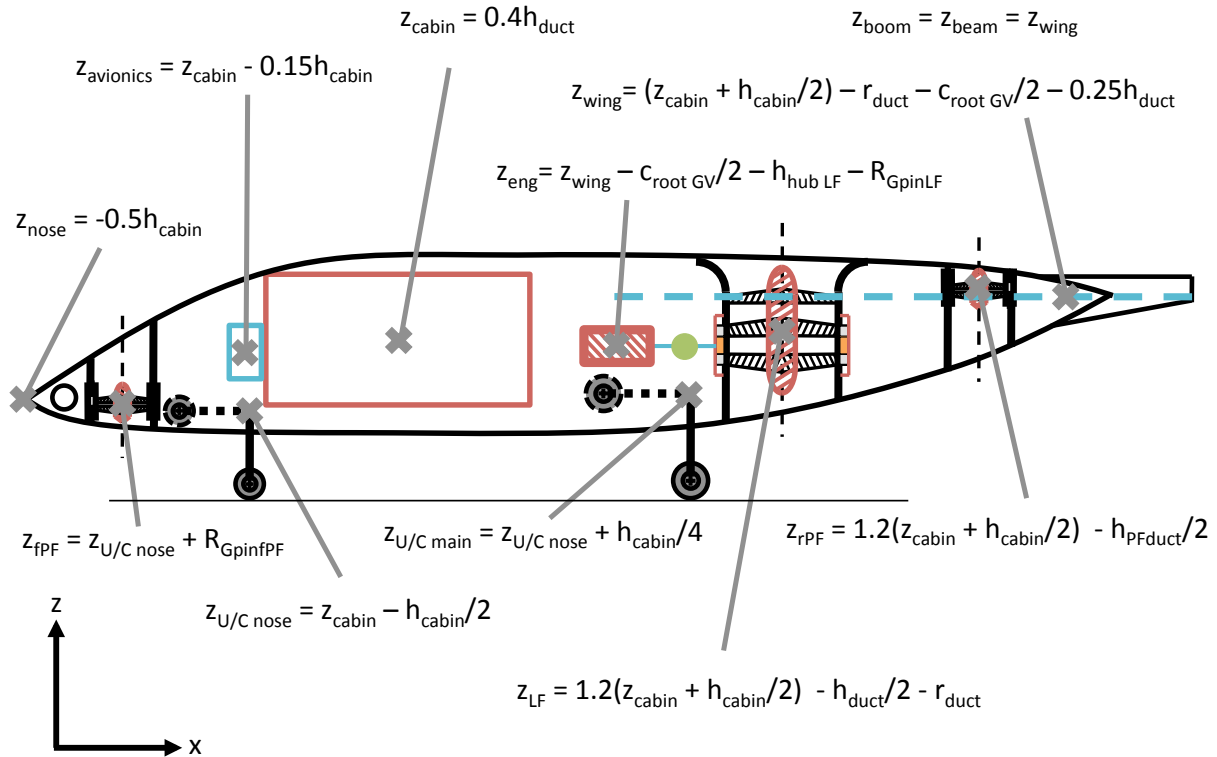


Figure 5.21: Internal component positioning x - z plane

The position of the rear propulsion fan was adjusted so that it was as close to the skin surface as possible. The cabin was vertically positioned (z -axis) to improve the streamline shape of the fuselage as much as possible, by aligning it with the top of the lift fan.

The gearboxes were positioned to avoid the beams and provide sufficient distance for the fan to tilt. The attachment point of the nose undercarriage was located at the same height as the cabin floor. Due to the varying shape of the fuselage skin towards the rear of the aircraft, the rear undercarriage attachment was positioned slightly higher than the nose undercarriage. To minimise the number of gearboxes required to drive the pitch fan as well as minimise the

fuselage height, the pitch fan was placed at a point where a long shaft from the engine could be threaded under the cabin and linked to the pitch fan.

The canard was placed at the height $z = 0$, ensuring that the canardvator actuator avoided the pitch fan shaft and nose undercarriage. The horizontal tails were mounted on the booms and thus shared the same height ($z_{htail} = z_{boom}$). The vertical tails were mounted on the end of the horizontal tail and were therefore subject to the dihedral of the horizontal tails ($z_{vtail} = z_{htail} + (b_{htail}/2) \cdot \sin(\Gamma_{htail})$).

A yaw fan was incorporated into the design, to allow for yaw control during hover. The yaw fan was sized to fit in the remaining space in the nose section forward of the pitch fan as can be seen in Figure 5.21. The fan would be driven by a small electric motor.

The wing fuel tanks were positioned according to the wing height and the feeder tanks were placed in the middle of the fuselage at their corresponding x and y -coordinates. Finally the avionics were positioned according to their dimensions allowing for a clear view for the pilots.

Figure 5.22 shows the fuselage skin (x, z) control points. The values for these positions can be seen in Table 5.3. The points were used to control the shape of the fuselage to make sure that all the internal components were vertically packaged within the aircraft and improve the aerodynamic profile of the fuselage. These points were then later used as guide in the 3D packaging section.

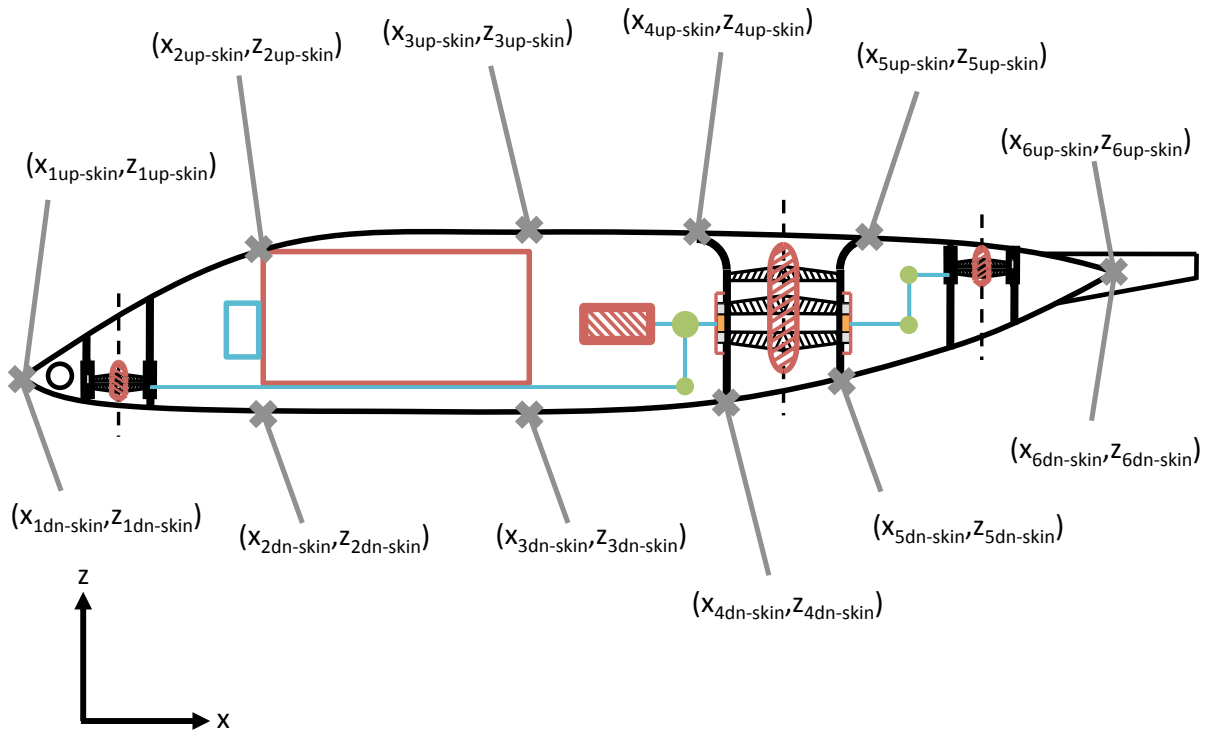


Figure 5.22: Fan, Gear and Shaft positioning x-z plane

Fuselage skin (x, z) control points		
i	$x_{upi-skin}$	$z_{upi-skin}$
1	0	z_{nose}
2	$x_{cabin} - L_{cabin}/2$	$z_{cabin} + h_{cabin}/2$
3	$x_{cabin} + L_{cabin}/2$	$1.2(z_{cabin} + h_{cabin}/2)$
4	$x_{LFC} - R_{LF} - r_{duct}$	$1.2(z_{cabin} + h_{cabin}/2)$
5	$x_{LFC} + R_{LF} + r_{duct}$	$1.2(z_{cabin} + h_{cabin}/2)$
6	L_{fus}	z_{wing}

i	$x_{dni-skin}$	$z_{dni-skin}$
1	0	z_{nose}
2	$x_{cabin} - L_{cabin}/2$	$1.55(z_{cabin} - h_{cabin}/2)$
3	$x_{cabin} + L_{cabin}/2$	$1.60(z_{cabin} - h_{cabin}/2)$
4	$x_{LFC} - R_{LF}$	$1.05(z_{cabin} - h_{cabin}/2)$
5	$x_{LFC} + R_{LF}$	$(z_{LF} - h_{duct}/2)$
6	L_{fus}	z_{wing}

Table 5.3: Fuselage skin (x, z) control points

5.6 3D Packaging

Lofting is the process of shaping the external geometry of an aircraft through mathematical defined shapes. One such mathematical model used is conic lofting (conic sections). A conic curve is defined by the general equation Eqn 5.11. A conic curve can also be defined graphically as can be seen in Figure 5.23. The conic curve is defined using a shoulder (points *ADB*) and shape parameter Eqn 5.12 [11].

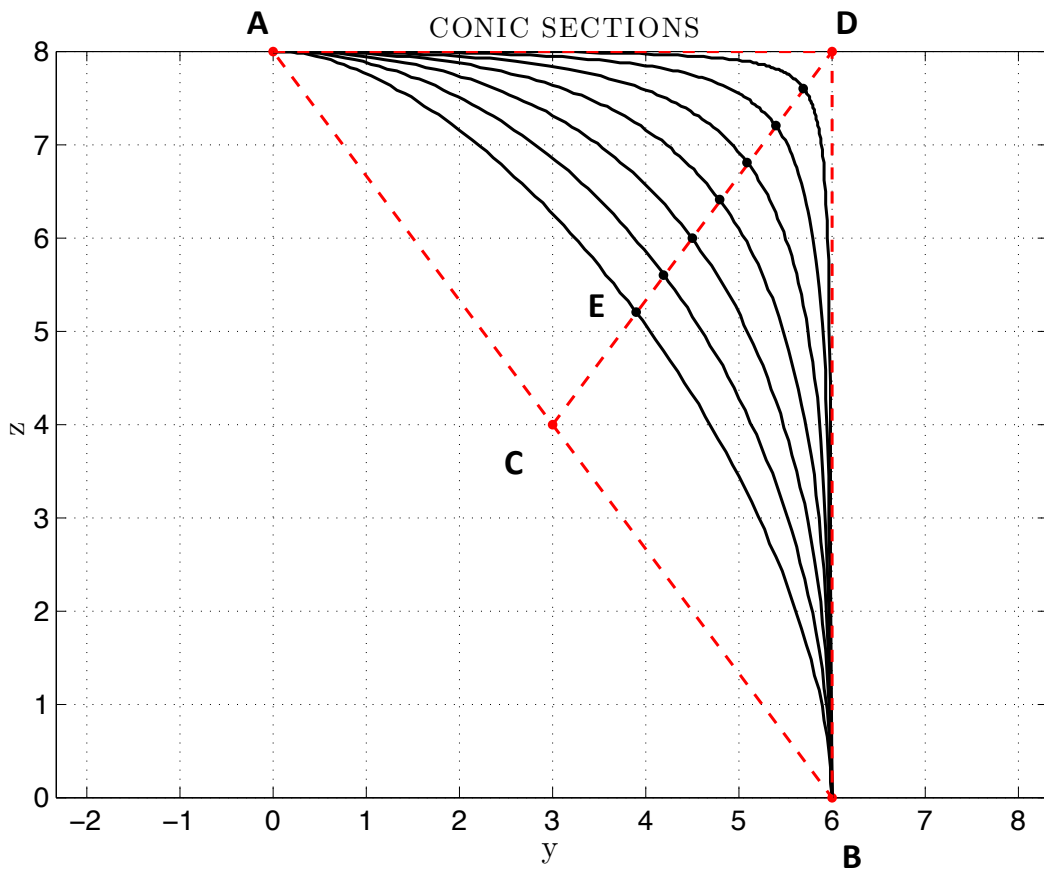


Figure 5.23: Conic sections

$$C_1X^2 + C_2XY + C_3Y^2 + C_4X + C_5Y + C_6 = 0 \quad (5.11)$$

By moving the point *E* along the line *DC* (where point *C* is the midpoint of line *AB*), the conic shape parameter varies and thus the conic curve changes shape. Examples of various

curves can be seen in Figure 5.23. For shape parameters $\zeta > 0.5$ the curve that can be created is hyperbolic. A shape parameter $\zeta = 0.5$ creates a parabolic curve and shape parameter $\zeta < 0.5$ creates an elliptical curve. When the shoulder lines $AD = BD$, a shape parameter of $\zeta = 0.4142$ gives a circular curve [11].

$$\zeta = \frac{|DE|}{|DC|} \quad (5.12)$$

Using linear interpolation and the 2D fuselage skin points Tables 5.2 & 5.3 the fuselage was divided up into multiple stations along the x -axis. These curves outlined the maximum height and width of the fuselage along its length as can be seen in Figures 5.24 & 5.25. Using the technique of conic lofting and the outline of the fuselage, cross sections with a shape parameter of 0.6 were constructed at each station as in Figure 5.26. These techniques were also used to produce 3D components such as the cabin and booms.

All the major internal components can be seen in Figures 5.24, 5.25, & 5.26. The propulsion system (fans, ducts, gears, gearboxes and shafts), engine, cabin, fuel tanks and undercarriage are all packaged according to their positions defined in the 2D packaging method.

Since all the components were packaged correctly in the 2D method, it was assumed that the 3D model would also be correctly packaged. This was true of all of the components except the side propulsion fans and under carriage, because of their off centre lateral positioning. The side propulsion fans were positioned at the height of the wing in order to fit within the wing-fuselage blended aerofoil section. The height of the duct was checked against the maximum thickness of the wing-fuselage blended aerofoil section and adjusted accordingly. Conversely, the undercarriage was designed to be retracted far enough into the fuselage to always be within the limits of the fuselage (i.e. retracted undercarriage angle $\simeq -5^\circ$).

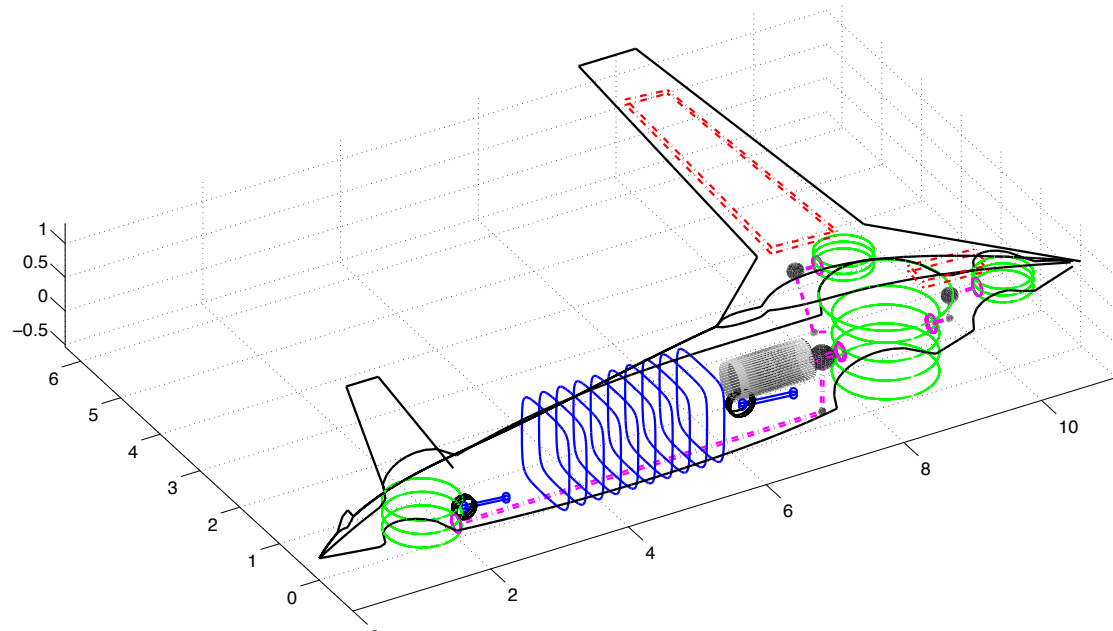


Figure 5.24: 3D packaged PAV - *Front view*

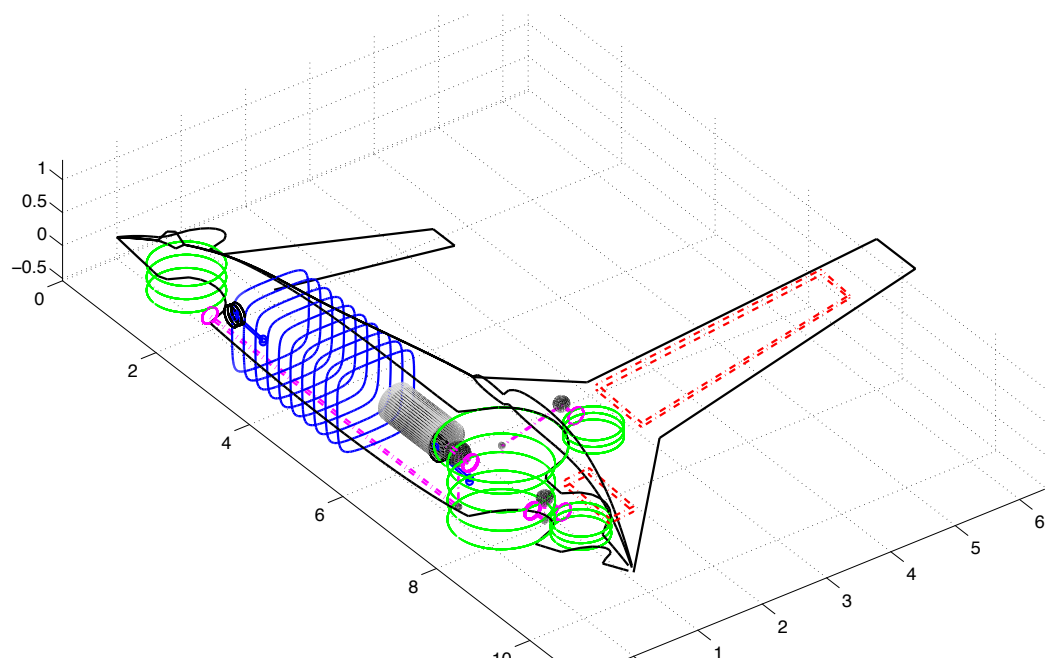


Figure 5.25: 3D packaged PAV - *Rear view*

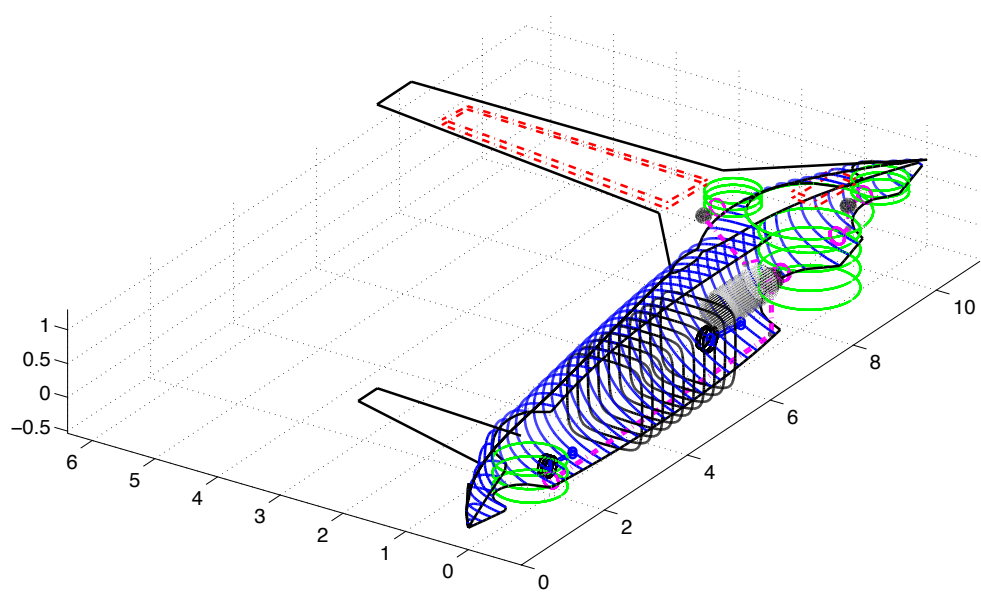


Figure 5.26: 3D packaged PAV - *Lofted fuselage using conic sections*

Chapter 6

Weight & Balance

6.1 Overview

Weight and Balance of the aircraft are key to determining its CG positions and as a consequence allow for the correct placement of the undercarriage and adjustment of the aircraft's stability. Coupling the CG position with the aerodynamic characteristics of the PAV, the static stability can be evaluated, after which the dynamic stability.

The individual component weights were calculated using methodologies developed from empirical data. Methodologies to calculate the weight of components that were unique to this aircraft such as fans, gear, guide vanes and so forth were developed from their sizing methodologies.

Having packaged the aircraft and positioned all the components, the individual CG positions (x_{CG} , y_{CG} , z_{CG}) of each component were then calculated and used to determine the CG position of the aircraft. The aircraft's CG position was adjustable through the movement of individual components (such as the wing) further forward or aft in order to accommodate stability and aerodynamic criteria, as can been seen in Chapter 8.

6.2 Component Weights

Most of the component weights were calculated using the existing methodologies that can be seen in Appendix E.1. These methodologies were gathered from different sources (i.e. references [12, 13, 14]) and then validated against existing aircraft.

The volume data of the fans and guide vanes designed for the CFD simulations were gathered to form parametric models seen in Eqns 6.1 & 6.2. The models were then multiplied by the relevant material density to determine the weight of the components. As the blades were designed to have maximum operational values at transonic tip speeds and small radii, the centrifugal forces were expected to be relatively small. The blades are also supported at the root and tip, ensuring that bending moments are smaller than for free tip blades. These criteria allowed for the chosen blade material to be carbon fibre composite ($\rho_{comp} = 1800 \text{ kg/m}^3$), similar to propeller and helicopter blades. Structural tests using Eqn 4.45 showed that the stresses encountered by the fans were well within the yield stress of the material. This ensures the weight of the fans and guide vanes was minimised and their strength maximised.

$$\text{Vol}_{fan} = 10^{-0.2381} \cdot R_{fan}^{3.1011} \cdot N_{b_{fan}}^{-1.8815} \cdot \sigma_{fan}^{1.8324} \quad (6.1)$$

$$\text{Vol}_{GV} = 10^{-1.4672} \cdot R_{GV}^{2.742} \cdot N_{b_{GV}}^{-0.0032} \cdot c_{r_{GV}}^{1.9563} \quad (6.2)$$

The weights of the hubs carrying the blades were calculated by first determining their height Eqn 5.1. The inner to outer radius ratio of the hubs was determined to be $\frac{r_{hub_i}}{r_{hub_0}} = 0.85$. The volume of the hub could then be calculated using the Eqn 6.3. The hub was designed to be thick enough and strong enough to hold the blades in position, but also to minimise weight. Thus the hub material was chosen to be aluminium ($\rho_{alum} = 2700 \text{ kg/m}^3$).

$$\text{Vol}_{hub} = \pi(r_{hub_0}^2 - r_{hub_i}^2)h_{hub} \quad (6.3)$$

The gears were sized using the methodology in Chapter 4, from which their volume was calculated using Figure 4.21 and the equations in Appendix B.2. The material chosen for its strength and fatigue resistant properties was steel ($\rho_{steel} = 7800 \text{ kg/m}^3$). The shaft volumes were calculated after they were sized using the methodology in Chapter 4, and then multiplied by the density of steel to obtain their weight. A methodology for determining the weight of the engine based on its power was developed from empirical data as can be seen in Eqn 4.52. The weight of the avionics was determined using references [14] and [47]. The weight of conventional avionics components was determined from the methodology in reference [14]. Reference [47] suggests that a glass cockpit saves approximately 45 kg from that of conventional avionics. Consequently 45 kg was subtracted from the conventional avionics weight to represent the avionics weight in a glass cockpit (76 kg). The gear casing of the lift fan gears was assumed to have a 5 mm thick wall formed of carbon fibre composite. The inner radius of the wall was assumed to be 5% larger than that of the lift fan gear. The height of the gear casing was assumed to be 85% of the total duct height. The volume and weight of the gear casing was calculated accordingly. The weight of the gearbox was assumed to be an added 50% of the gear weights. While the weight of the fan doors were assumed to be an added 15% to the structural weight of the ducts.

To minimise weight and thus in turn minimise the power required for take-off, the aircraft would be manufactured from carbon fibre composite where possible. The weight reduction was calculated using the composite weight factors in Table 6.1. However, the fuselage weight was increased by 10% to account for the structural reinforcement required for the increased bending loads experienced as a consequence of VTOL.

Composite weight factors	
Primary structures (wing, canard, tail, fuselage)	0.75
Secondary structures (flaps, slats, access panels)	0.60
Undercarriage	0.88
Air Induction (ducts)	0.70

Table 6.1: Composite weight factors [14]

The component weights of a 4-passenger PAV (including pilot) with a range of 2778 km (1500 nm), cruise altitude of 9450 m (31000 ft) and a cruise speed of 555 km/h (300 kts) were broken down as can be seen in Figures 6.1 & 6.2 and Table 6.2.

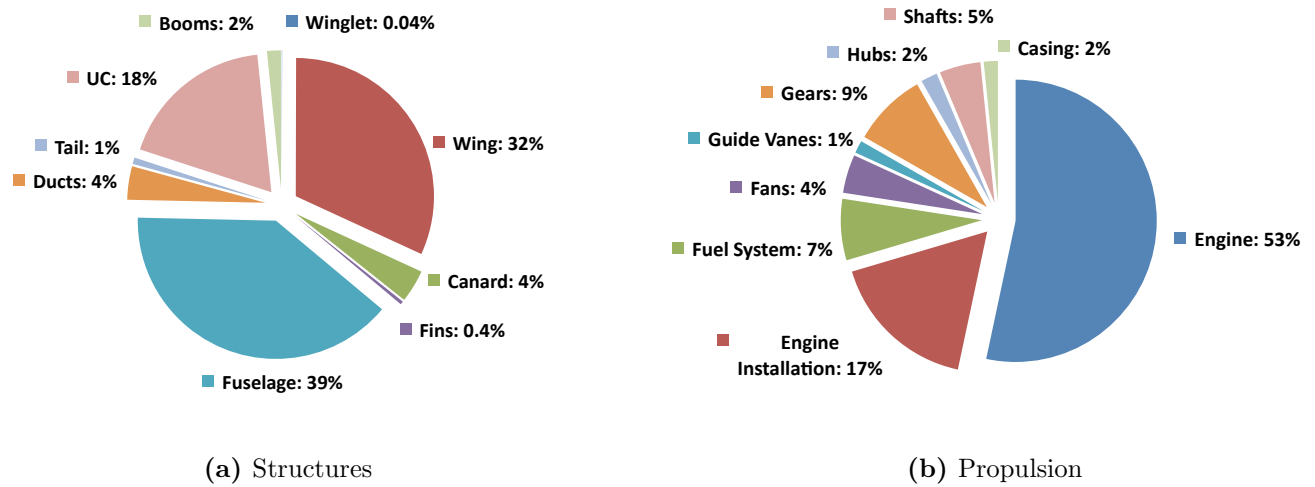


Figure 6.1: Structural and Propulsion weight component proportions

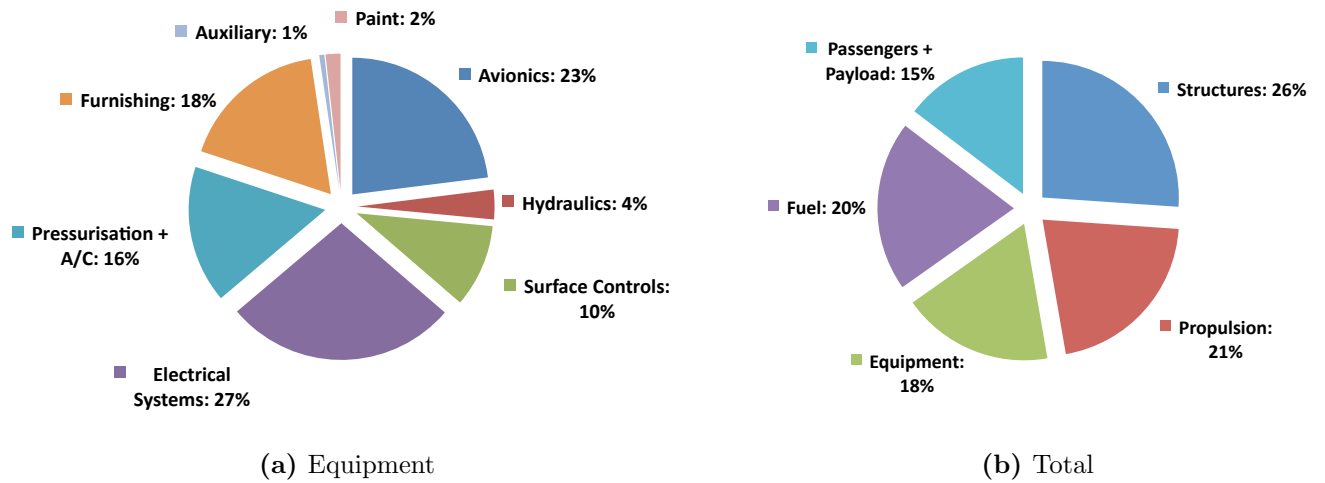


Figure 6.2: Equipment and Total weight component proportions

Component Weights - PAV					
Wing	153.1 <i>kg</i>	Engine	208.1 <i>kg</i>	Avionics	76.1 <i>kg</i>
Canard	18.4 <i>kg</i>	Engine Installation	66.6 <i>kg</i>	Hydraulics	11.6 <i>kg</i>
Horizontal Tail	3.6 <i>kg</i>	Fuel System	27.4 <i>kg</i>	Surface Controls	32.5 <i>kg</i>
Fins	1.8 <i>kg</i>	Fans	17.2 <i>kg</i>	Electrical System	90.9 <i>kg</i>
Fuselage	188.9 <i>kg</i>	Guide Vanes	5.6 <i>kg</i>	Pressurisation + A/C	53.8 <i>kg</i>
Ducts	18.8 <i>kg</i>	Hubs	7.4 <i>kg</i>	Furnishing	58.1 <i>kg</i>
Undercarriage	88.3 <i>kg</i>	Shafts	18.4 <i>kg</i>	Auxiliary	2.0 <i>kg</i>
Booms	7.8 <i>kg</i>	Gears	33.2 <i>kg</i>	Paint	5.8 <i>kg</i>
Winglet	0.2 <i>kg</i>	Gear Casing	6.3 <i>kg</i>		
Structure Total	480.7 <i>kg</i>	Propulsion Total	390.0 <i>kg</i>	Equipment Total	330.8 <i>kg</i>
Fuel		371.0 <i>kg</i>			
Passengers + Payload		360.0 <i>kg</i>			
Empty Weight		1201.5 <i>kg</i>			
MTOW		1932.5 <i>kg</i>			

Table 6.2: Component Weights of a 4 passenger PAV

6.3 Weight Validation

The weight estimation methodology used to calculate the weight of a PAV (e.g. Table 6.2) composed of the equations in Appendix E.1 was validated on four existing aircraft. Two examples can be seen below, and the other two in Appendix E.2. The relevant data was gathered on these aircraft and then the weight estimation methodology was applied. It was applied to a Cessna 400: Table 6.3, Socata TBM 850: Table 6.4, Pilatus PC-12: Table E.2 and Cessna 210: Table E.3. Details of the Cessna 400 and Socata TBM 850 can be seen in Tables 3.1 & 3.2 respectively.

The actual values for empty weight and maximum take-off weight of each aircraft were compared to the weight estimations. For the Cessna 400 it was found that there was an underestimation error of $\varepsilon_{W_e} = 2.0\%$ for empty weight and an overestimation of $\varepsilon_{W_0} = -0.6\%$ for maximum take-off weight. For the Socata TBM 850 the errors were $\varepsilon_{W_e} = 6.0\%$ and $\varepsilon_{W_0} = 0.8\%$. For the Pilatus PC-12 the errors were $\varepsilon_{W_e} = -0.2\%$ and $\varepsilon_{W_0} = -1.6\%$, while for

the Cessna 200 the errors were $\varepsilon_{W_e} = -2.9\%$ and $\varepsilon_{W_0} = -4.6\%$.

These results show that the weight estimation methodology was very accurate, with a root mean squared error of $\bar{\varepsilon}_{W_e} = 2.8\%$ for empty weight and $\bar{\varepsilon}_{W_0} = 1.9\%$.

Component Weights - Cessna 400					
Wing	219.0 <i>kg</i>	Fuel System	29.8 <i>kg</i>	Surface Controls	27.4 <i>kg</i>
Fuselage	162.6 <i>kg</i>	Engine	146.8 <i>kg</i>	Avionics	76.1 <i>kg</i>
Horizontal Tail	21.4 <i>kg</i>	Propeller	29.0 <i>kg</i>	Electrical System	107.7 <i>kg</i>
Fin	7.0 <i>kg</i>	Nacelle	25.3 <i>kg</i>	Furnishing	58.1 <i>kg</i>
Undercarriage	89.3 <i>kg</i>	Propeller Installation	29.6 <i>kg</i>	Pressurisation + A/C	51.5 <i>kg</i>
		Engine Installation	25.3 <i>kg</i>	Paint	4.9 <i>kg</i>
Structure Total	499.4 <i>kg</i>	Propulsion Total	286.0 <i>kg</i>	Equipment Total	325.8 <i>kg</i>
Fuel		176.0 <i>kg</i>			
Passengers + Payload		356.0 <i>kg</i>			
Empty Weight		1111.1 <i>kg</i>			
MTOW		1643.1 <i>kg</i>			

Table 6.3: Component Weights of a Cessna 400

Component Weights - Socata TBM 850					
Wing	413.7 <i>kg</i>	Fuel System	64.0 <i>kg</i>	Surface Controls	56.3 <i>kg</i>
Fuselage	363.5 <i>kg</i>	Engine	173.1 <i>kg</i>	Avionics	76.1 <i>kg</i>
Horizontal Tail	59.4 <i>kg</i>	Propeller	73.0 <i>kg</i>	Electrical System	120.0 <i>kg</i>
Fin	13.1 <i>kg</i>	Nacelle	69.4 <i>kg</i>	Furnishing	87.2 <i>kg</i>
Undercarriage	168.1 <i>kg</i>	Propeller Installation	55.4 <i>kg</i>	Pressurisation + A/C	101.7 <i>kg</i>
		Engine Installation	53.2 <i>kg</i>	Paint	10.1 <i>kg</i>
Structure Total	1018.0 <i>kg</i>	Propulsion Total	488.2 <i>kg</i>	Equipment Total	451.4 <i>kg</i>
Fuel		866.0 <i>kg</i>			
Passengers + Payload		504.0 <i>kg</i>			
Empty Weight		1957.5 <i>kg</i>			
MTOW		3327.5 <i>kg</i>			

Table 6.4: Component Weights of a Socata TBM 850

6.4 Aircraft Balance

The goal of balancing the aircraft is to establish the CG positions of the aircraft for different scenarios, in order to determine the most forward and aft CG positions. The most forward and aft CG positions are then used in Chapter 8 tune the stability of the aircraft.

Most of the individual component CG positions were calculated using methods in reference [12]. The PAV CG positions ($x_{CG_{PAV}}, y_{CG_{PAV}}, z_{CG_{PAV}}$) were calculated using the weight and CG of each individual component and Eqns 6.4, 6.5 & 6.6 [12]. The positions of these individual components can be seen in Figures 6.3, 6.4 & 6.5.

$$x_{CG_{PAV}} = \frac{\sum W_i \cdot x_{CG_i}}{\sum W_i} \quad (6.4)$$

$$y_{CG_{PAV}} = \frac{\sum W_i \cdot y_{CG_i}}{\sum W_i} \quad (6.5)$$

$$z_{CG_{PAV}} = \frac{\sum W_i \cdot z_{CG_i}}{\sum W_i} \quad (6.6)$$

The moments of inertia of the aircraft were approximated using Eqns 6.7, 6.8 & 6.9 [12]. These moments of inertia were used in the development of the dynamic stability methodology in Chapter 8.

$$I_{xx} = \sum W_i [(y_{CG_i} - y_{CG_{PAV}})^2 - (z_{CG_i} - z_{CG_{PAV}})^2] \quad (6.7)$$

$$I_{yy} = \sum W_i [(z_{CG_i} - z_{CG_{PAV}})^2 - (x_{CG_i} - x_{CG_{PAV}})^2] \quad (6.8)$$

$$I_{zz} = \sum W_i [(x_{CG_i} - x_{CG_{PAV}})^2 - (y_{CG_i} - y_{CG_{PAV}})^2] \quad (6.9)$$

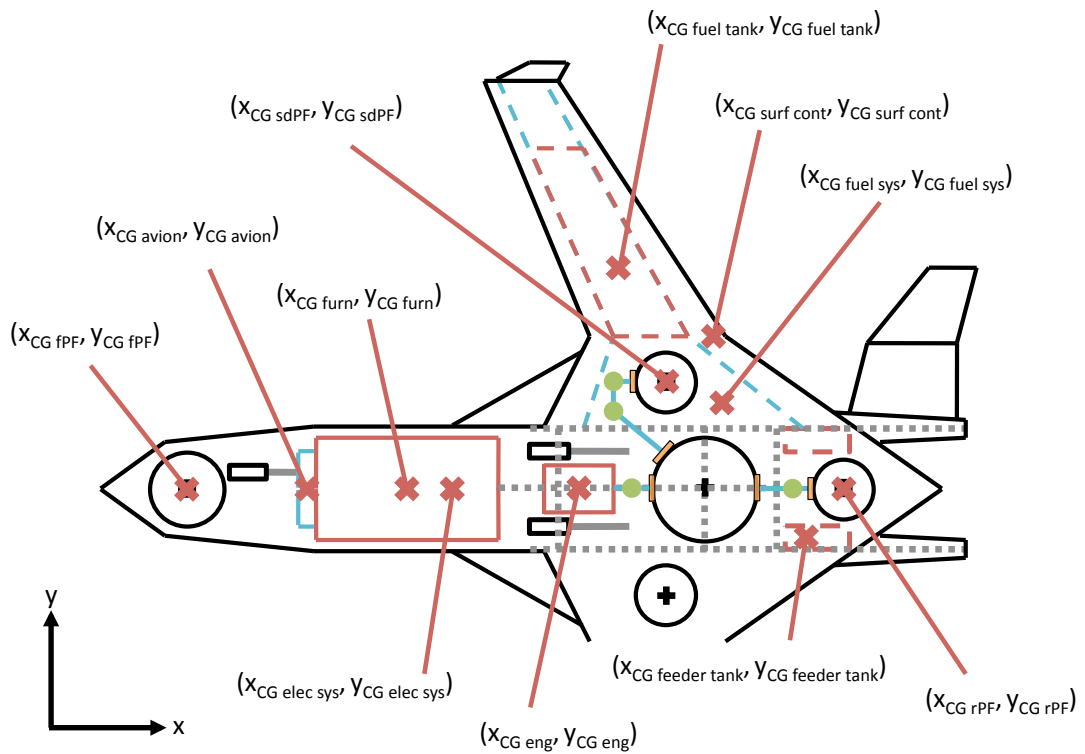


Figure 6.3: Component CG positions the x-y plane

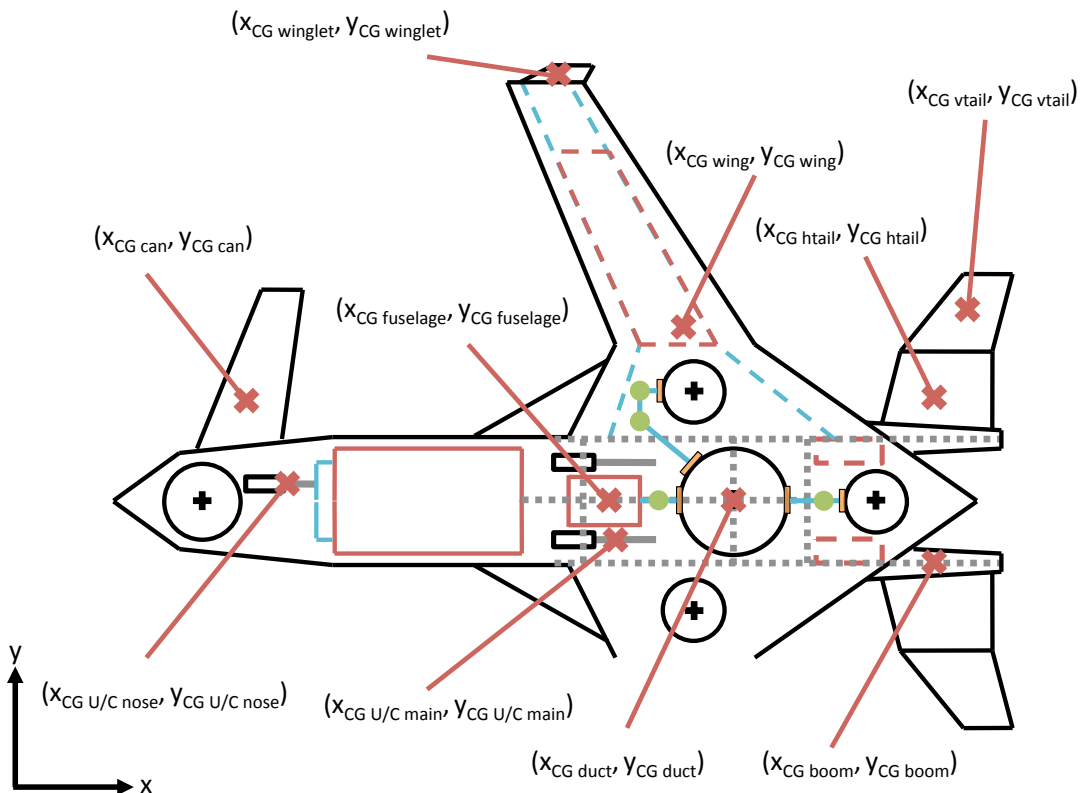


Figure 6.4: Structural component CG positions in the x-y plane

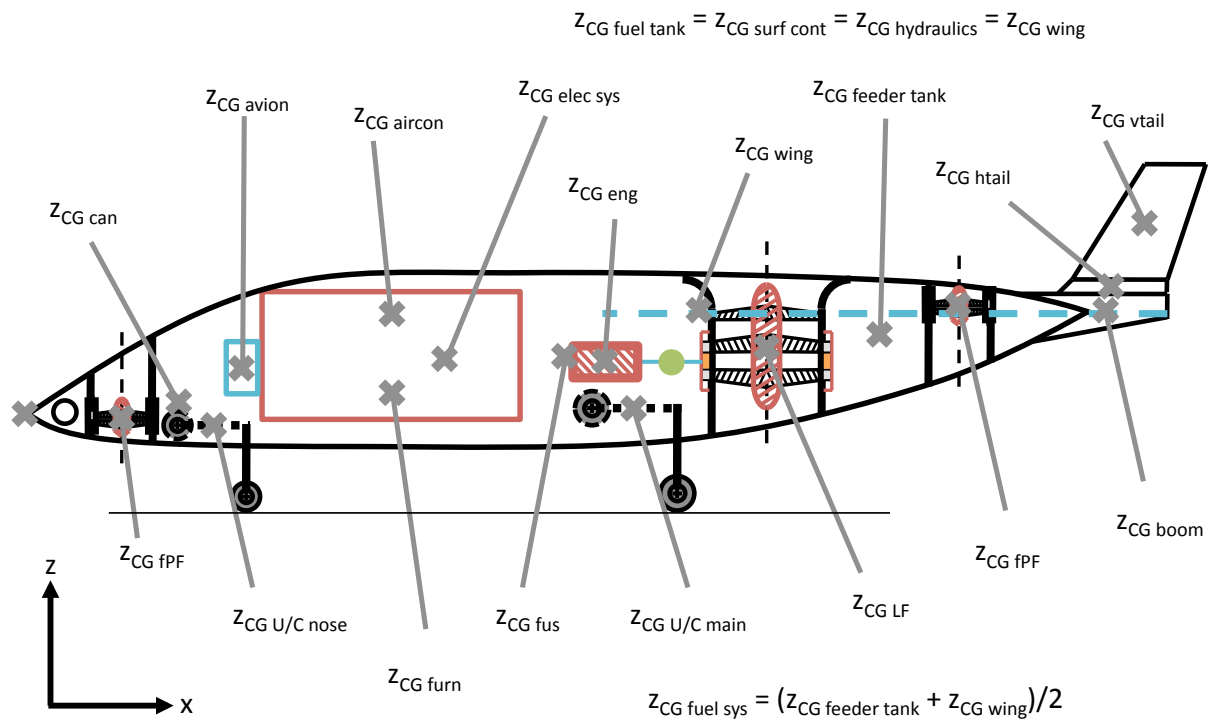


Figure 6.5: Component CG positions the x-z plane

Chapter 7

Aerodynamics

7.1 Overview

The goal of the Aerodynamics section is to ensure that the aircraft meets its performance requirements as well as satisfying all the wing loading criteria from the carpet plot Figure 3.3. The goal was thus to maximise the lift-to-drag ratio during cruise and produce enough lift to have a stall speed of 31.4 ms^{-1} .

An aft wing configured aircraft tends to experience larger pitch down moments than a forward wing configured aircraft. Consequently high lift low pitching moment aerofoils were selected for the wing. To minimise the induced drag of the PAV a high aspect ratio was chosen. The wing was then sized accordingly from the stall speed wing loading criteria given by the initial sizing methodology in Chatper 3.

The canard, horizontal and vertical tails aerofoils were selected using reference [48]. The size of the control surfaces were sized to meet the stability requirements in Chapter 8 as well as the trim drag requirements for cruise performance.

The MATLAB based vortex lattice method (VLM) *Tornado* was used to determine the clean maximum lift coefficient of the wing and provide the stability derivatives used in dynamic stability calculations Chapter 8. *Tornado* was also used to twist the wing to produce an

elliptical lift distribution.

The various components of drag (profile and induced) were then calculated for cruise configuration and landing configuration.

7.2 Wing

From the carpet plot in Figure 3.3 it can be seen that the only wing sizing criteria is the FAR23 requirement for stall speed at 31.4 ms^{-1} . The reference wing area also depends on the stall lift coefficient with flaps down ($C_{L_{max \ flaps}}$) as seen in Eqn 7.1.

$$C_{L_{max \ flaps}} = \frac{W_0}{\frac{1}{2}\rho V_{stall}^2 S_{ref}} \quad (7.1)$$

The higher the chosen $C_{L_{max \ flaps}}$, the lower the reference wing area and consequently the higher the lift-to-drag ratio during cruise. However attaining high values of $C_{L_{max \ flaps}}$ requires complex and heavier flap systems that produce large pitch down moments with associated increases in weight, cost and stability problems. Researching aircraft operating under the same requirements showed that to maximise the wing loading a design $C_{L_{max \ flaps}} \simeq 2.5$ was achieved. Initial calculations concluded that this $C_{L_{max \ flaps}}$ could was achieved through single slotted fowler flaps spanning up to 75% of the wing with flaperons on spanning the remaining 25% if required.

The wing aspect ratio was chosen to be an independent variable. To minimise induced drag a moderate to high aspect ratio is preferable, thus an aspect ratio range of 7 to 10 was chosen. To reduce the pitch down moment generated by an aft wing configuration, aerofoils with high lift and low moment coefficients were selected. It was found that 230xx 5-series NACA profiles had very low pitching moment coefficients ($C_{m0} \simeq -0.0113$) and high maximum lift coefficients ($C_{l_{max}} \simeq 1.65$) [48]. It was then decided that the root aerofoil of the wing would have a maximum $t/c = 0.15$ and the tip aerofoil a maximum $t/c = 0.12$. In order to reduce the wing twist required, a taper ratio producing close to an elliptical lift distribution

was chosen as $\lambda_w = 0.55$. The sweep of the wing-fuselage section (Λ) was set as a variable to adjust the position of the wing aerodynamic centre and fuel CG. A dihedral $\Gamma_w = 5^\circ$ was chosen as an initial value that could be adjusted depending on the lateral stability requirements.

Having established that the $C_{L_{max \text{ flaps}}}$ required was 2.5, the flaps needed to be designed accordingly. The flap chord ratio was restricted to a maximum values of $c_f/c = 0.25$ and to the packaging and rear spar requirements. The front spar was placed at $0.13c$ to maximise the space needed for the wing fuel tanks. Initial calculations showed that single slotted fowler flap with an extension ratio of $c'/c = 1.1$ could provide enough lift to achieve a $C_{L_{max \text{ flaps}}} = 2.5$ assuming a sufficient spanwise flap allocation.

The maximum lift coefficient clean $C_{L_{max \text{ clean}}}$ were calculated using the VLM software *Tornado*. The lift and moment increments were calculated using the equations in Appendix F and thus so was the maximum lift coefficient flaps down $C_{L_{max \text{ flap}}}$. The lift curve slope of the wing was calculated using Eqns 7.2 - 7.5 [11].

$$C_{L_\alpha} = \frac{2\pi AR}{2 + \sqrt{4 + \frac{AR^2\beta_{L_\alpha}^2}{\eta_{L_\alpha}^2} \left(1 + \frac{\tan^2 \Lambda_{\max t}}{\beta_{L_\alpha}^2}\right)}} \left(\frac{S_{exp}}{S_{ref}}\right) \cdot F \quad (7.2)$$

where:

$$\beta_{L_\alpha} = \sqrt{1 - M_\infty^2} \quad (7.3)$$

$$\eta_{L_\alpha} = \frac{C_{l_\alpha}}{2\pi/\beta_{L_\alpha}} \quad (7.4)$$

$$F = 1.07 \left(1 + \frac{H_{fus}}{B_{fus}}\right)^2 \quad (7.5)$$

To maximise the range of the aircraft and minimise its induced drag, it was decided that winglets should be integrated into the design. The winglets were designed according to Figure 7.1 to decrease the induced drag by increasing the effective AR of the aircraft, which was calculated using Eqn 7.6 [11].

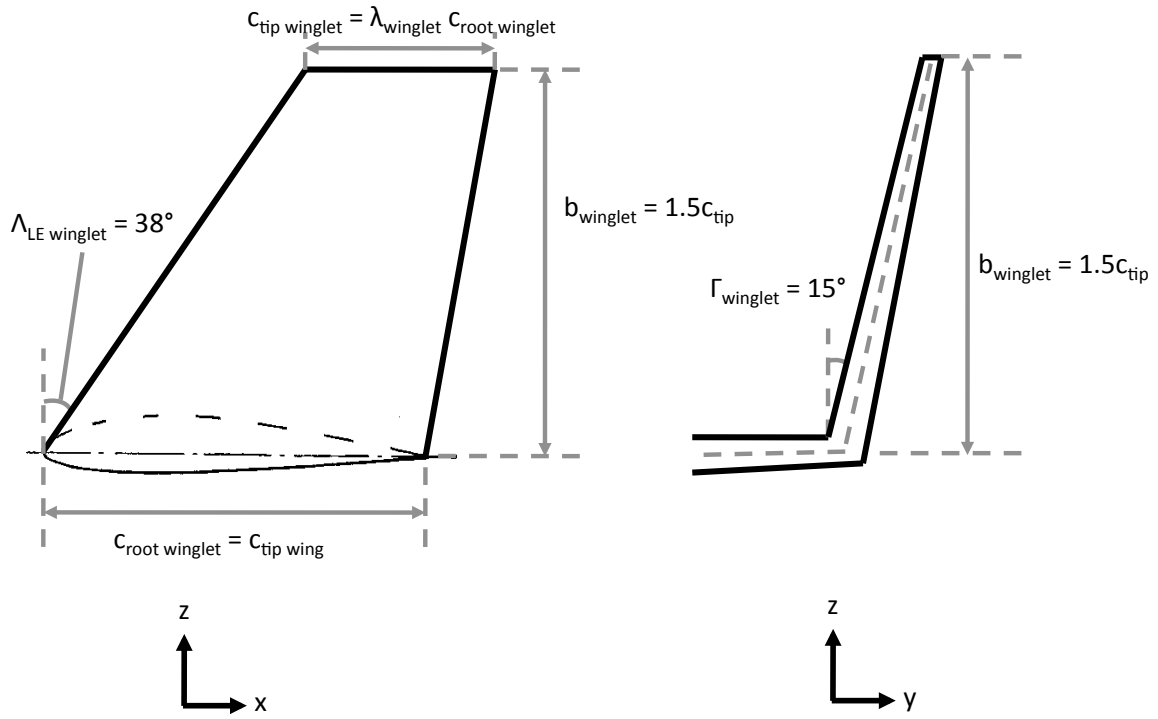


Figure 7.1: Winglets design

$$AR_{eff} = AR \left[1 + 1.9 \left(\frac{b_{winglet}}{b_w} \right) \right] \quad (7.6)$$

7.3 Canard & Tail

The canard and vertical tail were sized using volume coefficients seen below in Eqns 7.7, 7.8 & 7.9 [11]. The horizontal tail was sized depending on the requirements of the vertical tail, as one of its purposes is to position the vertical tail away from the wake of the propulsion fans.

$$C_{vtail} = \frac{L_{vtail} S_{vtail}}{b_w S_{ref}} \quad (7.7)$$

$$C_{htail} = \frac{L_{htail} S_{htail}}{\bar{c} S_{ref}} \quad (7.8)$$

$$C_{can} = \frac{L_{can}S_{can}}{\bar{c}S_{ref}} \quad (7.9)$$

To minimise induced drag, the canard aspect ratio was chosen to be medium to high (5-7) with a taper ratio of $\lambda_{can} = 0.55$. A dihedral $\Gamma_{can} = -3^\circ$ was chosen to minimise the interaction of the canard tip vortices with the flow over the wing. The canard was sized to meet trim drag requirement $\delta_{f_{can}} < 2^\circ$ during cruise, hence a volume coefficient of $C_{can} = 1$. Due the high pitch moments produced by the wing with flaps deployed, the canard control surface chord ratio (canardvator) was chosen as $(c_f/c)_{can} = 0.50$ to ensure pitch controllability of the aircraft.

As the secondary pitch control surface, the dimensions of the horizontal were mainly determined by the position and dimensions of the vertical tail. The tip chord of the horizontal tail was chosen to be the same length as the root chord of the vertical tail. Due to the horizontal tail dimensions being governed by the vertical tail, the horizontal tail span was short. To minimise the boom sizes and thus aircraft weight, the taper ratio was kept high $\lambda_{htail} = 0.80$ to reduce the horizontal tail root chord. The horizontal tail was given moderate sweep angle of $\Lambda_{c/4\ htail} = 15^\circ$ and a dihedral of $\Gamma_{htail} = 10^\circ$. Like the canard, the horizontal tail control surface chord ratio (elevator) was chosen as $(c_f/c)_{htail} = 0.50$.

The vertical tail was sized to meet lateral stability requirements using a volume coefficient $C_{vtail} = 0.03$. A low aspect ratio of (2-3) was chosen as well a low taper ratio of $\lambda_{vtail} = 0.35$. The sweep of the vertical tail was chosen as $\Lambda_{c/4\ vtail} = 35^\circ$ and was given a dihedral of $\Gamma_{vtail} = 15^\circ$. The vertical tail required a control surface chord ratio (rudder) of $(c_f/c)_{vtail} = 0.50$ to fulfil lateral stability criteria.

In order to produce effective controllability in pitch, the canard aerofoil was selected to have a large lift coefficient and zero angle of attack. The NACA aerofoil 64₁ – 412 with a $C_{l0} = 0.4$ was thus selected using reference [48]. Providing additional pitch control, the horizontal tail was expected to produce a pitch up moment through negative lift. It was decided that a symmetrical aerofoil was required and consequently the NACA 00xx series provided symmetrical aerofoils of varying thickness. The maximum thickness to chord ratio was chosen to

be $t/c = 0.12$ for root and tip. The same aerofoil and thickness were selected for the vertical tail.

The lift curve slopes of the individual aerofoils were gathered from experimental data [48]. The lift curve slopes for all the aerodynamics surfaces were then calculated using Eqns 7.2 - 7.5.

The incremental lift and moments (ΔC_L & ΔC_M) for each surface was calculated using the equations and data seen in Appendix F. These results were then used to determine the static stability as is shown in Chapter 8.

7.4 Vortex Lattice Method - *Tornado*

Tornado is a standard 3D vortex lattice method written on MATLAB that was readily available and easy to use. *Tornado* was chosen as it could output aerodynamic and stability data that could not be easily determined by traditional empirical methods.

Tornado was used to determine the maximum lift coefficient of the wing flaps up. The VLM also provided stability derivatives which were used to calculate the lateral static stability and the dynamic stability of the aircraft. The aerodynamic surface interaction (canard downwash on wing) was modelled and the twist of the wing was adjusted to produce an elliptic lift distribution during cruise.

7.5 Drag

The profile drag of the aircraft was calculated using a component build up method seen in Eqn 7.10. The aircraft was broken down into the the following components: fuselage, wing, canard, horizontal tail, vertical tail, booms, ducts and pylons. The skin friction coefficient (C_f), form factor (FF) and interference factor (Q) were calculated using the equations in Appendix F.7. The wetted area (S_{wet}) of each component was calculated from the 3D packaging models.

From reference [11] the inference factor for a canard was found to be $Q_{can} = 1.04$. The

interference factor of the booms, being mounted on the fuselage was found to be $Q_{boom} = 1.5$. And the interference factor of the fan nacelles during cruise, due to their close proximity to the fuselage was found to be $Q_{nacelle} = 1.3$. All other interference factors were found to be uniform $Q = 1$.

The skin friction coefficient could be calculated using two different equations, Eqn F.30 for a laminar boundary layer (lower Reynolds numbers) and Eqn F.31 for turbulent boundary layers (higher Reynolds numbers). Turbulent boundary layers exhibit higher skin friction values and so delaying boundary layer transition on aerodynamic surfaces can aid in drag reduction. Aircraft like the Piaggio P180 Avanti are designed precisely to delay transition to ensure that the profile drag of the aircraft is minimised. The Piaggio P180 Avanti has been designed such that 50% of the wetted area of the lifting surfaces experiences a laminar boundary layer, as compared to the normal 10-20%, while 25-30% of the wetted area over the fuselage is laminar as compared to $\sim 0\%$ for a typical aircraft [11]. Similar ratios of laminar to turbulent boundary layer flow (40-50%) were found using the 2D aerofoil design and analysis program *XFOIL*. Therefore the PAV was assumed to have the similar ratios of laminar and turbulent boundary layers to the Piaggio P180 Avanti.

$$C_{D_0} = \frac{\sum C_{f_i} \cdot FF_i \cdot Q_i \cdot S_{wet_i}}{S_{ref}} + C_{D_{LP}} \quad (7.10)$$

The induced drag of the aircraft was calculated using Eqns 7.11, 7.12 & 7.13 [11]. The Oswald efficiency (e) seen in Eqn 7.13 provided a simple method to estimate the increase in drag due to a non-elliptic lift distribution and flow imperfections.

$$C_{D_i} = K \cdot C_L^2 \quad (7.11)$$

$$K = \frac{1}{\pi \cdot AR \cdot e} \quad (7.12)$$

$$e = 1.78(1 - 0.045AR^{0.68}) - 0.64 \quad (7.13)$$

However with the implementation of winglets in the design, the effective aspect ratio of the wing is increased and thus decreasing the induced drag. The aspect ratio for the wing used in Eqn 7.12 was determined by Eqn 7.6.

The trim drag was calculated using Eqns 7.12, 7.13 & 7.14 [11], where the lift coefficients include the incremental lift due to any control surface deflection.

$$C_{D_{trim}} = K_{wing} \cdot C_{L_w}^2 + \left(\frac{S_{can}}{S_{ref}} \right) K_{can} \cdot C_{L_{can}}^2 + \left(\frac{S_{htail}}{S_{ref}} \right) K_{htail} \cdot C_{L_{htail}}^2 \quad (7.14)$$

The flap profile drag was calculated using Eqns 7.15 & 7.16. The pressure drag component equation, Eqn 7.16 was compiled from reference [12] graphical data for flap chord ratios $c_f/c = 0.25$. The interference drag $\Delta C_{D_{int}}$ is an added 25% increase of the total flap profile drag. The flap induced drag was calculated using Eqn 7.17, where the average induced drag factor for flaps K_{flap} is 0.12.

$$\Delta C_{D_{0_flaps}} = \Delta C_{d_p} \cos \Lambda_{c/4} \left(\frac{S_{flap}}{S_{ref}} \right) + \Delta C_{D_{int}} \quad (7.15)$$

$$\Delta C_{d_p} = 5 \times 10^{-5} \cdot \delta_f^2 - 8 \times 10^{-4} \cdot \delta_f + 7.3 \times 10^{-3} \quad (7.16)$$

$$\Delta C_{D_{i_flaps}} = K_{flap}^2 \cdot \Delta C_{L_w}^2 \cos \Lambda_{c/4} \quad (7.17)$$

The undercarriage profile drag was calculated using Eqns 7.18 & 7.19 [12], where S_{gear_i} is the undercarriage frontal area and $m_{U/C}$ is the ratio of S_{gear_i} and the undercarriage gross frontal area. The undercarriage gross frontal area is calculated by multiplying the total height of the undercarriage unit by the total width of the undercarriage unit.

$$C_{D_{0_U/C}} = \sum_{i=1}^n \left[C_{D_{gear_i}} \left(\frac{S_{gear_i}}{S_{ref}} \right) \right] \quad (7.18)$$

$$C_{D_{gear_i}} = 0.058 \cdot \exp(4.849 \cdot m_{U/C}) \quad (7.19)$$

7.6 Elliptical Lift Distribution

An elliptical lift distribution is the optimum for the reduction of induced drag. This is established by twisting the wing appropriately, varying the local angle of attack and thus the local lift value. With a rear wing configuration, the canard downwash will also affect the wing lift distribution by decreasing the local angle of attack for the inboard wing section. Consequently a non-linear wing twist is required with higher angles of incidence at the downwash affected regions.

Tornado models aerodynamic canard-wing interaction by calculating the effect of the canard trailing vortices on the panels of the wing. Thus *Tornado* models the change in lift distribution as a consequence of these interactions. The area of the wing directly behind the canard is the most affected. The downwash from the canard reduces the angle of attack and thus lift of the affected region.

Since the aircraft would spent most of the flight in cruise, it was decided that the twist should be optimised for cruise. To twist the wing appropriately and make the lift distribution elliptical, the semi-span of the wing was divided up into 5 sections with 6 control points from root to tip. The C_{L_w} was kept to cruise value by adjusting the wing incidence through increasing or decreasing all the control points by a constant value. The points were then adjusted individually by enforcing a change in local incidence at each control point. The local lift at each control point was compared with the local elliptical optimum. If the local lift was found to be below the elliptical optimum, the incidence was increased accordingly and vice versa.

The evolution of the lift distribution as the twist is varied can be seen in Figure 7.2 from the initial values x_0 , to a sample iteration x_i and to the final solution x_f . The twist values can be seen in Figure 7.3.

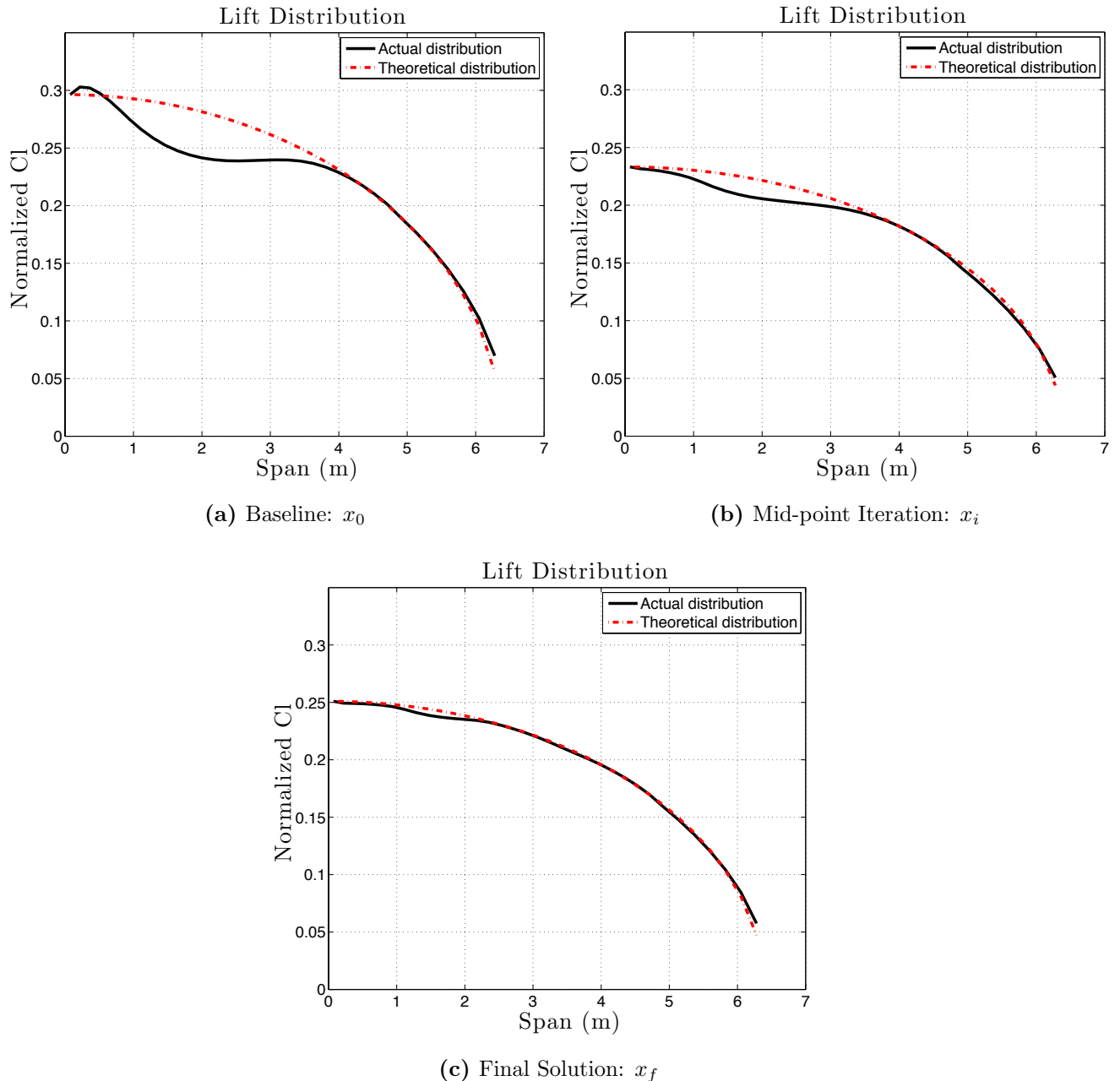


Figure 7.2: Lift distribution iterations

It can be seen clearly that the downwash of the canard reduces local lift of the inboard section of the wing. Consequently, the local twist increased as in Figure 7.3. The initial values seen in Figure 7.3 is the wing incidence angle at cruise i_w . The section inboard of 2.8 m span required an increase in incidence to increase the local lift to the desired values. Outboard of 2.8 m the local incidence was decreased accordingly to achieve the final distribution in Figure 7.2.

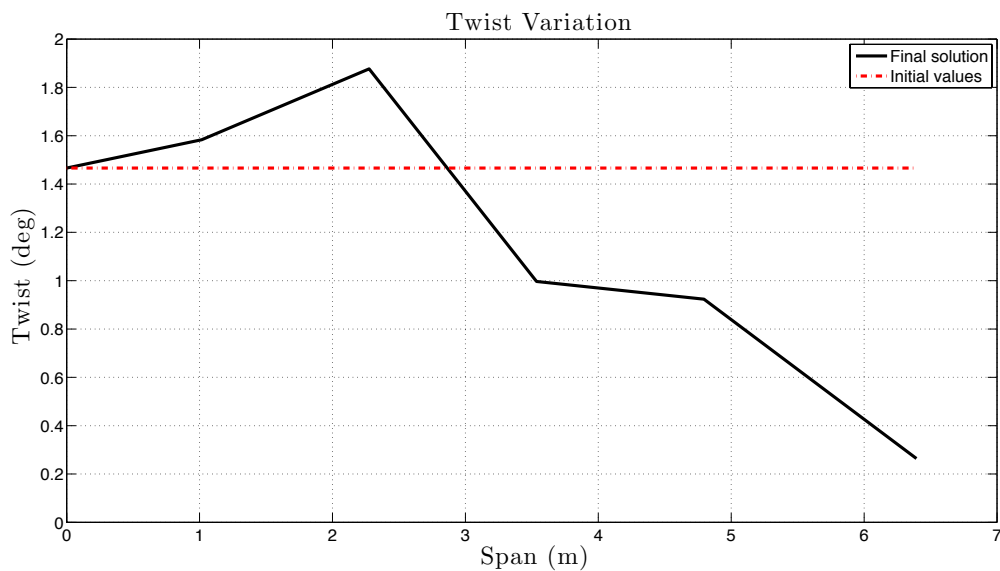


Figure 7.3: Twist distribution

Chapter 8

Stability

8.1 Overview

Having developed a methodology for determining the aerodynamic characteristics of the PAV, a methodology to ensure the stability of the aircraft could be developed. Static stability is the determination of whether an aircraft when perturbed into a new angular orientation can produce opposing moments that will return the aircraft to its original position. Consequently if the forces and moments of the aircraft can be balanced for a certain orientation, the aircraft will not deviate from that steady state. The aircraft orientation can then be established easily through control surface deflections, which are kept to a minimum to reduce trim drag during cruise and ensure controllability during landing. The sizing and design of these control surfaces are dependent on the longitudinal and lateral static stability requirements.

For longitudinal stability, another factor contributing to the magnitude of the deflections for a certain steady state is the static margin of the aircraft. The larger the static margin, the more deflection is required to maintain the same steady state. Consequently, altering the position of the static margin could come about by repositioning the aerodynamic surfaces, or repositioning the CGs. The wing was thus repositioned and the fuel was balanced between the wing and feeder tanks to reduce the static margin as much as required. For civilian aircraft, the aft most static margin is designed to be 4 – 10% [11].

Lateral static stability is dependent on the fin size and its control surface design. FAR23 requirements state that the aircraft must be able to operate at a sideslip angle of $\beta_{sideslip} = 11.5^\circ$ at stall velocity. The fins were sized accordingly.

With the aircraft statically stable, the next step was to ensure dynamic stability. Dynamic stability is the aircraft's inertial dynamic response once it has been perturbed. Stability in this case implies a damping force returning the aircraft to its original orientation. The four main stability modes: Phugoid, SPPO, Dutch Roll and Spiral were examined using stability derivatives provided by VLM (*Tornado*).

8.2 Static Stability

8.2.1 Longitudinal

Longitudinal stability specifically involves: making sure that enough lift is being produced by the aerodynamic surfaces, these forces as well as moments are balanced about the CG of the aircraft, and that $\partial C_m / \partial \alpha$ or $\partial C_m / \partial C_L < 0$ (i.e. the static margin is positive) [12].

It was decided that the aircraft was to be evaluated with flaps up initially. Since the cruise segment was to be the main segment of the PAV's operation, the first steady state to evaluate was chosen as cruise. As static margin was to be lowest with the aft most CG position, increasing as the CG moved forward, the design static margin of 4 – 6% had to be implemented for the aft most CG.

The first step was to ensure that lift produced by all the aerodynamic surfaces matched the required lift coefficient (calculated using Eqn 8.1). The total lift generated by the wing, canard and tail was calculated from Eqns 8.2 - 8.5 [12, 11]. For cruise it was assumed that the fuselage incidence and angle of attack was to be $\alpha = 0^\circ$ to minimise drag. The lift required was thus adjusted through the wing incidence (i_w). Since the cruise segment was the main operation point of the PAV, this dictated that the wing incidence had to be set optimally for this segment.

$$C_L = \frac{W_0}{\frac{1}{2}\rho V^2 S} \quad (8.1)$$

$$C_{L_{PAV}} = C_{L_w} + \left(\frac{S_{can}}{S_{ref}} \right) C_{L_{can}} + \left(\frac{S_{htail}}{S_{ref}} \right) C_{L_{htail}} \quad (8.2)$$

where:

$$\begin{aligned} C_{L_w} &= C_{L\alpha_w} \left[\left\{ \alpha \left(1 - \frac{\partial \epsilon}{\partial \alpha} \right) + i_w - \alpha_{0w} \right\} \left(\frac{b_{can}}{b} \right) \right. \\ &\quad \left. + \left\{ \alpha + i_w - \alpha_{0w} \right\} \left(1 - \frac{b_{can}}{b} \right) \right] + \Delta C_{L_w} \end{aligned} \quad (8.3)$$

$$C_{L_{can}} = C_{L\alpha_{can}} \left[\alpha \left(1 + \frac{\partial \epsilon}{\partial \alpha} \right) + i_{can} - \alpha_{0can} \right] + \Delta C_{L_{can}} \quad (8.4)$$

$$C_{L_{htail}} = C_{L\alpha_{htail}} \left[\alpha \left(1 - \frac{\partial \epsilon}{\partial \alpha} \right) + i_{htail} - \alpha_{0htail} \right] + \Delta C_{L_{htail}} \quad (8.5)$$

The canard and horizontal tail incidences were chosen to be $i_{can} = i_{htail} = 0^\circ$, to ensure minimal induced and trim drag during cruise. The moments of the lifting surfaces about the CG were calculated using their lift coefficients multiplied by their moment arm, where $\bar{x} = x/\bar{c}$. The moments about the CG of the aircraft were then balanced by deflecting the canardvators and elevators (δ_e) simultaneously so that in Eqn 8.6 [12, 11], $C_{m_{CG}} = 0$. The total C_L was calculated again and the wing incidence was readjusted. This was followed by the readjustment of the moments of the aircraft through the deflection of the control surfaces. The process was repeated iteratively until both values had converged.

$$\begin{aligned} C_{m_{CG}} &= C_{L_w}(\bar{x}_{ref} - \bar{x}_{ac_w}) + C_{m_w} + C_{m_{can}} + C_{m_{htail}} + C_{m_{fus}} \\ &+ \left(\frac{S_{can}}{S_{ref}} \right) C_{L_{can}}(\bar{x}_{ref} - \bar{x}_{ac_{can}}) + \left(\frac{S_{htail}}{S_{ref}} \right) C_{L_{htail}}(\bar{x}_{ref} - \bar{x}_{ac_{can}}) \\ &- \frac{T \cdot z_t}{S_{ref} \cdot q \cdot \bar{c}} + \Delta C_{m_w} + \Delta C_{m_{can}} + \Delta C_{m_{htail}} \end{aligned} \quad (8.6)$$

For longitudinal static stability the derivative is required to be $\partial C_m / \partial C_L < 0$ (i.e. the static margin is positive) [11]. The static margin as a percentage of the mean aerodynamic chord was calculated using Eqns 8.7 & 8.8 [12, 11]. From Eqn 8.8 it can be seen that the position of the neutral point is dependent on the lift curve slopes of the aerodynamic surfaces as well as their chordwise position. The lift curve slopes were determined by the aerodynamic quantities set in earlier calculations, and thus were assumed to be constant. The positions of the canard and horizontal tail could not be varied significantly due to packaging constraints, and therefore the only remaining variable that could be used to vary the static margin was the position of the wing. Consequently the wing was moved through the variation of the sweep of inboard wing/fuselage section ($\Lambda_{in\ LE}$, $\Lambda_{in\ TE}$) seen in Figure 5.8. The wing was iteratively positioned so that under cruise conditions the static margin for the aft-most CG was $SM = 4 - 6\%$.

The above processes were repeated with flaps down to determine whether sufficient control surface deflection could control the aircraft with the CG in its most forward position (i.e. highest static margin). If the deflections on the canardvator and elevator were in excess of 25° , then canard size was increased.

$$SM = \bar{x}_{NP} - \bar{x}_{CG} \quad (8.7)$$

where:

$$\begin{aligned} \bar{x}_{NP} = & \left[C_{L\alpha_w} \bar{x}_{ac_w} - C_{m\alpha_{fus}} + \left(\frac{S_{can}}{S_{ref}} \right) C_{L\alpha_{can}} \bar{x}_{ac_{can}} \right. \\ & \left. + \left(\frac{S_{htail}}{S_{ref}} \right) C_{L\alpha_{htail}} \bar{x}_{ac_{htail}} \right] / C_{L\alpha_{PAV}} \end{aligned} \quad (8.8)$$

Each time the wing was repositioned, the aerodynamic, weight estimation, propulsion and stability calculations were repeated until all the relevant values converged.

8.2.2 Lateral

Lateral static stability involves the ability of the aircraft to operate in sideslip conditions and the tendency for it to return to its original orientation i.e. for the yaw coefficient derivative with respect to sideslip to be negative ($\partial C_n / \partial \beta \equiv C_{n\beta} > 0$) [12]. FAR23 requirements state that the aircraft should be able to operate in a crosswind that is equivalent to holding an 11.5°

sideslip at 1.1 times stall speed. Another cursor of lateral static stability is the roll coefficient derivative with respect to sideslip, which is required to be positive ($\partial C_l / \partial \beta \equiv C_{l\beta} < 0$) [12]. The vertical tails and rudders were sized to meet $C_{n\beta} > 0$ requirement, and wing dihedral was adjusted to meet the $C_{l\beta} < 0$.

The stability derivatives of the aircraft were obtained from *Tornado*. It was found that the coordinate system of *Tornado* varied from that of the conventional as can be seen in Figure 8.1. The derivatives were modified accordingly for calculations.

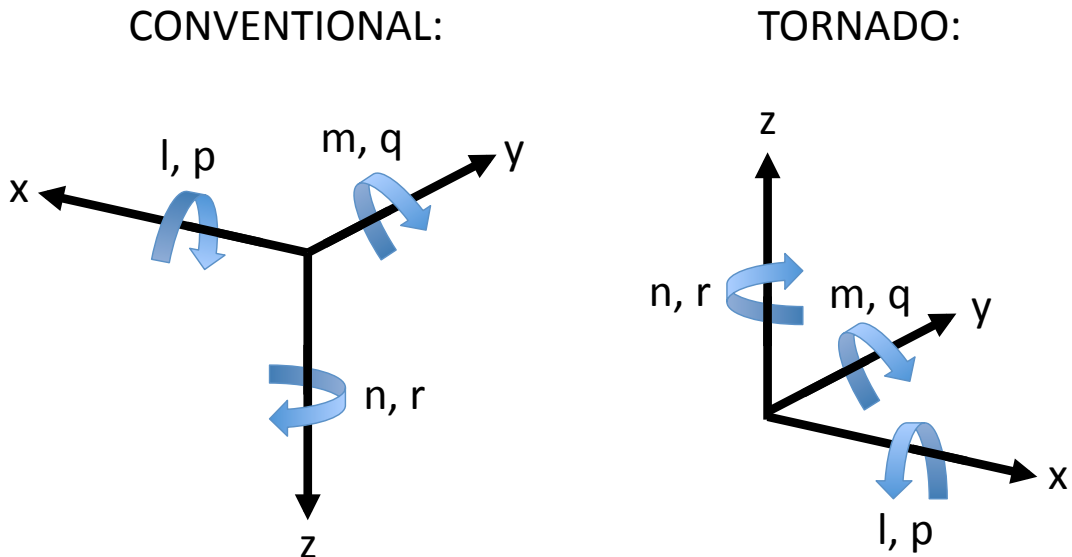


Figure 8.1: Coordinate system definitions for stability calculations

8.3 Dynamic Stability

8.3.1 Longitudinal

8.3.1.1 Phugoid

Dynamic stability involves determining the natural frequency of each dynamic mode and the corresponding damping ratio using stability derivatives. Modes that could potentially exhibit instability and still be acceptable are ones with large time periods such as Phugoid and

Spiral. A long period allows time for the pilot to recover the aircraft after such a mode is excited.

The Phugoid is a longitudinal stability mode that varies in pitch, airspeed and altitude. The aircraft pitches up and starts to climb losing airspeed, after which the aircraft starts to pitch down, lose altitude and gain airspeed. This cycle continues and reduces or increases depending on the availability of sufficient damping. The period of the Phugoid normally lies in the range of 30 – 60 seconds.

The natural frequency and damping ratio of the PAV were calculated using Eqns 8.9 & 8.10 [12]. The stability derivatives for drag and thrust were obtained using the equations in Appendix G.2.1. The subscript "1" in Eqns 8.9 - 8.16 denotes that these calculations were done at a steady state, i.e. all the forces and moments balanced.

As stated previously, FAR23 requirements dictate that a Phugoid motion can be unstable to the degree that it "*does not increase a pilot's workload or otherwise endanger the aircraft*".

$$\omega_{PH} = \frac{1.414 \cdot g}{U_1} \quad (8.9)$$

$$\xi_{PH} = \left[\frac{g}{2 \cdot C_{L1} \cdot U_1 \cdot \omega_{PH}} \right] \left[C_{D_U} + 2C_{D_1} - C_{T_{xU}} - 2C_{T_{x1}} \right] \quad (8.10)$$

8.3.1.2 Short Period Pitching Oscillation

Short Period Pitching Oscillation (SPPO) is a longitudinal stability mode that varies angle of attack. The aircraft pitches up and down rapidly about its CG with a very small period. If these oscillations are not appropriately damped, the aircraft could experience catastrophic loads causing structural failure. SPPO could also trigger pilot induced oscillations (PIO). In an attempt to correct the oscillations, the pilot control input lag time pushes excites the mode further, causing structural failure again. The period for SPPO is normally 0.5 – 1.5 seconds.

The natural frequency and damping ratio of the PAV were calculated using Eqns 8.11 & 8.12 [12]. The pitch moment and vertical force stability derivatives were obtained using the combination of values from *Tornado* and the equations in Appendix G.2.2.

FAR23 regulations state that any SPPO mode must be "*heavily damped*", i.e. the motion must completely damp within 2 cycles and 4 seconds.

$$\omega_{SPPO} = \left[\frac{Z_\alpha \cdot M_q}{U_1} - M_\alpha \right]^{\frac{1}{2}} \quad (8.11)$$

$$\xi_{SPPO} = - \left[M_q + \frac{Z_\alpha}{U_1} + M_\alpha \right] / (2 \cdot \omega_{SP}) \quad (8.12)$$

8.3.2 Lateral

8.3.2.1 Spiral

Spiral is a lateral non-oscillatory dynamic mode. The aircraft is perturbed into a position with an initial roll angle. Depending on whether this mode is stable or not, the roll angle will decrease returning the aircraft to its original position, or begin to increase. If the mode is unstable the aircraft will continue to increase its bank angle and enter into a tighter and tighter downwards spiral, eventually causing the aircraft to impact into the ground.

For the Spiral mode to be stable the criteria in Eqn 8.13 must hold. If this is not the case, the time for the period to double can be calculated using Eqn 8.14 [12]. The stability of the Spiral mode is controlled by the dihedral of the wing and the height of the vertical tail. Like the Phugoid, FAR23 requirements dictate that the spiral mode of an aircraft can be unstable as long as its time period to double is sufficiently large allowing time for pilot to recover the aircraft.

$$L_\beta \cdot N_r - N_\beta \cdot L_r > 0 \quad (8.13)$$

$$T_{2SP} = \frac{L_\beta \cdot \ln 2}{L_\beta \cdot N_r - N_\beta \cdot L_r} \quad (8.14)$$

8.3.2.2 Dutch Roll

Dutch Roll is a lateral stability mode that couples yaw and roll. When perturbed, the aircraft begins to roll and yaw simultaneously in an oscillatory out of phase motion. If the mode is stable, the aircraft returns to its original position. If this mode is not sufficiently damped, the motion can easily continue for many cycles, making the flight unpleasant for the pilots or any passengers. The period for Dutch Roll normally lies in the region of 1 – 2 seconds for small aircraft.

The natural frequency and damping ratio of the PAV were calculated using Eqns 8.15 & 8.16 [12]. The remaining lateral stability derivatives for these equations were determined from equations in Appendix G.2.4 and values obtained from *Tornado*.

Like the Spiral mode, the Dutch Roll characteristics can be modified by the amount of dihedral applied to the wing. However, the Dutch Roll damping is inversely affected with the increase of dihedral. Consequently a balance must be struck between maintaining enough dihedral to stabilise the Spiral mode and reducing the dihedral enough to stabilise Dutch Roll.

FAR23 requirements state that Dutch Roll "*must be damped to 1/10th amplitude in 7 cycles*". Thus the wing dihedral was initially set to $\Gamma_w = 5^\circ$ and adjusted if needed to meet both the Spiral and Dutch Roll requirements.

$$\omega_{DR} = \left[\frac{Y_\beta \cdot N_r + N_\beta(U_1 - Y_r)}{U_1} \right]^{\frac{1}{2}} \quad (8.15)$$

$$\xi_{DR} = - \left[N_r + \frac{Y_\beta}{U_1} \right] \Big/ (2 \cdot \omega_{DR}) \quad (8.16)$$

Chapter 9

Performance

9.1 Overview

Determining the performance of the aircraft is key to finding out whether the targets for range, loiter, climb rate, take-off distance and landing distance were met. The operational flight envelope of the aircraft was also determined using specific excess power (P_s) calculations.

Having precise, thrust, drag, lift and weight data from previous sections, the performance of the aircraft was evaluated. With the performance of the aircraft evaluated, the performance values could be compared with the completed synthesis input variables as can be seen in Chapter 10.

An elliptical lift distribution is the optimal solution for the minimising the induced drag. This can be established by twisting the wing appropriately, varying the local angle of attack and thus the local lift value. The appropriate twist was applied using the lift distribution from *Tornado*.

9.2 Cruise

The cruise performance of an aircraft can be determined using the Breguet range equation seen Eqn 9.1 [11]. The same equation was used in previous sections to estimate the weight fraction for a given cruise velocity, lift to drag ratio, SFC and range. However with more

accurate data for the propulsive efficiency, SFC and aerodynamics of the aircraft, the cruise segment could be broken up into smaller sections to be analysed more accurately. The cruise segment was therefore broken up into four smaller segments by dividing the weight of the fuel used for cruise into four segments. The propulsive and aerodynamic data for a given altitude with varying velocity was gathered for each segment.

From Eqn 9.1, it can be seen that to maximise range, the propulsive efficiency and lift to drag ratio need to be maximised and the SFC needs to be minimised. Consequently the propulsive data was gathered by thrust matching (varying blade pitch) for a given velocity, and finding the maximum propulsive efficiency (η_p) at that point. A limit was put on the blade tip speed of $M_{tip} < 0.95$ as stated in Chapter 4. The thrust available was dependent on the engine power available for a given altitude, and was calculated using Eqns 4.54, 4.55, 4.56 & 4.57.

From all the data gathered, the maximum capable distance travelled was calculated. The range performance of the aircraft was then compared to the target range inputted into the synthesis.

$$Range = \frac{\eta_p}{SFC} \cdot \frac{L}{D} \cdot \ln \left(\frac{W_i}{W_{i+1}} \right) \quad (9.1)$$

The range is heavily dependent on the propulsive and aerodynamic characteristics of the aircraft. The calculated range can be larger or smaller than the inputted range depending on the other input variables. These variations are discussed in more detail in Chapter 10.

9.3 Loiter

The endurance performance (loiter) is evaluated using a modified Breguet range equation as seen Eqn 9.2 [11]. Like Eqn 9.1, Eqn 9.2 was used in earlier sections to determine the weight of fuel required to loiter for 30 minutes. With more accurate propulsive and aerodynamic data, the endurance of the aircraft was calculated.

$$Endurance = \frac{\eta_p}{V \cdot SFC} \cdot \frac{L}{D} \cdot \ln \left(\frac{W_i}{W_{i+1}} \right) \quad (9.2)$$

9.4 Climb Rate

The climb angle (γ_{climb}) and climb rate (V_v) of an aircraft were analysed using Eqns 9.3 & 9.4 [11]. It can be seen from Eqn 9.4, that the maximum climb velocity can be achieved by having the available power/thrust to overcome the drag being generated during climb. Consequently the maximum thrust available for a given velocity is crucial to providing the maximum climb rate.

The propulsive data was gathered by determining the maximum thrust generated for a given velocity. The same limits on the blade tip speed $M_{tip} < 0.95$ and engine power availability used for the range and loiter calculations were also used for the climb calculations. The maximum climb rate for each altitude was extracted from the data.

$$\gamma_{climb} = \sin^{-1} \left[\frac{P \cdot \eta_p}{V \cdot W} - \frac{D}{W} \right] \quad (9.3)$$

$$V_v = V \cdot \sin \gamma_{climb} = \frac{P \cdot \eta_p}{W} - \frac{D \cdot V}{W} \quad (9.4)$$

This data could also be used to determine shortest time and the fuel required to climb to cruise altitude.

9.5 Turn Rate

The turn rate performance of the aircraft was analysed using Eqns 9.5 & 9.6 [11]. Although there are no turn requirements for civilian aircraft, the ability for it to turn quickly is still a

beneficial. The turn performance was calculated from maximum thrust data used for the climb rate calculations.

$$\dot{\psi} = \frac{g\sqrt{n^2 - 1}}{V} \quad (9.5)$$

$$n = \left[\frac{q}{K_{wing} \cdot (W/S)} \left(\frac{T}{W} - \frac{q \cdot C_{D0}}{(W/S)} \right) \right]^{\frac{1}{2}} \quad (9.6)$$

9.6 Specific Excess Power

The performance map of an aircraft can be defined by its specific excess power. The specific excess power is the energy available to the aircraft at a certain altitude and velocity. This translates into a contour plot for which various performance attributes such as; absolute ceiling, maximum speed, climb rates and so on can be extracted. The operating envelope is normally covered by $P_s = 0$, implying that the aircraft has reached its energy limit.

The specific excess power of the aircraft was analysed using Eqn 9.7 [11]. The maximum thrust data with varying velocity and altitude was used to calculate the specific excess power. The load factor (n) was varied for these calculations, where $n = 1$ represents the aircraft in a steady state. The constant $P_s = const$ curves were extracted and a contour plot the performance of the aircraft was developed.

$$P_s = V \left[\frac{T}{W} - \frac{q \cdot C_{D0}}{(W/S)} - n^2 \cdot \frac{K_{wing}}{q} \frac{W}{S} \right] \quad (9.7)$$

Since the PAV was designed with VTOL capability, it was evident that it would have an abundance of excess power. This in turn gives the aircraft the capability to reach altitudes that are beyond the expertise and licensing of a private pilot. As a solution, once in flight the engine could be flat rated to limit the absolute ceiling to 10668 m (35000 ft).

9.7 Take-off Distance

The take-off distance performance was calculated using Eqn 9.8 [12]. The mean thrust to weight ratio $(\bar{T}/W)_{t/o}$ for take-off was calculated using the maximum thrust performance data. The lift off velocity (V_{LOF}) is equivalent to 1.2 times the stall speed ($V_{stall\ clean}$), Eqn 9.9. With the correct lift off speed the thrust and drag at this point could be determined to calculate the lift off angle, Eqn 9.10. The ground rolling resistance coefficient was calculated using Eqn 9.11, where the resistance factor ($\mu_g = 0.02$) was assumed to be that of asphalt.

FAR 23 requirements state that the take-off distance includes clearance of an obstacle 15.24 m (50 ft) high, i.e. $h_{t/o} = 15.24$ m. Reference [12] also states that the take off factor ($f_{t/o}$) conforming to FAR 23 is assumed to be 1. The ratio of the velocity at the obstacle's height to the stall velocity is assumed to be $V_3/V_{STO} = 1.3$, where the take-off stall velocity is assumed to be the flaps up stall velocity ($V_{STO} = V_{stall\ clean}$).

The FAR 23 requirements states that a CTOL aircraft take-off distance should be no more than 914 m (3000 ft). However with an aircraft with so much available excess power the likelihood of this requirement being violated is notional.

$$s_{t/o} = f_{t/o} \cdot h_{t/o} \left[\frac{1}{\gamma_{LOF}} + \left\{ \left(\frac{V_3}{V_{STO}} \right) \left(\frac{W}{S} \right)_{t/o} \left(\left[\left(\frac{\bar{T}}{W} \right)_{t/o} - \mu' \right]^{-1} + 1.414 \right) \right\} \times \left\{ h_{t/o} \cdot \rho \cdot g \cdot C_{L_{max\ clean}} (1 + 1.414 \cdot \gamma_{LOF}) \right\}^{-1} \right] \quad (9.8)$$

where:

$$V_{LOF} \simeq 1.2 \cdot V_{STO} \quad (9.9)$$

$$\gamma_{LOF} = \left(\frac{T - D}{W} \right)_{LOF} \quad (9.10)$$

$$\mu' = \mu_g + 0.72 \left(\frac{C_{D0}}{C_{L_{max \text{ clean}}}} \right) \quad (9.11)$$

9.8 Landing Distance

The landing distance performance was calculated using Eqns 9.12, 9.13 & 9.14 [12]. The approach velocity (V_{APP}) is assumed to be 1.3 times the stall velocity flaps down (V_{stall}), Eqn 9.15. The touch down velocity (V_{TD}) is calculated from Eqn 9.16. Reference [12] suggests that the average approach angle should be assumed to be $\bar{\gamma}_L = 0.10 \text{ rads}$ and the approach factor $\Delta n = 0.10$. It also suggests that for light aircraft, the average deceleration on the ground is $\bar{a} = 0.35g$ to $0.45g$.

Like take-off the FAR 23 requirements state that the aircraft when landing should be able to avoid an obstacle 15.24 m (50 ft) high, i.e. $h_L = h_{t/o} = 15.24 \text{ m}$.

$$s_L = s_{air} + s_{ground} \quad (9.12)$$

$$s_{air} = \left(\frac{1}{\bar{\gamma}_L} \right) \left(\frac{V_{APP}^2 - V_{TD}^2}{2g + h_L} \right) \quad (9.13)$$

$$s_{ground} = \frac{V_{TD}^2}{2\bar{a}} \quad (9.14)$$

where:

$$V_{APP} = 1.3 \cdot V_{stall} \quad (9.15)$$

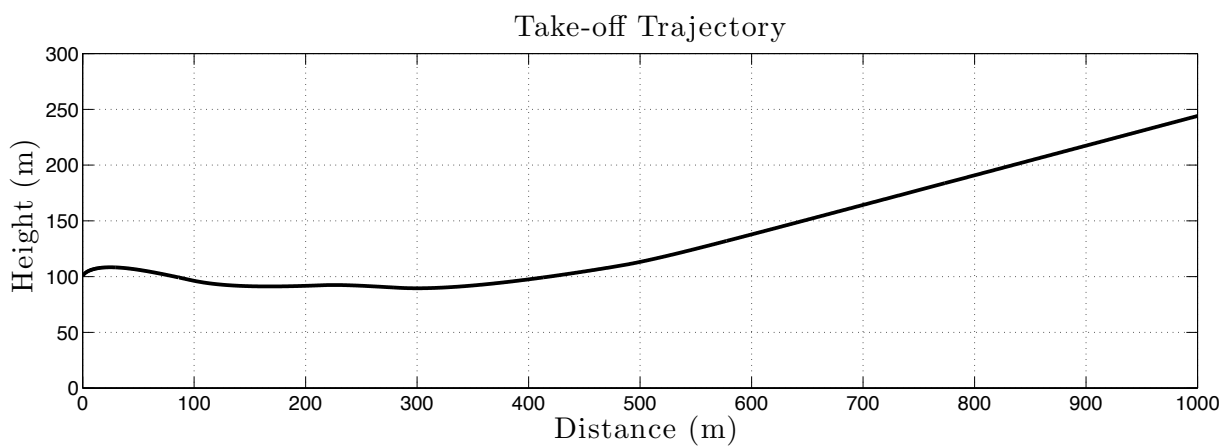
$$V_{TD} = V_{APP} \left[1 - \frac{\bar{\gamma}_L^2}{\Delta n} \right]^{\frac{1}{2}} \quad (9.16)$$

9.9 Transition Model

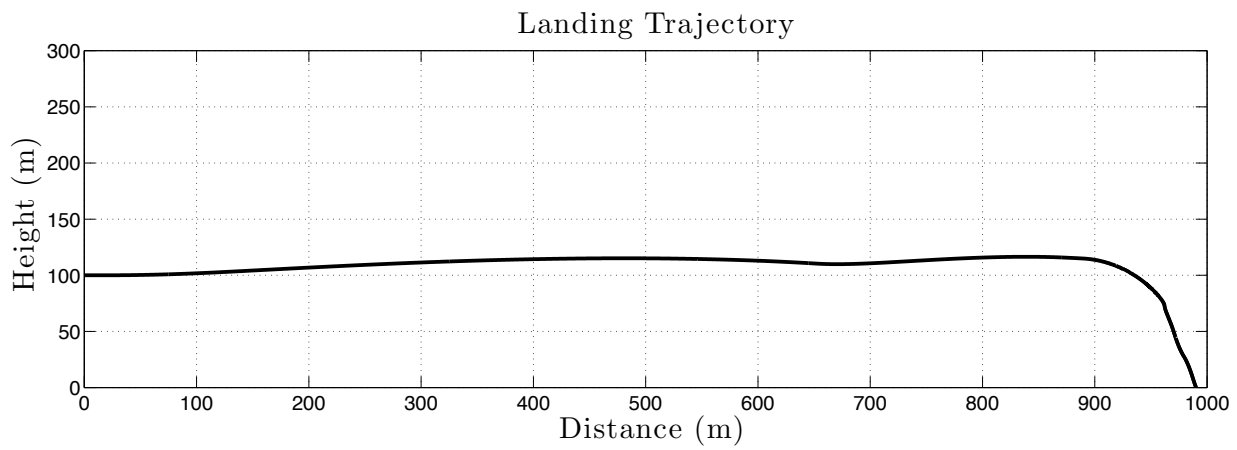
The transition from hover to forward flight and vice versa was simulated using a time marching method, the equations of motion and the aerodynamic characteristics of the aircraft. An example of the simulation of the trajectory of the aircraft can be seen in Figure 9.1.

The take-off model starts with the aircraft at hover at a height of 100 m. The propulsion fans then start to rotate and the aircraft begins to transition. The fans complete their rotation within 10 seconds. The aircraft starts to gain forward speed and lose altitude as can be seen in Figure 9.1, reaching its lowest altitude of 95 m approximately 130 m from the starting position. At 200 m forward of the starting position the aircraft reaches 1.1 times its stall speed, and begins to reduce power to the lift fan and pitch fan. At 240 m the aircraft reaches 1.3 times the stall speed, the lift fan and pitch fan are off and the aircraft begins to retract its flaps. At 300 m the aircraft is accelerating to climb speed and begins to climb at a 10° angle of attack.

The landing model starts with the aircraft at a height of 100 m with a forward speed of 1.3 times stall speed with flaps fully down. The propulsion fans then start to rotate, the lift fan and pitch fan are initiated and the aircraft begins to transition. The propulsion fans are completely retracted to the hover position within 3 seconds. The aircraft is flared at an angle of 5° and begins to lose forward speed and gain a little altitude as can be seen in Figure 9.1. At 400 m forward of the starting position the aircraft reaches stall speed, and the flap deflection is increased to 50° to increase the drag of the aircraft. As the aircraft reduces below 0.6 times stall speed the aircraft is flared to 15° until the aircraft speed is significantly reduced. At 900 m forward of the starting point, the aircraft is at 0.15 times stall speed and begins to reduce power to descend. The aircraft descends at 2 ms^{-1} and lands approximately 1000 m from the starting position.



(a) Take-off Trajectory



(b) Landing Trajectory

Figure 9.1: VTOL transition performance of a 4-passenger PAV

Chapter 10

Optimisation

10.1 Overview

The aim of optimisation is to find the best solution for a given set of inputs or requirements. Multi-dimensional, non-linear problems such as the design of a PAV are complex and can have various solutions. However determining the global optimum solution is difficult, requiring a global optimiser algorithm.

The most suitable optimisation technique would involve a multi-dimensional gradient and pattern search algorithm. This would involve searching for minima in a given design space (constrained problem). Suitable algorithms for this type of optimisation are the intrinsic MATLAB functions *fmincon* and *GlobalSearch*. The *fmincon* function retrieves a local minimum for a given multi-parameter start point using gradient search methods, while the *GlobalSearch* function retrieves minimum for a given design space using pattern search methods.

To develop an optimisation algorithm, the independent parameters that governed the design of the aircraft were identified (inputs) and a merit function was developed (output). The merit function *MF*, bundled the output parameters into an equation which the optimiser would try to minimise. The PAV design synthesis was run as a subroutine of a global optimisation algorithm headed by the MATLAB functions *fmincon* and *GlobalSearch*.

10.2 Global Optimiser

10.2.1 Interior-Point Algorithm

The intrinsic MATLAB function *fmincon* is a minimisation function that can utilise an interior-point algorithm to find a local solution minimum given a starting point and constraints. The interior-point method minimisation process solves a sequence of approximate minimisation problems. The original problem can be seen in Eqn 10.1 [16, 49]. For each $\mu > 0$ the problem is approximated as seen in Eqn 10.2 [16, 49]. As μ tends to zero then the approximated problem minimum f_μ tends to the actual minimum f .

$$\min_x f(x) \text{ subject to } h(x) = 0 \text{ and } g(x) \leq 0 \quad (10.1)$$

The logarithmic term added to approximate the problem is a barrier function. The barrier function restricts the function from violating the constraints.

$$\min_{x,s} f_\mu(x, s) = \min_{x,s} f(x) - \mu \sum_i \ln(s_i) \text{ subject to } h(x) = 0 \text{ and } g(x) + s = 0 \quad (10.2)$$

The *fmincon* interior-point algorithm attempts to find the local minimum point through a multi-variate Newton-Raphson method. This involves solving the Karush-Kuhn-Tucker (KKT) conditions Eqns 10.4, 10.5 & 10.6 [16, 49]. The KKT conditions are necessary for the solution to be optimal and are typical to the nature of the gradient being zero at a minimum. The KKT conditions use the Lagrangian function in Eqn 10.3 [16, 49].

$$L(x, \lambda) = f(x) + \sum \lambda_{g,i} g_i(x) + \sum \lambda_{h,i} h_i(x) \quad (10.3)$$

$$\nabla_x L(x, \lambda) = 0 \quad (10.4)$$

$$\lambda_{g,i} g_i(x) = 0 \quad \forall i \quad (10.5)$$

$$\begin{cases} g(x) \leq 0 \\ h(x) = 0 \\ \lambda_{g,i} \geq 0 \end{cases} \quad (10.6)$$

The multi-variate Newton-Raphson equation is developed from the Hessian of the Lagrangian of f_μ in Eqn 10.7 and the KKT conditions Eqns 10.4, 10.5 & 10.6. This produces the Eqn 10.8, where: J_g is the Jacobian of the constraint function g , J_h is the Jacobian of the constraint function h , S is diagonal of the matrix s , λ is the Lagrange multiplier vector associated with constraints g , Λ is the diagonal of the matrix λ , y is the Lagrange multiplier vector associated with h and e is a vector of ones the same size as g .

$$H = \nabla^2 f(x) + \sum_i \lambda_i \nabla^2 g_i(x) + \sum_j \lambda_j \nabla^2 h_j(x) \quad (10.7)$$

Solving Eqn 10.8 gives the gradient and thus the required step direction (Δ) of each variable required to reach a minimum point. The process is repeated until the minimum point is established (gradient is zero) [16, 49].

$$\begin{bmatrix} H & 0 & J_h^T & J_g^T \\ 0 & S\Lambda & 0 & -S \\ J_h & 0 & I & 0 \\ J_g & -S & 0 & I \end{bmatrix} \begin{bmatrix} \Delta x \\ \Delta s \\ -\Delta y \\ -\Delta \lambda \end{bmatrix} = \begin{bmatrix} \nabla f - J_h^T y - J_g^T y \\ S\lambda - \mu e \\ h \\ g + s \end{bmatrix} \quad (10.8)$$

The *fmincon* interior-point algorithm is setup in MATLAB by defining a set of input parameters x_0 (i.e. Wing Aspect Ratio, Fan Radii) that are part of a problem function (i.e. PAV Design Synthesis). The *fmincon* algorithm is constrained by user defined lower and upper bounds for the parameters. The algorithm is then given a start point for those parameters and can then be run. However the algorithm will only output a minimum solution that is closest to the user defined starting point. This does not guarantee a global solution, unless the problem is

very well defined and the correct starting point can be chosen. For complex non-linear problem functions the problem is not easily defined and thus a global optimiser is required.

10.2.2 Global Search Algorithm

Another intrinsic MATLAB function is the *GlobalSearch* function. This function utilises a multi-start heuristic approach to find a global minimum solution. The *GlobalSearch* function determines a given number of start points and uses the local solver *fmincon* to find local minima at each point, and storing the solutions most promising to be a global solution.

The *GlobalSearch* function operates in 2 stages. In the first stage, the *fmincon* function is run for a user defined start point with relevant input parameters (x_0). In the second stage the function uses a scatter-search mechanism to generate starting trial points. These starting trial points are analysed and any points that are unlikely to show improvement on best local minimum found initially are discarded. The best starting trial point found from the remaining starting trial points is then run using the *fmincon* function. If the *fmincon* function finds a minimum, it is stored in a solution vector. The process is then repeated until all the remaining starting trial points are rejected or explored [17, 49].

To setup the global optimiser, the independent input parameters of the PAV need to be identified. A merit function (*MF*) composed of output parameters also needs to be determined.

10.3 Input Parameters & Merit Function

Determining the input parameters that were independent variables that governing the variation of the PAV design, first required the identification of the dependent variables. The main input variables for the design synthesis can be seen in Table 10.1.

Since the design synthesis was initially developed to be run for a given number of passengers, N_{PAX} was kept constant during optimisation. However, the seating configuration would alter the shape of the cabin and thus that of the fuselage for a given number of passengers. Consequently $SEAT_I$ was set as an independent variable. The initial sizing MTOW guess $W_{0,I}$

had no consequence on the synthesis other than to provide a starting point for the initial sizing methodology in Chapter 3. The cruise altitude ALT_{cruise} is only used as an input to setup a specific flight configuration (personal aircraft or air taxi).

The input cruise speed and input range serve only as target markers for the synthesis. The actual range $Range_O$ and cruise speed/mach number M_{cruise_O} are outputted in the performance section of the synthesis. Consequently these variables were kept as dependent variables that remained constant input values during optimisation.

The remaining variables that were then considered were the independent variables that would be used in the optimisation process. The fan radii R_{PF}, R_{LF}, R_{fPF} define the shape of the aircraft and as a consequence its aerodynamics. The fan radii also defined the propulsion characteristics P_{total}, T, η_p , and as consequence influence the performance and fuel consumption rate of the aircraft. The input lift-to-drag (L/D)_{cruise_I} defines the optimum design point for the aerodynamics of the aircraft, by defining the fuel weight requirement from the Breguet range equation Eqn 9.1 used in the weight estimation section in Chapter 6. The input cruise lift-to-drag ratio defines the design point for the fans by defining the thrust required at cruise. This in turn influences the fan efficiency η_p and thus the performance of the aircraft.

The aerodynamics of the aircraft are also governed by the wing geometry. The wing aerofoil choices and taper ratio were kept constant to minimise pitching moments and produce an elliptic lift distribution respectively. Subsequently the only remaining wing geometrical variables were the aspect ratio AR and quarter-chord sweep $\Lambda_{c/4}$. The aspect ratio has an inversely proportional effect on induced drag and wing weight, the higher the aspect ratio the lower the induced drag, and the higher the wing weight and vice versa. For this reason the optimum aspect ratio for each aircraft flight configuration is different. Sweep is not normally required for subsonic flight because the aerofoil critical Mach numbers are not encountered. Sweep also decreases the lift produced by the wing. However low sweep $\pm 15^\circ$ has negligible effect on the lift, but can alter the stability of the aircraft by moving the aerodynamic centre of the wing. This can reduce trim drag and also alter the weight of the aircraft.

N_{PAX}	Number of passengers
W_{0_I}	Initial Sizing MTOW guess
V_{cruise_I}	Input cruise speed
ALT_{cruise}	Cruise altitude
$Range_I$	Input Range
R_{PF}	Radius of propulsion fans
R_{LF}	Radius of lift fan
R_{fPF}	Radius of pitch fan
AR	Wing aspect ratio
$\Lambda_{c/4}$	Wing sweep at quarter chord
$(L/D)_{cruise_I}$	Input cruise lift-to-drag ratio
$SEAT_I$	Seating configuration

Table 10.1: Design synthesis input variables

The dependent input variables were used to setup a given flight configuration. The independent variables were used to form the foundations of the optimisation algorithm. The lower and upper bounds of the variables were setup according to their maximum and minimum sizes of applicability for the aircraft, Table 10.2.

$R_{PF} \in \mathbb{R}$	$0.30 \leq R_{PF} \leq 0.60 \text{ m}$
$R_{LF} \in \mathbb{R}$	$0.40 \leq R_{LF} \leq 1.30 \text{ m}$
$R_{fPF} \in \mathbb{R}$	$0.30 \leq R_{fPF} \leq 0.70 \text{ m}$
$AR \in \mathbb{R}$	$7 \leq AR \leq 11$
$\Lambda_{c/4} \in \mathbb{R}$	$-15 \leq \Lambda_{c/4} \leq 15^\circ$
$(L/D)_{cruise_I} \in \mathbb{R}$	$8 \leq (L/D)_{cruise_I} \leq 20$
$SEAT_I \in \mathbb{Z}$	$1 \leq SEAT_I \leq n$

Table 10.2: Optimiser input variables ranges

With the optimisation variables set, a merit function was developed for the optimisation algorithm to minimise. Typical optimisation of transport aircraft involves trying to maximise the cruise Mach number, lift-to-drag ratio and minimise the weight for a given range Eqn 10.9.

$$MF = \left[\frac{M_{cruise} (L/D)_{cruise}}{W_0} \right] \quad (10.9)$$

However the PAV design synthesis input and output range varied depending on the configuration and other input variable values. Thus a range violation factor Δ_{Range} calculated in Eqn 10.11 was added to the Merit function to keep the range constant. Unlike typical syntheses, the aircraft MTOW weight was allowed to vary through the design process. Thus the empty weight was chosen to be minimised instead of the MTOW. As a result of minimising the empty weight, the power required for VTOL is also reduced.

Since the *fmincon* function locates minima, the merit function was made negative Eqn 10.10. To make the range violation factor significant to the merit function but not over power it, the terms were multiplied by constants to change them to similar orders of magnitude.

$$MF = -1000 \left[\frac{M_{cruise_O} (L/D)_{cruise_O}}{W_e} \right] + 3 \cdot \Delta_{Range} \quad (10.10)$$

$$\Delta_{Range} = \frac{|Range_O - Range_I|}{Range_I} \quad (10.11)$$

A sample of the optimisation process can be seen in Figure 10.1. The merit value calculated from Eqn 10.10 can be seen to vary with the components that quantify it. In Figure 10.1 after almost 800 iterations it can be seen that one global solution was located around the 600th iteration with a merit function of approximately -4.35.

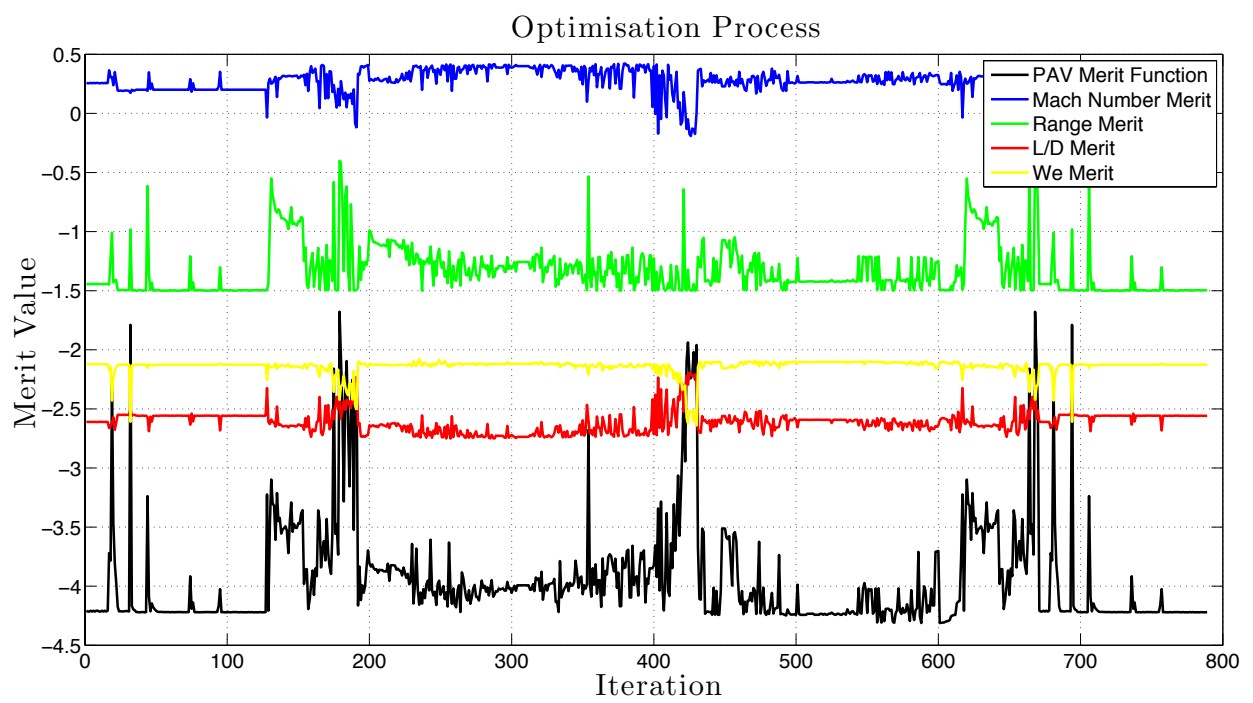


Figure 10.1: Evolution of optimisation process

Chapter 11

Full Methodology Implementation

11.1 Operations of Design Methodology & Optimisation

All the methodologies from the previous sections were gathered into a complete PAV design synthesis as can be seen in Figure 11.1. The individual design methodologies were ordered in a rational sequence to create a completed conceptual design for a PAV given specific mission requirements.

The inputs in Table 10.1 that define the mission requirements and performance targets are inputted into the synthesis. The first stage involves several modules such as initial sizing, propulsion and lift. This stage is a check to see if the aircraft is feasible given the input variables, especially fan sizes. If the aircraft is feasible, the aircraft aerodynamic surfaces are sized and a more detailed weight estimation is performed in the second stage. The weight estimation is then coupled with the systems packaging, balance, longitudinal static stability and VLM modules. Consequently the shape, weight, balance, lift and propulsion of the aircraft are all finalised, after which the drag module determines the drag of the aircraft using the 3D models to calculate surface areas and other relevant factors.

The third and final stage involves analysing a more or less finalised design and fine tuning some of the aerodynamic and stability characteristics. The dimensions and specifications of the aerodynamic surfaces are passed on to the VLM module, which then provides the stability

derivatives to the static lateral and dynamic stability modules. The canard-wing interaction is analysed in the VLM module and the wing twist is then iteratively adjusted to ensure the wing lift distribution is elliptical. Finally, using all the data from the previous modules, the completed PAV design has its performance and VTOL transition capability analysed.

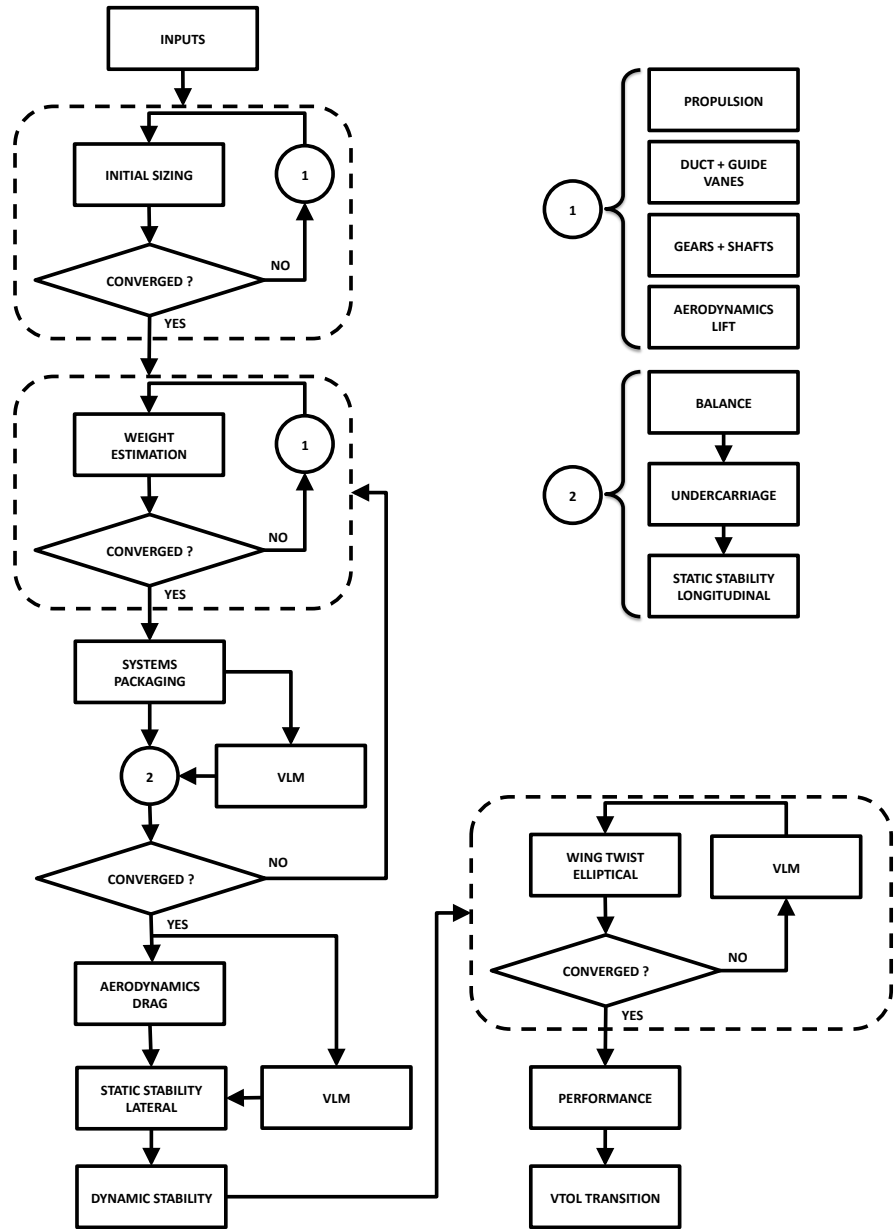


Figure 11.1: PAV design synthesis flow chart

The PAV design synthesis used with the optimiser was truncated, streamlined and reduced to essential modules to speed up the optimisation process, thus reducing a single iteration time from approximately 10 minutes to 66 seconds using a standard PC with a 2.93 GHz

Intel Core 2 Duo processor and 4GB of RAM. The fine tuning section containing the lateral stability, dynamic stability and elliptical twist modules relied heavily on the VLM module. These modules increased the synthesis run time significantly. Since these modules did not significantly alter the finalised design or affect its performance, it was decided that they could be bypassed and run after the optimisation process. Thus the performance of the aircraft was analysed directly after the drag module. The complete optimisation process can be seen in Figure 11.2.

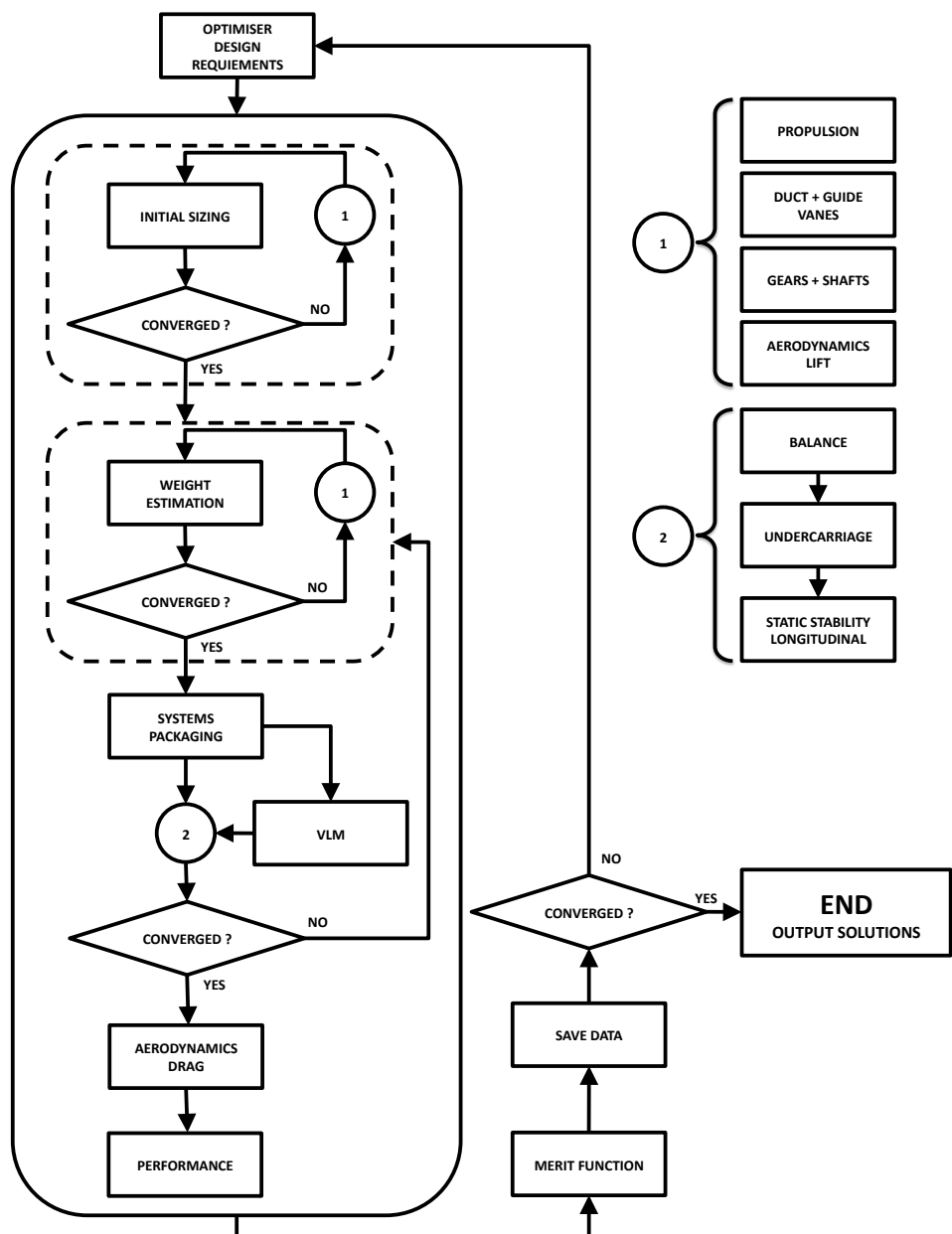


Figure 11.2: PAV Optimisation flow chart

It was found that the optimisation process could take several days if necessary. However sufficiently converged solutions could be observed within 12 to 24 hours of starting the process. The convergence tolerance of the optimiser was 1×10^{-6} , and so beyond 24 hours the improvement rate of the solution decreased significantly implying that the solution was near optimum.

11.2 Computer Program Architecture

11.2.1 MATLAB

MATLAB was chosen as the main programming platform for this project for several reasons. The notation is simple and powerful and the implementation fast. It is also very good at producing data visualisation, both graphical as well as 2D/3D models of the aircraft. There are a large number of intrinsic toolboxes (modules) that can be utilised and even tailored to specific requirements. MATLAB also provides a programming platform that could be linked with external modules such as VLM programs (*Tornado*).

The 2D/3D models were used to check if the packaging of the aircraft was correct, Chapter 5. The 2D plots also provided easy visualisation of data as can be seen in Figure 4.9. The 3D models were also used to determine the the wetted area (S_{wet}) of the aircraft, thus assisting in the calculation of profile drag C_{D0} , Chapter 7.

The *Statistics* and *Global Optimisation* toolboxes were utilised for linear regression and global optimisation respectively. The linear regression proved useful in producing various methods as that for propulsion, Chapter 4.

11.2.2 VLM - *Tornado*

Tornado, the VLM code is written in MATLAB and consequently could be modified to run along the main design synthesis. This allowed the synthesis to obtain the required data for the aerodynamic (Chapter 7) and stability analysis (Chapter 8) of the aircraft.

Firstly, the *Tornado* folders were placed inside the synthesis directory. Then the relevant folder directories for aircraft, aerofoils, flight conditions and saved data were mapped and stored. That allowed for the calling of the correct scripts from the correct directory at any point during the synthesis.

The scripts **Wing_Geometry.m** and **Aircraft_Geometry.m** were developed to form *Tornado* geometry input files. *Tornado* geometry input files were studied and replicated using data from the synthesis. **Wing_Geometry.m** provided the dimensions of just the wing for stall tests. While **Aircraft_Geometry.m** provided the dimensions of all the lifting surfaces (i.e. the whole aircraft). The script **State.m** was developed to form a *Tornado* flight conditions input file. The geometry of the PAV and CG positions from the synthesis were incorporated into these input files.

Tornado normally functions with a user-friendly interface, prompting user inputs to initiate the solver or save data. To integrate the VLM solver into the synthesis smoothly, this interface had to be bypassed. The relevant scripts **fLattice_setup2.m** and **solverloop5.m**, used to setup the VLM lattice and initiate the solver respectively were located. Copies of these scripts, named **PAV_fLattice_setup2.m** and **PAV_solverloop5.m**, were edited and embedded in the *Tornado* directory. The new scripts could take input data directly from the synthesis, initiate the solver and then store the data in the relevant folder without interruption.

11.2.3 CFD - *ANSYS*

The CFD package *ANSYS* provides several codes that are tailored specifically for rotating machinery design and simulation. The package contains turbomachinery specific geometry and mesh-generation tools *Bladegen* and *Turbogrid*. These models are then run with the CFD solver *CFX*, which provides a full suite of interface models to capture the interaction between rotating and stationary components. *CFX* also provides inbuilt post-processing tools that can be utilised to output relevant results rapidly and accurately.

11.2.4 Programming Assessments

The complete design synthesis in Figure 11.1 contains a number of methodologies, of which some contain internal performance and modelling subroutines (e.g. propulsion). Other methodologies also contain subroutines that use interpolation techniques on 3D coordinate files for complex 3D shaping (e.g. systems packaging). These internal subroutines either require several iterations to converge, or are time consuming due to their detailed approach. Despite the use of current computer technologies the execution time for the full synthesis could reach up to 10 minutes.

Although 10 minutes is a reasonable run time for the synthesis of a single PAV design, this is amplified significantly when coupled with a global optimiser. With an optimisation run taking 1500-2000 iterations for a solution to converge, the run time can be up to 14 days. Thus the computation time for the design synthesis needed to be reduced. Consequently the synthesis was studied carefully and the sections that were most computationally time expensive were identified.

The sections that were the most computationally time expensive relied on heavy use of the VLM module. These were modules such as the lateral stability, dynamic stability and elliptical twist modules. It was decided that since these modules did not significantly alter the finalised design or effect its performance, that they could bypassed during the optimisation process. The optimised model could then be fine tuned using these modules after the optimisation process.

The second most computationally time expensive sections showed excessive iterations to converge on a local solution (e.g. propulsion), due to too many iterative loops or very high tolerance convergence values. To reduce the complexity of propulsion methodology and thus the number of iterations to obtain an optimum solution, two variables (N_b, σ) were removed from the methodology. These variables were reassigned as user defined constants in the main program. As the number of blades and solidity were the least sensitive values to variation of thrust and power, they would not affect the optimum fan solution significantly and thus could be varied manually. This reduced the propulsion module runtime from 30 seconds to 0.7 seconds.

Very high tolerance convergence values were used throughout the synthesis, particularly in the weight estimation, system packaging and static stability modules. Though reducing the tolerance of these values would decrease the number of iterations to convergence, it would also result in solutions of a lower accuracy. Therefore a compromise between accuracy and speed was required. It was decided that the weight tolerance would be increased to $\pm 0.1 \text{ kg}$ and the location of the aerodynamic surfaces tolerance to $\pm 0.01 \text{ m}$.

Another computationally time expensive section was identified in the the interpolation techniques used on 3D coordinate files for complex 3D shaping in the systems packaging module. To produce a complex 3D shape, an object is broken down into multiple cross sections that are blended into each other. The shape definition of each cross section used either conic sections or 3D interpolation from coordinate files. Although increasing the number of cross sections provides a more accurate shape, the 3D shaping techniques used become more computationally time expensive. Therefore a compromise between accuracy and speed was again required. It was decided that the number of fuselage sections would be reduced to 100 and the number sections of other components (wing, tail, boom) would be reduced to 100-300.

For the synthesis to operate with the optimiser, it was required to be robust. This involved careful purging of any synthesis bugs that could either crash the process or increase its run time significantly. The design synthesis was tested with as many input variable variations as possible to determine the boundaries and bugs of the methodologies. These bugs were purged and safeguards were installed in the relevant modules. This allowed to synthesis to output a merit function $MF = 1$ in case any module failed or could not produce results. One such example can be found in the propulsion module. As there is a maximum thrust attainable for a given radius, a solution is not always available. Consequently the synthesis exits the module and returns an error message “**Resize fan**” and a merit function $MF = 1$.

Through careful study of the implemented design methodologies (modules), the design synthesis was streamlined and made robust for optimisation. This resulted in a synthesis run time reduction from 10 minutes to 66 seconds and as a consequence, reduced the maximum

optimisation run time from 14 days to 36 hours, an 89% time reduction.

Chapter 12

Case Study

12.1 Synthesis and Optimisation of a 4-Passenger PAV

A case study was performed to provide an example of the design synthesis and optimisation of a PAV. The mission profile Figure 3.4 designed in Chapter 3 was used to determine the configuration optimisation point. Since the PAV would spent most of its time in cruise, the factors involved in the cruise segment are what determined the configuration of the aircraft. Compiling data on various personal aircraft, it was found that they operate mainly around and below an altitude $\sim 3000\text{ m}$ and carry an average of 4-passengers. The average cruise speed was found to be $325 - 370\text{ km/h}$ and maximum range up to 1850 km . Hence, as a case study, a 4-passenger PAV with a cruise altitude of 3000 m , cruise speed of 370 km/h ($M_{cruise_I} = 0.314$) and a range of 1852 km was designed and optimised.

A summary of the optimisation process can be seen in Tables 12.1 & 12.2 and Figure 12.1. The mid-point iteration is a selected single sample point to illustrate the evolution of the aircraft during the optimisation process. In reality there were approximately 2000 iterations (variations), of which the final solution was the one with the lowest merit function.

Table 12.1 shows the input variables the optimiser used to vary the design of the PAV. It can be seen that the propulsion fans were reduced to their minimum size to maximise their efficiency for cruise and to also reduce the bulkiness of the design. It is interesting to note that

the optimiser reduced the size of the lift fan and increased the size of the pitch fan, almost matching the radii of both. This infers that the optimum solution that minimises weight and power is one where the thrust for VTOL is distributed to two main fans instead of only one (lift fan).

Main Input Variables of 4-passenger PAV					
Baseline (x_0)		Mid-point Iteration (x_i)		Final Solution (x_f)	
R_{PF}	0.35 m	R_{PF}	0.35 m	R_{PF}	0.31 m
R_{LF}	0.60 m	R_{LF}	0.50 m	R_{LF}	0.51 m
R_{fPF}	0.40 m	R_{fPF}	0.35 m	R_{fPF}	0.44 m
AR	10.00	AR	8.04	AR	7.73
$\Lambda_{c/4}$	0.00°	$\Lambda_{c/4}$	-10.11°	$\Lambda_{c/4}$	0.99°
$(L/D)_{cruise_I}$	13.00	$(L/D)_{cruise_I}$	15.06	$(L/D)_{cruise_I}$	14.77
Seating Configuration	1 – 3	Seating Configuration	2 – 2	Seating Configuration	2 – 2

Table 12.1: Input variables of a 4-passenger PAV optimisation

Tables 12.1 & 12.2 and Figure 12.1 show that the seating configuration affects the weight of the aircraft and thus the power required for VTOL. This is due to the fuselage width being larger in the baseline with 3 passenger in the rear row. The aspect ratio of the wing decreases significantly from baseline $AR = 10.0$ to $AR = 7.7$, thus reducing the structural weight of the aircraft. Although reducing the aspect ratio increases induced drag, the lift-to-drag ratio at cruise remains almost constant, settling on a value of $(L/D)_{cruise_O} = 13.97$ for the final solution.

Main Output Variables of 4-passenger PAV					
Baseline (x_0)		Mid-point Iteration (x_i)		Final Solution (x_f)	
M_{cruise_O}	0.298	M_{cruise_O}	0.284	M_{cruise_O}	0.295
$Range_O$	2000 km	$Range_O$	1852 km	$Range_O$	1851 km
W_e	1177 kg	W_e	1055 kg	W_e	1030 kg
W_0	1839 kg	W_0	1662 kg	W_0	1636 kg
$(L/D)_{cruise_O}$	13.371	$(L/D)_{cruise_O}$	14.506	$(L/D)_{cruise_O}$	13.972
P_{total}	1013 kW	P_{total}	980 kW	P_{total}	926 kW

Table 12.2: Output variables of a 4-passenger PAV optimisation

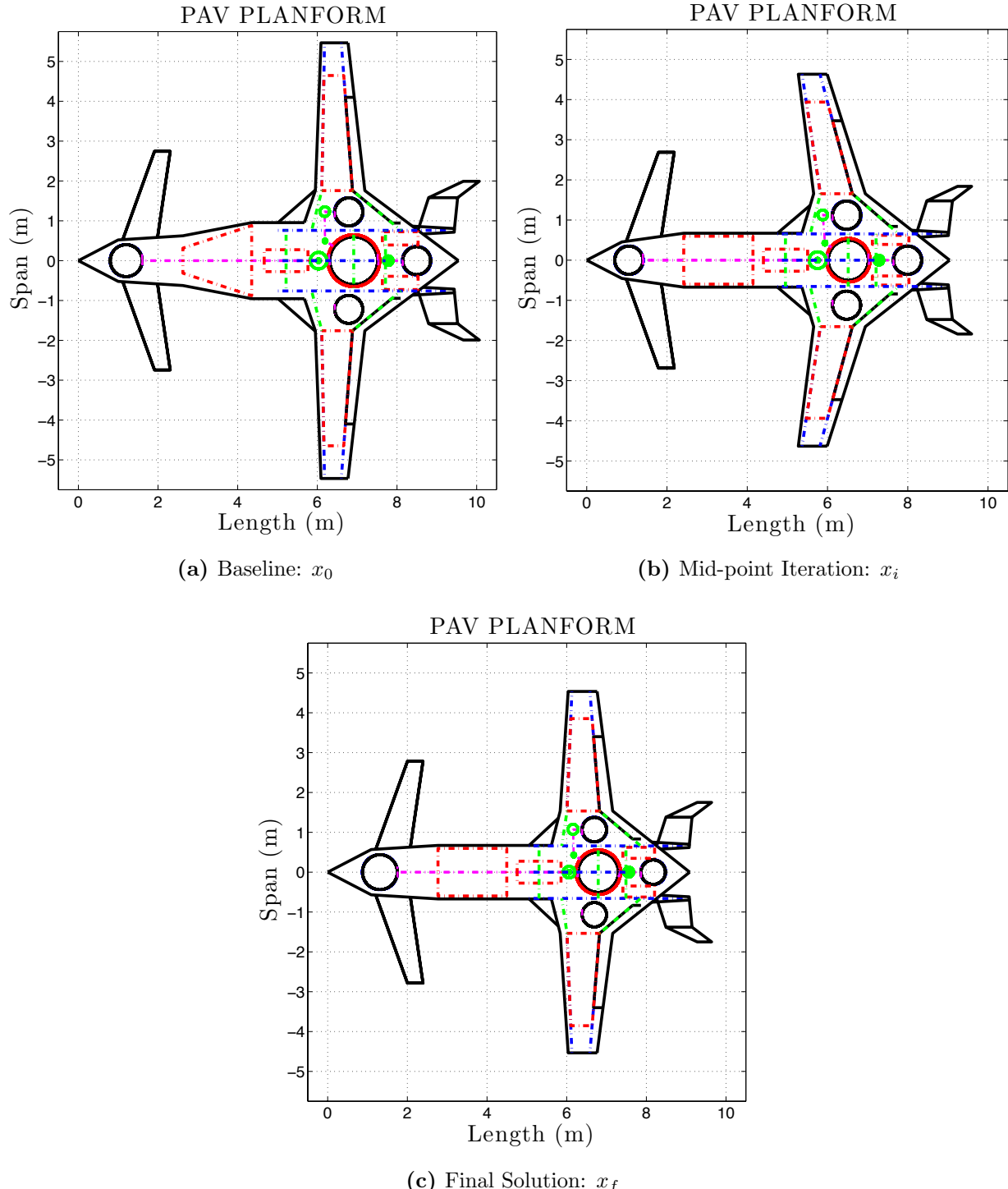


Figure 12.1: Optimisation of a 4-passenger PAV

As the power for VTOL is directly proportional to the MTOW, it can be seen that the power decreases as the MTOW weight is minimised. The reduction in weight can be seen in the variation of shape of the PAV in Figure 12.1. The wing aspect ratio decreases, the fuselage width decreases and the propulsion fans and lift fan reduce in size. This results in a more compact, and thus a structurally lighter design. The lift-to-drag ratio remains reasonable and thus the fuel required for cruise decreases.

Although the sweep does not have any aerodynamic benefit due to the subsonic cruise conditions, it sometimes helped in the balance or the stability of the aircraft. Ultimately it can be seen that the added structural weight penalty for swept wings overrode any stability or balance benefits in the final solution.

The 3D model of the optimised PAV can be seen in Figures 12.2 - 12.7, where Figure 12.7 shows the packaging of the aircraft.

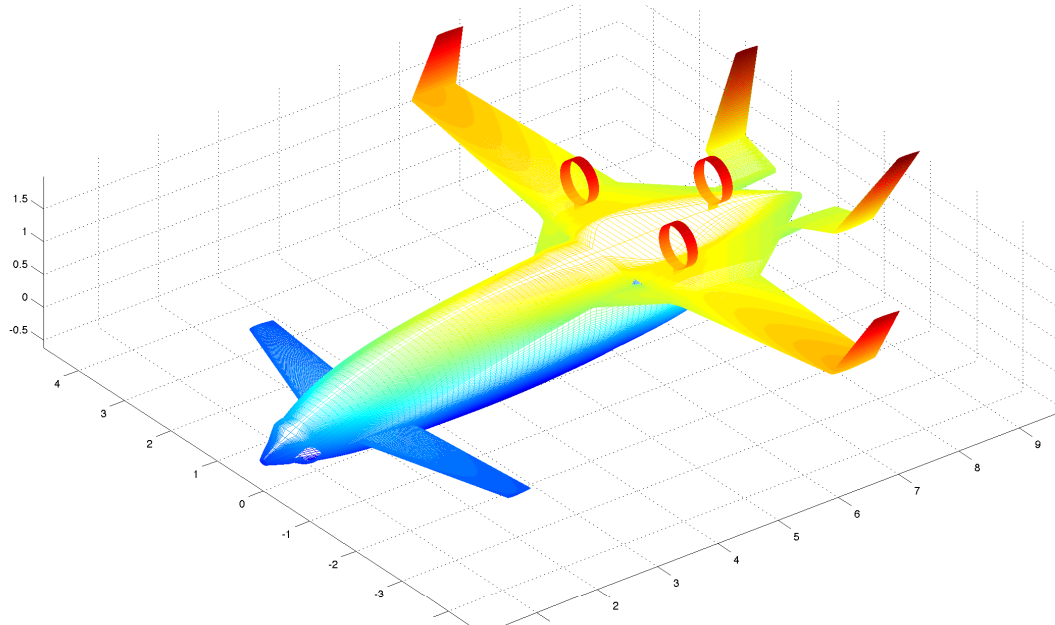


Figure 12.2: MATLAB generated 3D model of 4-passenger PAV - *Left front view, forward flight configuration*

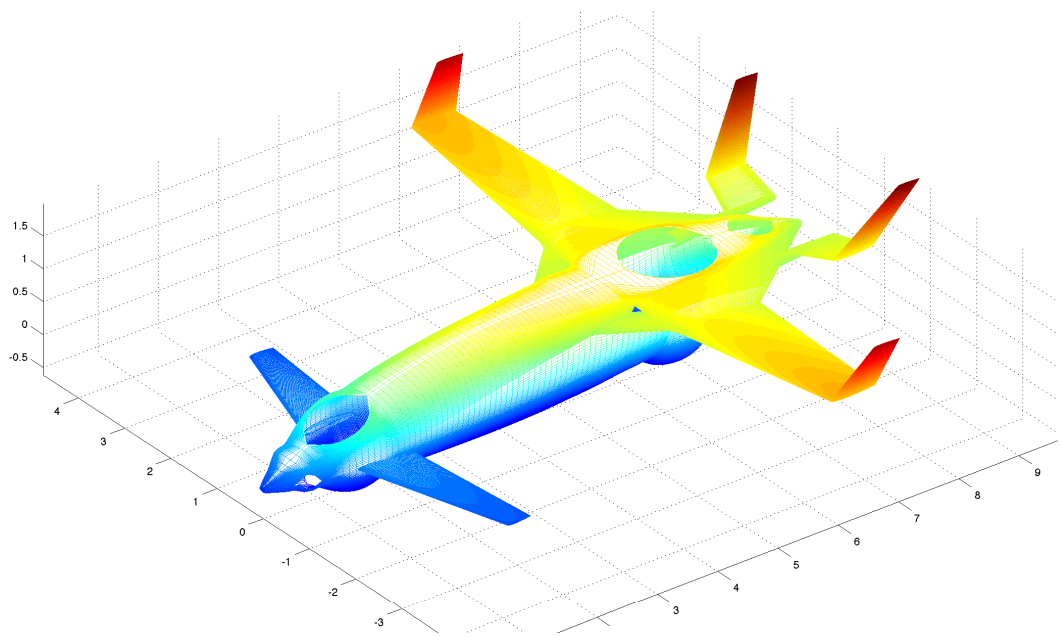


Figure 12.3: MATLAB generated 3D model of 4-passenger PAV - *Left front view, hover configuration*

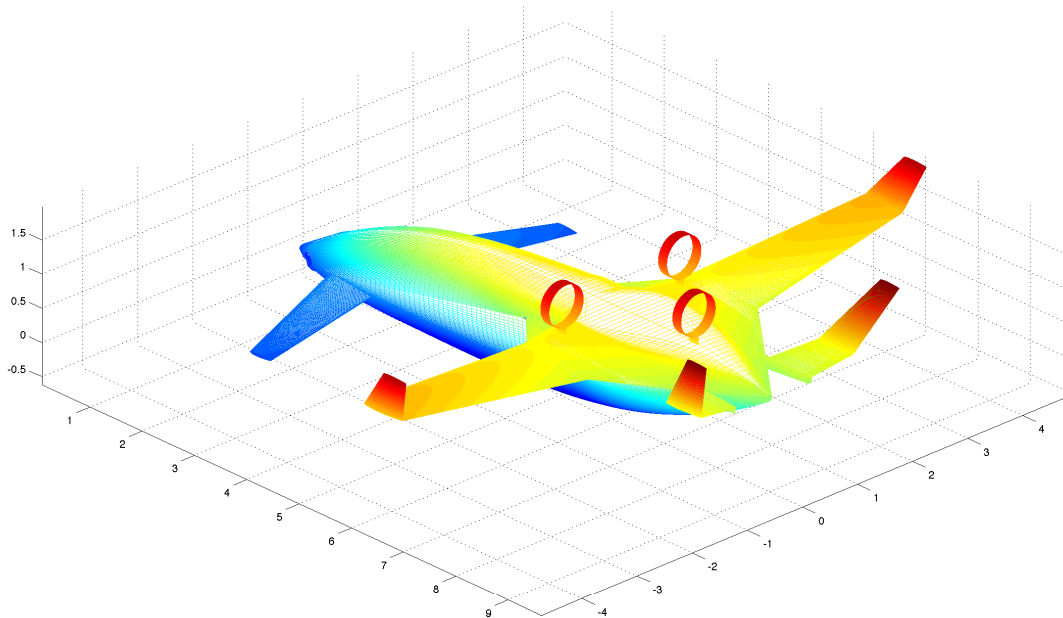


Figure 12.4: MATLAB generated 3D model of 4-passenger PAV - *Left rear view, forward flight configuration*

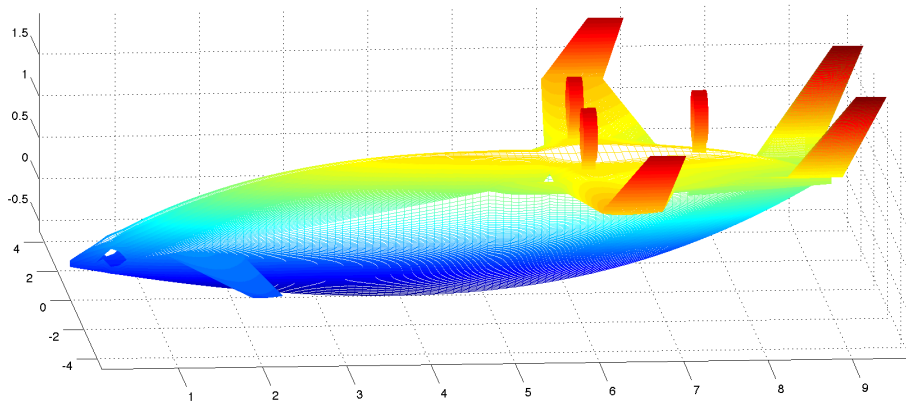


Figure 12.5: MATLAB generated 3D model of 4-passenger PAV - *Side view, forward flight configuration*

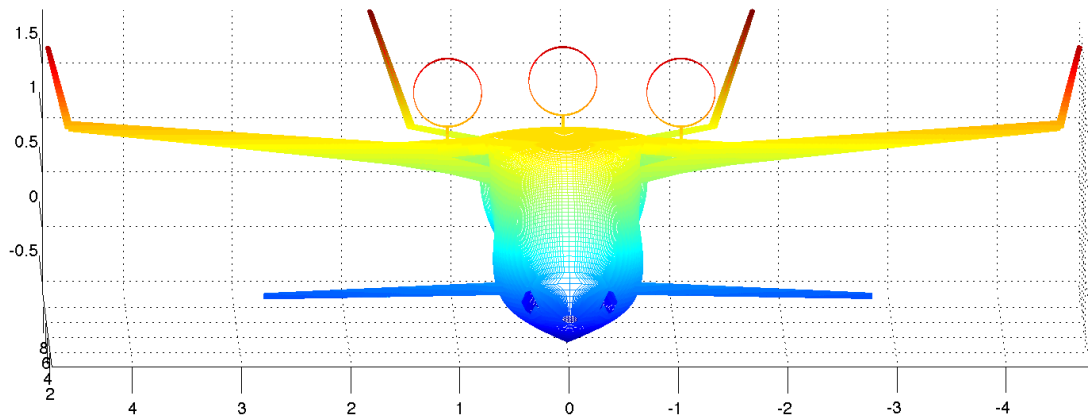


Figure 12.6: MATLAB generated 3D model of 4-passenger PAV - *Front view, forward flight configuration*

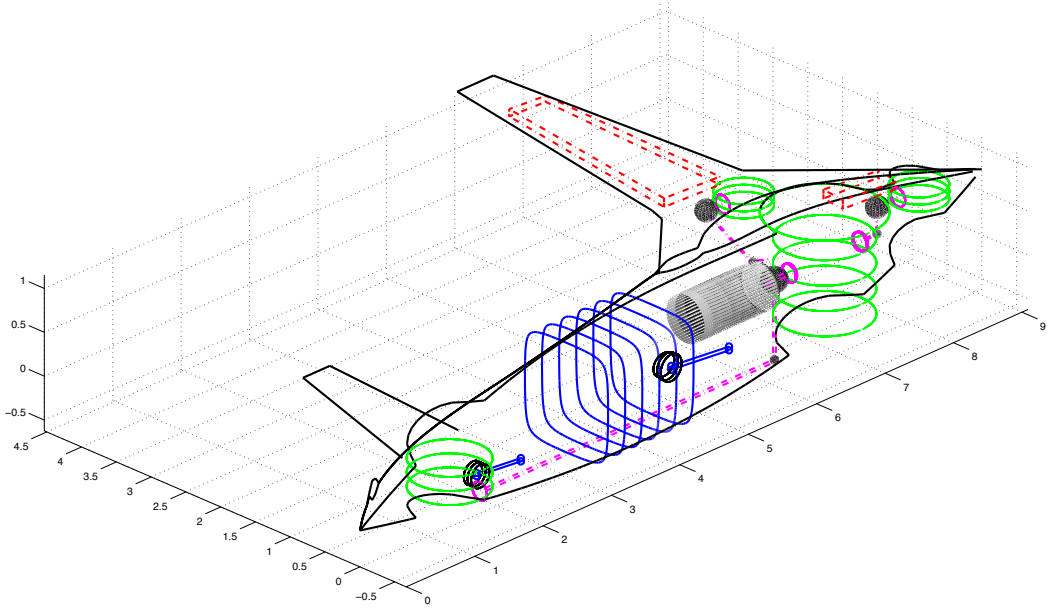


Figure 12.7: MATLAB generated 3D model of 4-passenger PAV - *Systems Packaging*

12.1.1 Dimensions & Weights

A detailed view of the dimensions, component weights, aerodynamics, stability and performance of the aircraft can be seen in the next sections. The dimensions of the optimised PAV and its component weight break down are shown in Tables 12.3 & 12.4.

The weight of the aircraft is similar to that of a 4-passenger light aircraft (single piston or twin piston) with a similar range. The added structural weight of the fans and their components are negated by incorporating composites into the design. The design is longer than a typical personal aircraft, due to the extra space needed to package the fans. However this is not a significant increase and the rest of the dimensions seem to be within expected limits.

Dimensions of an Optimised 4-passenger PAV					
b_w	9.07 m	AR_{vtail}	2.00	Γ_{htail}	10°
b_{can}	4.42 m	$\Lambda_{c/4}$	0.99°	Γ_{vtail}	20°
b_{htail}	1.44 m	$\Lambda_{c/4 \ can}$	17°	\bar{c}	1.23 m
b_{vtail}	1.02 m	$\Lambda_{c/4 \ htail}$	15°	L_{PAV}	9.64 m
S_{ref}	10.64 m ²	$\Lambda_{c/4 \ vtail}$	35°	H_{PAV}	3.14 m
S_{can}	2.79 m ²	λ_w	0.55	L_{cabin}	1.73 m
S_{htail}	1.06 m ²	λ_{can}	0.55	H_{cabin}	1.25 m
S_{vtail}	0.52 m ²	λ_{htail}	0.80	W_{cabin}	1.19 m
AR	7.73	λ_{vtail}	0.55	$\sigma_{PF}, \sigma_{fPF}, \sigma_{LF}$	0.55
AR_{can}	7.00	Γ_w	5°	$N_{b_{PF}}, N_{b_{fPF}}$	12
AR_{htail}	1.95	Γ_{can}	-3°	$N_{b_{LF}}$	16

Table 12.3: Dimensions of the optimised 4-passenger PAV

Component Weights of an optimised 4-passenger PAV					
Wing	109.7 kg	Engine	192.0 kg	Avionics	76.1 kg
Canard	14.1 kg	Engine Installation	56.0 kg	Hydraulics	9.8 kg
Horizontal Tail	1.9 kg	Fuel System	20.3 kg	Surface Controls	27.5 kg
Fins	1.3 kg	Fans	13.2 kg	Electrical System	87.7 kg
Fuselage	128.2 kg	Guide Vanes	3.3 kg	Pressurisation + A/C	47.8 kg
Ducts	15.9 kg	Hubs	5.7 kg	Furnishing	58.1 kg
Undercarriage	78.6 kg	Shafts	12.3 kg	Auxiliary	2.0 kg
Booms	7.8 kg	Gears	44.0 kg	Paint	4.9 kg
Winglet	0.1 kg	Gear Casing	14.4 kg		
Structure Total	355.0 kg	Propulsion Total	361.1 kg	Equipment Total	313.8 kg
Fuel			245.9 kg		
Passengers + Payload			360.0 kg		
Empty Weight			1029.9 kg		
MTOW			1635.8 kg		

Table 12.4: Component Weights of the optimised 4-passenger PAV

12.1.2 Aerodynamics, Stability & Balance

The aerodynamic quantities of the PAV can be seen in Table 12.5. All the lift curve slopes were calculated at cruise conditions except $C_{L_{\alpha_w \text{ flap}}}$, which was calculated at stall conditions. The drag values were all calculated at cruise conditions except for $C_{D_{0 \text{ flap}}}$ and $C_{D_{0 \text{ landing}}}$. The sum of the trim drag and induced drag $C_{D_{i \text{ trim}}}$ during cruise was minimal due to the minor deflection needed to trim the aircraft. The canard and horizontal tail were deflected equally, giving $\delta_{can_{cruise}} = 0.51^\circ$ and $\delta_{htail_{cruise}} = -0.51^\circ$.

Aerodynamic Values of an Optimised 4-passenger PAV			
i_w	1.84°	$C_{D_{trim}}$	0.0031
$C_{L_{\alpha_{PAV}}}$	6.92 rad^{-1}	$C_{D_{cruise}}$	0.0222
$C_{L_{\alpha_w}}$	5.22 rad^{-1}	$C_{D_{0 \text{ flap}}}$	0.0294
$C_{L_{\alpha_{can}}}$	4.88 rad^{-1}	$C_{D_{0 \text{ landing}}}$	0.0547
$C_{L_{\alpha_{htail}}}$	2.55 rad^{-1}	$C_{L_{max \text{ clean}}}$	1.529
$C_{L_{\alpha_w \text{ flap}}}$	5.53 rad^{-1}	$C_{L_{max \text{ flap}}}$	2.488
C_{D_0}	0.0191	$C_{L_{cruise}}$	0.293

Table 12.5: Aerodynamic values of the optimised 4-passenger PAV

The stability and balance values are displayed in Table 12.6. Due to packaging constraints, the balance of the aircraft showed a large variation of static margin from 3.9% at the most aft position to 33.6% at the most forward position. This is due to the cabin and passengers being towards the front of the aircraft because of the fan packaging at the rear.

Designing the aircraft to have a $C_{L_{max \text{ flap}}} = 2.5$ with flaps maximised the wing loading and thus decreased the wing area. To attain the $C_{L_{max \text{ flap}}} = 2.5$ at MTOW to achieve the stall requirement, both the flaps and flaperons were fully deflected to $\delta_{f_{MTOW}} = 35^\circ$ and $\delta_{flaperon_{MTOW}} = 20^\circ$ respectively. Although the flaperons were deflected to large angles, to allow for roll control they were designed to have a maximum deflection of 30° . The aircraft satisfies also the FAR23 sideslip stability yaw and roll requirements as can be seen in Table 12.6 ($C_{n_\beta} > 0$ and $C_{l_\beta} < 0$). The 20° deflection is to satisfy the stall speed requirements incase of engine failure. The aircraft is not multi-engined and thus would not suffer asymmetrical loads

given an engine failure minimising the need for large flaperon deflections for roll control. With an engine failure the approach speed of the aircraft will also be much higher than the stall speed allowing for sufficient roll control.

Although the lower wing area gave the PAV a reasonable $(L/D)_{cruise_O} = 13.97$ for cruise, the aircraft showed a tendency to pitch down during landing. To minimise the pitch down moments, the flaps were not deflected fully $\delta_{f_{FWD\ CG}} = 12^\circ$ when landing with the forward most CG configuration. Consequently the trim required was reduced significantly, with the canardvator and elevator deflected equally and in opposite directions at $\delta_{can_{cruise}} = 18.38^\circ$ and $\delta_{htail_{cruise}} = -18.38^\circ$. Satisfying the forward most CG trim and it being the worst case scenario, all other longitudinal static stability criteria were satisfied.

The lateral static stability of the aircraft was also satisfied. The lateral stability derivatives obtained from the VLM met the requirements, $C_{n_\beta} > 0$ and $C_{l_\beta} < 0$. The dynamic stability of the aircraft was also satisfied. Both longitudinal modes and both lateral modes were stable. The short period pitching oscillation mode is highly damped and has a time period of $T_{SPPO} = 1.740\ secs$. The short period pitching oscillation mode satisfies FAR23 requirements by damping to 1/600th amplitude (~ 0) within 2 cycles. The Dutch-roll is moderately damped and has a time period of $T_{DR} = 2.264\ secs$. The dutch-roll mode satisfies FAR23 requirements by damping to 1/10th amplitude within 7 cycles ($t_{1/10} = 11.99\ secs, 5.30\ cycles$).

Stability and Balance Values of an Optimised 4-passenger PAV					
$x_{CG_{MTOW}}$	5.11 m	SM_{AFT}	3.94 %	C_{l_β}	-0.0727
$z_{CG_{MTOW}}$	1.64 m	SM_{cruise}	11.65 %	ω_{PH}	$0.1348 \text{ rad s}^{-1}$
$x_{CG_{AFT}}$	5.22 m	$SM_{MTOW_{flaps}}$	14.28 %	ξ_{PH}	0.1041
$z_{CG_{AFT}}$	1.68 m	$SM_{FWD_{flaps}}$	33.62 %	ω_{SPPO}	$3.6117 \text{ rad s}^{-1}$
$x_{CG_{FWD}}$	4.87 m	$SM_{AFT_{flaps}}$	5.08 %	ξ_{SPPO}	0.5099
$z_{CG_{FWD}}$	1.56 m	$\delta_{f_{AFT\ CG}}$	10°	ω_{DR}	$2.7747 \text{ rad s}^{-1}$
$\delta_{can_{cruise}}$	0.51°	$\delta_{f_{MTOW}}$	35°	ξ_{DR}	0.0692
$\delta_{htail_{cruise}}$	-0.51°	$\delta_{f_{FWD\ CG}}$	12°	$L_\beta \cdot N_r - N_\beta \cdot L_r$	0.4589
$\delta_{can_{FWD\ CG}}$	18.38°	$\delta_{flaperon_{MTOW}}$	20°	$t_{1/2PH}$	49.4 secs
$\delta_{htail_{FWD\ CG}}$	-18.38°	C_{n_β}	0.0819	$t_{1/2SP}$	27.7 secs

Table 12.6: Stability and Balance values of the optimised 4-passenger PAV

12.1.3 Performance

The performance values of the PAV are displayed in Table 12.7 and Figures 12.8 & 12.18. The flight envelope of the aircraft bar its stall speed can bee seen in Figure 12.8. The maximum Mach number $M_{max} = 0.325$ at an altitude of 7620 m (25000 ft). The ceiling (service and absolute) of the aircraft is much higher than that of an aircraft with similar mission requirements, due to the excess power produced from VTOL design. As a consequence the aircraft must be flat rated after take-off to limit its ceiling to a specified altitude.

The excess power also translates into a high maximum climb rate of $V_{v_{max}} = 645 \text{ m/min}$ at sea level conditions. The thrust capability also gives the aircraft a high maximum turn rate of $\dot{\psi}_{max} = 26.88 \text{ deg/s}$. The conventional take-off and landing distances achieved by the PAV are also very low due to the excess power available. Generally the PAV design out performs CTOL aircraft with similar mission requirements.

The transition to and from forward flight and simulation of VTOL capability can be seen in Figure 12.18. For the take-off analysis, the aircraft begins to transition after reaching an altitude of 100 m off the ground with the flaps fully deflected; the aircraft then begins to gain

Performance Values of an Optimised 4-passenger PAV			
$Range_O$	1851 km	Absolute ceiling	10973 m
M_{cruise_O}	0.295	Time to climb to cruise altitude	9.51 mins
$(L/D)_{cruise_O}$	13.972	$\dot{\psi}_{max}$	26.88 deg/s
$V_{v_{max}}$	645 m/min @ S.L.	Loiter time	44.66 mins
$\gamma_{climb_{max}}$	11.53°	$s_{t/o}$	383 m
Service ceiling	10363 m	s_L	408 m

Table 12.7: Performance values of the optimised 4-passenger PAV

speed and lose altitude reaching a minimum height of 84 m from the ground at 150 m forward of the starting position. When the aircraft has gained sufficient forward speed ($1.3V_{stall}$), the lift fan and pitch fan are both stopped. This corresponds to the point 300 m forward of the starting position, shortly after which the flaps are retracted and the aircraft begins to climb.

For the landing analysis, the aircraft begins at an altitude of 100 m off the ground, a forward speed of $1.3V_{stall}$ and with the flaps fully deflected. At 100 m forward of the starting position the aircraft transitions the propulsion fans to hover and initiates the lift and pitch fan. At this same point, the flaps are deflected to $\delta_f = 50^\circ$ to act as speed brakes. The aircraft flares slightly and begins to slow. Once at a low enough speed the power is reduced and the PAV begins to lose altitude gently. Shortly before touching down the aircraft flares further and increases its thrust to touch down gently.

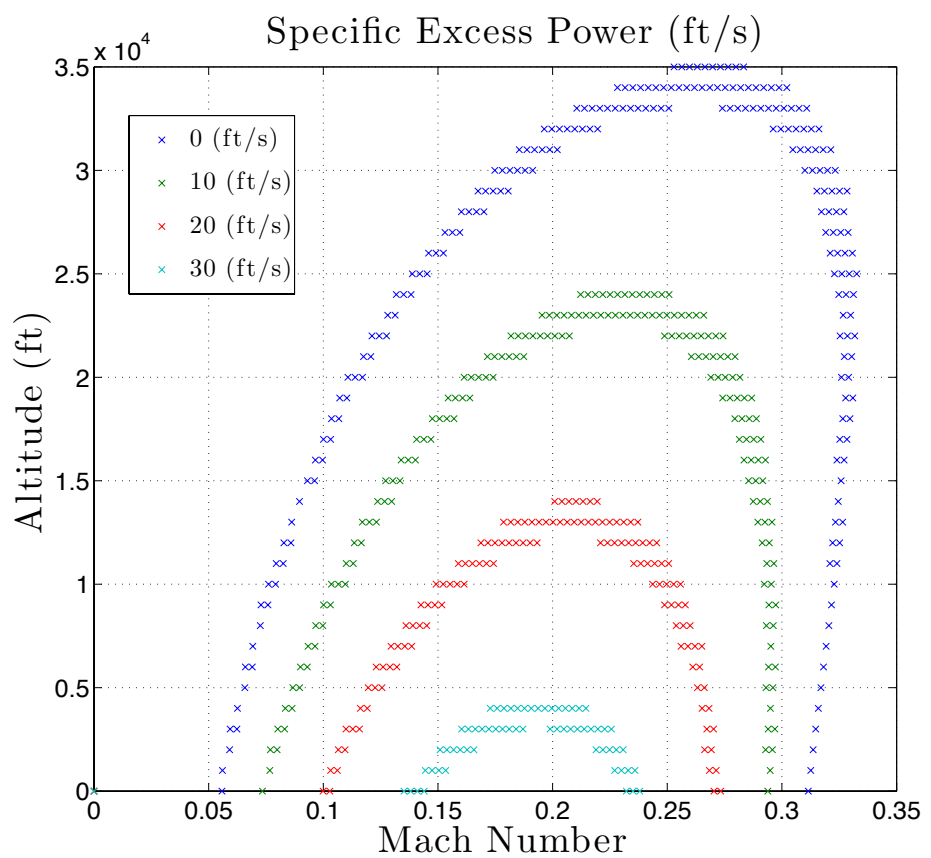
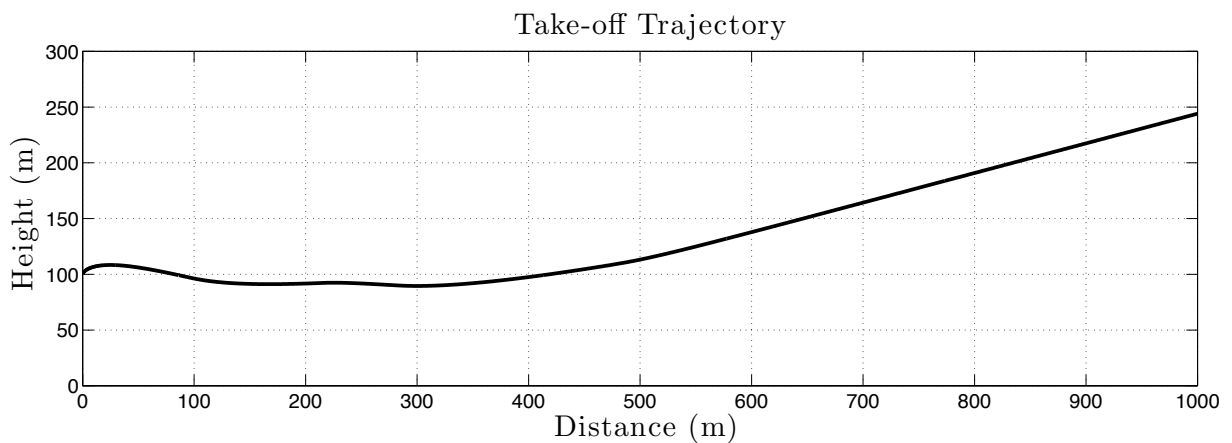
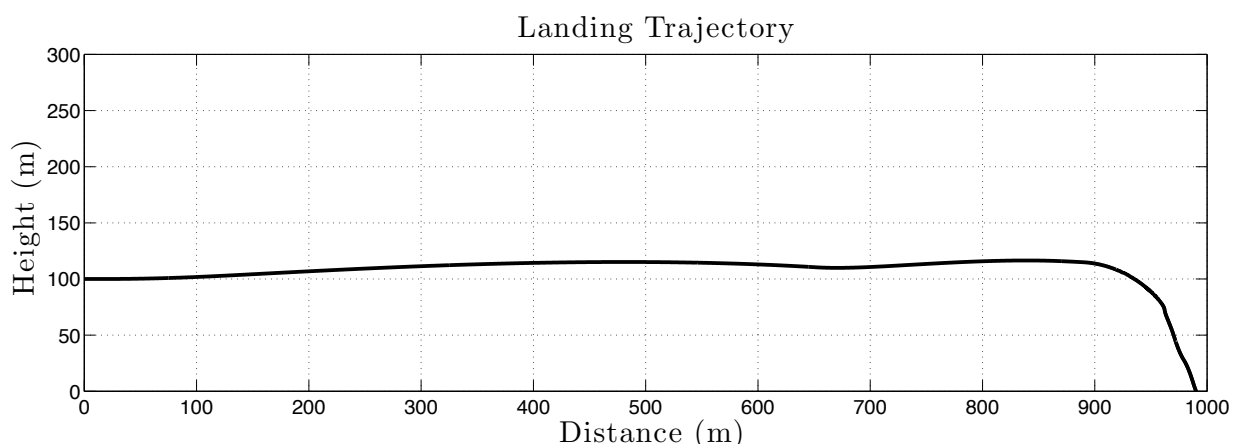


Figure 12.8: Specific Excess Power plot of the optimised 4-passenger PAV



(a) Take-off Trajectory



(b) Landing Trajectory

Figure 12.9: VTOL transition performance of the optimised 4-passenger PAV

12.2 Synthesis and Optimisation of a 6-Passenger PAV

A further case study was performed to illustrate the flexibility of the design synthesis. This case study focused on the design synthesis and optimisation of a 6-passenger air taxi. The mission profile was altered to reflect that of a typical 6-passenger turboprop air taxi, such as the Socata TBM 850. Compiling data on various single engine turboprop aircraft, it was found that they cruise at altitudes of $\sim 9450\text{ m}$, cruise at an average speed of $460 - 570\text{ km/h}$, and have maximum ranges of up to 2780 km . Hence, the following mission profile values were chosen: a cruise altitude of 9448 m , cruise speed of 555 km/h ($M_{cruise_I} = 0.511$) and a range of 2778 km .

A summary of the optimisation process can be seen in Tables 12.8 & 12.9 and Figure 12.10. The mid-point iteration is a selected single sample point to illustrate the evolution of the aircraft during the optimisation process.

Main Input Variables of 6-passenger PAV					
Baseline (x_0)		Mid-point Iteration (x_i)		Final Solution (x_f)	
R_{PF}	0.40 m	R_{PF}	0.36 m	R_{PF}	0.38 m
R_{LF}	0.80 m	R_{LF}	0.67 m	R_{LF}	0.65 m
R_{fPF}	0.40 m	R_{fPF}	0.49 m	R_{fPF}	0.50 m
AR	10.00	AR	10.04	AR	9.55
$\Lambda_{c/4}$	-15.00°	$\Lambda_{c/4}$	-4.62°	$\Lambda_{c/4}$	-2.23°
$(L/D)_{cruise_I}$	15.00	$(L/D)_{cruise_I}$	15.05	$(L/D)_{cruise_I}$	16.90
Seating Configuration	1 – 2 – 3	Seating Configuration	3 – 3	Seating Configuration	2 – 2 – 2

Table 12.8: Input variables of a 6-passenger PAV optimisation

Table 12.8 shows the input variables the optimiser used to vary the design of the PAV. In a similar fashion to the optimisation pattern of the 4-passenger PAV, it is interesting to note that the optimiser reduced the size of the lift fan and increased the size of the pitch fan. Again this infers the optimum solution that minimises weight and power is one where the thrust for VTOL is distributed to two main fans instead of only one.

The results in Table 12.8 also imply that a narrower longer, fuselage reduced weight and

proved to be a better solution. The aspect ratio of the wing decreases very slightly from baseline $AR = 10.0$ to $AR = 9.6$. A high aspect ratio reduces induced drag and consequently the lift-to-drag ratio at cruise is a reasonable value of $(L/D)_{cruise_O} = 15.89$ for the optimised solution. The sweep can again be seen to have a minimal effect on the optimisation process since no aerodynamic effect is gained from subsonic flight other than weight variation.

Main Output Variables of 6-passenger PAV					
Baseline (x_0)		Mid-point Iteration (x_i)		Final Solution (x_f)	
M_{cruise_O}	0.427	M_{cruise_O}	0.431	M_{cruise_O}	0.433
$Range_O$	2580 km	$Range_O$	2626 km	$Range_O$	2782 km
W_e	1858 kg	W_e	1681 kg	W_e	1628 kg
W_0	2953 kg	W_0	2744 kg	W_0	2632 kg
$(L/D)_{cruise_O}$	16.305	$(L/D)_{cruise_O}$	16.181	$(L/D)_{cruise_O}$	15.885
P_{total}	1832 kW	P_{total}	1690 kW	P_{total}	1562 kW

Table 12.9: Output variables of a 6-passenger PAV optimisation

Even though the air taxi design Figure 12.10 has 2 more passengers than the PAV designed previously Figure 12.1, it can be seen that a change in the mission profile has produced a vastly different aircraft. Cruising at a higher altitude and higher Mach number, the air taxi has a much higher aspect ratio. The reduction in induced drag now outweighs the penalty of increased structural weight. Even scaling up the 4-passenger PAV to accommodate 2 extra passengers, it can still be seen that the air taxi would generally be a heavier and more powerful aircraft.

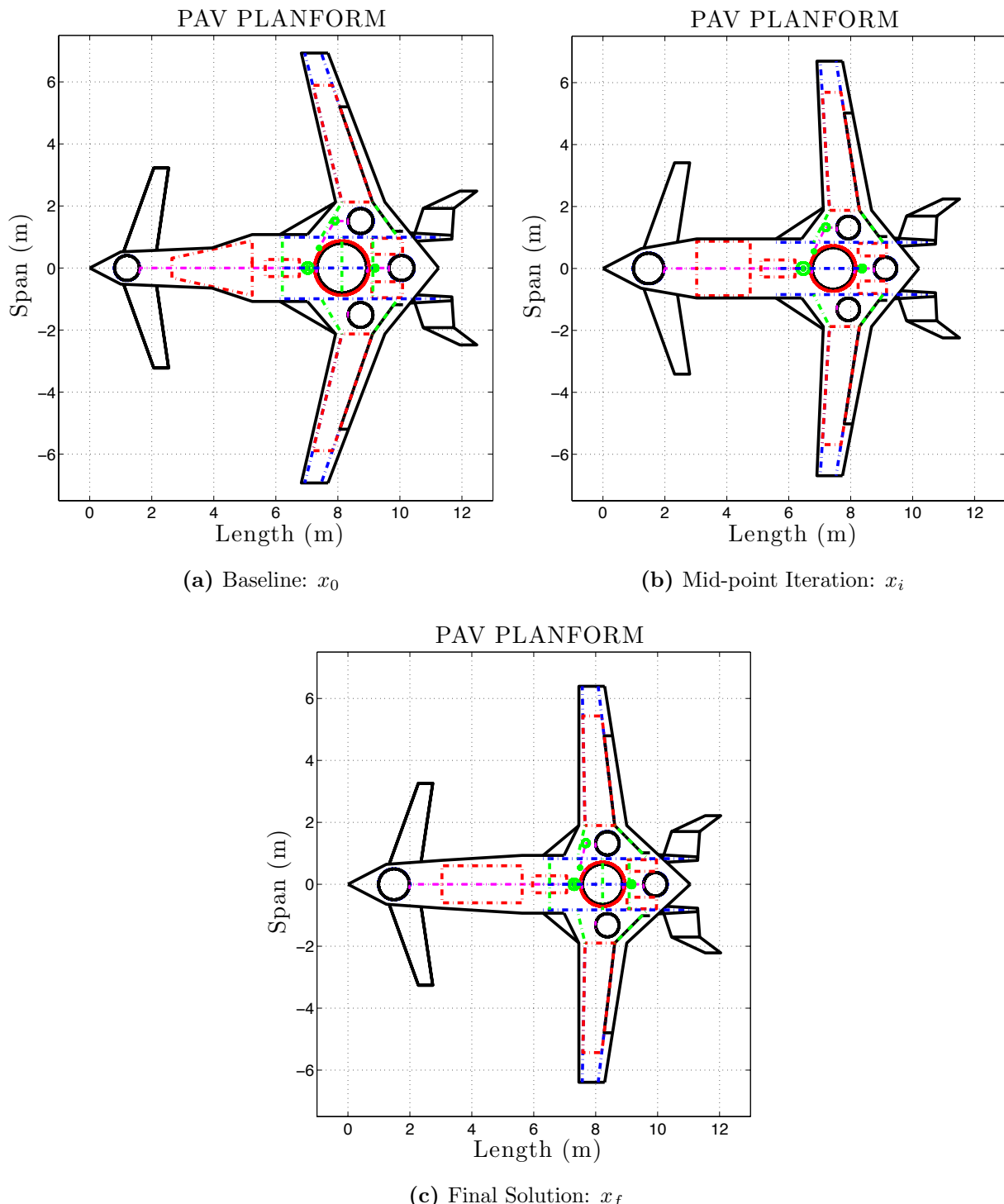


Figure 12.10: Optimisation of a 6-passenger PAV

The 3D model of the optimised PAV can be seen in Figures 12.11 - 12.16, where Figure 12.16 shows the packaging of the aircraft.

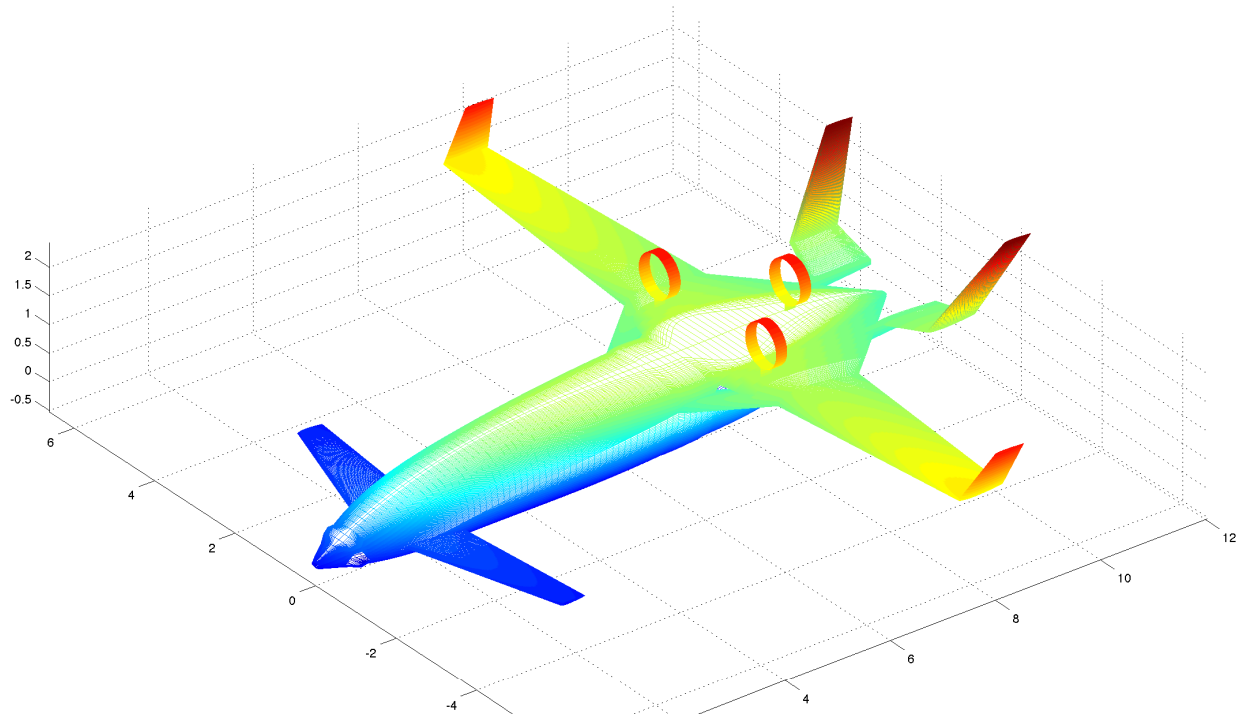


Figure 12.11: MATLAB generated 3D model of 6-passenger PAV - *Left front view, forward flight configuration*

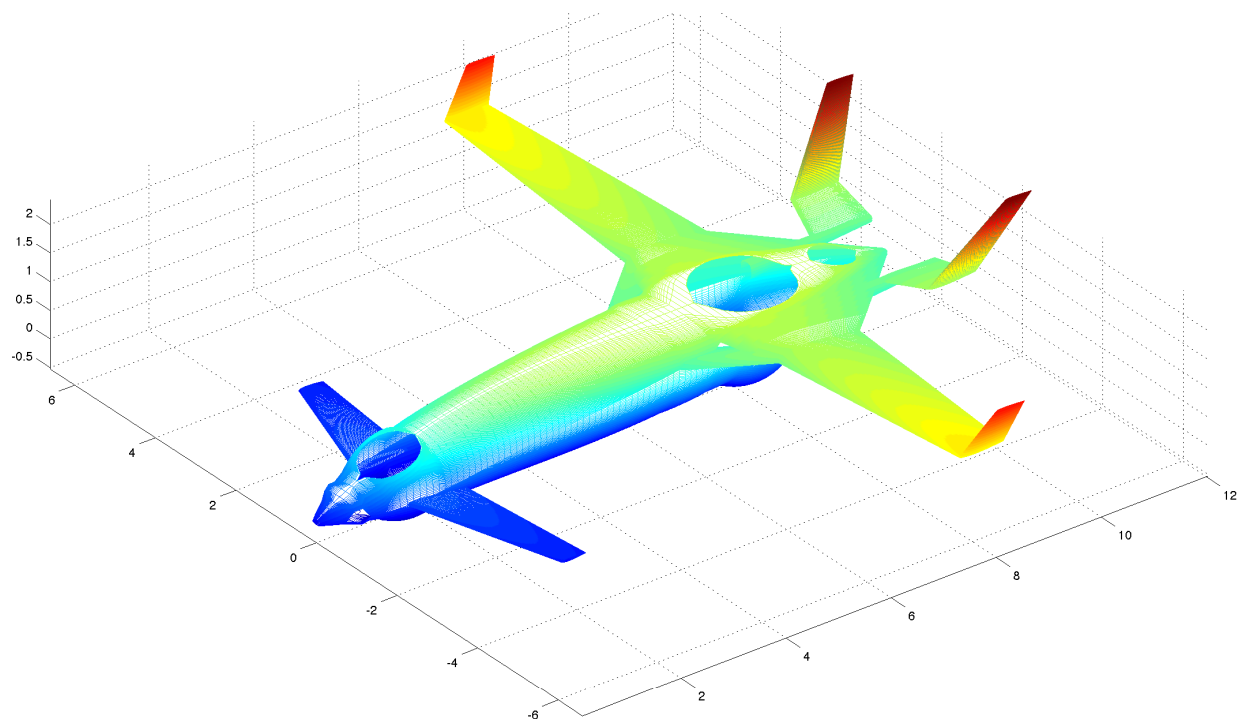


Figure 12.12: MATLAB generated 3D model of 6-passenger PAV - *Left front view, hover configuration*

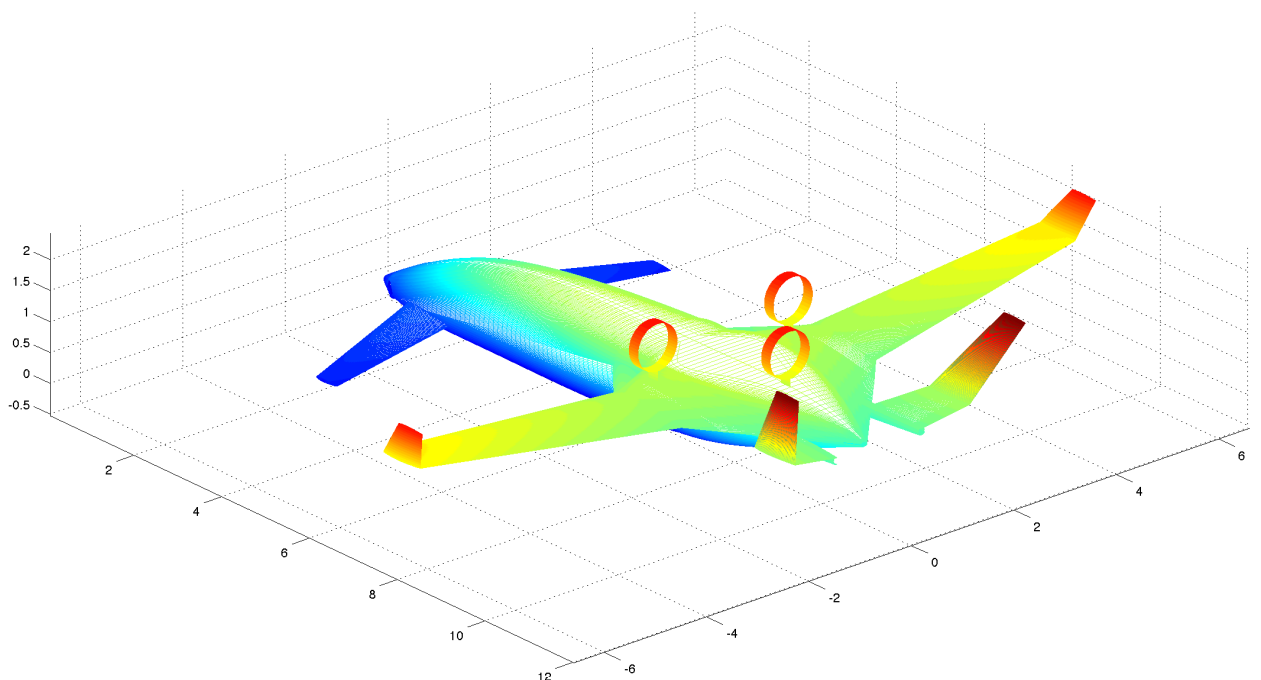


Figure 12.13: MATLAB generated 3D model of 6-passenger PAV - *Left rear view, forward flight configuration*

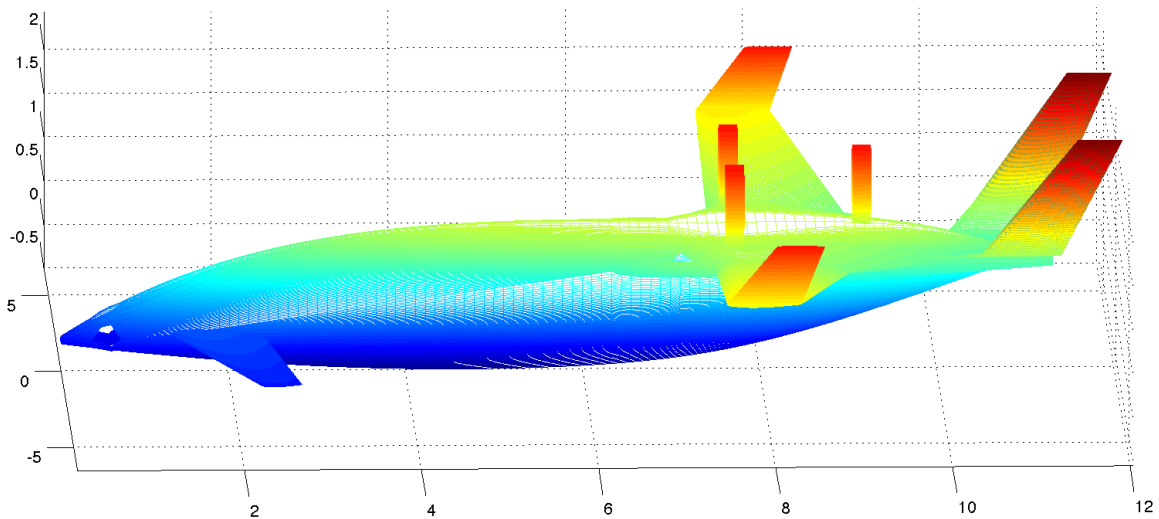


Figure 12.14: MATLAB generated 3D model of 6-passenger PAV - *Side view, forward flight configuration*

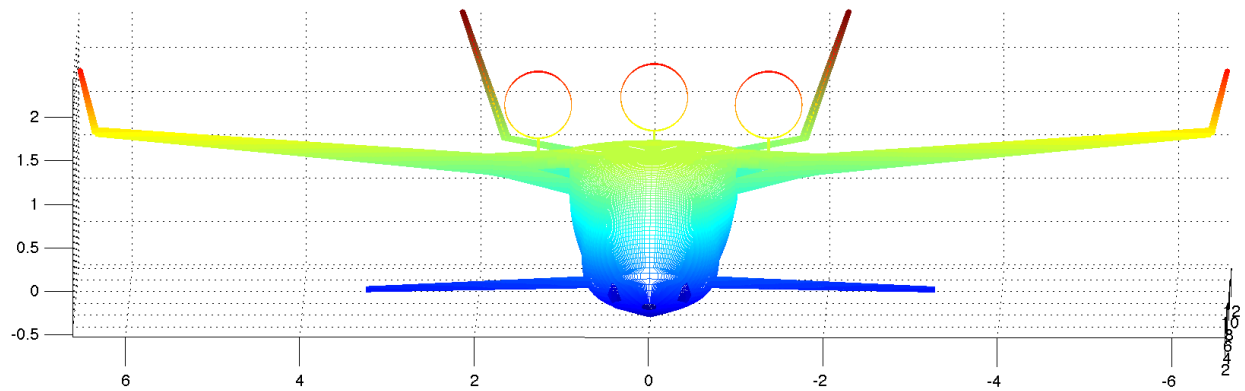


Figure 12.15: MATLAB generated 3D model of 6-passenger PAV - *Front view, forward flight configuration*

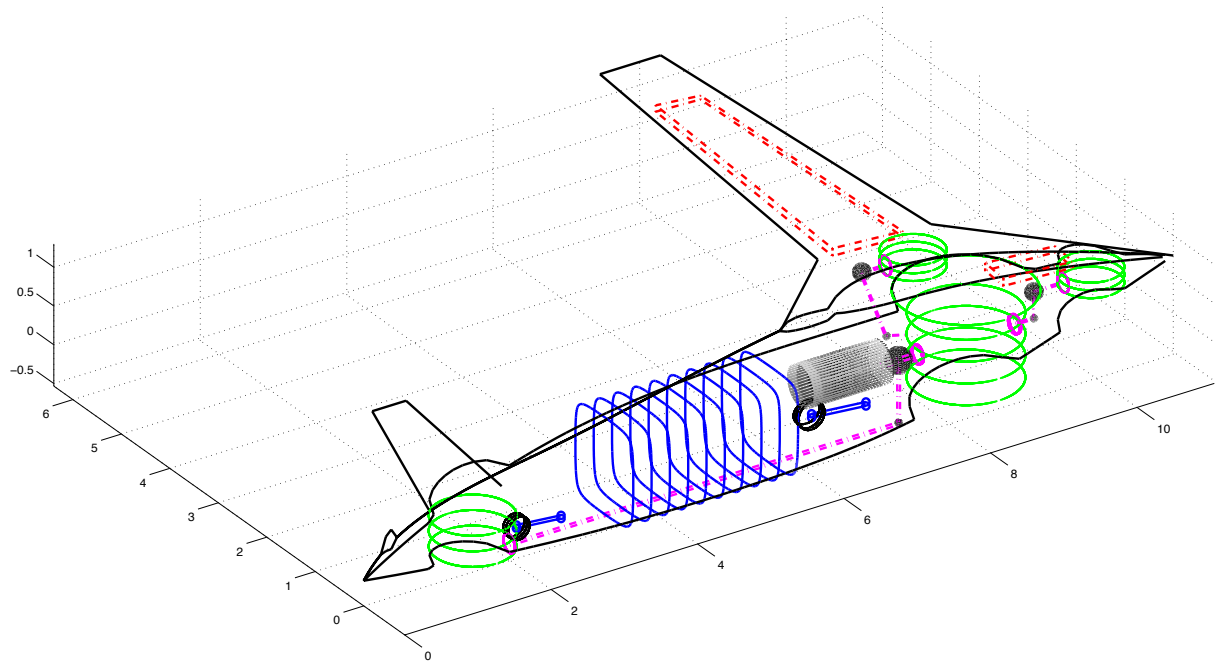


Figure 12.16: MATLAB generated 3D model of 6-passenger PAV - *Systems Packaging*

12.2.1 Dimensions & Weights

A detailed view of the dimensions, component weights, aerodynamics, stability and performance of the aircraft can be seen in the next sections. The dimensions of the optimised air taxi and its component weight breakdown are shown in Tables 12.10 & 12.11.

The weight of the aircraft was lower than that of 6-passenger air taxies with equivalent mission requirements, even with the added structural weight of the fans and their components the composite design reduces the weight. The design is longer than that of 6-passenger air taxies with equivalent mission requirements due to the extra space needed to package the fans. However this increase in length is not significant. The rest of the dimensions seem to be within expected limits.

Dimensions of an Optimised 6-passenger PAV					
b_w	12.79 m	AR_{vtail}	2.00	Γ_{htail}	10°
b_{can}	5.22 m	$\Lambda_{c/4}$	-2.233°	Γ_{vtail}	20°
b_{htail}	1.76 m	$\Lambda_{c/4 \ can}$	17°	\bar{c}	1.40 m
b_{vtail}	1.41 m	$\Lambda_{c/4 \ htail}$	15°	L_{PAV}	12.04 m
S_{ref}	17.12 m ²	$\Lambda_{c/4 \ vtail}$	35°	H_{PAV}	3.51 m
S_{can}	3.90 m ²	λ_w	0.55	L_{cabin}	2.59 m
S_{htail}	1.79 m ²	λ_{can}	0.55	H_{cabin}	1.25 m
S_{vtail}	0.99 m ²	λ_{htail}	0.80	W_{cabin}	1.19 m
AR	9.550	λ_{vtail}	0.55	$\sigma_{PF}, \sigma_{fPF}, \sigma_{LF}$	0.55
AR_{can}	7.00	Γ_w	5°	$N_{b_{PF}}, N_{b_{fPF}}$	12
AR_{htail}	1.72	Γ_{can}	-3°	$N_{b_{LF}}$	16

Table 12.10: Dimensions of the optimised 6-passenger PAV

Component Weights of an optimised 6-passenger PAV					
Wing	262.6 kg	Engine	233.5 kg	Avionics	76.1 kg
Canard	36.5 kg	Engine Installation	91.6 kg	Hydraulics	15.8 kg
Horizontal Tail	5.5 kg	Fuel System	32.2 kg	Surface Controls	44.2 kg
Fins	4.4 kg	Fans	26.0 kg	Electrical System	93.1 kg
Fuselage	257.1 kg	Guide Vanes	7.6 kg	Pressurisation + A/C	83.2 kg
Ducts	22.1 kg	Hubs	65.1 kg	Furnishing	87.1 kg
Undercarriage	109.7 kg	Shafts	11.0 kg	Auxiliary	2.0 kg
Booms	13.9 kg	Gears	18.0 kg	Paint	7.9 kg
Winglet	0.3 kg	Gear Casing	21.8 kg		
Structure Total	712.0 kg	Propulsion Total	506.6 kg	Equipment Total	409.4 kg
Fuel			464.4 kg		
Passengers + Payload			540.0 kg		
Empty Weight			1628.0 kg		
MTOW			2632.4 kg		

Table 12.11: Component Weights of the optimised 6-passenger PAV

12.2.2 Aerodynamics, Stability & Balance

The aerodynamic quantities of the PAV can be seen in Table 12.12. All the lift curve slopes were calculated at cruise conditions except $C_{L_{\alpha_w \text{ flap}}}$, which was calculated at stall conditions. The drag values were all calculated at cruise conditions except for $C_{D_0 \text{ flap}}$ and $C_{D_0 \text{ landing}}$. The sum of the trim drag and induced drag $C_{D_{i \text{ trim}}}$ during cruise was minimal due to the minor deflection needed to trim the aircraft. The canard and horizontal tail were deflected equally, giving $\delta_{can \text{ cruise}} = 0.31^\circ$ and $\delta_{htail \text{ cruise}} = -0.31^\circ$.

Aerodynamic Values of an Optimised 6-passenger PAV			
i_w	1.47°	$C_{D_{\text{trim}}}$	0.0024
$C_{L_{\alpha_{PAV}}}$	7.18 rad^{-1}	$C_{D_{\text{cruise}}}$	0.0205
$C_{L_{\alpha_w}}$	5.68 rad^{-1}	$C_{D_0 \text{ flap}}$	0.0310
$C_{L_{\alpha_{can}}}$	4.85 rad^{-1}	$C_{D_0 \text{ landing}}$	0.0543
$C_{L_{\alpha_{htail}}}$	2.32 rad^{-1}	$C_{L_{\max \text{ clean}}}$	1.544
$C_{L_{\alpha_w \text{ flap}}}$	6.03 rad^{-1}	$C_{L_{\max \text{ flap}}}$	2.502
C_{D_0}	0.0181	$C_{L_{\text{cruise}}}$	0.263

Table 12.12: Aerodynamic values of the optimised 6-passenger PAV

The stability and balance values are displayed in Table 12.13. Due to packaging constraints, the balance of the aircraft showed a large variation of static margin from 3.1% at the most aft position to 45.2% at the most forward position. Increasing the size of the aircraft seems to increase the variation in static margin due to the heavier cabin being towards the front of the aircraft because of the fan packaging at the rear.

Designing the aircraft to have a $C_{L_{\max \text{ flap}}} = 2.5$ with flaps, maximised the wing loading and thus decreased the wing area. To attain the $C_{L_{\max \text{ flap}}} = 2.5$ at MTOW to achieve the stall requirement, the flaps were fully deflected $\delta_{f_{MTOW}} = 35^\circ$ and the flaperons were deflected to $\delta_{flaperon_{MTOW}} = 11.5^\circ$.

Although the lower wing area gave the PAV a reasonable $(L/D)_{\text{cruise}_O} = 15.89$ for cruise, the aircraft showed a tendency to pitch down during landing. To minimise the pitch down

moments, the flaps were not deflected fully, only to $\delta_{f_{FWD\ CG}} = 10^\circ$ when landing with the forward most CG configuration. Consequently the trim required was reduced to a manageable quantity with the canardvator and elevator deflected equally and in opposite directions to $\delta_{can_cruise} = 24.58^\circ$ and $\delta_{htail_cruise} = -24.58^\circ$. Satisfying the forward most CG trim and it being the worst case scenario, all other longitudinal static stability criteria were satisfied.

The lateral static stability of the aircraft was also satisfied. The lateral stability derivatives obtained from the VLM met the requirements, $C_{n_\beta} > 0$ and $C_{l_\beta} < 0$. The dynamic stability of the aircraft was also satisfied. Both longitudinal modes and both lateral modes were stable. The short period pitching oscillation mode is highly damped and has a time period of $T_{SPPO} = 1.208\ secs$. The short period pitching oscillation mode satisfies FAR23 requirements by damping to 1/865th amplitude (~ 0) within 2 cycles. The dutch-roll is moderately damped and has a time period of $T_{DR} = 1.649\ secs$. The dutch-roll mode satisfies FAR23 requirements by damping to 1/10th amplitude within 7 cycles ($t_{1/10} = 7.58\ secs$, 4.60 cycles).

Stability and Balance Values of an Optimised 6-passenger PAV					
$x_{CG_{MTOW}}$	6.56 m	SM_{AFT}	3.12 %	C_{l_β}	-0.0686
$z_{CG_{MTOW}}$	1.62 m	SM_{cruise}	17.18 %	ω_{PH}	$0.0898\ rad\ s^{-1}$
$x_{CG_{AFT}}$	6.75 m	$SM_{MTOW\ flaps}$	21.13 %	ξ_{PH}	0.1051
$z_{CG_{AFT}}$	1.66 m	$SM_{FWD\ flaps}$	45.22 %	ω_{SPPO}	$5.2020\ rad\ s^{-1}$
$x_{CG_{FWD}}$	6.22 m	$SM_{AFT\ flaps}$	7.70 %	ξ_{SPPO}	0.5382
$z_{CG_{FWD}}$	1.53 m	$\delta_{f_{AFT\ CG}}$	15°	ω_{DR}	$3.8110\ rad\ s^{-1}$
δ_{can_cruise}	0.31°	$\delta_{f_{MTOW}}$	35°	ξ_{DR}	0.0797
δ_{htail_cruise}	-0.31°	$\delta_{f_{FWD\ CG}}$	10°	$L_\beta \cdot N_r - N_\beta \cdot L_r$	1.8654
$\delta_{can_{FWD\ CG}}$	24.58°	$\delta_{flaperon_{MTOW}}$	11.5°	$t_{1/2_{PH}}$	73.42 secs
$\delta_{htail_{FWD\ CG}}$	-24.58°	C_{n_β}	0.0907	$t_{1/2_{SP}}$	12.97 secs

Table 12.13: Stability and Balance values of the optimised 6-passenger PAV

12.2.3 Performance

The performance values of the PAV are displayed in Table 12.14 and Figures 12.17 & 12.18. The flight envelope of the aircraft bar its stall speed can bee seen in Figure 12.17. The maximum Mach number $M_{max} = 0.52$ at an altitude of 10668 m (35000 ft). The ceiling (service and absolute) of the aircraft is much higher than that of an aircraft with similar mission requirements. This is due to the excess power produced from VTOL design. As a consequence the aircraft must be flat rated after take-off to limit its ceiling to a specified altitude.

This excess power also translates into a high maximum climb rate of $V_{v_{max}} = 990 \text{ m/min}$ at sea level conditions. The thrust capability also gives the aircraft a high maximum turn rate of $\dot{\psi}_{max} = 29.81 \text{ deg/s}$. The conventional take-off and landing distances achieved by the PAV are also very low due to the excess power available. Generally the PAV design out performs CTOL aircraft with similar mission requirements.

Performance Values of an Optimised 6-passenger PAV			
$Range_O$	2782 km	Absolute ceiling	14020 m
M_{cruise_O}	0.433	Time to climb to cruise altitude	21.12 mins
$(L/D)_{cruise_O}$	15.885	$\dot{\psi}_{max}$	29.94 deg/s
$V_{v_{max}}$	990 m/min @ S.L.	Loiter time	29.81 mins
$\gamma_{climb_{max}}$	12.40°	$s_{t/o}$	424 m
Service ceiling	13564 m	s_L	407 m

Table 12.14: Performance values of the optimised 6-passenger PAV

The transition to and from forward flight and simulation of VTOL capability can be seen in Figure 12.18. For the take-off analysis, the aircraft begins to transition after reaching an altitude of 100 m off the ground, with the flaps fully deflected. The aircraft begins to gain speed and lose altitude reaching a minimum height of 84 m from the ground at 150 m forward of the starting position. When the aircraft has gained sufficient forward speed ($1.3V_{stall}$) the lift and pitch fans are both stopped. This corresponds to the point 300 m forward of the starting position, shortly after which the flaps are retracted and the aircraft begins to climb.

For the landing analysis, the aircraft begins at an altitude of 100 m off the ground, with a forward speed of $1.3V_{stall}$ and with the flaps fully deflected. At 100 m forward of the starting position the aircraft transitions the propulsion fans to hover and initiates the lift and pitch fans. At this same point, the flaps are deflected to $\delta_f = 50^\circ$ to act as speed brakes. The aircraft flares slightly and begins to slow. Once at a low enough speed, the power is reduced and the PAV begins to lose altitude gently. Shortly before touching down the aircraft flares further and increases its thrust to touch down gently.

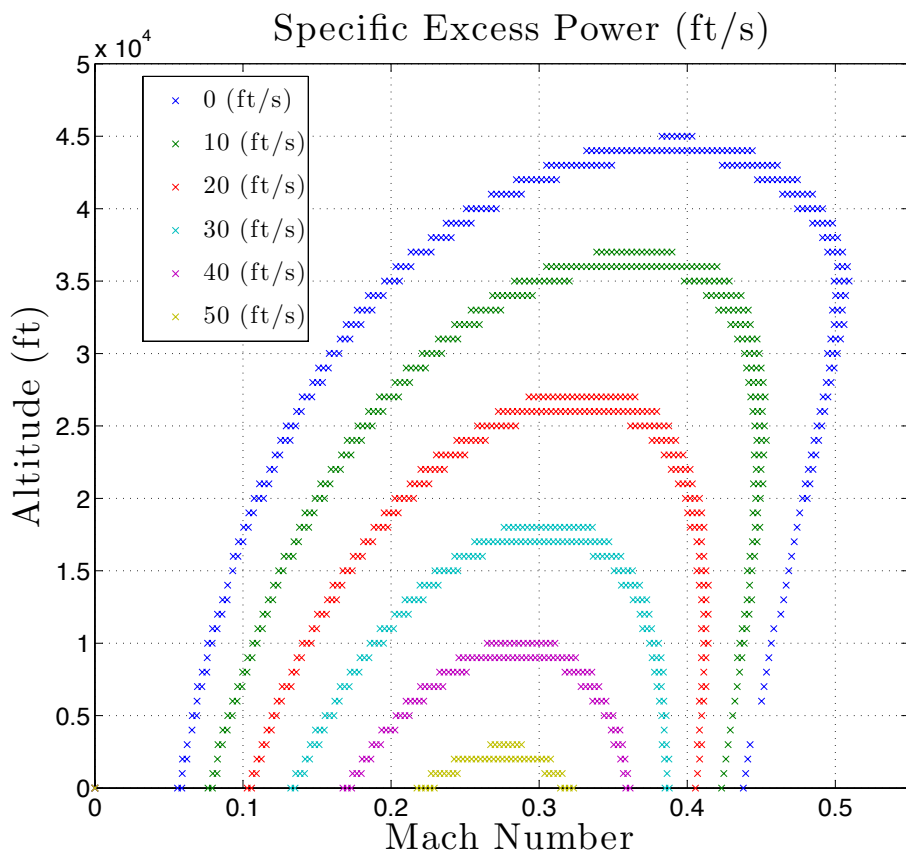
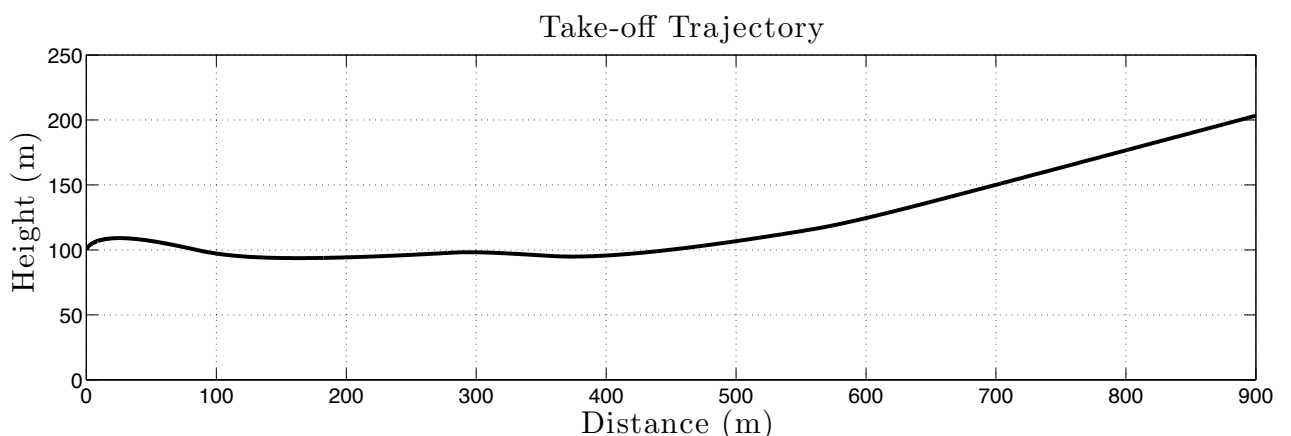
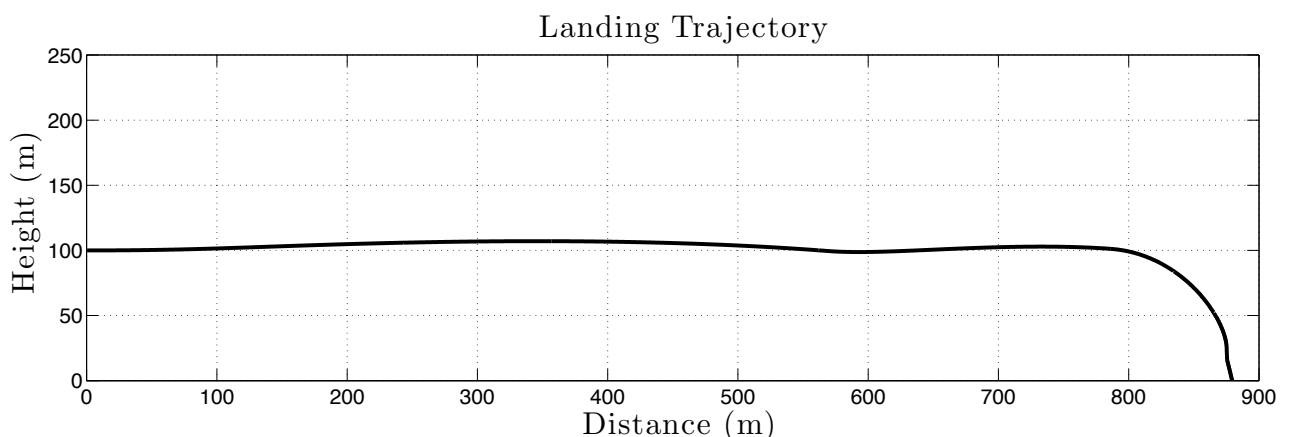


Figure 12.17: Specific Excess Power plot of the optimised 6-passenger PAV



(a) Take-off Trajectory



(b) Landing Trajectory

Figure 12.18: VTOL transition performance of the optimised 6-passenger air taxi

Chapter 13

Concluding Remarks

13.1 Discussion

PAV concepts VTOL or otherwise have been considered for development as long as manned flight has existed. It has not however been until recently that demand has increased for such a vehicle to come to market in order to relieve congestion problems. With new technologies such as composite materials and high speed fan/propeller designs becoming more advanced, readily available and cheaper, the feasibility of a high speed PAV has become attainable. This research programme aimed to develop a preliminary design and optimisation methodology for an innovative vertical take-off and landing (VTOL) PAV with a ducted fan propulsion system driven by a single turboshaft engine. Such a design required investigation and development of a ducted fan design methodology as well as methods for the propulsion system's interconnecting gears, gearboxes and shafts. A further investigation into packaging of all of the components within a configuration that could function both in hover and forward flight was also needed. These design methodologies were to be developed so that they could be evaluated computationally, such that a complete design synthesis could be put together and optimised using a global optimiser.

Although many fan/propeller theories such as blade element theory and axial fan theory exist, they require detailed design of the aerofoils and blades. These theories cannot predict the stall behaviour of the blades without further experimental or CFD tests. Therefore the pro-

duction of an optimised fan or propeller for a specific mission requirement demands extensive resources and time. For this reason, a methodology from CFD tests and regression techniques was developed to provide parametric equations that model the behaviour of a ducted fan given a number of geometrical and fluid flow inputs.

These newly developed ducted fan models proved an effective and flexible tool for predicting the propulsion requirements of the PAV. However, due to the time limitation of the project, the simplifications made in the propulsion investigation in order to integrate the results with the design synthesis affected the performance of the fan models. The fan models in forward flight could only operate at or close to maximum efficiency within small pitch variations of the design value. The methodology predicts blade stall within a 5° to 10° pitch increment from the optimum design pitch. Fans and propellers are designed to operate over a wide pitch range in order to maximise efficiency at off design points and thus maximise overall performance. Nonetheless the performance of the PAV was not markedly affected, since these slight reductions in off design performance were negated by the excess power of the engine. The optimum model would however provide better performance over a wider range of pitch values. Consequently the ducted fan models (equations) are an effective tool for the preliminary design of a ducted fan, but not for detailed design.

The fan layout and packaging of the aircraft were designed in such a way that the rear components (fans and wing) would balance with the cabin at the front of the aircraft. Due to the quantity of fans and their positioning, the packaging of the PAV was severely constrained. The positioning of individual components was restricted by all the gears, gearboxes, shafts and structural reinforcement required. The only components that could be repositioned were the canard and the wing, of which the latter was also limited to small changes due to the side propulsion fans. Consequently to balance the aircraft, the configuration was limited to moving the wing and its fuel tanks. That created a moderate variation in static margin. Since the design was compact and the length of the fuselage short, to provide an adequate moment arm a large canard was required.

FAR 23 requirements state that the aircraft must have a stall speed no greater than

31.4 ms^{-1} . To maximise the lift-to-drag during cruise, the wing loading needed to be high. Thus the $C_{L_{max \ flap}}$ was decided to be maximised to 2.5. This posed longitudinal static stability challenges. The rear wing configuration exhibits a greater nose down pitching moment behaviour, which is further increased with high lift devices. The canard was sized to be able to trim with the CG in the most forward position.

Although these constraints existed, the packaging and balance of the aircraft was achieved through careful adjustment of the wing. All the constraints were given parametric dimensions based on fan sizes in order to accommodate all the components. The aircraft was packaged around the lift fan. The engine and propulsion fans were placed at distances according to their radii and their need to rotate during transition. The remaining components were packaged around this propulsion system. The aircraft was packaged methodically in 2D and then in 3D using visualisation models plotted in MATLAB. The conic section equations allowed for the incorporation of all the components within the fuselage, through the variation of the cross section. Mathematical modelling of all these sections allowed for changes in fan sizes and fuselage seating configurations.

The component weights of the aircraft estimated with an appropriate methodology that was validated against 4 existing aircraft. These component weights were used to estimate the CG and balance the aircraft. The wing was positioned so that the static margin was around 4-6%, in order to minimise the trim required for all flight configurations. The flaps occupied most of the wing to achieve the target of $C_{L_{max \ flap}} = 2.5$. That was because the spar positions were restricted by the side fan position and thus the maximum flap chord ratio maximum was set to $c_f/c = 0.25$. The large pitch down moment was counteracted by reducing the flap deflection for different CG positions. The worst case scenario being with the CG most forward. The deflection was limited to $10^\circ \leq \delta_f \leq 15^\circ$. The canard reference area was also increased to cope with that.

The canard downwash affects the lift distribution of the wing and that results in an increase in induced drag. A VLM code was integrated into the synthesis to analyse the lift distribution and adjust the twist accordingly to make it elliptical. The VLM code was also used to determine

the $C_{L_{max\ clean}}$ of the wing and provide the stability derivatives of the aircraft. For preliminary design, the VLM code is more than sufficient at analysing the aerodynamic interaction between the canard and wing. Although the VLM only takes into account the lifting surfaces in its analysis of the stability derivatives, the values provide a sufficient indication of the dynamic behaviour of the aircraft. Due to time limitations and a number of other complicated research areas, the focus was put on the accuracy of the design synthesis as whole. Hence for preliminary design the VLM code provided adequate results for some aerodynamic and stability challenges.

The methodologies used were developed under various assumptions and were not without uncertainties. However these assumptions were kept pessimistic and the uncertainties were not significant enough to invalidate the findings of this research programme. The bulk of the aircraft was assumed to be constructed from carbon fibre composite materials. Although this would make the aircraft more expensive the weight saving benefit was essential for VTOL capability. The gears and shafts were over designed to avoid fatigue failure and extreme loads in order to eliminate the possibility of failure. The aircraft is technically advanced and it is assumed that onboard computers would assist the pilot during hover and transition to forward flight. The onboard computers would also serve to aid the aircraft in case of engine or gear failure during hover or forward flight. During hover the computer would prevent asymmetric thrust by instantly cutting the power to all the fans and thus preventing large pitching or roll moments. The design of the aircraft allows the added safety of the ability to glide in case of engine or gear failure given sufficient altitude. This is illustrated in Figure 12.18 where the aircraft is seen to initially lose altitude and gain airspeed during transition from hover to forward flight. At a lower height hover failure the design of the undercarriage is designed to take a increased undercarriage sink rate ($\sim 4.9\ ms^{-1}$) as can be seen in Table 5.1.

Figure 4.10 shows that the CFD tends to over estimate the thrust produced and the power required at higher inlet velocities. However the simplified design of the blades suggests that a more optimised fan would be within the error margin of 2-6% and thus the errors are not significant enough invalidate the propulsion methodology. Although the regression models also have an error margin of 4-7% the error in thrust or power would only yield a slightly heavier and power expending aircraft. This weight and power could be recovered through the detailed

design of the propulsion system (fans, gears and shafts) as well other components.

It was found that similar ratios of laminar to turbulent boundary layer flow of 40-50% were found using the 2D aerofoil design and analysis program *XFOIL*. Reducing the assumed value of 50% wetted area laminar boundary layer flow over lifting surfaces to 40% for the 4-passenger PAV case study in Chapter 12 yielded 0.4% reduction in the lift-to-drag ratio, 4% reduction in cruise Mach number and a 0.2% reduction in range. The performance of the aircraft was reduced only very slightly in cruise speed to compensate for the increase in drag. It also has to be noted that the propulsion fans could be redesigned in the optimiser to compensate for the drag increase. Consequently this shows that the design is robust to any variations in assumptions and uncertainties in the methodologies. The synthesis is still able to produce a high performance VTOL PAV design.

The performance of the aircraft was dependent on two major factors, the aerodynamic and propulsive efficiency of the aircraft. The propulsion performance was discussed earlier, and it was concluded that with a more detailed design of the fans the overall performance of the aircraft could be more efficient at off design points. The aerodynamic design of the PAV pushes the limits for personal aircraft design, with the extensive use of high lift devices. FAR 23 stall requirements limit the maximum wing loading achievable and thus the maximum lift-to-drag ratio is limited. For a given range, to achieve higher cruise Mach numbers, the aircraft would have to cruise at lower lift-to-drag ratios than the maximum. This in turn meant higher fuel consumption and thus a higher fuel load and overall weight. Increasing the aspect ratio decreased the induced drag but also increased the weight of the aircraft; since the aircraft was designed with VTOL capability, the weight needed to be kept to a minimum and thus the solution was not always straightforward and required an optimisation process.

The optimisation process involved the merit function Eqn 10.10. Like all the other variables in the merit function, the cruise Mach number was set as a variable to test whether a solution that exceeds the mission requirements could be found. The optimisation process highlighted the constraints of designing a VTOL PAV. The optimal solution did not always meet all the mission requirements, specifically that of the cruise Mach number. This was especially evident

at higher cruise speeds. The 4-passenger PAV design showed a 6% reduction in cruise Mach number from that of the design requirement. The 6-passenger air taxi showed 15% reduction in cruise Mach number from that of the design requirement. As stated earlier, this was because the maximum lift-to-drag ratio was offset from the design cruise speed and hence the optimum solution was located at a lower cruise speed.

Nonetheless, the complete synthesis and optimisation process proved successful, producing optimum solutions for different sets of mission requirements. The reduction in cruise Mach number is not significant considering the cruise speed of existing personal aircraft and air taxies. The cruise speed is still exceptionally high for a 4-passenger personal aircraft, while the cruise speed of the 6-passenger air taxi matches the economical cruise speeds achieved by air taxies with the similar mission requirements. The robustness of the synthesis and optimisation process offers the possibility of modifying the merit function to constrain the cruise Mach number and thus eliminating it as a variable. Though the power requirements and weight would increase, such a solution would keep the Mach number within the design requirements and yield an optimal solution for the merit function.

The aim of this research programme was to develop an affordable easily utilised PAV. The feasibility study in Chapter 2 highlighted the safety problems and design complexities of a dual-mode vehicle. To ensure freedom of mobility and safety an innovative VTOL with a ducted fan propulsion system concept was developed. The research showed that the concept needed to be technically advanced in order to satisfy VTOL and performance requirements. Consequently the cost of aircraft would place it into the luxury market of general aviation. Although the affordability of the aircraft was reduced it still provided an attractive option to higher income individuals requiring high performance mobile personal transport. This research programme has developed a design and optimisation methodology for an innovative VTOL PAV. A VTOL PAV provides point-to-point mobility at high speeds through a compact, lightweight design.

13.2 Conclusion

The VTOL PAV designed in this research programme is a novel concept which could provide an alternative solution to modern transport problems. The design synthesis also allows for flexibility in the design requirements and it may provide solutions for other operational roles such as air taxies, ambulances, rescue and police support. To make a PAV a viable transport solution, the cost of such an aircraft should be comparable to that of an existing light aircraft. However for this design to function as it is intended, a transport infrastructure with set regulations must be in place allow for safe operation. To oversee this infrastructure, a PAV licensing body is also needed. Operation under current regulations would require a private pilot's licence and a large space to operate from and air traffic control. Such conditions exist in flying communities where people use light aircraft for personal travel, storing their aircraft in personal hangars. One such example, are the Airpark communities in Florida [50]. A PAV, however in such communities would help eliminate the need for a runway.

The innovations and new methodologies developed for this project led to valuable and flexible tools for computationally designing and optimising a PAV. They have not been without their limitations, but they have given clear insight into the challenges and solutions required to design a VTOL PAV. The propulsion methodology provides an innovative and quick approach to determining the characteristics of a fan (T , P and η) for given geometrical and fluid inputs, however due to the complexity and non-linearity of blade stall, the methodology lacks high efficiency at off design points.

The design of the PAV placed rigid constraints on the packaging of the aircraft and thus limited the it to a rear wing configuration with moderate variation in static margins, which when coupled with FAR 23 requirements, created stability design challenges. The design was sensitive to nose down pitch moments, consequently the wing aerofoil selection and flap design were crucial to maximising the cruise lift-to-drag ratio and minimising the nose pitch down moments. A large canard surface area and maximum flap deflections were also incorporated into the design to minimise nose down pitching moments. However this did not reduce the performance of the aircraft.

The aerodynamic interaction of the canard and wing as well as the stability derivatives were analysed using a VLM code. Although VLM has its limitations, it proved a sufficient method for calculating the wing stall lift coefficient, twisting the wing and obtaining stability derivatives for lateral static stability and dynamic stability analyses.

The methodologies used were developed under certain assumptions and were not without uncertainties. However these assumptions were kept pessimistic and the uncertainties were not significant enough to invalidate the findings of this research programme. The losses in performance of the aircraft from uncertainties could be regained through weight saving detailed design.

The safety and reliability concerns of complex propulsion system were negated by the over design of the gears and shafts, the incorporation of computer safety system and the over design of the undercarriage system.

MATLAB provided a versatile programming platform throughout the project. Its flexibility and visualisation techniques aided in the speed and validation of the synthesis. It provided a platform that could be linked to the VLM code *Tornado* while it also provided a methodology for global optimisation.

The performance methodology showed that the aircraft was limited by a mismatch of the maximum lift-to-drag ratio speed and the cruise speed. The optimisation process highlighted this further with optimised solutions that did not meet all cruise Mach number design requirements. Nonetheless this reduction in cruise Mach number was not significant and it did not invalidate the design.

The compromises required to develop a high speed long range VTOL PAV resulted in a higher cost aircraft than initially expected. The higher cost reduced the marketability of the aircraft to the general population. However the PAV design would provide an attractive option to higher income individuals seeking flexible high speed personal mobility. Overall this research

has delivered a comprehensive set of design methodologies and demonstrated that PAVs can provide a practical alternative solution to modern transport problems.

13.3 Suggestions for Further Work

A number of difficult research problems were involved in creating the design synthesis and optimisation methodology. Consequently time did not permit detailed investigation into some topics and thus reasonable simplifications were made. Further work is recommended in the following research topics.

Research should be conducted in the analysis of a PAV traffic infrastructure and the logistics of handling large volumes of air traffic over various flight levels; since the project is centred around the propulsion system, more research is required to determine a more accurate fan methodology for off design performance. This research could also involve investigation into transonic aerofoil design, blade taper ratio, sweep and chord distribution. A fan noise design approach should also be incorporated into the propulsion methodology.

Although the gears and shafts were designed to withstand fatigue failure, more detailed design and optimisation of those components could reduce their weight and increase their efficiency.

The transition simulation provides a reasonable estimate of the behaviour of the aircraft during transition from hover to forward flight. However to further validate this methodology, a full flight simulation model could be created and tested. This X-Plane model would also provide a more extensive validation for the performance and stability of the aircraft in all regimes of flight.

A detailed structural analysis of the aircraft is required. This investigation should involve the airframe loads caused by VTOL and also the structural innovations required to house so many ducted fans within the fuselage and wings.

Finally, a detailed cost analysis of the aircraft is required. The cost of the aircraft determines its marketability and thus reinforces its feasibility as a concept.

Bibliography

- [1] World Business Council For Sustainable Development. Mobility 2030: Meeting the challenges to sustainability. Technical report, World Business Council For Sustainable Development, 2004.
- [2] Mark D. Moore. Personal air vehicles: A rural/regional and intra-urban on-demand transportation system, 2003.
- [3] European Commission. Panorama of transport. Technical report, European Union Commission, 2007.
- [4] Airbus. Airbus global market forecast 2007-2026. Technical report, Airbus, 2007.
- [5] Boeing. Boeing current market outlook. Technical report, Boeing, 2007.
- [6] J.-H. Lewe, A. Khalid, E. Upton, and T. Kang. Agent-based forecasting tool for nasa's sats program, 2004.
- [7] D. DeLaurentis, J.-H. Lewe, B. Ahn, D. Mavris, and D. Schrage. An integrated decision-making method to identify design requirements through agent-based simulation for personal air vehicle system. *AIAA*, 2002.
- [8] H.I.H. Saravanamutto, G.F.C. Rogers, and H. Cohen. *Gas Turbine Theory*. PEARSON - Prentice Hall, fifth edition, 2001.
- [9] R. Allan Wallis. *Axial Flow Fans & Ducts*. Wiley-Interscience, 1983.
- [10] J. Gordon Leishman. *Principles of Helicopter Aerodynamics*. Cambridge University Press, 2000.

- [11] Daniel P. Raymer. *Aircraft Design: A Conceptual Approach*. American Institute of Aeronautics and Astronautics, Inc., third edition, 1999.
- [12] Jan Roskam. *Airplane Design: Part I - VIII*. Roskam Aviation and Engineering Corporation, 1987.
- [13] Egbert Torenbeek. *Synthesis of Subsonic Airplane Design*. Kluwer Academic Publishers, 1982.
- [14] Leland M. Nicolai. *Fundamentals of Aircraft Design*. METS, INC., 1975.
- [15] V. C. Serghides. *Design synthesis for Canard-Delta combat aircraft*. PhD thesis, Cranfield University, 1987.
- [16] R.H. Byrd, J. C. Gilbert, and J. Nocedal. A trust region method based on interior point techniques for nonlinear programming. *Mathematical Programming*, 89:149–185, 2000.
- [17] Zsolt Ugray, Leon Lasdon, John C. Plummer, Fred Glover, James Kelly, and Rafael Mart. Scatter search and local nlp solvers: A multistart framework for global optimization. *INFORMS Journal on Computing*, 19:328–340, 2007.
- [18] Dwight A. Hennessy and David L. Wiesenthal. The relationship between traffic congestion, driver stress and direct versus indirect coping behaviours. *Ergonomics*, 40(3):348–361, 1997.
- [19] Flight Global. <http://www.flightglobal.com/>.
- [20] Jane's All The World's Aircraft. <http://jawa.janes.com/>.
- [21] National Museum of the USAF. Avrocar. <http://www.nationalmuseum.af.mil/>.
- [22] Moller International. <http://www.moller.com/>.
- [23] Terrafugia. <http://www.terrafugia.com/>.
- [24] AMV Aircraft. <http://www.amvaircraft.com/>.
- [25] Carter Aviation Technoogies. Cartercopter. <http://www.cartercopters.com/>.

- [26] Aviation Week. Propfan. <http://www.aviationweek.com/>.
- [27] Robert J. Englar and Bryan A. Campbell. Experimental development and evaluation of pneumatic powered-lift super-stol aircraft, 2004.
- [28] ACEA. European automobile manufacturers' association.
- [29] Richard de Neufville and Odoni Amedeo. *Airport Systems: Planning, Design and Management*. McGraw Hill, 2003.
- [30] Paul C. Schutte, Kenneth H. Goodrich, David E. Cox, E. Bruce Jackson, Michael T. Palmer, Alan T. Pope, Robin W. Schlecht, Ken K. Tedjojuwono, Anna C. Trujillo, Ralph A. Williams, J. Bryan Kinney, and Jr John S. Barry. The naturalistic flight deck system: An integrated system concept for improved single-pilot operations, 2007.
- [31] G. Pappas, C. Tomlin, J. Lygeros, D. Godbole, and S. Sastry. A next generation architecture for air traffic management systems, 1997.
- [32] Harry Swenson. Next generation air transportation system (ngats) air traffic management (atm)-airspace project, 2006.
- [33] Heinz Erzberger and Russell A. Paielli. Concept for next generation air traffic control system, 2002.
- [34] Daniel M. Williams, Marvin C. Waller, John H. Koelling, Danial W. Burdette, William R. Capron, John S. Barry, Richard B. Gifford, and Thomas M. Doyle. Concept of operations for commercial and business aircraft synthetic vision systems, 2001.
- [35] H. Möller and G. Sachs. Synthetic vision for enhancing poor visibility flight operations, 1999.
- [36] Arthur Richards, John Bellingham, Michael Tillerson, and Jonathan How. Co-ordination and control of multiple uavs, 2002.
- [37] G. Pappas, Claire Tomlin, and Shankar Sastry. Conflict resolution for air traffic management: A study in multiagent hybrid systems. *IEEE TRANSACTIONS ON AUTOMATIC CONTROL*, 43, 1998.

- [38] Cessna. <http://www.cessna.com/>.
- [39] Daher-Socata. <http://www.tbm850.com/>.
- [40] B. Saeed and G. B. Gratton. An evaluation of the historical issues associated with achieving non-helicopter v/stol capability and the search for the flying car. *The Aeronautical Journal*, 114:91–102, 2010.
- [41] L. He and W. Ning. Efficient approach for analysis of unsteady viscous flows in turbomachines. *AIAA*, 36, 2005.
- [42] Douglas C. Montgomery, Elizabeth A. Peck, and G. Geoffrey Vining. *Introduction to Linear Regression Analysis*. Wiley-Blackwell, fourth edition, 2006.
- [43] Kenneth W. Mort and Paul F. Yaggy. Aerodynamic characteristics of a 4-foot diameter ducted fan mounted on the top of a semispan wing. Technical Report TN D-1301, NASA, 1962.
- [44] Raymond J. Drago. *Fundamentals of Gear Design*. Butterworth Publishers, 1988.
- [45] Emerson Power Transmission Corporation. <http://www.emerson-ept.com/>.
- [46] Stuart H. Loewenthal. Design of power transmitting shafts. Technical Report RP-1123, NASA, 1984.
- [47] Garmin. <http://www.garmin.com/>.
- [48] Ira H. Abbott and Albert E. Von Doenhoff. *Theory of Wing Sections*. Dover Publications, 1959.
- [49] MathWorks. <http://www.mathworks.co.uk/>.
- [50] Bardell Real Estate. <http://www.floridaairporthomes.com/>.

Appendix A

Feasibility Study

A.1 Current PAV Performance Tables

Number of passengers	2
GTOW	650 kg
Useful Load	210 kg
Fuel Capacity	87 l
Engine	Rotax 912 S (four-stroke) 75 kW
V_S	83 km/h
V_{CRUISE} (75% power)	172 km/h
Range	787 km
Fuel type	Super-unleaded
Wingspan	8 m
Length	6 m
Height	2 m
On-Road Width	2.3 m

Table A.1: The Transition's performance data and dimensions [23]

Number of passengers	2
Length	6.1 <i>m</i>
Wing Span	6.1 <i>m</i>
Empty Weight	726 <i>kg</i>
GTOW	1043 <i>kg</i>
Fuel Capacity	303 <i>l</i>
Payload	318 <i>kg</i>
Engine	Lycoming T53 Turboshaft 671 <i>kW</i>
Propellor	2.39 <i>m</i> diameter 5 blade
Rate of climb	1372 <i>mpm</i>
V _{MAX}	483 <i>km/h</i>
V _{CRUISE} (60% power)	402 <i>km/h</i>
Range	1111 <i>km</i>
Service ceiling	7620 <i>m</i>

Table A.2: The AMV-211's performance data and dimensions [24]

Number of passengers	4
V _{MAX} @ 7620 <i>m</i>	531 <i>km/h</i>
V _{MAX} @ S.L.	579 <i>km/h</i>
V _{CRUISE} @ 7620 <i>m</i>	491 <i>km/h</i>
Maximum rate of climb	1463 <i>m/min</i>
Range	1207 <i>km</i>
Payload excluding fuel	340 <i>kg</i>
Operational ceiling	10973 <i>m</i>
GTOW	1088 <i>kg</i>
Engine Power	537 <i>kW</i>
Engine Power with boost	861 <i>kW</i>
Fuel type	Ethanol
Fuselage Length	5.9 <i>m</i>
Fuselage Span	2.6 <i>m</i>
Target noise level	65 dBA
Emergency parachutes	Yes

Table A.3: The Moller Skycar M400's performance data and dimensions [22]

Number of passengers	2
V_{MAX} @ 3048 m	266 km/h
V_{CRUISE} @ 3048 m	209 km/h
Range	1207 km
Empty Weight	340 kg
GTOW	612 kg
Engine	Rotax 914 75 kW
Rotor Diameter	10.4 m
Wing Span	7.3 m

Table A.4: The 2-seater CarterCopter's performance data and dimensions [25]

Number of passengers	1-2
V_{CRUISE}	241 km/h
BFL	76-152 m
Range	644 km
GTOW	454 kg
Engine	75 kW

Table A.5: The NASA PAV concept's performance data and dimensions [2]

Appendix B

Propulsion

B.1 Fan Parametric Equations

The equations below are for forward flight with fans that have a design axial speed range of $V_x \leq 125 \text{ ms}^{-1}$ and pitch range $-0.175 \text{ rads} < \delta \leq 0.349 \text{ rads}$.

$$V_{xa}/V_x = 1.5361 - 0.2596 \cdot R + 0.4296 \cdot M_{tip}^U + 0.0005 \cdot N_b + 0.1775 \cdot \sigma - 0.0049 \cdot V_x - 0.7213 \cdot V_{ratio} + 0.0032 \cdot V_\infty + 1.0979 \cdot \delta \quad (\text{B.1})$$

$$P = -742.9 + 0.1518 \cdot T - 288.1 \cdot M_{tip} + 1005 \cdot R + 0.0889 \cdot \Omega - 5.3457 \cdot N_b + 103.0 \cdot \sigma - 6.5819 \cdot V_{xa} + 5.3111 \cdot V_\infty + 2.2362 \cdot V_x + 671.8 \cdot \delta \quad (\text{B.2})$$

B.2 Gear Volume Equations

WHEEL VOLUME:

$$V_{w_1} = \text{WD} \cdot F_{wd} \cdot \pi \left[R_w - \left(\frac{k_1 + l_1}{2} \right) \right] \quad (\text{B.3})$$

$$V_{w_2} = h_1 \cdot l_1 \cdot \pi \left[R_w - k_2 - \left(\frac{l_1}{2} \right) \right] \quad (\text{B.4})$$

$$V_{w_3} = h_1 \cdot \pi \left[(R_w - k_2 - l_1)^2 - (R_w - k_2 - l_1 - l_2)^2 \right] \quad (\text{B.5})$$

$$V_{w_4} = h_2 \cdot \pi \left[(R_w - k_2)^2 - (R_w - k_2 - l_1 - l_2)^2 \right] \quad (\text{B.6})$$

$$V_w = \sum V_{w_i} \quad (\text{B.7})$$

PINION VOLUME:

$$V_{p_1} = \text{WD} \cdot F_{wd} \cdot \pi [R_p - k_3] \quad (\text{B.8})$$

$$V_{p_2} = h_1 \cdot l_1 \cdot \pi \left[R_p - k_3 - \left(\frac{h_1}{2} \right) \right] \quad (\text{B.9})$$

$$V_{p_3} = h_1 \cdot \pi \left[(R_p - k_3 - h_1)^2 - (R_p - k_3 - h_1 - 2F_{wd})^2 \right] \quad (\text{B.10})$$

$$V_p = \sum V_{p_i} \quad (\text{B.11})$$

B.3 Example of Thrust Calculation

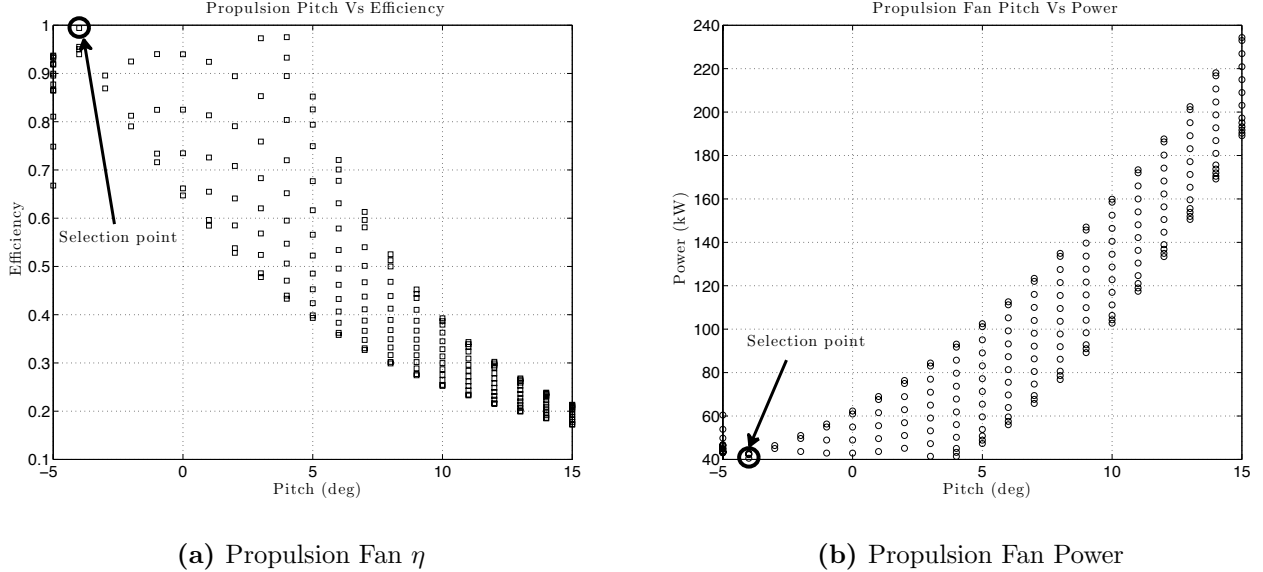


Figure B.1: Propulsion fan thrust calculation

An example of the data extracted using fan methodology developed in Chapter 4 based on the case study of a 4-passenger PAV in Chapter 12 can be seen in Figures B.1, B.2 & B.3.

Figure B.1 shows the multiple fan designs and their power and efficiency for a given thrust. The data illustrated in Figure B.1 was obtained using the fan methodology outlined in Figures 4.12, 4.13 & 4.14 and Eqns 4.28 - 4.33. The most efficient and least power consuming propulsion fan is selected from the data as illustrated in Figure B.1 and its characteristics used in the rest of the synthesis.

The same technique is used to extract the most efficient and least power consuming lift fan and pitch fan as can be seen in Figures B.2 & B.3. The process outlined in Figures 4.12 - 4.14 & B.1 - B.3 is repeated throughout the whole synthesis to ensure the selected fans are optimum with the evolving vertical thrust and forward flight drag requirements.

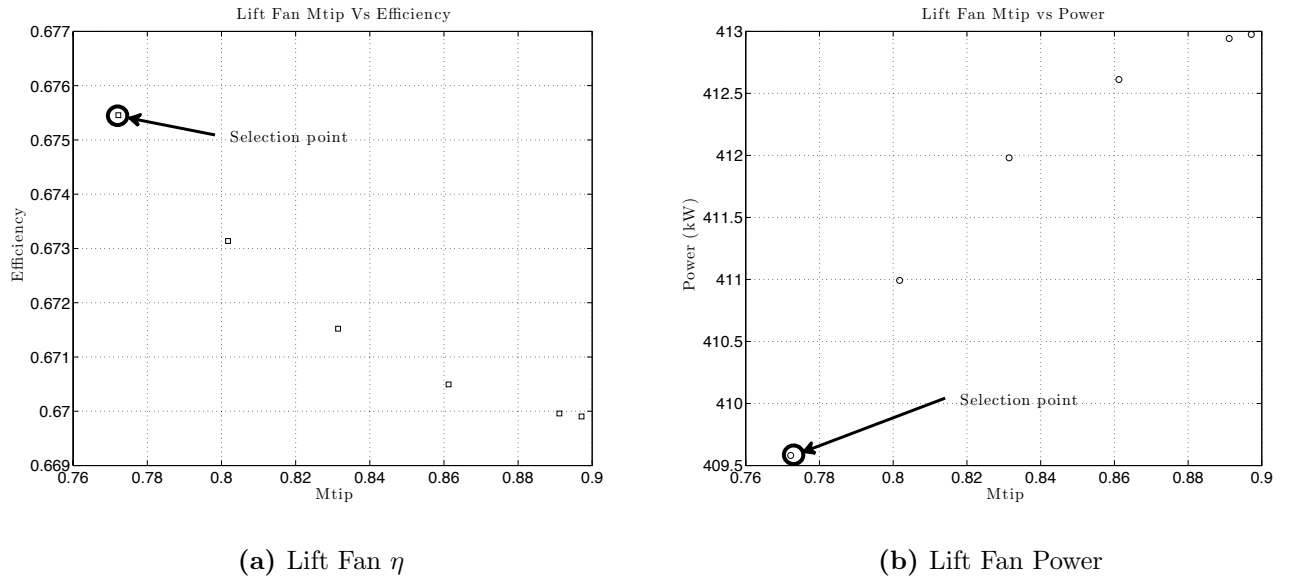


Figure B.2: Lift fan thrust calculation

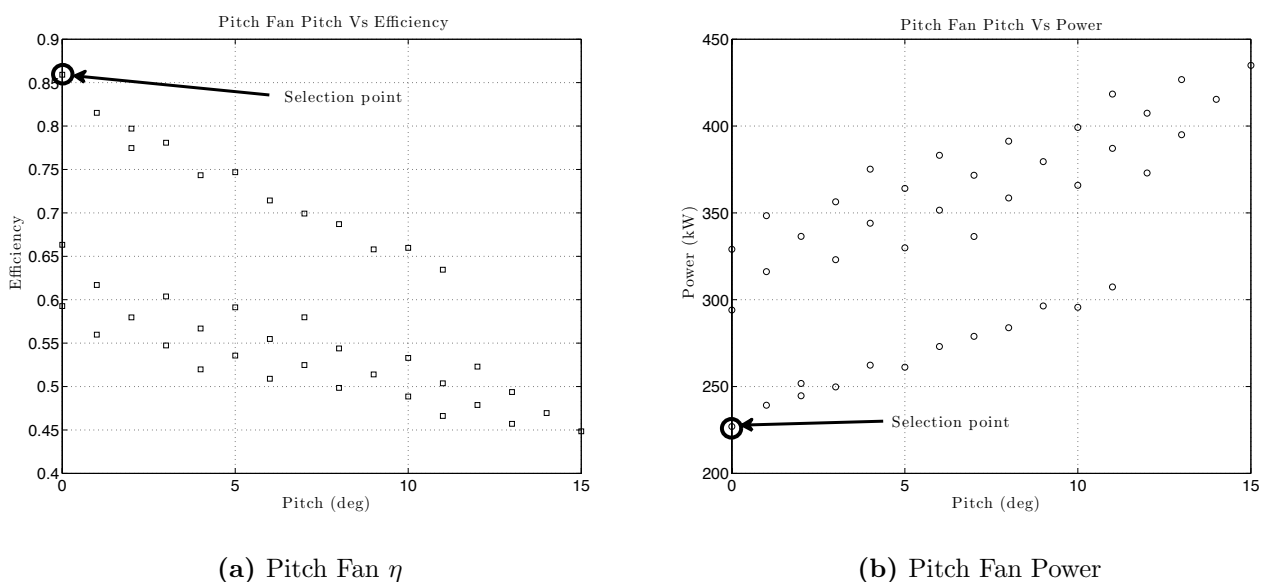


Figure B.3: Pitch fan thrust calculation

Appendix C

Initial Sizing

C.1 Carpet Plot Equations

All units are S.I. unless stated otherwise, W/S (kg/m^2) and W/P (kg/kW):

$$\left(\frac{W}{S}\right)_{stall} = \frac{1}{2} \rho V_{stall}^2 C_{L_{max_flaps}} \quad (C.1)$$

$$\left(\frac{W}{S}\right)_{landing} = \frac{1}{2} \rho V_{landing}^2 C_{L_{max_flaps}} \quad (C.2)$$

$$\left(\frac{W}{S}\right)_{cruise} = I_p^3 \sigma \left(\frac{W}{P}\right) \quad (C.3)$$

$$\left(\frac{W}{S}\right)_{climb} = \left[\left(\frac{\eta_p}{1.644(W/P)} - \frac{V_v}{10058.4} \right) \frac{25.555(ARe)^{3/4}}{C_{D0}^{1/4}} \sigma^{1/2} \right]^2 \quad (C.4)$$

$$\left(\frac{W}{S}\right)_{take-off} = \frac{\rho \cdot s_{t/o}}{k_1} \left[C_{Lt/o} \left(\frac{k_2}{(W/P)} - \mu_G \right) - 0.72 \cdot C_{D0} \right] \quad (C.5)$$

$$\left(\frac{W}{S}\right)_{eshort\ take-off} = \frac{\rho \cdot s_{t/o}}{k_1} \left[(C_{Lt/o} + C_T) \left(\frac{k_2}{(W/P)} - \mu_G \right) - 0.72 \cdot C_{D0} \right] \quad (C.6)$$

where $I_p = 4.054$, $\eta_p = 0.9$, $k_1 = 1.210$, $k_2 = 1.023$ and $\mu_G = 0.025$

Appendix D

Systems Packaging

D.1 2D Packaging

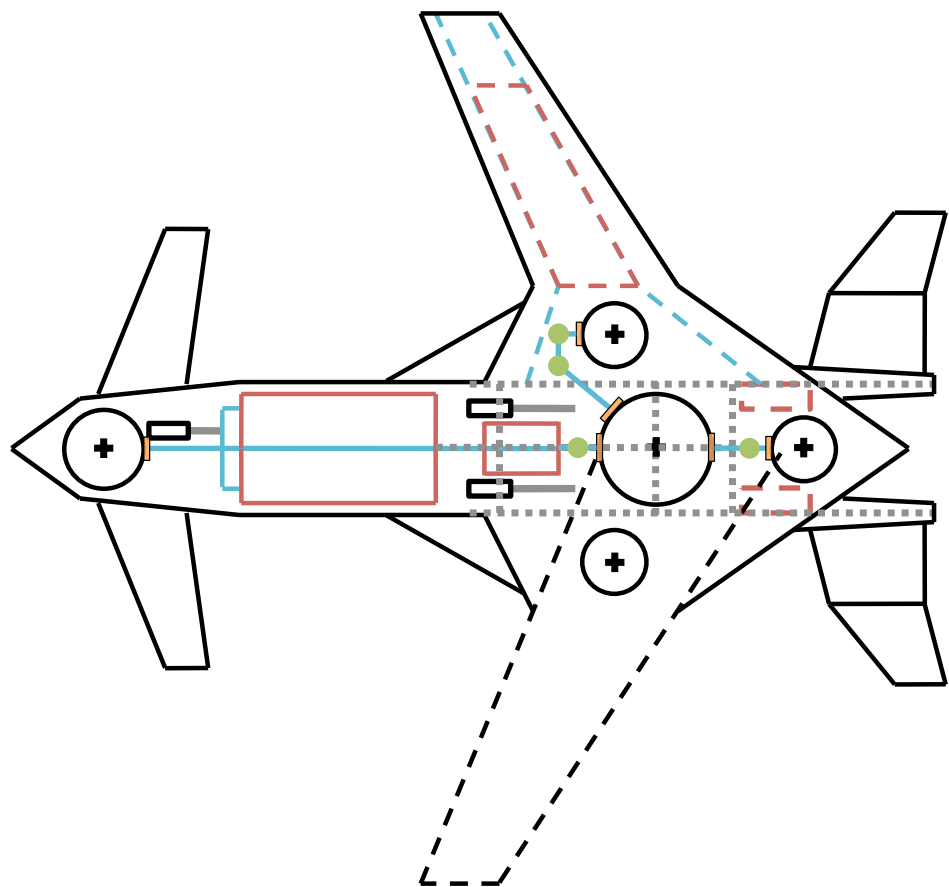


Figure D.1: Packaging of PAV in the $x - y$ plane

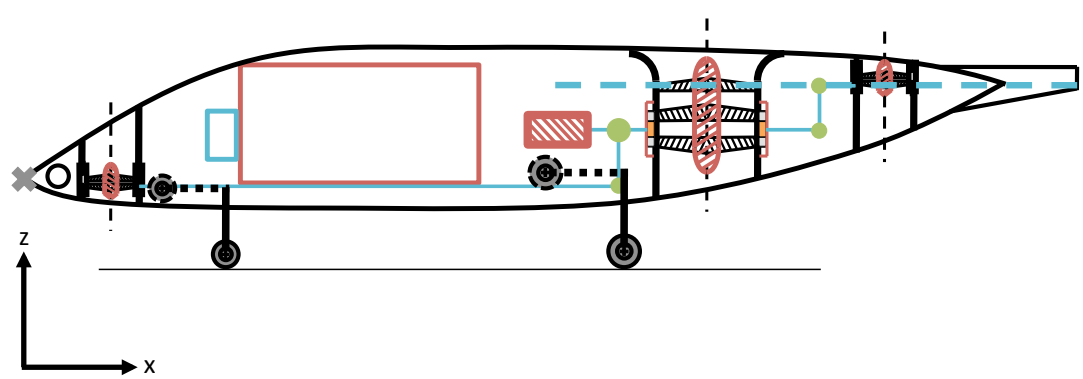


Figure D.2: Packaging of PAV in the $x - z$ plane

Appendix E

Weight & Balance

E.1 Component Weight Equations

E.1.1 Wing Group

S.I. UNITS:

$$W_{WING_{basic}} = 4.58 \times 10^{-3} k_{no} k_e k_\lambda k_{uc} k_{st} [k_b \cdot N(W_0 - 0.8 \cdot W_{WING})]^{0.55} \times b^{1.675} \left(\frac{t}{c}\right)_{root}^{-0.45} (\cos \Lambda_{c/2})^{-1.325} \quad (E.1)$$

$$W_{FLAPS} = S_{flapped} \left[2.706 \cdot k_f (S_{flapped} \cdot b_{fs})^{\frac{3}{16}} \left\{ \left(\frac{1.3 \cdot V_{stall}}{100} \right)^2 \frac{\sin \delta_f \cos \Lambda_f}{(t/c)_{flap}} \right\}^{\frac{3}{4}} \right] \quad (E.2)$$

$$W_{WING} = W_{WING_{basic}} + 1.2 \cdot W_{FLAPS} \quad (E.3)$$

Wing weight factors:

$$k_{no} = 1 + \left(\frac{b}{b_s} \right)^{0.5} \quad (E.4)$$

$$b_s = \frac{b}{\cos \Lambda_{c/2}} \quad (E.5)$$

$$k_\lambda = (1 + \lambda)^{0.5} \quad (E.6)$$

$$k_{st} = 1 + 1.5 \times 10^{-5} \frac{(b \cos \Lambda)^3}{W_0} \left[\frac{V_{max_{dive}}/100}{t_{max_{root}}} \right]^2 \cos \Lambda_{c/2} \quad (\text{E.7})$$

Wing component weight factors	
k_e	1
k_{uc}	0.95
k_b	1
k_f	1

Table E.1: Wing component weight factors

E.1.2 Remaining Components

IMPERIAL UNITS:

$$W_{CANARD} = 127 \left[\left(\frac{W_0 \cdot N}{1 \times 10^5} \right)^{0.87} \left(\frac{S_{can}}{100} \right)^{1.2} \left(\frac{l_{can}}{10} \right)^{0.483} \left(\frac{b_{can}}{t_{max_{root}}} \right)^{0.5} \right]^{0.485} \quad (\text{E.8})$$

$$W_{HTAIL} = 127 \left[\left(\frac{W_0 \cdot N}{1 \times 10^5} \right)^{0.87} \left(\frac{S_{htail}}{100} \right)^{1.2} \left(\frac{l_{htail}}{10} \right)^{0.483} \left(\frac{b_{htail}}{t_{max_{root}}} \right)^{0.5} \right]^{0.485} \quad (\text{E.9})$$

$$W_{VTAIL} = 98.5 \left[\left(\frac{W_0 \cdot N}{1 \times 10^5} \right)^{0.87} \left(\frac{S_{vtail}}{100} \right)^{1.2} \left(\frac{b_{vtail}}{t_{max_{root}}} \right)^{0.5} \right]^{0.485} \quad (\text{E.10})$$

$$W_{WINGLET} = 98.5 \left[\left(\frac{W_0 \cdot N}{1 \times 10^5} \right)^{0.87} \left(\frac{S_{winglet}}{100} \right)^{1.2} \left(\frac{b_{winglet}}{t_{max_{root}}} \right)^{0.5} \right]^{0.485} \quad (\text{E.11})$$

$$W_{FUSELAGE} = 200 \left[\left(\frac{W_0 \cdot N}{1 \times 10^5} \right)^{0.286} \left(\frac{L_{fus}}{10} \right)^{0.857} \right. \\ \left. \times \left(\frac{B_{fus} + H_{fus}}{10} \right) \left(\frac{V_{max_{S.L.}}}{100} \right)^{0.338} \right]^{1.1} 1.05 \quad (\text{E.12})$$

$$W_{DUCT} = 1.735 [H_{duct} \cdot N_{inlet} \cdot A_{inlet} \cdot p_2 \cdot K_{geo} \cdot K_M]^{0.7331} \quad (\text{E.13})$$

$$W_{U/C} = 0.054 \cdot L_{U/C_{main}}^{0.501} (W_0 \cdot N)^{0.684} \quad (\text{E.14})$$

$$W_{BOOM} = k_{wf} \left(\frac{V_{max_{dive}} \cdot L_{boom}}{B_{boom} + H_{boom}} \right)^{0.5} S_{boom}^{1.2} \quad (\text{E.15})$$

$$W_{ENGINE INST} = 0.0162 \cdot W_0 - 2.4403 \quad (\text{E.16})$$

$$W_{FUEL SYS} = 2.49 \left[F_G^{0.6} \left(\frac{1}{1 + INT} \right)^{0.3} N_{tanks}^{0.2} \cdot N_{eng}^{0.13} \right]^{1.21} \quad (\text{E.17})$$

$$W_{AVIONICS} = 167.8 \text{ lbs} \quad (\text{E.18})$$

$$W_{HYDRAULICS} = 0.006 \cdot W_0 \quad (\text{E.19})$$

$$W_{SURF CONTROLS} = 0.0168 \cdot W_0 \quad (\text{E.20})$$

$$W_{ELECTRICAL SYS} = 426 \left(\frac{W_{FUEL SYS} + W_{AVIONICS}}{1000} \right)^{0.51} \quad (\text{E.21})$$

$$W_{AIRCON} = 0.265 \cdot W_0^{0.52} \cdot N_{PAX}^{0.68} \cdot W_{AVIONICS}^{0.17} \cdot M_{max_{S.L.}}^{0.08} \quad (\text{E.22})$$

$$W_{FURNISHING} = 32.03 \cdot N_{PAX} \quad (\text{E.23})$$

$$W_{AUX} = 0.003 \cdot W_0 + 4.41 \quad (\text{E.24})$$

E.2 Weight Validation

Component Weights - Pilatus PC-12					
Wing	675.2 <i>kg</i>	Fuel System	80.7 <i>kg</i>	Surface Controls	79.6 <i>kg</i>
Fuselage	475.1 <i>kg</i>	Engine	190.2 <i>kg</i>	Avionics	76.1 <i>kg</i>
Horizontal Tail	75.7 <i>kg</i>	Propeller	101.5 <i>kg</i>	Electrical System	125.7 <i>kg</i>
Fin	21.2 <i>kg</i>	Nacelle	98.0 <i>kg</i>	Furnishing	159.8 <i>kg</i>
Undercarriage	238.2 <i>kg</i>	Propeller Installation	76.2 <i>kg</i>	Pressurisation + A/C	180.5 <i>kg</i>
		Engine Installation	75.7 <i>kg</i>	Paint	14.2 <i>kg</i>
Structure Total	1485.4 <i>kg</i>	Propulsion Total	622.4 <i>kg</i>	Equipment Total	635.9 <i>kg</i>
Fuel		1226.0 <i>kg</i>			
Passengers + Payload		924.0 <i>kg</i>			
Empty Weight		2743.7 <i>kg</i>			
MTOW		4893.7 <i>kg</i>			

Table E.2: Component Weights of a Pilatus PC-12

Component Weights - Pilatus Cessna 210					
Wing	229.7 <i>kg</i>	Fuel System	27.2 <i>kg</i>	Surface Controls	29.0 <i>kg</i>
Fuselage	123.7 <i>kg</i>	Engine	146.8 <i>kg</i>	Avionics	76.1 <i>kg</i>
Horizontal Tail	38.0 <i>kg</i>	Propeller	29.0 <i>kg</i>	Electrical System	90.9 <i>kg</i>
Fin	2.8 <i>kg</i>	Nacelle	25.3 <i>kg</i>	Furnishing	87.2 <i>kg</i>
Undercarriage	84.3 <i>kg</i>	Propeller Installation	31.0 <i>kg</i>	Pressurisation + A/C	67.1 <i>kg</i>
		Engine Installation	26.8 <i>kg</i>	Paint	5.2 <i>kg</i>
Structure Total	1485.4 <i>kg</i>	Propulsion Total	622.4 <i>kg</i>	Equipment Total	635.9 <i>kg</i>
Fuel		274.6 <i>kg</i>			
Passengers + Payload		504.0 <i>kg</i>			
Empty Weight		1120.1 <i>kg</i>			
MTOW		1898.6 <i>kg</i>			

Table E.3: Component Weights of a Cessna 210

Appendix F

Aerodynamics

F.1 Wing Lift Coefficient Increment

$$\Delta C_{l_w} = C_{l\alpha_w} \cdot \delta_f \cdot \alpha_\delta \cdot \left(\frac{c'}{c} \right) \quad (\text{F.1})$$

$$\alpha_\delta = -0.381\delta_f + 0.952 \cdot \delta_f + 0.5132 \quad (\text{F.2})$$

$$\Delta \alpha_{0_{aerofoil}} = \frac{-(C_{l0_w} + \Delta C_{l_w})}{C_{l\alpha_w}} \quad (\text{F.3})$$

$$C_{L\alpha_w \ flap} = C_{L\alpha_w} \left[1 + \left(\frac{c'}{c} - 1 \right) \left(\frac{S_{flap}}{S_{ref}} \right) \right] \quad (\text{F.4})$$

$$\Delta \alpha_{0_w \ flap} = \Delta \alpha_{0_{aerofoil}} \left(\frac{S_{flap}}{S_{ref}} \right) \cos \Lambda_{flap} \quad (\text{F.5})$$

$$\Delta C_{L_w} = C_{L\alpha_w \ flap} \cdot \Delta \alpha_{0_w \ flap} \quad (\text{F.6})$$

F.2 Wing Moment Coefficient Increment

$$C_{m\alpha_{fus}} = \frac{k_f \cdot B_{fus} \cdot L_{fus}}{S_{ref} \cdot \bar{c}} \quad (\text{F.7})$$

$$C_{m_w} = C_{m0_{foil}} \left(\frac{AR \cos^2 \Lambda_{c/4}}{AR + 2 \cos \Lambda_{c/4}} \right) \quad (\text{F.8})$$

$$\begin{aligned} \Delta C_{m_w} = & (\bar{x}_{ref} - \bar{x}_{ac_w}) \Delta C_{L_w} + K_\Lambda \frac{AR}{1.5} \tan \Lambda_{c/4} \\ & + K_p \left[\frac{\Delta C'_m}{\Delta C_{L_{ref} w}} \Delta C_{L_{ref} w} \left(\frac{c'}{c} \right)^2 \right] \\ & - K_p \left[0.25 \cdot C_{L_w} \left\{ \left(\frac{c'}{c} \right)^2 - \left(\frac{c_f}{c} \right)^2 \right\} \right] + K_p \cdot C_{m_w} \left[\left(\frac{c'}{c} \right)^2 - 1 \right] \end{aligned} \quad (\text{F.9})$$

$$K_{\Lambda_{\lambda=0.55}} = 0.0987 \cdot \eta^3 - 0.4045 \cdot \eta^2 + 0.3069 \cdot \eta + 0.0008 \quad (\text{F.10})$$

$$K_{p_{\lambda=0.55}} = -0.6268 \cdot \eta^2 + 1.6718 \cdot \eta - 0.0026 \quad (\text{F.11})$$

$$\Delta C_{L_{ref} w} = 1.05 \cdot \Delta C_{l_w} \left(\frac{C_{L\alpha_w \ M=0}}{C_{l\alpha_w \ m=0}} \right) \quad (\text{F.12})$$

Wing Lift & Moment Increment Factors	
$C_{l\alpha_w}$ (rad^{-1})	6.303
$\frac{c'}{c}$	1.1
$\frac{c_f}{c}$	0.25
δ_f ($^\circ$)	35
$\frac{\Delta C'_m}{\Delta C_{L_{ref} w}}$	-0.20

Table F.1: Wing lift and moment increment factors

F.3 Canard Lift Coefficient Increment

$$\Delta C_{l_{can}} = \delta_e \cdot \left(\frac{C_{l\delta}}{C_{l\delta_{theo}}} \right) C_{l\delta_{theo}} \cdot k' \quad (\text{F.13})$$

$$C_{l\delta_{theo}} = -13.429 \cdot (c_f/c)^2 + 16.637 \cdot (c_f/c) + 0.768 \quad (\text{F.14})$$

$$k'_{c_f/c=0.5} = 5.5767 \cdot \delta_e^3 - 5.9152 \cdot \delta_e^2 + 0.6372 \cdot \delta_e + 1.0534 \quad (\text{F.15})$$

$$\Delta C_{L_{can}} = K_b \cdot \Delta C_{l_{can}} \left(\frac{C_{L\alpha_{can}}}{C_{l\alpha_{can}}} \right) \left(\frac{\alpha_{\delta_{C_L}}}{\alpha_{\delta_{C_l}}} \right) \quad (\text{F.16})$$

$$K_{b_{\lambda=0.55}} = -0.5201 \cdot \eta^2 + 1.5347 \cdot \eta - 0.005 \quad (\text{F.17})$$

F.4 Canard Moment Coefficient Increment

$$C_{m_{can}} = C_{m0_{foil}} \left(\frac{AR \cos^2 \Lambda_{c/4}}{AR + 2 \cos \Lambda_{c/4}} \right) \left(\frac{S_{can} \cdot \bar{c}_{can}}{S_{ref} \cdot \bar{c}} \right) \quad (\text{F.18})$$

$$\begin{aligned} \Delta C_{m_{can}} &= (\bar{x}_{ref} - \bar{x}_{ac_{can}}) \Delta C_{L_{can}} \left(\frac{S_{can}}{S_{ref}} \right) \\ &+ K_p \left[\frac{\Delta C'_m}{\Delta C_{L_{ref can}}} \Delta C_{L_{ref can}} \left(\frac{c'}{c} \right)^2 \right] \left(\frac{S_{can} \bar{c}_{can}}{S_{ref} \cdot \bar{c}} \right) \end{aligned} \quad (\text{F.19})$$

$$K_{p_{\lambda=0.55}} = -0.6268 \cdot \eta^2 + 1.6718 \cdot \eta - 0.0026 \quad (\text{F.20})$$

$$\Delta C_{L_{ref can}} = 1.02 \cdot \Delta C_{l_{can}} \left(\frac{C_{L\alpha_{can} M=0}}{C_{l\alpha_{can} M=0}} \right) \quad (\text{F.21})$$

F.5 Horizontal Tail Lift Coefficient Increment

$$\Delta C_{l_{htail}} = \delta_e \cdot \left(\frac{C_{l\delta}}{C_{l\delta_{theo}}} \right) C_{l\delta_{theo}} \cdot k' \quad (\text{F.22})$$

$$C_{l\delta_{theo}} = -13.429 \cdot (c_f/c)^2 + 16.637 \cdot (c_f/c) + 0.768 \quad (\text{F.23})$$

$$k'_{c_f/c=0.5} = 5.5767 \cdot \delta_e^3 - 5.9152 \cdot \delta_e^2 + 0.6372 \cdot \delta_e + 1.0534 \quad (\text{F.24})$$

Canard Lift & Moment Increment Factors	
$C_{l\alpha_{can}} \text{ (rad}^{-1}\text{)}$	6.250
K_Λ	0
$\frac{c'}{c}$	1.0
$\frac{c_f}{c}$	0.5
$\frac{\Delta C'_m}{\Delta C_{L_{ref can}}}$	-0.20
$\left(\frac{\alpha_{\delta C_L}}{\alpha_{\delta C_l}} \right)$	1.02

Table F.2: Canard lift and moment increment factors

$$\Delta C_{L_{htail}} = K_b \cdot \Delta C_{l_{htail}} \left(\frac{C_{L\alpha_{htail}}}{C_{l\alpha_{htail}}} \right) \left(\frac{\alpha_{\delta C_L}}{\alpha_{\delta C_l}} \right) \quad (\text{F.25})$$

$$K_{b_{\lambda=0.8}} = -0.4196 \cdot \eta^2 + 1.4368 \cdot \eta - 0.0079 \quad (\text{F.26})$$

F.6 Horizontal Tail Moment Coefficient Increment

$$\begin{aligned} \Delta C_{m_{htail}} &= (\bar{x}_{ref} - \bar{x}_{achtail}) \Delta C_{L_{htail}} \left(\frac{S_{htail}}{S_{ref}} \right) \\ &+ K_p \left[\frac{\Delta C'_m}{\Delta C_{L_{ref htail}}} \Delta C_{L_{ref htail}} \left(\frac{c'}{c} \right)^2 \right] \left(\frac{S_{htail} \cdot \bar{c}_{htail}}{S_{ref} \cdot \bar{c}} \right) \end{aligned} \quad (\text{F.27})$$

$$K_{p_{\lambda=0.8}} = -0.2786 \cdot \eta^2 + 1.2986 \cdot \eta - 0.0011 \quad (\text{F.28})$$

$$\Delta C_{L_{ref htail}} = 1.02 \cdot \Delta C_{l_{htail}} \left(\frac{C_{L\alpha_{htail} M=0}}{C_{l\alpha_{htail} M=0}} \right) \quad (\text{F.29})$$

Horizontal Tail Lift & Moment Increment Factors	
$C_{l\alpha_{htail}} \text{ (rad}^{-1}\text{)}$	6.446
K_Λ	0
$\frac{c'}{c}$	1.0
$\frac{c_f}{c}$	0.5
$\frac{\Delta C'_m}{\Delta C_{L_{ref \ htail}}}$	-0.20
$\left(\frac{\alpha_{\delta C_L}}{\alpha_{\delta C_l}} \right)$	1.05

Table F.3: Horizontal tail lift and moment increment factors

F.7 Drag

$$C_{f_{lam}} = \frac{1.328}{\sqrt{Re}} \quad (\text{F.30})$$

$$C_{f_{turb}} = \frac{0.455}{(\log_{10} Re)^{2.58}(1 + 0.144M^2)^{0.65}} \quad (\text{F.31})$$

$$Re_{cutoff} = 38.21 \left(\frac{l}{0.052 \times 10^{-5}} \right)^{1.053} \quad (\text{F.32})$$

Wing, Tail, Strut & Pylon:

$$FF = \left[1 + \frac{0.6}{(x/c)_m} \left(\frac{t}{c} \right) + 100 \left(\frac{t}{c} \right)^4 \right] \left[1.34M^{0.18}(\cos \Lambda_m)^{0.28} \right] \quad (\text{F.33})$$

Fuselage & Smooth Canopy:

$$FF = \left(1 + \frac{60}{f^3} \frac{f}{400} \right) \quad (\text{F.34})$$

Nacelle & Smooth External Store:

$$FF = 1 + \left(\frac{0.35}{f} \right) \quad (\text{F.35})$$

where

$$f = \frac{l}{d} = \frac{l}{\sqrt{(4/\pi)A_{max}}} \quad (\text{F.36})$$

$$C_{D_{LP}} = 1.05 \cdot C_{D0} \quad (\text{F.37})$$

Appendix G

Stability

G.1 Static Stability

$$\frac{\partial \epsilon}{\partial \alpha} = 4.44 \left[\left(K_A K_\lambda K_h \sqrt{\cos \Lambda_{c/4}} \right)^{1.19} \right] \left[\frac{C_{L\alpha_w M=0}}{C_{l\alpha_w M=0}} \right] \quad (\text{G.1})$$

$$K_A = \frac{1}{AR} - \frac{1}{1 + AR^{1.7}} \quad (\text{G.2})$$

$$K_\lambda = \frac{10 - 3\lambda}{7} \quad (\text{G.3})$$

$$K_h = \left(1 - \left| \frac{h_{ac}}{b} \right| \right) \left/ \left(\frac{2 \cdot l_{ac}}{b} \right)^{1/3} \right. \quad (\text{G.4})$$

$$\alpha_0 = \alpha_{0_foil} + \frac{\Delta \alpha_0}{\epsilon_t} \epsilon_t \quad (\text{G.5})$$

$$\left. \frac{\Delta \alpha_0}{\epsilon_t} \right|_{\lambda=0.55} = 0.0252 \cdot \Lambda_{c/4} - 0.4128 \quad (\text{G.6})$$

G.2 Dynamic Stability

G.2.1 Phugoid

$$C_{D_U} = M_1 \frac{\partial C_D}{\partial M} \quad (\text{G.7})$$

$$C_{T_{x_1}} = \frac{T_{x_1}}{q_1 \cdot S_{ref}} \quad (\text{G.8})$$

For steady state:

$$C_{T_{x_1}} = C_{D_1} \quad (\text{G.9})$$

$$C_{T_{x_U}} = -3C_{T_{x_1}} \quad (\text{G.10})$$

G.2.2 SPPO

$$Z_\alpha = -q_1 \cdot S_{ref} \left[\frac{C_{L_{\alpha PAV}} + C_{D_1}}{(W/g)} \right] \quad (\text{G.11})$$

$$M_q = \frac{C_{m_q} \cdot q_1 \cdot S_{ref} \cdot \bar{c}^2}{2 \cdot I_{yy} \cdot U_1} \quad (\text{G.12})$$

$$M_\alpha = \frac{C_{m_\alpha} \cdot q_1 \cdot S_{ref} \cdot \bar{c}}{I_{yy}} \quad (\text{G.13})$$

$$M_{\dot{\alpha}} = \frac{C_{m_\alpha} \cdot q_1 \cdot S_{ref} \cdot \bar{c}^2}{2 \cdot I_{yy} \cdot U_1} \quad (\text{G.14})$$

G.2.3 Sprial

$$L_\beta = \frac{C_{l_\beta} \cdot q_1 \cdot S_{ref} \cdot b}{I_{xx}} \quad (\text{G.15})$$

$$L_r = \frac{C_{l_r} \cdot q_1 \cdot S_{ref} \cdot b^2}{2 \cdot I_{xx} \cdot U_1} \quad (\text{G.16})$$

$$N_\beta = \frac{C_{n_\beta} \cdot q_1 \cdot S_{ref} \cdot b}{I_{zz}} \quad (\text{G.17})$$

$$N_r = \frac{N_{n_r} \cdot q_1 \cdot S_{ref} \cdot b^2}{2 \cdot I_{zz} \cdot U_1} \quad (\text{G.18})$$

G.2.4 Dutch Roll

$$Y_\beta = \frac{C_{y_\beta} \cdot q_1 \cdot S_{ref}}{(W/g)} \quad (\text{G.19})$$

$$Y_r = \frac{C_{y_r} \cdot q_1 \cdot S_{ref} \cdot b}{2 \cdot (W/g) \cdot U_1} \quad (\text{G.20})$$